STABLE METAL ORGANIC FRAMEWORKS FOR THE CATALYTIC DESTRUCTION OF CHEMICAL WARFARE AGENTS

Caroline Elliott

A Thesis Submitted for the Degree of PhD
at the
University of St Andrews

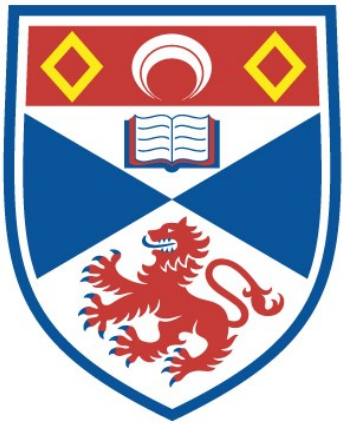

2023

Stable Metal Organic Frameworks for the Catalytic Destruction of Chemical Warfare Agents

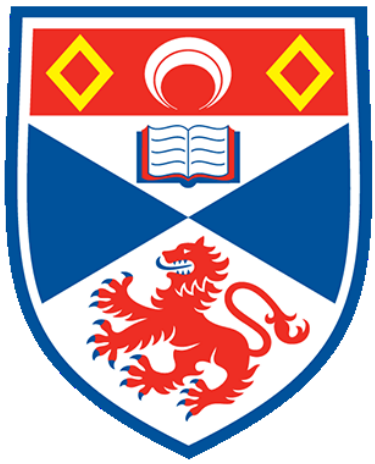

University of
St Andrews

Caroline Elliott

PhD Thesis

This thesis is submitted in partial fulfilment for the degree of

Doctor of Philosophy (PhD)

at the University of St Andrews

June 2023

Declaration

Candidate's declaration

I, Caroline Elliott, do hereby certify that this thesis, submitted for the degree of PhD, which is approximately 47,000 words in length, has been written by me, and that it is the record of work carried out by me, or principally by myself in collaboration with others as acknowledged, and that it has not been submitted in any previous application for any degree. I confirm that any appendices included in my thesis contain only material permitted by the 'Assessment of Postgraduate Research Students' policy.

I was admitted as a research student at the University of St Andrews in September 2018.

I received funding from an organisation or institution and have acknowledged the funder(s) in the full text of my thesis.

Date June 22, 2023 Signature of candidate

Supervisor's declaration

I hereby certify that the candidate has fulfilled the conditions of the Resolution and Regulations appropriate for the degree of PhD in the University of St Andrews and that the candidate is qualified to submit this thesis in application for that degree. I confirm that any appendices included in the thesis contain only material permitted by the 'Assessment of Postgraduate Research Students' policy.

Date June 22, 2023 Signature of supervisor

Permission for publication

In submitting this thesis to the University of St Andrews we understand that we are giving permission for it to be made available for use in accordance with the regulations of the University Library for the time being in force, subject to any copyright vested in the work not being affected thereby. We also understand, unless exempt by an award of an embargo as requested below, that the title and the abstract will be published, and that a copy of the work may be made and supplied to any bona fide library or research worker, that this thesis will be electronically accessible for personal or research use and that the library has the right to migrate this thesis into new electronic forms as required to ensure continued access to the thesis.

I, Caroline Elliott, confirm that my thesis does not contain any third-party material that requires copyright clearance.

The following is an agreed request by candidate and supervisor regarding the publication of this thesis:

Printed copy

No embargo on print copy.

Electronic copy

No embargo on electronic copy.

Date June 22, 2023 Signature of candidate

Date June 22, 2023 Signature of supervisor

Underpinning Research Data or Digital Outputs

Candidate's declaration

I, Caroline Elliott, understand that by declaring that I have original research data or digital outputs, I should make every effort in meeting the University's and research funders' requirements on the deposit and sharing of research data or research digital outputs.

Date June 22, 2023 Signature of candidate

Permission for publication of underpinning research data or digital outputs

We understand that for any original research data or digital outputs which are deposited, we are giving permission for them to be made available for use in accordance with the requirements of the University and research funders, for the time being in force.

We also understand that the title and the description will be published, and that the underpinning research data or digital outputs will be electronically accessible for use in accordance with the license specified at the point of deposit, unless exempt by award of an embargo as requested below.

The following is an agreed request by candidate and supervisor regarding the publication of underpinning research data or digital outputs:

No embargo on underpinning research data or digital outputs.

Date June 22, 2023 Signature of candidate

Date June 22, 2023 Signature of supervisor

Acknowledgements

First and foremost, I would like to thank my supervisor Russell Morris for giving me the oppurtunity to pursue my PhD in his group. I have greatly enjoyed this project, and have appreciated the guidance and support throughout the last few years.

I would also like to thank the EPSRC, University of St Andrews and CRITICAT Centre for Doctoral Training for financial support (grant number EP/L016419/1) and Capital for Great Technologies (grant number EP/L017008/1).

A big thank you to all those from CRITICAT who made the start of my PhD a great experience through laughs in the office, pub trips and the occasional unexpected visit to 601. Especially thank you to Ellie Reid who made settling into Scotland so much easier and who it was great to live with. Another big thank you to Kevin Jones for all his organisational work for CRITCAT, but also for his insightful and enjoyable chats throughout my PhD.

To the REM group, and tag alongs, past and present I owe you a huge thank you for all your help getting through this PhD. I will take away so many happy memories of wine clubs, conferences and even beam time with you all! I hope you all continue having fun and continue the REM group's reputation long into the future!

A special thank you to the friends I could not have done this without. To Simon, I am so grateful for all your help and guidance through the last few years, but most importantly for your friendship. We had some great times in Eddie court, especially those games and cocktail nights that ended so well! To Ella, firstly thank you for being there in that last year of undergrad - how did we made it out! But also for the much needed chats about the PhD, coupled with nights out in Edinburgh. Also to Alice, although we have lived on the other side of the country for the last 5 years, the trips down to see you or to Aviemore were some of the best times in my PhD. I really value your down to earth chats and your friendship for the last 13 years.

I will be eternally grateful for the love and support from my family over the last few years. To Mum, Dad, Louise and Herb, thank you for being there unconditionally. It has not been an easy few years, and knowing that I could always come home to you has meant the world.

And finally to Cam, I could not have done this without you. Thank you for always listening and cheering me up through your cooking, cocktail making, and willingness to play boardgames. Your constant love and support these last years have meant so much.

For Uncle Bry.

Abstract

The work described within this Thesis has focused on the preparation and characterisation of metal-organic frameworks (MOFs) as catalysts for the hydrolysis of the nerve agent simulant dimethyl 4-nitrophenyl phosphate (DMNP).

Mixed-metal MOFs were explored for this application using a combination of zirconium and hafnium in known MOFs in order to investigate the role of Lewis-acidity on catalysis. A series of mixed-metal MOFs were prepared and successfully catalysed the hydrolysis of DMNP. For UiO-66 and NU-1000 the highest rates were seen for the Zr 100% samples. For MOF-808 the most successful catalyst was found to be the Zr 33% Hf 66% sample. Further investigations compared properties of each sample and concluded that a change in Lewis-acidity plays a role in the catalytic activity, despite differences in material characteristics.

Mixed-linker MOFs were also investigated through the addition of di-topic linkers to a MOF-808 synthesis. For each sample, *ca.* 10% of a chosen di-topic linker, as a proportion of linker present, was incorporated into the MOF-808 structure. Further investigations using the 5-amino isophthalic acid di-topic linker found up to 25% of 5-amino isophthalic acid could be incorporated into MOF-808. All samples successfully hydrolysed DMNP, with the 20% 5-amino isophthalic acid MOF-808 sample giving the highest rate and out-performing the parent MOF-808 sample.

Investigations into preparing MOF-composite materials were also carried out. This focused on incorporating MOF-808 into the materials PET, cotton, silk and nylon, using a range of synthesis methods. Loading estimates were calculated through q-NMR measurements. All materials saw MOF-808 successfully deposited on the surface, with the exception of one sample. All materials tested as catalysts for the hydrolysis of DMNP outperformed the blank samples. MOF-808

had therefore retained catalytic properties within the composite material. The hydrothermal synthesis method using PET displayed the highest initial rate for all composite materials prepared.

Publications

Publications outside the scope of this work:

Controlled Synthesis of Large Single Crystals of Metal-Organic Framework CPO-27-Ni Prepared by a Modulation Approach: In situ Single-Crystal X-ray Diffraction Studies.
Simon M. Vornholt, Caroline G. Elliott, Cameron M. Rice, Samantha E. Russell, Peter J. Kerr, Daniel N. Rainer, Michal Mazur, Mark R. Warren, Paul S. Wheatley, and Russell E. Morris, *Chem. Eur. J.*, 2021, **27**, 18537-8546.

Surface-Functionalized MetalOrganic Frameworks for Binding Coronavirus Proteins
Aamod V. Desai, Simon M. Vornholt, Louise L. Major, Romy Ettlinger, Christian Jansen, Daniel N. Rainer, Richard de Rome, Venus So, Paul S. Wheatley, Ailsa K. Edward, Caroline G. Elliott, Atin Pramanik, Avishek Karmakar, A. Robert Armstrong, Christoph Janiak, Terry K. Smith, and Russell E. Morris, *ACS Appl. Mater. Interfaces*, 2023, **15**, 90589065

In situ single-crystal synchrotron X-ray diffraction studies of biologically active gases in metal-organic frameworks.
Russell M. Main, Simon M. Vornholt, Cameron M. Rice, Caroline G. Elliott, Samantha E. Russell, Peter J. Kerr, Mark R. Warren and Russell E. Morris, *Commun Chem*, 2023, **6**, 44.

List of Abbreviations

BDC - 1,4-Benzenedicarboxylic acid (Terephthalic acid)
BSE - Back-scattered secondary electrons
BTC - 1,3,5-Benzenetricarboxylic acid
CWA - Chemical Warfare Agent
DLS - Dynamic Light Scattering
DMF - Dimethylformamide
DMNP - N,N-Dimethylethylamine
EDS - Energy Dispersive X-ray Spectroscopy
MOF - Metal Organic Framework
NEM - *N*-Ethylmorpholine
PET - Polyethylene terephthalate
PPE - Personal protective equipment
PSE - Post-synthetic exchange
PSM - Post-synthetic modification
PTE - Phosphotriesterase
PXRD - Powder X-ray Diffraction
SBU - Secondary building unit
SEM - Scanning Electron Microscopy
TGA - Thermogravimetric analysis

Contents

Chapter 1

Introduction

1.1 Chemical Warfare Agents

Harmful chemicals have been used throughout history, with records of hazardous materials being used as weapons dating back to ancient times. Evidence for the use of these chemicals can be found as far back as ancient Greek and Roman times (*ca.* 600 B.C.). The first reports of chemicals used in warfare include hellebores roots being used by humans to contaminate water supplies, containers of venomous snakes thrown towards enemy troops, and poisoning wine to sedate enemies.[1] Throughout history reports exist of chemical use in warfare; however, the industrial era is where weaponised chemicals became a heightened threat to the global community.

Chemical production accelerated in the industrial era, enabling the large-scale manufacture of many chemicals. This increased production capacity, combined with increased knowledge of toxicological effects, resulted in the development and synthesis of chemicals specifically designed to be used as weapons: chemical warfare agents (CWAs). Due to the relatively small amounts of chemicals needed to cause widespread death and destruction, compared to conventional weapons, CWAs are classed as weapons of mass destruction (WMDs).[2]

Table 1.1: Classes of major chemical warfare agents. All symbols designated by the US Army.

Group	Chemical	Common Name	Symbol
Nerve agents	Ethyl-textit{N,N}-dimethyl -phosphoramidocyanidate	Tabun	GA
	Isopropyl methyl phosphonofluoridate	Sarin	GB
	Cyclohexyl methyl phosphonofluoridate	Cyclosarin	GF
	Pinacolyl methyl phosphonofluoridate	Soman	GD
	textit{o}-Ethyl-S-(2-diisopropylamino-ethyl) -methyl phosphonothiolate	-	VX
Vesicant agents	Bis(2-chloroethyl)sulfide	Sulfur Mustard	HD
	Bis(2-chloroethylthioethyl)ether	Agent T	HT
	Tris(2-chloroethyl)amine	Nitrogen Mustard	HN-3
	2-Chlorovinyl dichloroarsine	Lewisite	L
Lung-damaging agents	Carbonyl chloride	Phosgene	CG
	Trichloromethyl chloroformate	Diphosgene	DP
Blood agents	Hydrogen Cyanide	-	AC
	Cyanogen chloride	-	CK

All chemical warfare agents are chemicals intended to incapacitate, seriously injure or kill individuals upon exposure. A large number of chemicals have been discovered and synthesised for use. Currently known chemical weapons can be split into classes given in Table 1.2. Biological weapons are also classed as warfare agents due to their toxic and destructive properties; however, these will not be discussed in this thesis. Of the classes given, vesicant and nerve agents are the most used, and most destructive, therefore will be discussed further below.

1.1.1 Vesicant agents

1.1.1.1 History

Vesicant agents are chemicals which cause severe irritation and blistering upon contact with the skin or respiratory system. Structures of the main vesicant agents can be seen in Figure 1.1. Sulfur mustard (HD) is the most widely deployed, produced and stockpiled CWA due to its prolific use in WWI.[3]

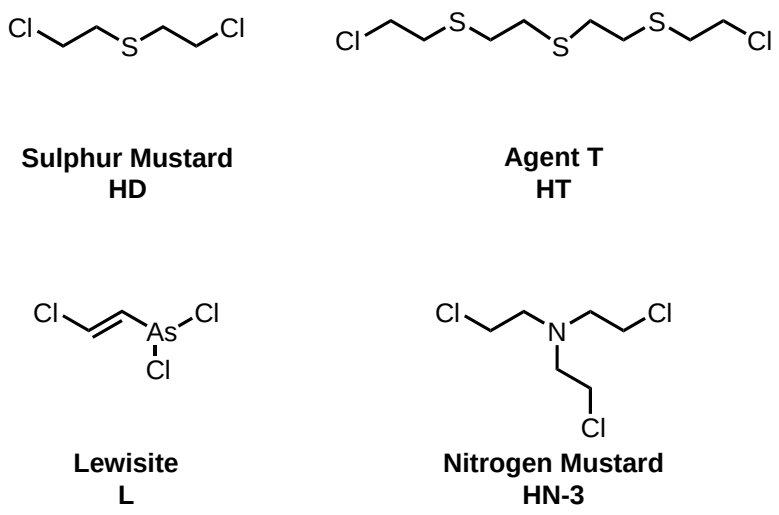

Figure 1.1: Chemical structures of vesicant agents.

Sulfur mustard was first synthesised in 1822, however the toxic properties were only recognised in 1860 and production of the purified compound was first reported in 1886.[4] Although toxic chemicals had previously been used in warfare such as phosgene and chlorine in WWI, these chemicals had been used previously within industry. Sulfur mustard became the first chemical to be explicitly developed for use as a chemical warfare agent.

The first use of sulfur mustard on the battlefield was by German forces in July 1917. This was the first agent that injured masked soldiers as exposure caused skin blistering and cutaneous uptake. After the use of HD the number of injured soldiers increased rapidly, although the comparative lethality was low (2%), the number reporting ongoing effects was higher than other weapons.[5]

After WWI many nations explored analogues of sulfur mustard in order to identify those with higher efficacy. Nitrogen analogues were investigated, with the most prominent being tris-(2-chloroethyl)amine (HN-3). Organic arsenicals were also investigated by both Germany and the USA due to vesicant-like properties; 2-chlorovinyl dichloroarsine (Lewisite) was identified as the most favourable. However, Lewisite was found to be inferior to HD in producing lesions and persistence. During WWII, a superior HD analogue, bis-(2-chloroethylthioethyl)ether (HT), was found through a non-purified HD synthesis. This was over 3 times more toxic than sulfur mustard and was subsequently used as a mixture of 60% HD, 40% HT.[6]

1.1.1.2 Destruction Methods

Since the first use of these agents, methods for detoxifying and destroying them have been investigated. These efforts increased with the ratification of the Chemical Weapons Convention in 1997 which prohibits the development, synthesis, stock piling and use of all chemical warfare agents.[7]

Methods to detoxify vesicant agents focus mainly on sulfur mustard as it is the most notorious vesicant agent, with hundreds of thousands of tonnes having been stockpiled since WWI. Sulfur mustard has also been reportedly used against civilian and military personnel in the Middle East within the last decade,[8] therefore the need for on-going development of materials to adsorb and destroy this agent is necessary.

The three primary routes for HD detoxification are hydrolysis,[6] dehydrohalogenation,[9] and oxidation[10] [Figure 1.2]. As vesicant agents have poor solubility in water; droplets of HD dispersed in water form a polymeric crust, the hydrolysis degradation route is very slow and limits the effectiveness in large scale degradation applications.[11] This is also true for the dehydrohalogenation route, where using CaO nanoparticles as a catalyst results in a half life of 4 hours.[9]

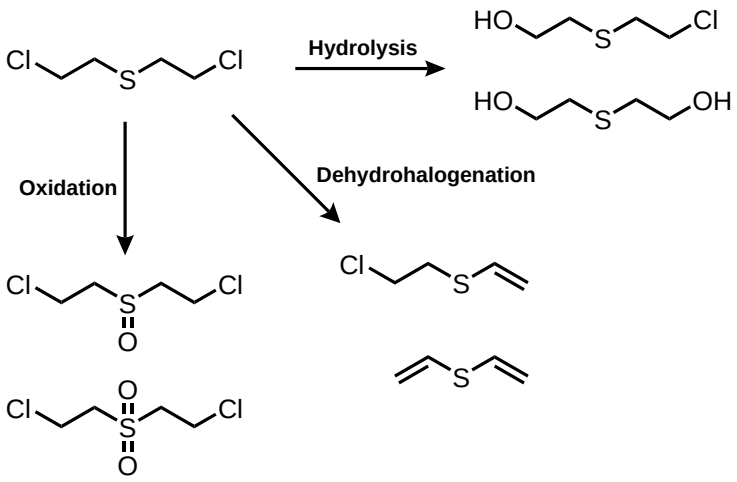

Figure 1.2: Common pathways of detoxifying sulfur mustard. Adapted from Howarth *et al.* [12].

The most promising route for sulfur mustard detoxification is the oxidation route. However, the oxidant must be chosen that only partially oxidises the agent to the sulphoxide (HD−O), as complete oxidation results in the undesirable sulphone product (HD−O_2) which is also a vesicant agent that causes blistering.[11]

As this project focuses on the hydrolysis pathway for the degradation of CWAs, further work on vesicant agents will not be carried out owing to the immiscibility of HD with water.

1.1.2 Nerve Agents

1.1.2.1 History

The other, and more notorious, category of CWA are the organophosphorous (OP) nerve agents. Nerve agents can be split into two further categories; German(G)-agents and Venomous(V)-agents. These compounds are extremely toxic to humans and more deadly than vesicant agents. Structures of the G and V nerve agents can be seen in Figure 1.3.

The first highly toxic OP synthesised was tetraethylpyrophosphate in the mid-1800s in France. However the high toxicity of these compounds was not recognised until the 1930s when the P−F bond was investigated.[13]

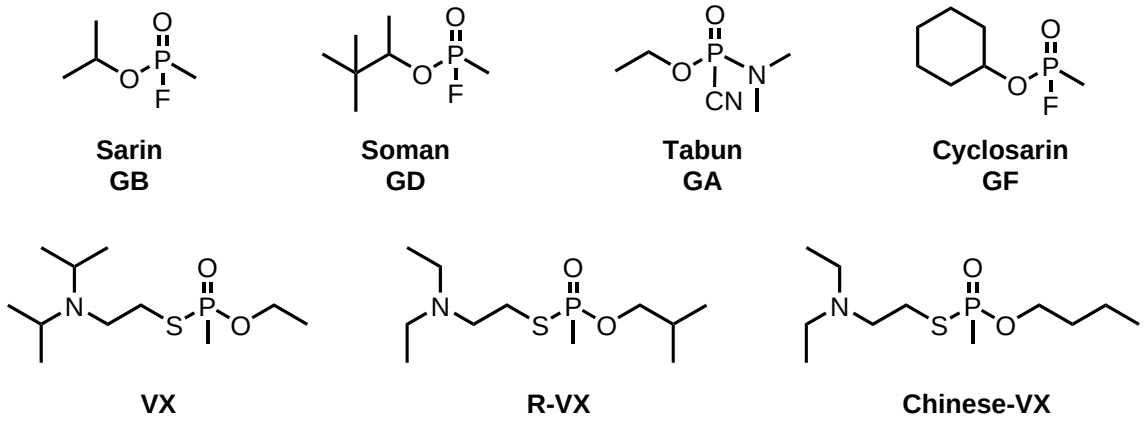

Figure 1.3: Chemical structures of organophosphorus nerve agents with G-agents (top) and V-agents (bottom).

In 1934, German investigations into synthesising insecticides was started. This led to the synthesis of over 2000 compounds containing O−P bonds, including the highly toxic ethyl-*N*,*N*-dimethylphosphor-amidocyanidate (tabun), iso-propyl methylphosphonofluoridate (sarin) and pinacolyl methylphosphonofluoridate (soman) prepared in 1936, 1937 and 1944 respectively. When the extent of the toxicity of these compounds became apparent, the German Ministry of War declared all patents relating to these compounds as top secret. During that time over 200 compounds were designated top secret due to the possible military significance they posed.

Of these compounds, only tabun, soman and sarin were selected to become industrially prepared as CWAs.[2] Industrial preparation of these CWAs was hampered by the corrosive nature of precursors such as hydrofluoric acid, and the industrial scale-up of soman production was never completed. However, by the end of WWII, 10,000 - 12,000 tonnes of tabun and 600 tonnes of sarin had been synthesised.

Outside of Germany, both the UK and USA labs had focussed attention on other chemical agents and only became aware of the German nerve agent project after WWII was over. Intensive research on these chemicals soon started in the USA, UK, France and the Soviet Union as the military significance became apparent. Stockpiling of CWAs began shortly after, with both the USA and USSR having stockpiles of sarin amounting to several thousand tonnes.

The preparation of OP esters containing 2-aminoethanethiols was achieved by ICI laboratories in the 1950s and shared with the UK government who started investigations in the military lab at Porton Down. A combined study by the UK and USA laboratories resulted in the discovery of a new agent, ethyl-S-2-diisopropylaminoethylmethylphosphonothioate (VX), and with it a new class of even deadlier nerve agents: V-class agents.

Until recent studies, VX, remained the most deadly CWA produced with a lethal dose of 0.3 mg/person inhalation or 5 mg/person through dermal exposure.[14] Both the USSR and China prepared a variant of VX: R-VX and Chinese-VX, respectively. Further research into sarin and V-class agents continued in the USA where the weaponisation of these agents was attempted. The Binary Weapons Programme of the 1950s researched the concept of containing two less toxic reagents separately, which when detonated react to produce the required nerve agent. Binary projectiles for sarin and VX were successfully developed in the USA.

Unknown to the USA, whilst the Binary Weapons Programme was underway, further investigations on nerve agents were being carried out by the USSR. This research let to the development of the third generation of nerve agents with higher toxicity compared to the other known nerve agents known as A-agents. At the time these CWAs were synthesised in order to evade the standard NATO detection equipment.

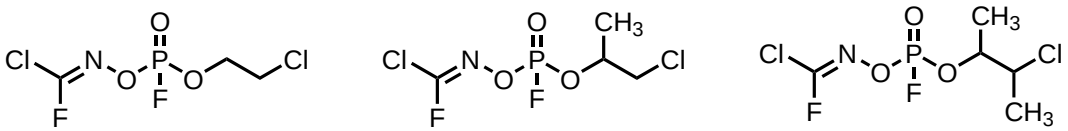

Figure 1.4: Potential chemical structures of A-agents.[15]

The little information known about these agents has been based on published works by Soviet chemists known to have worked on this project. From these publications it is thought that three A-agents were synthesised although the exact structures and toxicities are unknown but plausible structures can be seen in Figure 1.4. The USSR used the Binary Weapons concept to overcome the instability of A-agents by using more stable precursors. These precursors

were common in the chemical industries and referred to as NOVICHOKs. The information on synthesis, chemical properties, toxicity and military intentions of A-agents and NOVICHOKs are still classified as "top secret".[15]

1.1.2.2 Mode of action

Nerve agents act by inhibiting the active site of the acetylcholinesterase (AChE) enzyme [Figure 1.5]. AChE is an enzyme responsible for hydrolysing the neurotransmitter acetylcholine (ACh) in postsynaptic membranes and neuromuscular junctions. Acetylcholine is released when nerve impulses reach a nerve ending, and binds to the ACh receptor site on the postsynaptic membranes, where it causes stimulation of the nerve. AChE hydrolyses the ACh which allows the muscles to relax. The enzymatic hydrolysis comprises of acid-based reactions and nucleophilic addition involving the catalytic trio of glutamic acid, serine and histidine.[16]

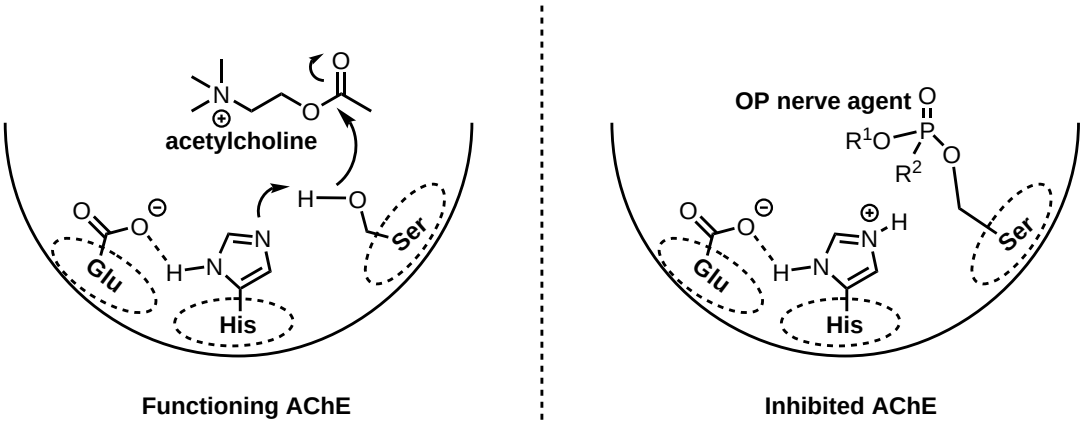

Figure 1.5: The active site of the AChE enzyme. AChE hydrolysis of acetylcholine (left), and inhibition of AChE with organophosphate nerve agent (right).

The inhibition of AChE by organophosphate nerve agents proceeds through irreversibly binding to the active site, preventing ACh from binding and subsequently hydrolysing. The build-up of ACh in the body results in constant stimulation of nerves and muscles, leading to seizures, respiratory failure, and eventually death. The phosphorylated AChE is stable and may undergo secondary processes such as reactivation-hydrolysis, however this hydrolysis is much slower compared to the ACh hydrolysis. The other process is the breaking of the $P-OR^1$ bond on the bound organophosphorus which leads to "aging" of

the enzyme. If this occurs the AChE cannot be reactivated and the inhibition is completely irreversible.[7]

The rate of binding between organophosphorus nerve agents and AChE results in the difference in toxicity: lethal dose (LD_{50}) and lethal concentration (LC_{50}) varies between agents [Table 1.2]. The toxicity of V-agents are an order of magnitude larger than G-agents; the G-agent sarin has a estimated human lethal percutaneous does of 1500 mg/man, whereas the respective lethal dose of the V-agent VX is 6 mg/man.[17]

Table 1.2: Toxicity of nerve agents. Adapted from reference 7.

Nerve agent	**LD_{50} (mg/man)**	**LC_{50} (ppm)**
GB (Sarin)	1500	1.2
GA (Tabun)	1000	2
GD (Soman)	350	0.9
GF (Cyclo-sarin)	30	-
VX	6	0.3

1.1.2.3 Destruction Methods

Efforts to develop methods to destroy and protect against nerve agents has intensified in the last few decades due to the increasing frequency of nerve agent attacks against civilians and military personnel. During the first Gulf War in 1991 as many as 100,000 US troops may have been exposed to sarin,[18] and a terrorist attack in Japan in 1995 left 12 dead and 5000 injured when sarin was released on the metro.[19] More recently, attacks in the Syrian conflict in August 2013 saw the use of sarin against the civilian population which resulted in 1400 deaths,[20] and in 2018 the use of NOVICHOK agents was detected in the UK.[15]

The ratification of the Chemical Weapons Convention (CWC) also resulted in countries with significant stockpiles of nerve agents (USA and Russia) to begin decontamination efforts. To date, stockpiles are still being steadily reduced with the 2013 Noble Peace Prize being awarded to the Organisation for the Prohibition of Chemical Weapons (OPCW).

For stockpiled nerve agents, there are two primary methods employed: incineration and neutralisation by base hydrolysis. Incineration is known as the

"baseline" system and was first endorsed in 1982. Large scale incineration systems have been in place since 1993 and operate in the USA, Germany and the UK.[14] The incineration process is given in Scheme 1.1 and is a three stage process, requiring furnaces of temperatures 1480 °C and 1090 °C. The products of the incineration are treated in a pollutant abatement system, however, concerns about possible dangerous emissions from this process has lead to other methods being explored.

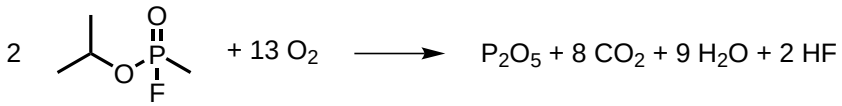

Scheme 1.1: Incineration of sarin used in stockpile destruction.

The alternative method to incineration is base hydrolysis which has been implemented in the USA, UK, Canada and Iraq.[14] The hydrolysis of G-agents with sodium hydroxide is possible at ambient temperatures and is given in Scheme 1.2. The products of this process are loaded into steel drums and kept in hazardous waste deposits. V-agents can also be hydrolysed by sodium hydroxide in the same process, however the room temperature synthesis also produces the hazardous by-product EA 2192 which is subjected to further treatment before final disposal.[21]

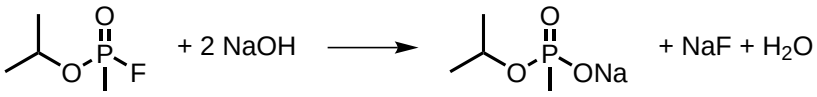

Scheme 1.2: Base hydrolysis of sarin used in stockpile destruction.

Although methods exist that are suitable for stockpile destruction, other methods must be investigated for use in protective equipment for military and civilian personnel in the event of an attack. This equipment must capture and degrade nerve agents in real-time, whilst being suitable to wear and a stable shelf life for facile use in the event of an attack.

As both sarin and soman are totally miscible in water, hydrolysis is a promising choice for detoxification of these agents. For both agents, the reaction proceeds via an S_N2 mechanism on the phosphorus to give the non-toxic final product of methylphosphonic acid (MPA) [Scheme 1.3]. In the case of sarin, the water hydrolysis is temperature and pH dependent: at 20 °C and pH 6.5 the half life of

sarin is 461 h, this reduces considerably at pH 7.5 with a half life of 46 h. If the temperature is also raised to 25 °C the half life reduced further to 24 h at pH 7.5. At 0 °C the reaction is negligible with a half life of 8300 h (pH 6.5).[6] For soman, the reaction proceeds slower with a half life of 60 h at 25 °C and pH 6.5. Reaction rates for both sarin and soman can be greatly approved if the pH is raised above 10; both agents reach complete hydrolysis after a few minutes. With the product of the reaction being acidic, excess base is required to maintain the pH and the elevated rate.[22]

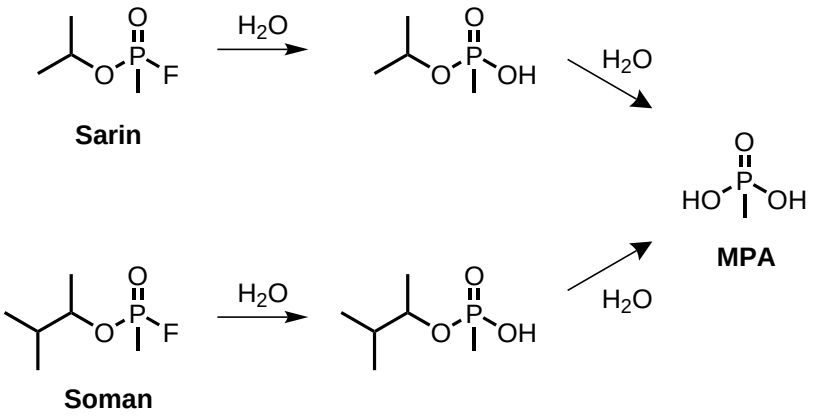

Scheme 1.3: Water hydrolysis of sarin (top) and soman (bottom) to produce the non toxic product MPA.

The hydrolysis pathway for tabun depends on the pH of the solution but results in phosphoric acid in either case [Scheme 1.4]. For neutral and basic conditions the by-product is cyanide, whereas in the acidic case, dimethylamine is formed. The rate is slowest at neutral conditions, with a half life of 8 h at 20 °C and pH 7.4. However this is around four times as fast as the rate seen for soman.[7]

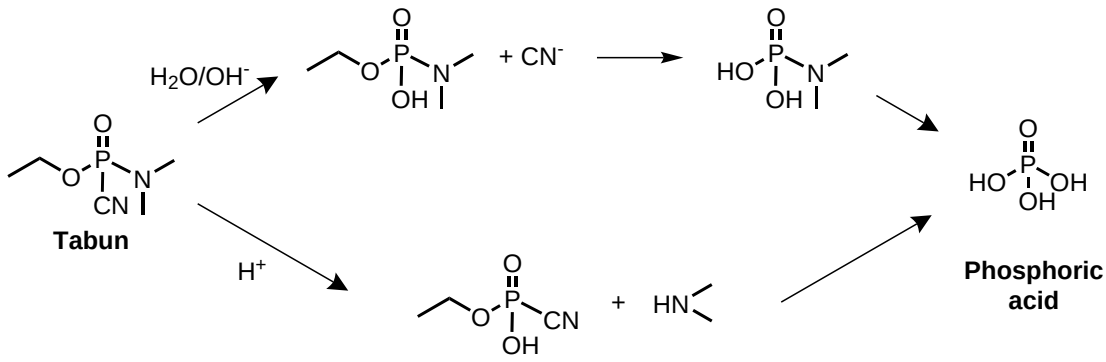

Scheme 1.4: Water hydrolysis of tabun showing alternative routes to phosphoric acid depending on the reagent.

The water hydrolysis of VX is more complex than for the G-agents, and the lack of solubility in water results in half lives of between 17 - 42 days at 25 °C at pH 7.[23] The reaction pathway is also dependent on pH, with either P−S or P−OEt bond cleavage [Scheme 1.5]. At neutral or slighly basic pH (7-10) the breaking of the P−OEt bond predominates, resulting in the formation of (S)-(2-diisopropylaminoethyl)methyl phosphonothioate (EA 2192); a chemical as toxic as VX. At more acidic or more basic conditions (pH <6, >10) the P−S bond cleavage is favoured and the non-toxic products ethyl methylphosphonic acid (EMPA) and diisopropylethyl mercaptoamine (DESH) are formed.[21]

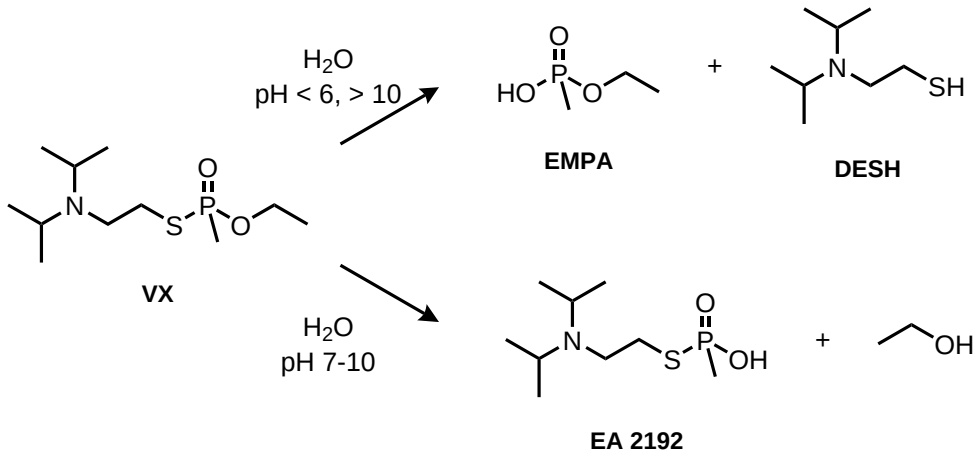

Scheme 1.5: Water hydrolysis of VX showing alternative products depending on pH.

Even at a controlled pH a mix of products are seen in the hydrolysis of VX; in an aqueous 0.1 M NaOH solution VX was hydrolysed to 87% EMPA and 13% EA 2192 with a half life of 13 min. EA 2192 is very stable in water with no degradation observed after 1000 h at room temperature. Only at temperatures of 90°C in concentration sodium hydroxide can EA 2192 be decomposed to the non-toxic products of a methyl phosphite and a thiolate.[6]

Other methods to decompose nerve agents have been investigated such as perhydrolysis, where peroxides are used for decontamination. This has shown advantages at cold temperatures and in some cases faster rates than the water hydrolysis for sarin.[24] Oxidation with bleach and related reagents, the original decontamination technique in WWI, have also been thoroughly investigated,[25] and using alkoxides as nucleophiles has been successful in destroying VX with more efficiency than the water hydrolysis.[21]

1.1.3 Simulants

As nerve agents possess such high toxicity, they are unsuitable for use in research without specialist training and equipment. Strict controls in place on the use of nerve agents also mean few institutions are able obtain and use these agents for research purposes. Instead, comparatively non-toxic simulant molecules are used which share similar structures and reactivity to nerve agents, allowing initial research to be undertaken without specialist regulations.

Examples of simulants that are used in-place of G-agents include dimethyl methylphosphate (DMMP), diisopropylfluorophosphate (DFP), dimethyl chlorophophate (DMCP), and dimethyl 4-nitrophenylphosphate (DMNP) [Figure 1.6]. These simulants are all P(V) based, with some used as organophosphate pesticides (DMNP). These simulants hydrolyse with the same mechanism as nerve agents, therefore are used for investigations into catalytic hydrolysis of nerve agents. The most commonly used simulants are DMNP and DMMP.[7,26]

Figure 1.6: Chemical structures of simulants used to mimic G-agents in research.

Although simulants have practical advantages over nerve agents, the reactivity does not exactly correlate. Catalytic hydrolysis rates can differ between nerve agents and simulants, as well as between simulants; in one instance DMMP did not react, whilst DMCP displayed a faster rate than either sarin or soman.[27] It is also interesting that although DFP hydrolysis cleaves the same bond as many nerve agents: P−F, reaction rates are slower. Overall, DMNP has been found to have the most comparable hydrolysis rates as sarin and soman when MOFs are used as catalysts.[26]

Whilst suitable simulants have been identified for G-agents, V-agents exhibit a more complicated structure that is difficult to replicate due to the unique intramolecular amino nitrogen effect with most simulants only capable of mimicking limited aspects of VX reactivity.[21] Many studies require the live agent to be monitored by ^{31}P-NMR spectroscopy when investigating P−S

bond cleavage; a hazardous and slow process.[28] Recently, a V-agent simulant, *O*,*O*-diethyl *S*-phenyl phosphorothioate (DEPPT), has been investigated that is somewhat successful in emulating the P−S bond reactivity whilst allowing monitoring via UV-Vis spectroscopy through the use of a reporter molecule 5,5-dithiobis(2-nitrobenzoic acid) (DTNB) [Scheme 1.6].[29]

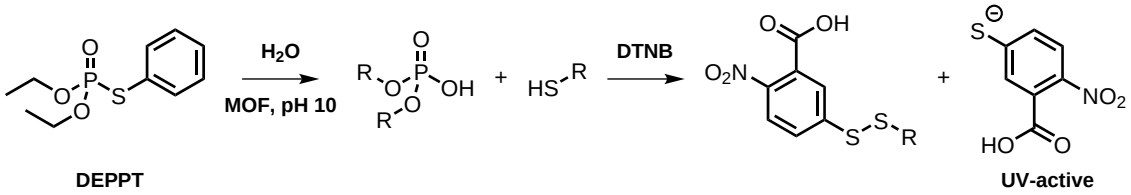

Scheme 1.6: MOF catalysed water hydrolysis of the VX simulant, DEPPT, with a reporter molecule allowing for monitoring via UV-Vis spectroscopy.

An alternative to using simulants in place of live agents is to simulate nerve agent reactions computationally. Reaction mechanisms can be studied without safety considerations and can be used to develop and advance experimental studies. Modelling studies have been used to identify optimum routes for nerve agent degradation,[30] successful catalysts,[31,32] and reaction mechanisms.[33,34] Computational studies can also be used to identify simulants with reaction mechanisms that most closely compare to live agents, allowing better understanding of experimental studies.[35]

1.2 Metal Organic Frameworks

This section introduces metal-organic Frameworks (MOFs); a class of porous materials. The research into these materials is extensive so this section will mainly focus on catalytic applications, and specifically MOFs that have previously shown success as catalysts for the hydrolysis of CWAs and simulants.

1.2.1 History

Since the mid-20th century there has been considerable interest given to the research of porous materials. These materials are classed by pore size as determined by the International Union of Pure and Applied Chemistry (IUPAC). Microporous materials have a pore size smaller than 2 nm, mesoporous materials have pore sizes in the range of 2 nm - 50 nm, and macroporous are those materials with pores exceeding 50 nm.[36]

Zeolites are a type of microporous material that have been investigated since the 1940s for industrial uses. The structure of zeolites is made of corner sharing TO_4 (Ti = Al, Si) tetrahedra which form porous structures.[37] These materials show excellent thermal and chemical stability and have found widespread application in many areas such as catalysis,[38] gas adsorption and separation,[39] and ion-exchange.[40]

Although zeolites have found success in a range of applications, there is a limit to the structures that can be synthesised or found in nature. Most zeolites also have pore sizes of less than 2 nm and are challenging to functionalise,[41] therefore, there was a need for easily tunable porous materials. Considerable work and discussions in the late 1980s and early 1990s resulted in the first of such a material to be reported by Yaghi *et al.* in 1995.[42] Yaghi first coined the term metal-organic framework (MOF) to describe the material: zinc acetate connected by terephthalic acid (BDC) to form an infinite framework with permanent porosity of 2300 m^2/g. This material, named MOF-5, broke surface-area records for these materials at the time.

Since the publishing of MOF-5, research into MOFs has increased at an astonishing rate with almost 100,000 structures recorded in the Cambridge Structural Database (CSD) as of 2020.[43] The continued interest and research into these

materials can be attributed to the immeasurable variety of building units and organic linkers. Structures and functionality of MOFs can be tuned through the precursors to form highly porous materials with applications in gas storage,[44] catalysis,[45,46] drug delivery,[47,48] and CO_2 capture.[49]

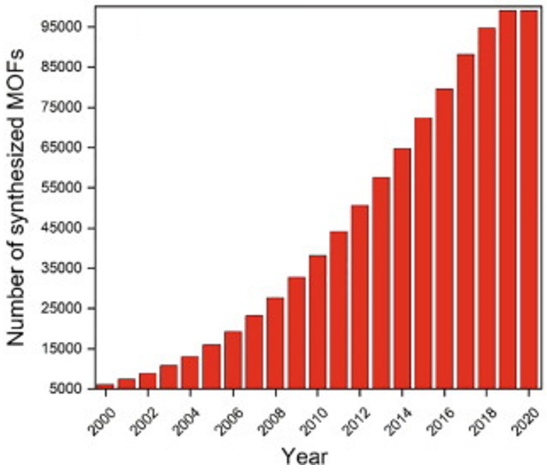

Figure 1.7: Cumulative number of structures within the CSD by year.[43]

1.2.2 Structure and Design

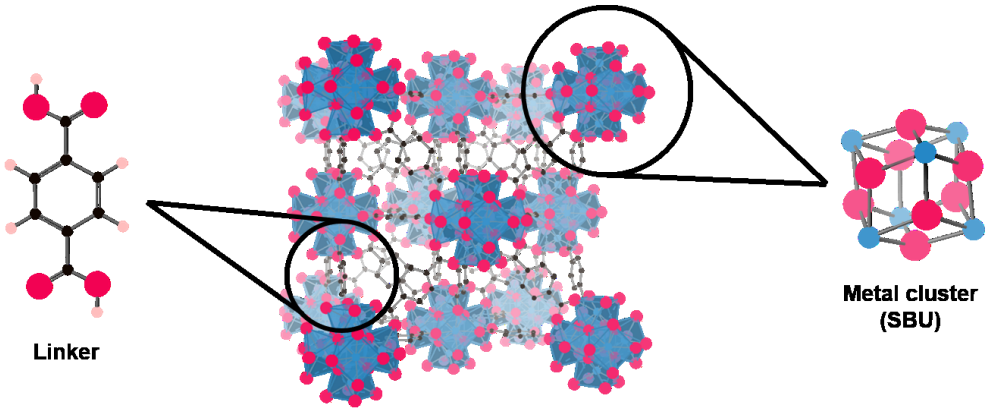

Figure 1.8: A structural representation of a metal organic framework showing the constituent elements; the metal secondary building units (SBUs) and organic linkers.

The immense attention that has surrounded MOF research over the last few decades can be attributed to the ability to tune and "design" these materials. Although the term "design" has been contested, the chemistry of the components that make up MOFs, the metal containing secondary building unit (SBU) and the

organic linker, aid understanding and direction of synthesis efforts. As different applications require different functionality, porosity and stability the SBU and linker can be chosen accordingly. An example of a typical MOF structure and components is shown in Figure 1.8.

In recent years, a strategy for developing MOFs has used reticular chemistry, where reticular is derived from the Latin "reticulum" meaning net-like.[50] Preselecting MOF components with desired geometry allows the formation of underlying nets in which a material can be based upon. This has been widely successful in allowing deliberate design and construction of materials for a range of applications [Figure 1.9].[51,52]

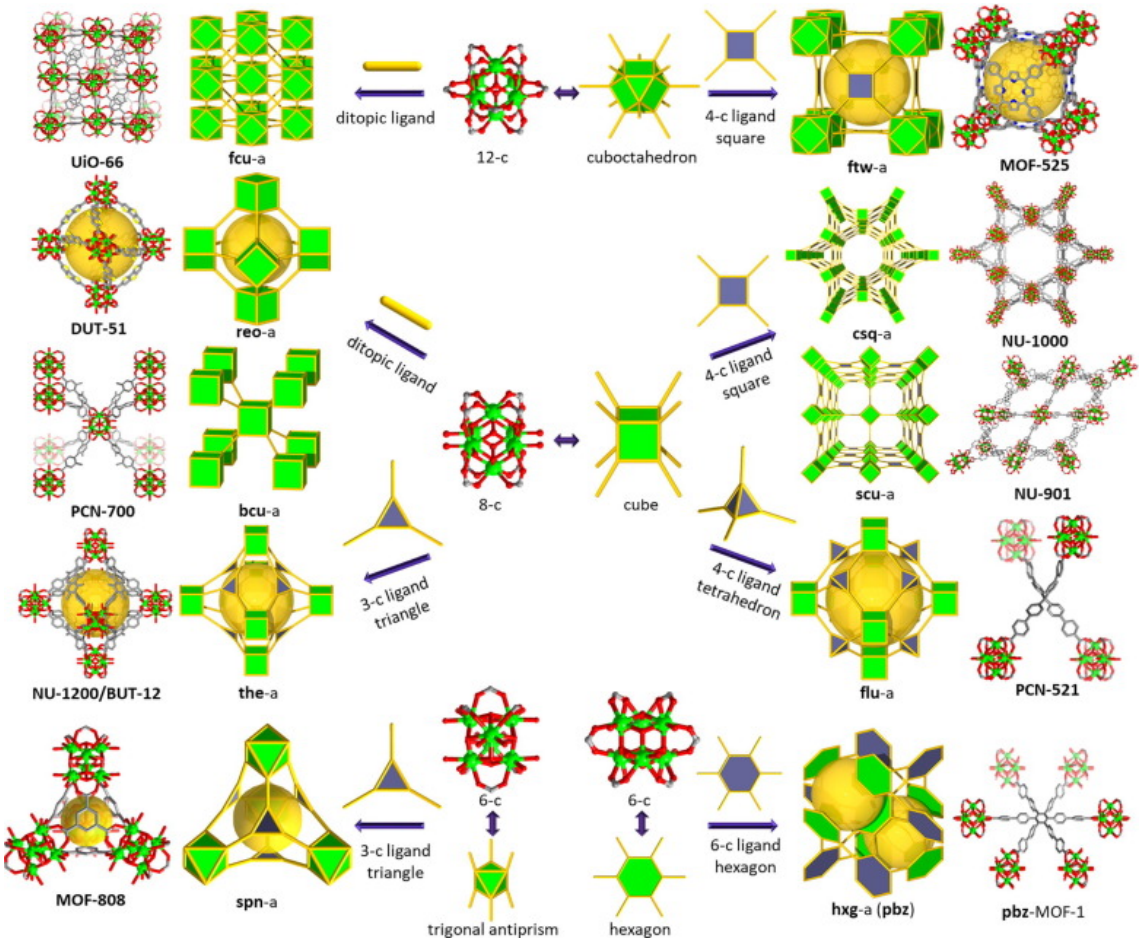

Figure 1.9: Illustration of the use of reticular chemistry in the design of MOFs applied to Zr-MOFs. SBUs and linkers are represented as nets to illustrate the topology of each structure. Figure taken from reference 52.

1.2.2.1 Secondary building units

Secondary building units (SBUs) are polynuclear clusters consisting of metal ions held together by organic functional groups such as carboxylates. These bring thermodynamic stability to the MOF structure due to the strong bonds within the SBU (M−O, C−O and C−C), as well as mechanical stability as the metal ions are held in position to form long range crystalline structures.[53]

SBUs can adopt a range of structures depending on the metal ion chosen and synthesis conditions [Figure 1.10]. The SBU observed in MOF-5 by the reaction of zinc ions with BDC resulted in the structure $[Zn_4O(BDC)_3]$,[42] the zinc metal can be exchanged for many different metals to give the same underlying SBU structure. The paddle-wheel SBU is observed in the Cu-MOF HKUST-1 formed from copper and benzene-tricarboxylate (BTC) $[Cu_3(BTC)_2(H_2O)_3]$,[54] this paddle-wheel structure can also be formed with zinc. Using the same linker as MOF-5, BDC, but changing the metal to zirconium with altered reaction conditions, the well known MOF UiO-66 forms with the SBU $[Zr_6O_4(OH)_4(BDC)_6]$.[55] This SBU can also be formed with other Group 4 metals such as Ti and Hf.

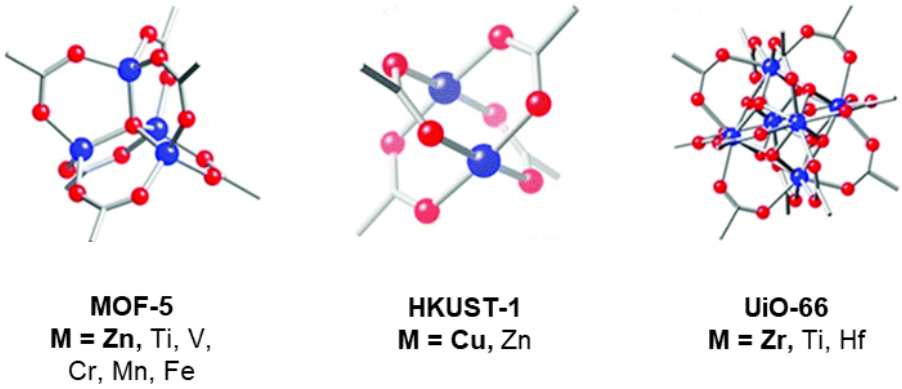

Figure 1.10: SBUs of well known MOFs (blue - metal, red - oxygen, grey - carbon). Bold metal indicates species found in named MOF. Figure adapted from reference 56.

The chemical nature of SBUs has a strong influence on the MOF application as the bonds between linkers and SBUs exhibit the highest reactivity within the structure. This allows post-synthetic modifications (PSMs) to be carried out on the SBU, with one of the most important being the creation of open metal sites. The creation of coordinatively unsaturated metal centers at the SBU is primarily achieved by removing neutral terminating linkers through heating MOFs under dynamic vacuum.[57] MOFs that are successful in achieving open-metal sites

display superior catalytic activity due to the large unoccupied orbital of a Lewis-acidic nature on the metal.[50] This leads to high rates for acid-base reactions and strong host-guest interactions. Functionalisation of these open metal sites is also well studied with respect to gas adsorption and catalysis.[58]

1.2.2.2 Linkers

Whilst the SBUs are formed *in situ*, the linker chosen for MOF preparation is pre-formed, allowing the linker geometry and connectivity to dictate the structure of the resulting MOF synthesis. The choice of organic linker is practically limitless with the only condition being at least two coordinating groups are present. Typically carboxylic acids are used, however other coordinating groups such as pyridines, amides, phosphates, and sulphonates have shown success in MOF syntheses.[59] The choice of linker connectivity, length and functional group can tune the size, shape and porosity of the resulting MOF for a specific application.

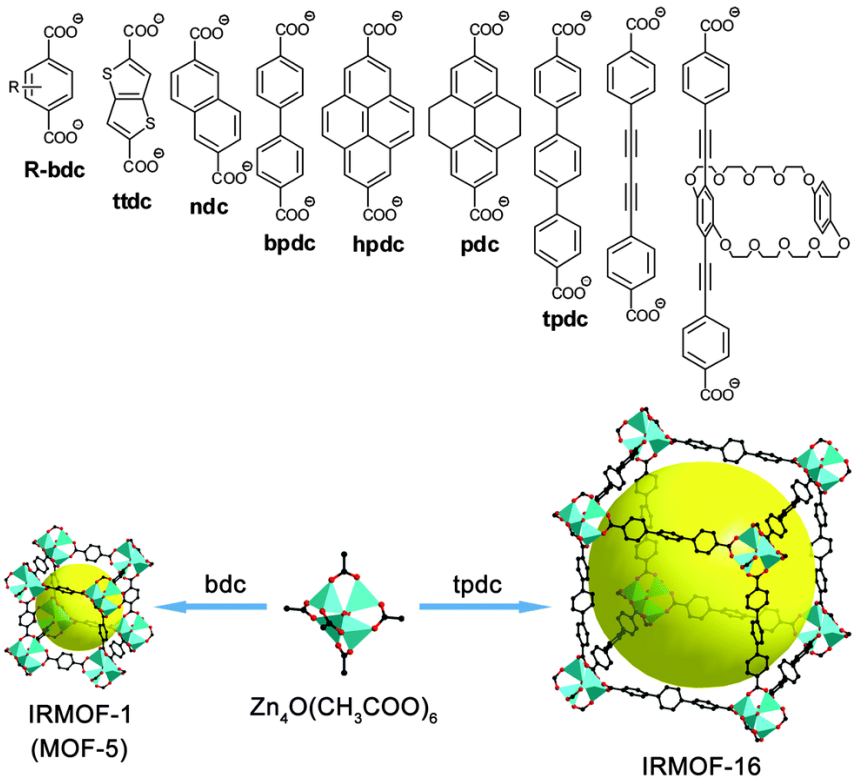

Figure 1.11: Structure of di-topic linkers used to form isoreticular MOFs (blue - zinc, red - oxygen, black - carbon). Yellow sphere indicates pore size of MOF. Figure taken from reference 59.

Changing the length of linkers has led to the study of isoreticular chemistry, where the structural topology of the material is constant although the pre-cursors are changing. This was first investigated with MOF-5: the same zinc SBU could be connected with di-topic linkers of increasing length to produce a series of MOFs with the same network topology and increasing pore size.[60] As well as changing length, the di-topic linkers could be functionalised with organic groups such as $-NH_2$, $-Br$ and crown ethers, resulting in a structure isoreticular to MOF-5 [Figure 1.11]. These materials show increasing porosity with pore size up to 28.8 angstroms.[61]

1.2.2.3 Modulators

Conventional synthesis of MOFs involves the combination of a metal source and an organic linker, which under the right conditions self-assemble into a crystalline material. However, further control over this synthesis is beneficial to optimize the structure for particular applications. One method that has emerged is the addition of monotopic linkers which function as a "modulator" for the synthesis [Figure 1.12].

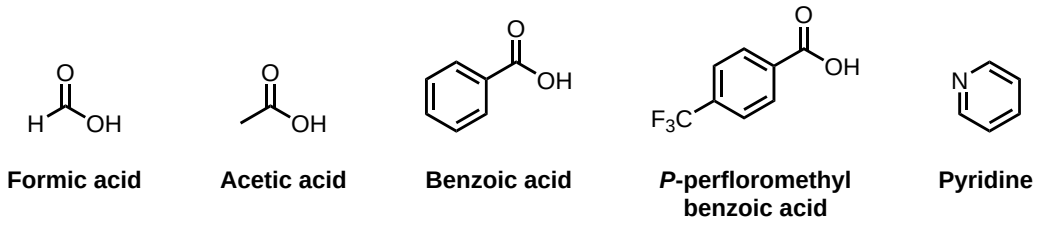

Figure 1.12: Chemical structures of monotopic linkers commonly used as modulators in MOF synthesis.

Modulators were first used by Hermes *et al.* to control particle size by incorporating *p*-perfuoromethylbenzoic acid into the synthesis. This resulted in the particle size reducing from 350 nm in the non-modulated synthesis, to 100-150 nm with modulator.[62] It was hypothesised that the monotopic acid was competing with the di-topic linker and acting as a capping agent to control growth. Further evidence for this was seen by using varying modulating agents in the synthesis of a Cu-MOF that controlled the direction of growth to give nanocubes, nanosheets or nanorods.[63]

As the understanding of modulators has increased so has their use in MOF

syntheses. The control of crystal size using modulators has been used to improve catalytic applications, whilst also indicating that modulators enhance the quality of MOF crystals by slowing crystallisation.[55] Deliberate incorporation of modulators into a MOF structure to replace linkers has also allowed defects to be introduced into a MOF and increasing porosity.[64] Surface functionalisation and phase selection has also been successfully carried out through the use of modulating agents.[65,66]

1.2.3 Synthesis Methods

Diverse synthetic methods are employed to form MOFs of varying topologies and properties. Reaction conditions can be varied extensively through temperature, reaction time and solvents to impact on yield, particle size and morphology. A selection of MOF synthesis techniques will be discussed below with focus on methods used for this thesis.

1.2.3.1 Solvothermal synthesis

Solvothermal synthesis is the "conventional" MOF synthesis technique and is defined as reactions taking place in closed vessels under pressure generated by heating over the boiling point of the solvent, with hydrothermal used to describe these reactions taking place with water as the solvent.[67] These reactions commonly take place in an autoclave [Figure 1.13] allowing a range of solvents, temperatures and reaction times in order to prepare a variety of MOFs.

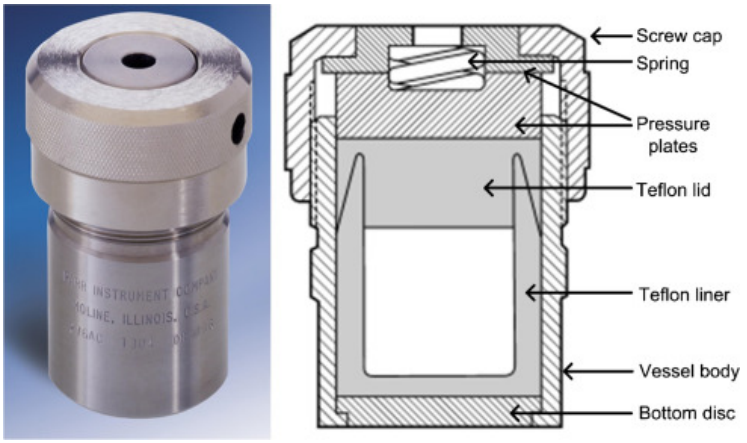

Figure 1.13: Example image of an autoclave with labelled diagram.[68]

The choice of solvent in solvothermal synthesis is an important parameter as, although not directly incorporated into the MOF structure, many solvents reside within the pores upon MOF formation. In some cases the choice of solvent can determine which structure is formed due to the polarity or linker solubility, as seen in Fe^{3+} MOF studies.[69] The removal of the chosen solvent upon activation of the MOF must also be possible without compromising the framework. Some MOFs have been shown to change framework parameters after the removal of solvent due to flexibility in the structure.[70]

One of the most commonly used solvents in MOF synthesis is dimethylformamide (DMF); its polarity allows excellent solubility of both inorganic and organic MOF components and it can act as a modulating agent. Upon heating, DMF will thermally decompose to give dimethyl ammonium which may act as directing agent within the reaction to aid in MOF formation.[71] However, due to the harsh nature of DMF, it is not considered environmentally or economically beneficial, therefore becomes problematic upon scale-up.[72]

The temperature of solvothermal reactions can also impact the preparation of MOFs by effecting both the nucleation and crystal growth rates. The majority of MOF syntheses are carried out at high temperatures to give highly crystalline structures, yet at sustained high temperatures multiple phases may be prepared, or the MOF is at risk of degradation.[73] Investigations into room temperature synthesis has successfully obtained MOF-5, HKUST-1, and ZIF-8.[74,75] A low temperature synthesis of CPO-27 has also been achieved at -78°C.[76]

The solvothermal synthesis method has been successful in producing many MOFs, however novel MOF discovery is a time consuming process. To accelerate MOF discoveries, high-throughput methods have been investigated as they are a systemic way to optimise MOF syntheses. Parallel reactors with 96 well-plates have been used, with the ability to automatically characterise materials.[77] From these methods a large number of MOFs have been discovered, mainly of carboxylate-based materials,[78] but also imidazolate-,[77] phosphonate-,[79] and tetrazolate-based MOFs.[80]

1.2.3.2 Sonochemical

Sonochemical synthesis refers to the method of applying high-energy ultrasound to the reaction mixture. Ultrasound has a frequency of between 20 - 10 MHz with a wavelength larger than molecular dimensions which results in no direct interaction between the ultrasound waves and the reagents. The reaction takes place due to the high-energy ultrasound interacting with liquid to form alternating areas of low and high pressure. Within the low pressure areas, small bubbles are formed due to the drop below the vapour pressure of the solvent and reagents. As the pressure alternates these bubbles grow and accumulate ultrasonic energy, reaching a point where the bubbles become unstable and collapse. This process of bubble formation, growth and collapse is known as cavitation and leads to the rapid release of energy to reach temperatures of *ca.* 5000 K, and pressures of *ca.* 1000 bar.[81]

When cavitation occurs, chemical reactions occur within and around the formed cavity which results in bond breaking, bond formation, and the production of radicals that will go on to initiate further reactions. This method was first carried out to form MOF-5 by Son *et al.* where the synthesis time was reduced from 24 hours to 30 mins and resulted in the formation of smaller MOF particles.[82] Further studies on sono-chemical synthesis have been carried out and have been successful in synthesising known MOFs: MOF-177 and HKUST-1.[74,83]

1.2.3.3 Other techniques

Many other alternative MOF synthesis methods have been investigated over the last few decades. Microwave synthesis was first used to synthesise Cr-MIL-100,[84] and has since been used for many different MOF syntheses due to the advantages of shorter reaction times and growth of nano-sized crystallites.[85] Electrochemical synthesis has also been seen in industrial procedures as it allows the exclusion of anions from the synthesis. To-date procedures to prepare Cu- and Zn-based MOFs through electrochemistry methods have been reported.[78] Mechanochemistry is yet another method to prepare MOFs which has garnered interest in recent years. This can be attributed to the environmentally friendly synthesis method; room temperature with little to no solvent, and shorter reaction times than conventional synthesis methods.[86]

1.2.4 MOFs for the Destruction of Nerve Agents

Catalysts for the destruction and decontamination of nerve agents have been widely investigated and consist of a range of materials. The majority of these materials consist of a porous structure with adsorption sites, with activated carbons being widely reported for this application.[87]

Metal-oxide based materials have also shown success for the catalytic degradation of nerve agents,[88] with inspiration taken from naturally occurring enzymes that detoxify organophosphorus compounds: phosphotriesterase (PTE), methyl parathion hydrolase, and paraoxonase[89] These enzymes contain a pair of Zn(II) ions bridged by a hyroxyl group which acts as a Lewis-acidic active site for catalysis. The stability of enzymes hinders their use for large-scale applications, however this same metal-hydroxy bridging motif is present in metal-oxide based materials without the stability issues [Figure 1.14].

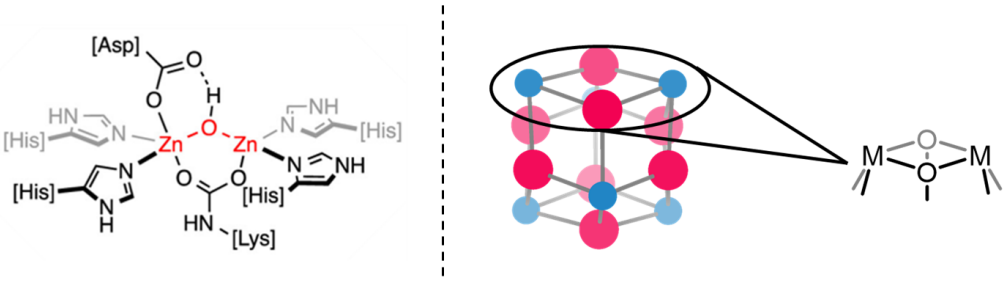

Figure 1.14: (Left) Structure of the active site in PTE where the metal-hydroxy active site is highlighted. (Right) Illustration of metal-hydroxy SBU present in MOFs (blue: metal, pink: oxygen). Figure adapted from 90.

Metal-organic frameworks have emerged as promising materials for this application as they exhibit high porosity seen in activated carbons but with the advantageous ability to tune the structure. Alongside the metal-hydroxy moiety exhibited by organophosphorus destroying enzymes such as PTE, but with much higher stability. Many studies have focused on the adsorption of CWAs by MOFs,[91,92] but this thesis will focus on MOF catalysts with Lewis-acid sites that can both adsorb and degrade nerve agents.

The first MOF used for the capture of nerve agents was an α-PbO_2 replica MOF with the structure $[Zn_2Ca(BTC)_2(H_2O)_2](DMF)_2$ which successfully adsorbed the simulant methylphosphonic acid (MPA).[93] This was closely followed by a study

on a MOF-5 based MOF, consisting of the 3,5-dimethyl-4-carboxypyrazole linker in place of the regular BDC linker. This was shown to successfully adsorb the simulant diisopropylfluorophosphate (DFP).[94]

The first reported MOF that both adsorbed and catalytically hydrolysed a nerve agent simulant was NENU-11; a Cu-based MOF containing a polyoxometalate (POM) guest.[95] The open Lewis-acidic metal sites at the SBU allowed the successful hydrolysis of DMMP with a conversion of 34% at room temperature. Further studies on MOFs containing Lewis-acidic metals such as Cu^{2+}, Al^{3+} and Cr^{3+} have shown to be successful catalysts for nerve agent hydrolysis.[96–98] These materials typically reported half lives of the order of hours to days with poor long-term stability.

1.2.4.1 Zr-MOFs

Zirconium-based MOFs display notable advantages to be used as catalysts for the hydrolysis of nerve agents when compared to previously studies MOFs. Zr(IV)-MOFs are thermally and chemically stable under harsh conditions; the structure stays intact up to *ca.* 500°C and between pH 1 - 12.[99] These properties originate from the strength of the $Zr-O-Zr$ bonds within the Zr_6-based SBU. These MOFs also lend themselves to this catalysis due to the Lewis-acidic nature of the Zr(IV), with the ability to induce open-metal sites into the structures by reducing the number of bridging hydroxyl groups.[100]

Three Zr-MOFs have emerged as leading catalysts for the hydrolysis of nerve agents: UiO-66, MOF-808, and NU-1000. All three contain the same Zr_6 node [$Zr_6(\mu_3\text{-}O)_4(\mu_3\text{-}OH)_4$] connected by the linkers BDC, BTC and 1,3,6,8-tetrakis(*p*-benzoic acid)pyrene respectively [Figure 1.15]. The breakthrough result for Zr-MOFs for this application was in 2014 when UiO-66 reported a half life ($t_{1/2}$) of 45 mins for the hydrolysis of the nerve agent simulant DMNP.[101] This was the shortest half life by 1 order of magnitude than was previously seen for other Lewis-acidic metal containing MOFs.[26]

Although UiO-66 gave promising results for this catalysis, the rates were limited by both the pore size and connectivity of the SBU. The UiO-66 structure consists of pore sizes of 6Å diameter which is too small to allow nerve agents within the structure. This limits the catalytic activity to the external surface of the MOF; for

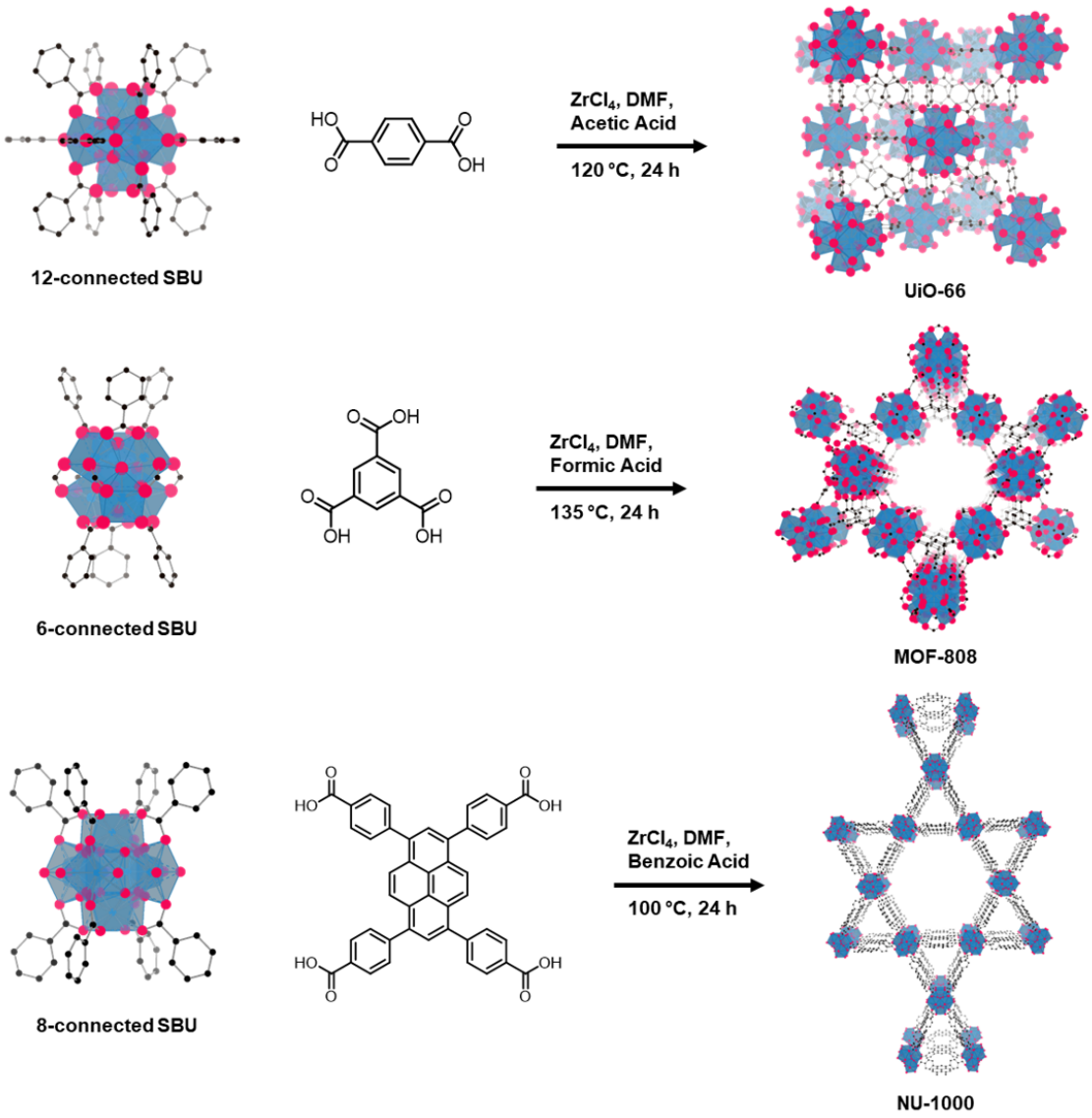

Figure 1.15: Structures of UiO-66 (top), MOF-808 (middle) and NU-1000 (bottom) with SBU connectivity, linker used, synthesis conditions and final structure.

a 400 nm UiO-66 crystallite, only 0.75% of the total Zr_6 sites reside on the surface and therefore accessible for catalysis.[101] Alongside this, the Zr_6-SBU has the maximum connectivity of 12 linkers, meaning all Zr atoms are fully coordinated within the pristine structure. This also hinders the accessibility to the Zr−O−Zr active sites.

In order to investigate the effect of pore size for this catalyss, an iso-reticular MOF to UiO-66 was prepared using a longer di-topic linker, biphenyl-4,4-dicarboxylic acid (BPDC), forming UiO-67. This MOF showed significantly improved catalytic results with a half life of 4.5 min for the hydrolysis of DMNP. This increase

in rate is mainly attributed to the larger pore diameter in UiO-67 of between 8 and 11.5 Å, allowing the nerve agent simulant greater access to the active sites.[102]

To further evidence that the greater accessibility to the Zr_6 active sites gives better catalytic results, NU-1000 was synthesised. This Zr_6 based MOF consists of meso-pores with a diameter of 31 Å and an 8-connected SBU. NU-1000 reported a half life of 15 min for the catalytic hydrolysis of DMNP under the same conditions as the UiO-66 study. The wide pore structure allows the simulant or nerve agent to permeate the entire structure and give excellent accessibility to the Zr_6 node. This rate was further improved after dehydration of the NU-1000 structure, removing coordinated water and hydroxyl groups from the SBU, and increasing the number of open metal sites. This resulted in a half life of 1.5 min and 3 min for the hydrolysis of DMNP and sarin, respectively; the fastest catalytic MOF hydrolysis rate reported at the time.[103]

The increased rate for the dehydrated structure of NU-1000 was attributed to the increased access to the Zr_6 nodes by inducing open metal sites. Although NU-1000 has a lower SBU connectivity that UiO-66; 8- and 12-connected respectively, this can be further reduced by the incorporation of a tri-topic linker, BTC, to form MOF-808. This MOF exhibits 6-connected Zr_6 SBUs with a pore size of 18.4 Å. To-date, using MOF-808 as the catalyst gives the fastest rate of hydrolysis of DMNP with a half life of 30 s.[104]

Alongside increasing pore size and decreasing the connectivity of the SBUs, investigations into other factors influencing catalytic rates have been carried out such as particle size and the addition of functional groups on the linker. The particle size has particular significance in the case of UiO-66, where the pores are too small to allow nerve agent species within the structure to access the active sites. It was found that decreasing the particle size of UiO-66 resulted in an increase in catalytic rate as a greater number of Zr_6 active sites are accessible with decreasing particle size.[105] This study also found that a smaller particle size correlated with increasing defect sites, providing open metal sites, and a higher catalytic rate.

One study found that the addition of an amine functional group on the BDC linker, forming UiO$-66\text{-}NH_2$, resulted in a 20-fold increase in catalytic activity over the non-functionalised UiO-66 to give a half life of 1 min for the hydrolysis

of DMNP.[102] Further investigations have been carried out on functionalisation of UiO-66 through the addition of halogen containing BTC linkers [Figure 1.16]. It was found that the addition of any halogen group results in better catalytic activity than the parent UiO-66 MOF, with the BDC-I resulting in the highest rate of catalysis with an initial rate of 600 mM/s $x\,10^{-6}$.[106]

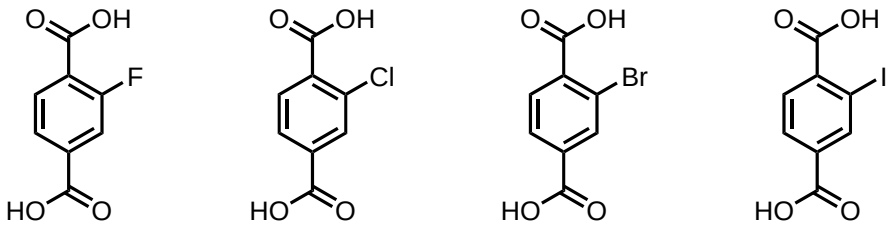

Figure 1.16: Structures of halogen containing BDC linkers used in the synthesis of UiO-66 derivatives.

Overall, from the investigations into Zr-MOFs for the catalytic hydrolysis of nerve agents and simulants the strategies employed to optimise catalysis can be split into two complementary directions. One is to increase the accessibility of Zr_6 sites through pore size expansion, reducing particle size and inducing defects into the MOF structure. The other is to introduce functionality into the MOF through the addition of functionalised linkers as seen in the case of UiO-66.[90]

1.3 References

[1] L. Szinicz, *Toxicology*, 2005, **214**, 167–181.

[2] J. P. Robinson and M. Leitenberg, *The rise in CB weapons. In: The Problem of Chemical and Biological Warfare*, Almqvist & Wiksell, 1971, p. 395.

[3] R. Black, in *Chem. Warf. Toxicol. Vol. 1 Fundam. Asp.*, The Royal Society of Chemistry, 2016, vol. 1, pp. 1–28.

[4] V. Meyer, *Berichte der deutschen chemischen Gesellschaft*, 1886, **19**, 3259–3266.

[5] L. Szinicz and S. I. Baskin, in *Toxicology*, ed. H. Marquardt, S. G. Schäfer, R. McClellan and F. Welsch, Academic Press, San Diego, 1999, pp. 851–877.

[6] N. B. Munro, S. S. Talmage, G. D. Griffin, L. C. Waters, A. P. Watson, J. F. King and V. Hauschild, *Environ. Health Perspect.*, 1999, **107**, 933–974.

[7] Y. J. Jang, K. Kim, O. G. Tsay, D. A. Atwood and D. G. Churchill, *Chem. Rev.*, 2011, **111**, 5345–5403.

[8] S. Sezigen, R. K. Eyison and L. Kenar, *GULHANE Med. J.*, 2019, **61**, 64.

[9] G. W. Wagner, P. W. Bartram, O. Koper and K. J. Klabunde, *J. Phys. Chem. B*, 1999, **103**, 3225–3228.

[10] C. R. Ringenbach, S. R. Livingston, D. Kumar and C. C. Landry, *Chem. Mater.*, 2005, **17**, 5580–5586.

[11] B. M. Smith, *Chem. Soc. Rev.*, 2008, **37**, 470–478.

[12] A. J. Howarth, C. T. Buru, Y. Liu, A. M. Ploskonka, K. J. Hartlieb, M. McEntee, J. J. Mahle, J. H. Buchanan, E. M. Durke, S. S. Al-Juaid, J. F. Stoddart, J. B. DeCoste, J. T. Hupp and O. K. Farha, *Chem. Eur. J.*, 2017, **23**, 214–218.

[13] B. Holmstedt, in *Structure-Activity Relationships of the Organophosphorus Anticholinesterase Agents*, ed. G. B. Koelle, Springer Berlin Heidelberg, Berlin, Heidelberg, 1963, pp. 428–485.

[14] NRC, *Recommendations for the Disposal of Chemical Agents and Munitions*, National Academy Press, Washington, D.C., 1994.

[15] E. Nepovimova and K. Kuca, *Food Chem. Toxicol.*, 2018, **121**, 343–350.

[16] R. T. Delfino, T. S. Ribeiro and J. D. Figueroa-Villar, *J. Braz. Chem. Soc.*, 2009, **20**, 407–428.

[17] WHO, *Health Aspects of Chemical and Biological weapons*, World health organisation technical report, 1970.

[18] L. L. Chao, J. C. Rothlind, V. A. Cardenas, D. J. Meyerhoff and M. W. Weiner, *NeuroToxicology*, 2010, **31**, 493–501.

[19] L. Ember, *Chemical & Engineering News Archive*, 1995, **73**, 6–7.

[20] H. John, M. J. van der Schans, M. Koller, H. E. Spruit, F. Worek, H. Thiermann and D. Noort, *Forensic Toxicol.*, 2018, **36**, 61–71.

[21] Y. C. Yang, *Acc. Chem. Res.*, 1999, **32**, 109–115.

[22] H. J. Altmann, A. Richardt, Y. C. Yang, J. A. Baker and J. R. Ward, *Chem. Rev.*, 1992, **92**, 1729–1743.

[23] S. L. Bartelt-Hunt, D. R. Knappe and M. A. Barlaz, *Crit. Rev. Environ. Sci. Technol.*, 2008, **38**, 112–136.

[24] G. W. Wagner and Y.-C. Yang, *Industrial & Engineering Chemistry Research*, 2002, **41**, 1925–1928.

[25] S. Bjarnason, J. Mikler, I. Hill, C. Tenn, M. Garrett, N. Caddy and T. W. Sawyer, *Hum. Exp. Toxicol.*, 2008, **27**, 253–261.

[26] Y. Liu, A. J. Howarth, N. A. Vermeulen, S. Y. Moon, J. T. Hupp and O. K. Farha, *Coord. Chem. Rev.*, 2017, **346**, 101–111.

[27] A. M. Ploskonka and J. B. DeCoste, *J. Hazard. Mater.*, 2019, **375**, 191–197.

[28] M. C. de Koning, G. W. Peterson, M. van Grol, I. Iordanov and M. McEntee, *Chem. Mater.*, 2019, **31**, 7417–7424.

[29] J. M. Palomba, S. P. Harvey, M. Kalaj, B. R. Pimentel, J. B. Decoste, G. W. Peterson and S. M. Cohen, *ACS Appl. Mater. Interfaces*, 2020, **12**, 14672–14677.

[30] S. D. Khare, Y. Kipnis, P. J. Greisen, R. Takeuchi, Y. Ashani, M. Goldsmith, Y. Song, J. L. Gallaher, I. Silman, H. Leader, J. L. Sussman, B. L. Stoddard, D. S. Tawfik and D. Baker, *Nat. Chem. Biol.*, 2012, **8**, 294–300.

[31] T. Islamoglu, M. A. Ortuño, E. Proussaloglou, A. J. Howarth, N. A. Vermeulen, A. Atilgan, A. M. Asiri, C. J. Cramer and O. K. Farha, *Angew. Chemie., Int. Ed.*, 2018, **57**, 1949–1953.

[32] M. R. Momeni and C. J. Cramer, *J. Phys. Chem. C*, 2019, **123**, 15157–15165.

[33] E. Dyguda-Kazimierowicz, W. A. Sokalski and J. Leszczynski, *J. Phys. Chem. B*, 2008, **112**, 9982–9991.

[34] K. A. Daniel, L. A. Kopff and E. V. Patterson, *J Phys Org Chem*, 2008, **21**, 321–328.

[35] C. Vieira Soares, G. Maurin and A. A. Leitão, *J. Phys. Chem. C*, 2019, **123**, 19077–19086.

[36] K. S. W. Sing, in *Characterisation of Porous Solids II*, Elsevier Science Publishers, Amsterdam, 1991, vol. 62, pp. 1–9.

[37] R. M. Barrer, *J. Chem. Soc.*, 1948, 127–132.

[38] B. Yilmaz and U. Müller, *Top. Catal.*, 2009, **52**, 888–895.

[39] E. J. García, J. Pérez-Pellitero, G. D. Pirngruber, C. Jallut, M. Palomino, F. Rey and S. Valencia, *Ind. Eng. Chem. Res.*, 2014, **53**, 9860–9874.

[40] R. P. Townsend and E. N. Coker, in *Introduction to Zeolite Science and Practice*, ed. H. van Bekkum, E. Flanigen, P. Jacobs and J. Jansen, Elsevier, 2001, vol. 137 of Studies in Surface Science and Catalysis, pp. 467–524.

[41] Z. Wang, J. Yu and R. Xu, *Chem. Soc. Rev.*, 2012, **41**, 1729–1741.

[42] O. M. Yaghi, G. Li and H. Li, *Nature*, 1995, **378**, 703–706.

[43] H. Daglar and S. Keskin, *Coordination Chemistry Reviews*, 2020, **422**, 213470.

[44] B. Li, H. M. Wen, W. Zhou and B. Chen, *J. Phys. Chem. Lett.*, 2014, **5**, 3468–3479.

[45] J. Lee, O. K. Farha, J. Roberts, K. A. Scheidt, S. T. Nguyen and J. T. Hupp, *Chem. Soc. Rev.*, 2009, **38**, 1450–1459.

[46] D. Yang and B. C. Gates, *ACS Catalysis*, 2019, **9**, 1779–1798.

[47] P. Horcajada, R. Gref, T. Baati, P. K. Allan, G. Maurin, P. Couvreur, G. Férey, R. E. Morris and C. Serre, *Chem. Rev.*, 2012, **112**, 1232–1268.

[48] I. Abánades Lázaro and R. S. Forgan, *Coordination Chemistry Reviews*, 2019, **380**, 230–259.

[49] C. A. Trickett, A. Helal, B. A. Al-Maythalony, Z. H. Yamani, K. E. Cordova and O. M. Yaghi, *Nat. Rev. Mater.*, 2017, **2**, 17045.

[50] M. J. Kalmutzki, N. Hanikel and O. M. Yaghi, *Sci. Adv.*, 2018, **4**, 9180.

[51] V. Guillerm, D. Kim, J. F. Eubank, R. Luebke, X. Liu, K. Adil, M. S. Lah and M. Eddaoudi, *Chem. Soc. Rev.*, 2014, **43**, 6141–6172.

[52] Z. Chen, S. L. Hanna, L. R. Redfern, D. Alezi, T. Islamoglu and O. K. Farha, *Coord. Chem. Rev.*, 2019, **386**, 32–49.

[53] J. Jiang, Y. Zhao and O. M. Yaghi, *J. Am. Chem. Soc*, 2016, **138**, 3255–3265.

[54] S. S.-Y. Chui, S. M.-F. Lo, J. P. H. Charmant, A. G. Orpen and I. D. Williams, *Science*, 1999, **283**, 1148–1150.

[55] J. H. Cavka, S. Jakobsen, U. Olsbye, N. Guillou, C. Lamberti, S. Bordiga and K. P. Lillerud, *J. Am. Chem. Soc*, 2008, **130**, 13850–13851.

[56] P. Deria, J. E. Mondloch, O. Karagiaridi, W. Bury, J. T. Hupp and O. K. Farha, *Chem. Soc. Rev.*, 2014, **43**, 5896–5912.

[57] B. Chen, M. Eddaoudi, T. M. Reineke, J. W. Kampf, M. O'Keeffe and O. M. Yaghi, *J. Am. Chem. Soc*, 2000, **122**, 11559–11560.

[58] Y. Hwang, D.-Y. Hong, J.-S. Chang, S. Jhung, Y.-K. Seo, J. Kim, A. Vimont, M. Daturi, C. Serre and G. Férey, *Angew. Chemie., Int. Ed.*, 2008, **47**, 4144–4148.

[59] W. Lu, Z. Wei, Z.-Y. Gu, T.-F. Liu, J. J. Park, J. J. Park, J. Tian, M. Zhang, Q. Zhang, T. Gentle III, M. Bosch and H.-C. Zhou, *Chem. Soc. Rev.*, 2014, **43**, 5561–5593.

[60] N. W. Ockwig, O. Delgado-Friedrichs, M. O'Keeffe and O. M. Yaghi, *Accounts of Chemical Research*, 2005, **38**, 176–182.

[61] A. G. Wong-Foy, A. J. Matzger and O. M. Yaghi, *J. Am. Chem. Soc*, 2006, **128**, 3494–3495.

[62] S. Hermes, T. Witte, T. Hikov, D. Zacher, S. Bahnmüller, G. Langstein, K. Huber and R. A. Fischer, *J. Am. Chem. Soc*, 2007, **129**, 5324–5325.

[63] M.-H. Pham, G.-T. Vuong, F.-G. Fontaine and T.-O. Do, *Crystal Growth & Design*, 2012, **12**, 3091–3095.

[64] H. Wu, Y. S. Chua, V. Krungleviciute, M. Tyagi, P. Chen, T. Yildirim and W. Zhou, *J. Am. Chem. Soc*, 2013, **135**, 10525–10532.

[65] C. V. McGuire and R. S. Forgan, *Chem. Commun.*, 2015, **51**, 5199–5217.

[66] L. Yang, T. Zhao, I. Boldog, C. Janiak, X.-Y. Yang, Q. Li, Y.-J. Zhou, Y. Xia, D.-W. Lai and Y.-J. Liu, *Dalton Trans.*, 2019, **48**, 989–996.

[67] A. Rabenau, *Angew. Chemie., Int. Ed.*, 1985, **24**, 1026–1040.

[68] D. Nunes, A. Pimentel, L. Santos, P. Barquinha, L. Pereira, E. Fortunato and R. Martins, in *Metal Oxide Nanostructures*, ed. D. Nunes, A. Pimentel, L. Santos, P. Barquinha, L. Pereira, E. Fortunato and R. Martins, Elsevier, 2019, pp. 21 – 57.

[69] S. Bauer, C. Serre, T. Devic, P. Horcajada, J. Marrot, G. Férey and N. Stock, *Inorganic Chemistry*, 2008, **47**, 7568–7576.

[70] F. Millange, C. Serre, N. Guillou, G. Férey and R. Walton, *Angew. Chemie., Int. Ed.*, 2008, **47**, 4100–4105.

[71] A. D. Burrows, K. Cassar, R. M. Friend, M. F. Mahon, S. P. Rigby and J. E. Warren, *CrystEngComm*, 2005, **7**, 548–550.

[72] Y. Bai, Y. Dou, L.-H. Xie, W. Rutledge, J.-R. Li and H.-C. Zhou, *Chem. Soc. Rev.*, 2016, **45**, 2327–2367.

[73] F. Millange, R. El Osta, M. E. Medina and R. I. Walton, *CrystEngComm*, 2011, **13**, 103–108.

[74] D. J. Tranchemontagne, J. R. Hunt and O. M. Yaghi, *Tetrahedron*, 2008, **64**, 8553–8557.

[75] J. Cravillon, S. Münzer, S.-J. Lohmeier, A. Feldhoff, K. Huber and M. Wiebcke, *Chem. Mater.*, 2009, **21**, 1410–1412.

[76] S. M. Vornholt, S. E. Henkelis and R. E. Morris, *Dalton Trans.*, 2017, **46**, 8298–8303.

[77] R. Banerjee, A. Phan, B. Wang, C. Knobler, H. Furukawa, M. O'Keeffe and O. M. Yaghi, *Science*, 2008, **319**, 939–943.

[78] N. Stock and S. Biswas, *Chem. Rev.*, 2012, **112**, 933–969.

[79] M. Plabst, R. Köhn and T. Bein, *CrystEngComm*, 2010, **12**, 1920–1926.

[80] K. Sumida, S. Horike, S. S. Kaye, Z. R. Herm, W. L. Queen, C. M. Brown, F. Grandjean, G. J. Long, A. Dailly and J. R. Long, *Chem. Sci.*, 2010, **1**, 184–191.

[81] T. J. Mason and D. Peters, *Practical sonochemistry: Power ultrasound uses and applications*, Woodhead Publishing, 2002.

[82] W.-J. Son, J. Kim, J. Kim and W.-S. Ahn, *Chem. Commun.*, 2008, 6336–6338.

[83] M. Schlesinger, S. Schulze, M. Hietschold and M. Mehring, *Microporous Mesoporous Mater.*, 2010, **132**, 121–127.

[84] S.-H. Jhung, J.-H. Lee and J.-S. Chang, *Bulletin of the Korean Chemical Society*, 2005, **26**, 880–881.

[85] J. Klinowski, F. A. Almeida Paz, P. Silva and J. Rocha, *Dalton Trans.*, 2011, **40**, 321–330.

[86] T. Friščić, *J. Mater. Chem.*, 2010, **20**, 7599–7605.

[87] R. Osovsky, D. Kaplan, I. Nir, H. Rotter, S. Elisha and I. Columbus, *Environ. Sci. Technol.*, 2014, **48**, 10912–10918.

[88] G. W. Wagner, L. R. Procell, R. J. O'Connor, S. Munavalli, C. L. Carnes, P. N. Kapoor and K. J. Klabunde, *J. Am. Chem. Soc*, 2001, **123**, 1636–1644.

[89] Z. Prokop, F. Opluštil, J. DeFrank and J. Damborský, *Biotechnology Journal*, 2006, **1**, 1370–1380.

[90] K. O. Kirlikovali, Z. Chen, T. Islamoglu, J. T. Hupp and O. K. Farha, *ACS Appl. Mater. Interfaces*, 2020, **12**, 14702–14720.

[91] T. Islamoglu, Z. Chen, M. C. Wasson, C. T. Buru, K. O. Kirlikovali, U. Afrin, M. R. Mian and O. K. Farha, *Chem. Rev.*, 2020, **120**, 8130–8160.

[92] E. Barea, C. Montoro and J. A. Navarro, *Chem. Soc. Rev.*, 2014, **43**, 5419–5430.

[93] R. Zou, R. Zhong, S. Han, H. Xu, A. K. Burrell, N. Henson, J. L. Cape, D. D. Hickmott, T. V. Timofeeva, T. E. Larson and Y. Zhao, *J. Am. Chem. Soc*, 2010, **132**, 17996–17999.

[94] C. Montoro, F. Linares, E. Quartapelle Procopio, I. Senkovska, S. Kaskel, S. Galli, N. Masciocchi, E. Barea and J. A. R. Navarro, *J. Am. Chem. Soc*, 2011, **133**, 11888–11891.

[95] F.-J. Ma, S.-X. Liu, C.-Y. Sun, D.-D. Liang, G.-J. Ren, F. Wei, Y.-G. Chen and Z.-M. Su, *J. Am. Chem. Soc*, 2011, **133**, 4178–4181.

[96] A. Roy, A. K. Srivastava, B. Singh, D. Shah, T. H. Mahato and A. Srivastava, *Dalton Trans.*, 2012, **41**, 12346–12348.

[97] L. Bromberg, Y. Klichko, E. P. Chang, S. Speakman, C. M. Straut, E. Wilusz and T. A. Hatton, *ACS Applied Materials & Interfaces*, 2012, **4**, 4595–4602.

[98] S. Wang, L. Bromberg, H. Schreuder-Gibson and T. A. Hatton, *ACS Applied Materials & Interfaces*, 2013, **5**, 1269–1278.

[99] A. J. Howarth, Y. Liu, P. Li, Z. Li, T. C. Wang, J. T. Hupp and O. K. Farha, *Nat. Rev. Mater.*, 2016, **1**, 15018.

[100] R. C. Klet, Y. Liu, T. C. Wang, J. T. Hupp and O. K. Farha, *J. Mater. Chem. A*, 2016, **4**, 1479–1485.

[101] M. J. Katz, J. E. Mondloch, R. K. Totten, J. K. Park, S. T. Nguyen, O. K. Farha and J. T. Hupp, *Angew. Chemie., Int. Ed.*, 2014, **53**, 497–501.

[102] M. J. Katz, S. Y. Moon, J. E. Mondloch, M. H. Beyzavi, C. J. Stephenson, J. T. Hupp and O. K. Farha, *Chem. Sci.*, 2015, **6**, 2286–2291.

[103] J. E. Mondloch, M. J. Katz, W. C. Isley III, P. Ghosh, P. Liao, W. Bury, G. W. Wagner, M. G. Hall, J. B. DeCoste, G. W. Peterson, R. Q. Snurr, C. J. Cramer, J. T. Hupp and O. K. Farha, *Nat. Mater.*, 2015, **14**, 512–516.

[104] S.-Y. Moon, Y. Liu, J. T. Hupp and O. K. Farha, *Angew. Chemie., Int. Ed.*, 2015, **54**, 6795–6799.

[105] K. Y. Cho, J. Y. Seo, H.-J. Kim, S. J. Pai, X. H. Do, H. G. Yoon, S. S. Hwang, S. S. Han and K.-Y. Baek, *Appl. Catal. B.*, 2019, **245**, 635–647.

[106] M. Kalaj, M. R. Momeni, K. C. Bentz, K. S. Barcus, J. M. Palomba, F. Paesani and S. M. Cohen, *Chem. Commun.*, 2019, **55**, 3481–3484.

Chapter 2

Aims

The overall aim for this thesis was the preparation and investigation into MOFs for the destruction of CWAs and simulants.

Synthesis of mixed-metal MOFs will be attempted to investigate how changing the Lewis-acidity of the MOF impacts the catalytic properties. Special interest will be given to Group 4 metals as Zr-MOFs are known to catalytic hydrolyse CWAs and simulants with high performance. Hf will be introduced in varying mol% into known Zr-MOFs: UiO-66, MOF-808 and NU-1000. This will be attempted using solvothermal synthesis methods and all materials will be characterised using PXRD and EDS. Materials which are successfully synthesised will be used as catalysts for the hydrolysis of the nerve agent simulant DMNP.

A study on structural modifications will be carried out on MOF-808. This is a known Zr-MOF that exhibits superior catalytic activity for the hydrolysis of CWAs. By adding additional linkers, with fewer coordinating groups than the standard MOF-808 linker, defective frameworks may be synthesised. In some cases these linkers will have additional functional groups in order to introduce functionality into the MOF-808 framework. The prepared mixed-linker materials will be characterised using PXRD, q-NMR and TGA. Materials that have successfully synthesised will be tested as catalysts for the hydrolysis of DMNP.

A range of MOF/composite materials will be prepared to be used as catalysts for the catalytic hydrolysis of DMNP. Initially studies will be carried out to develop a MOF-808 synthesis method that is compatible with the composite materials chosen. Further studies will be carried out on synthesising MOF/fabric composites with a range of fabrics: polyphenylene ether, polyethylene tereph-

thalate, nylon, silk and cotton. Multiple synthesis methods will be carried out to investigate which technique gives optimum incorporation of MOF and greatest catalytic activity for the hydrolysis of a nerve agent simulant. Characterisation techniques such as TGA and q-NMR will be carried out in an attempt to gain accurate MOF-loading values for these materials. These studies will act as a proof of concept that these MOF catalysts may be implemented in protective equipment and clothing.

Chapter 3

Experimental Methods

3.1 X-ray Diffraction

X-ray Diffraction (XRD) is a powerful technique that allows the composition and structure of a crystalline sample to be analysed. Within this Thesis, XRD has been used solely to rapidly characterise known MOFs and to compare to literature structures. Although XRD can be used for further structural investigations such as LeBail and Rietveld refinements, and to identify new MOF structures, this is outside the scope of this work. Within the XRD techniques available, in this work only Powder X-ray Diffraction (PXRD) has been carried out.

3.1.1 Crystallography

A crystal is defined as: *a solid that contains a very high degree of long-range three-dimensional internal order of the component atoms, molecules, or ions.*[1] The simplest component of a crystal is the unit-cell which can be described as the complete representation of the contents of the repeating unit of a crystal structure. A unit cell is described by the three crystal axis: **a**, **b**, and **c**, with the angle between them being described by α, β and γ [Figure 3.1].

The faces of a crystal can be described by indexing three numbers: h, k and l which correspond to the crystal plane intercepting the unit cell axis **a**, **b**, and **c** respectively [Figure 3.1]. These crystal faces or planes are referred to as Miller planes after the nomenclature was introduced by William Whewell and William H. Miller.

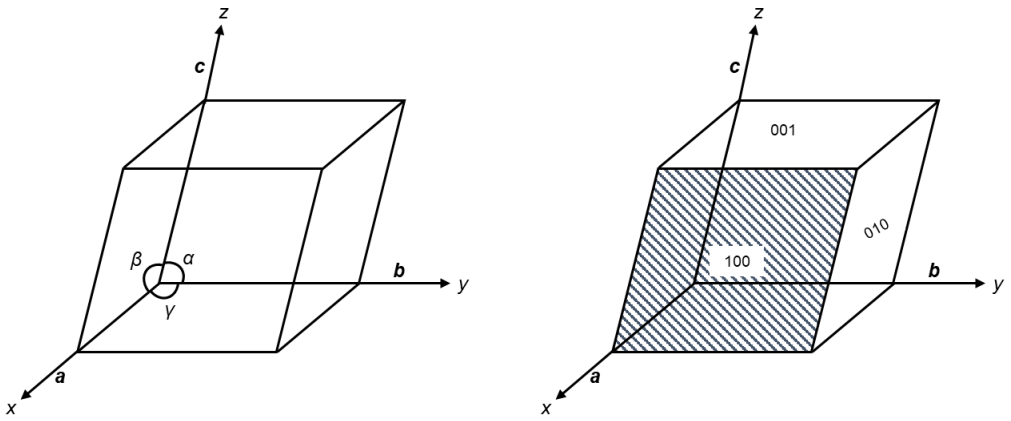

Figure 3.1: Left: A unit cell showing axial lengths **a**, **b**, and **c** and interaxial angles α, β and γ. **Right:** The crystal faces or miller planes (100), (010) and (001) shown on a unit cell.

A crystal lattice is formed when each unit cell in the crystal is replaced by a single point to generate an infinite three-dimensional network, and is used to highlight the repeating internal structure of a crystal. Both unit cells and crystal lattices can be classified according to their rotational symmetry. The symmetry can be described as n-fold, where n is any integer for when the unit cell is rotated $(360/n)^\circ$ the crystal is indistinguishable from the starting position. This application of rotational symmetry leads to seven distinct crystal systems [Table 3.1].

Table 3.1: The seven crystal systems with unit cell parameters.

Crystal System	**Axes**	**Angles**
Cubic	a = b = c	$\alpha = \beta = \gamma = 90^\circ$
Tetragonal	a = b $\neq$ c	$\alpha = \beta = \gamma = 90^\circ$
Orthorhombic	a $\neq$ b $\neq$ c	$\alpha = \beta = \gamma = 90^\circ$
Rhombohedral	a = b = c	$\alpha = \beta = \gamma \neq 90^\circ$
Hexagonal	a = b $\neq$ c	$\alpha = \beta = 90^\circ, \gamma = 120^\circ$
Monoclinic	a $\neq$ b $\neq$ c	$\alpha = \gamma = 90^\circ, \beta = 120^\circ$
Triclinic	a $\neq$ b $\neq$ c	$\alpha \neq \beta \neq \gamma$

Within a crystal, the symmetry of the atoms within each unit cell can also be related by symmetry operations. The smallest atomic arrangement within a unit cell is called the asymmetric unit and therefore is the smallest fragment from which the complete structure can be obtained through space-group symmetry operations. The possible combinations of symmetry elements, which include mirror planes, rotation axes and centres of symmetry, that are consistent with

the possible crystal lattices mean that there are 230 distinct combinations for three-dimensional crystals. These are listed in *International Tables for (X-ray) Crystallography* and used by crystallographers to describe crystal structures.

3.1.2 Powder X-ray Diffraction

Studies into crystalline materials have been carried out since ancient times as minerals were of interest. The first studies into structural determination of crystalline materials was by William L. Bragg in 1913 who discovered the structure of sodium chloride from X-ray diffraction studies.[2]

X-rays are chosen to examine the structure of crystals as the wavelength ranges from 10^{-9} to 10^{-10} m which is similar to the spacing between atoms within a crystal. This allows the waves to be diffracted off atoms and alter the direction of the beam by an incident angle (theta). Certain diffractions of the beam will cancel each other out, but if the incident beams have similar wavelengths then constructive interference of the diffracted beams occur. Constructive interference results in beams with greater wavelengths and therefore a greater signal is observed. Using Bragg's Law [Equation 3.1] the distance between the atomic planes of the crystal can be calculated which allows the structure to be determined [Figure 3.2].

$$n\lambda = 2\,d\sin\theta \tag{3.1}$$

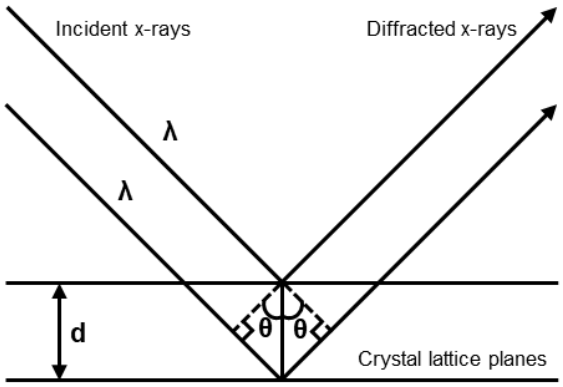

Figure 3.2: Schematic of Bragg's Law. Two incident x-rays are diffracted at an angle of θ on two atoms with a spacing of d between parallel planes within the crystal lattice.

Powder x-ray diffraction (PXRD) is used for materials synthesised as a poly-crystalline material, with crystals too small for single crystal x-ray diffraction experiments. The sample is ground to a fine powder prior to experiment to ensure random orientation of the crystallites. This lack of preferential orientation allows the diffraction of the incident beam by atoms of multiple crystals, generating a signal of concentric circles that satisfy Bragg's Law. A typical PXRD experiment set-up can be seen in Figure 3.3.

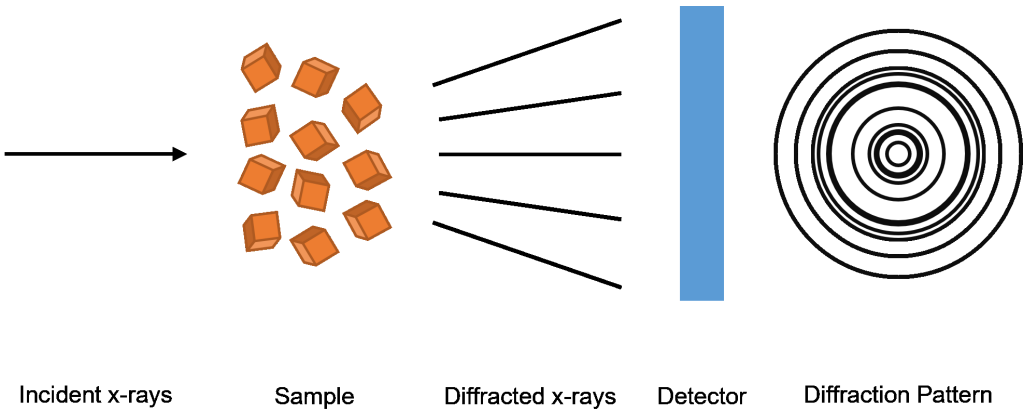

Figure 3.3: Schematic of a powder x-ray diffraction experimental set-up.

This signal, referred to as the Debye-Scherrer cone, is used to plot the intensity of the signal verses twice the angle of diffraction (2θ). These 2θ angles correspond to spacing between the atoms or planes within the sample. The intensity of the peaks is used to determine the number of atoms or molecules found with that particular spacing with the width of the peak inversely proportional to particle size; the broader the peak the smaller the crystallite. PXRD data can easily be used to compare similar samples and to confirm that the correct crystal structure or phases have been prepared.[3]

In this Thesis, all PXRD samples were ground and packed into glass capillaries with 0.5 mm diameter and measurements were carried out on STOE STADIP capillary diffractometers using Cu Kα radiation or Mo Kα radiation at room temperature. All PXRD plots are presented in Cu Kα format.

3.2 Electron Microscopy

SEM images in this Thesis were collected using a Jeol JSM-5600 (tungsten filament) with a resolution of 3.5 nm using an acceleration voltage of 5 kV and a working distance of 10 mm and later a Jeol JSM-IT200 (tungsten filament) with a resolution of 1.5 nm using an acceleration voltage of 5 - 10 kV and a working distance of 10 mm.

EDS data was collected using an integrated electron gun within a Jeol JSM-5600 (tungsten filament) with a resolution of 3.5 nm using an acceleration voltage of 20 kV and later a Jeol JSM-IT200 (tungsten filament) with a resolution of 1.5 nm using an acceleration voltage of 20 kV.

3.2.1 Scanning Electron Microscopy

Scanning Electron Microscopy (SEM) is a technique used for imaging on a small scale not possible through traditional microscopes. Electron microscopy produces an image that provides information about surface composition, topology of the sample and the elemental composition.

SEM forms images through the detection of signals produced by an electron beam interacting with a sample. Practically, the sample is placed upon a specimen holder within an evacuated chamber. A gold coating may be applied to the sample in order to prevent charge build up. Within the chamber, a focused beam of electrons are accelerated by an applied voltage (*ca.* 5 kV) towards the sample and scanned over the surface. The electrons interact with the sample in two ways: inelastic or elastic interactions which result in secondary scattered electrons (SSE) and back-scattered electrons (BSE) respectively [Figure 3.4]. Additionally the electron beam can produce the emission of characteristic x-rays (EDS).[4]

Inelastic scattering to produce secondary scattered electrons occurs when the electron beam transfers energy into the sample and ionises the atoms present. The electrons that are emitted are of low energy, typically 3-5 eV, therefore those that are detected originate from only nanometres below the surface of the sample. These signals give information about the surface topology of the sample such as texture and shape.

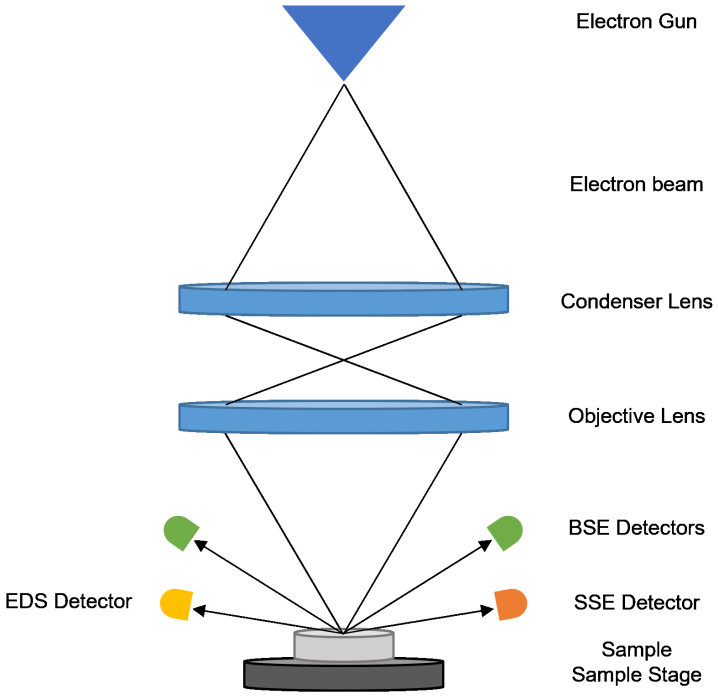

Figure 3.4: Schematic of a scanning electron microscope showing various detectors: secondary scattered electron (orange), back-scattered electron (green), and energy dispersive spectroscopy (yellow).

The elastic scattering that forms back-scattered electrons can provide both compositional and topographical information. BSE are caused from electrons colliding with the surface of the sample and back-scattering with an energy greater than 50 eV. The number of electrons that are back-scattered is proportional to the atomic number of the atoms within the sample; more electrons are scattered for larger elements therefore a larger signal is detected resulting in brighter areas in the SEM image. This allows compositional information about the sample to be gained.

3.2.2 EDS

Energy dispersive x-ray spectroscopy (EDS) is a technique that can quantify the elements within a sample and can be collected via SEM experiments [Figure 3.4]. Characteristic x-rays are produced from the interaction of the electron beam with a sample depending on the elemental composition; carried out in tandem with SEM, these x-rays can be used to map the elemental composition of a sample.

X-rays are emitted from the sample due to an electron from the incident electron

beam exciting an electron from within an inner shell of an atom within the sample. This creates an electron hole which can be filled by another electron falling from an outer shell with the energy difference between the two levels released as an x-ray. As each element comprises of characteristic energy levels, the emitted x-rays can be detected to give information about the elements present in the sample.

3.3 Thermogravimetric Analysis

Thermogravimetric Analysis (TGA) is a technique where the change in mass of a substance is measured as the temperature is increased. Measurements are carried out on samples placed within a small crucible; commonly this is composed of an inert material such as aluminium oxide, however in some cases a platinum crucible is used. The TGA apparatus uses a precision balance, allowing changes to the mass of the sample to be measured accurately.

A gas flows over the sample as it is heated to control the TGA atmosphere. This can be an inert or reactive gas and the gas flow can be accurately controlled. TGA curves are plotted as either temperature vs mass, or temperature vs weight percentage, with the starting weight as 100%.

TGA is a useful technique for MOF analysis as it can measure the stability of a sample under either inert, N_2, or reactive, O_2, gases to give an accurate thermal stability range for a sample. The mass loss at each temperature also gives information about the structure of the MOF, such as solvent within the pores, proportion of linker within the sample, and in some cases if the structure contains defects.

In this Thesis, all TGA measurements were carried out on a Stanton Redcroft STA-780. Each *ca.* 10 mg sample was heated from room temperature to 700 °C at a heating ramp of 5 °C/min under air.

3.4 UV-Vis Spectroscopy

UV-Vis spectroscopy is used to measure the absorbance of visible or ultra-violet light by a sample. These regions range from 190 - 400 nm for the UV region, and 400 - 800 nm for the visible light region. All molecules will undergo electronic excitation following the absorption of light if the wavelength of light corresponds to the same energy as an energy level transition within a molecule. For most molecules this requires high energy radiation (<200 nm), therefore, to adsorb in the UV-visible region the molecule must contain conjugated bonds or delocalised systems. As the amount of these bonds increase, the energy gap between orbitals decreases, and UV-vis light is absorbed. Transition metal complexes are also UV-active due to d-orbital splitting reducing the gap between energy levels due to metal-ligand interactions.

A general UV-Vis spectroscopy is carried out using a light source, typically a combination of halogen and deuterium lamps, which provide the UV-Vis wavelengths of light. Typical UV-Vis equipment can measure between 200 - 800 nm. These are focused and split into component colours and wavelengths by a dispersion device which acts like a prism. The selected wavelengths are passed through a sample within a cuvette or other sample holder. Typically a blank sample is also present or measured before hand that contains the solvent from a liquid sample. The wavelengths that are not absorbed by the sample are detected [Figure 3.5].

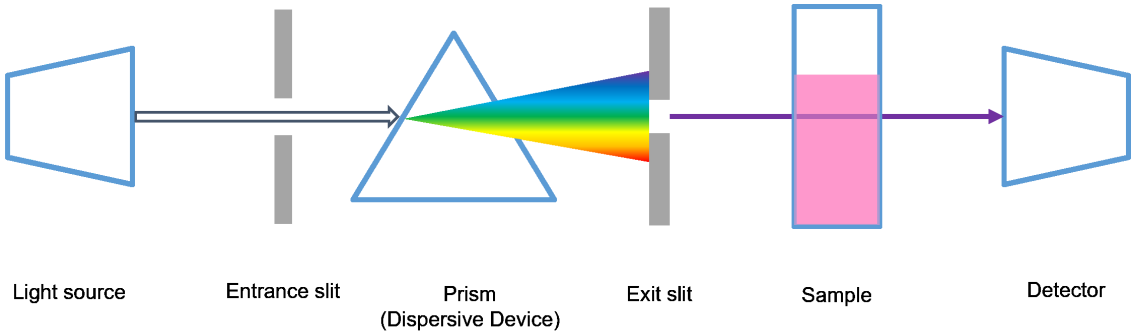

Figure 3.5: Schematic of a typical UV-Vis experimental set-up.

The detector measures the incoming wavelengths and converts them into a current; the higher the current the greater the intensity of that wavelength. This allows a plot of absorbance verses wavelength (nm) to be generated. The absorbance of each sample (**A**) is related to the intensity of light passing through

the blank ($\mathbf{I_0}$) and the sample ($\mathbf{I}$) according to Equation 3.2.

$$A = \log_{10} \frac{I_0}{I} \tag{3.2}$$

Absorbance is also related to the concentration of a species according to the Beer-Lambert Law [3.3] where ϵ is the molar extinction coefficient that is a constant for a particular substance at a particular wavelength ($dm^3 mol^{-1} cm^{-1}$), c is the concentration of solution ($mol\, dm^{-3}$), and l is the optical path length which is typically the length of the cuvette (cm).

$$A = \epsilon c l \tag{3.3}$$

If the Beer-Lambert Law is obeyed a plot of absorbance verses concentration will be linear. This also allows the molar extinction coefficient (ϵ) to be calculated through a calibration curve if the concentration of a species is known. Reaction kinetics can also be monitored via UV-Vis spectroscopy if a change in absorbance of a characteristic wavelength of either the products or reactants occurs throughout the reaction.

In this Thesis, UV-Vis spectroscopy was used to monitor the catalytic hydrolysis of the nerve agent simulant dimethyl 4-nitrophenylphosphate (DMNP) into para-nitro phenol (PNP). In-house UV-Vis measurements were carried out on a Agilent Cary 60 UV-Vis with a stainless-steel fibre-optic probe to allow *in-situ* monitoring [Figure 3.6].

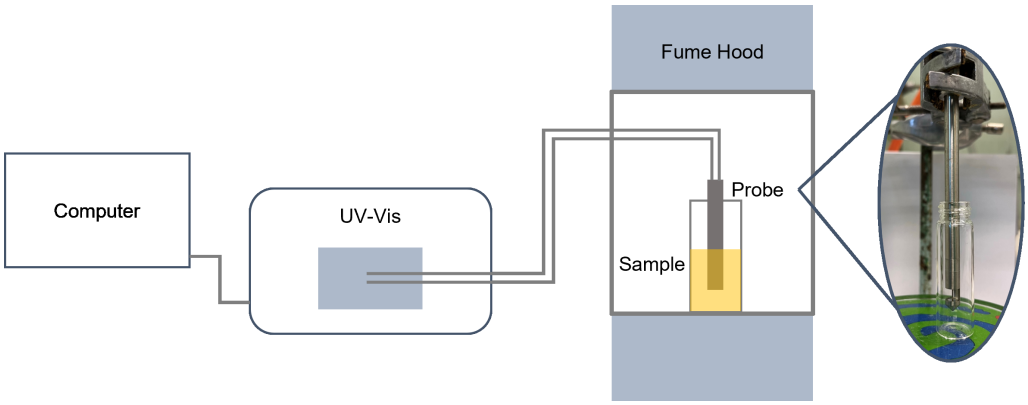

Figure 3.6: Agilent stainless steel fibre-optic probe to monitor UV-active reactions *in-situ* (pathlength 10 mm).

The concentration of PNP can be calculated from the absorbance data collected throughout the reaction using the Beer-Lambert Law [Equation 3.3]. In order to do this an ϵ value for PNP was calculated through an in-house calibration curve for para-nitro phenol (PNP) in an N-ethyl morpholine (NEM) solution at pH 10. This value was calculated to be 7.53 $dm^3mol^{-1}cm^{-1}$.

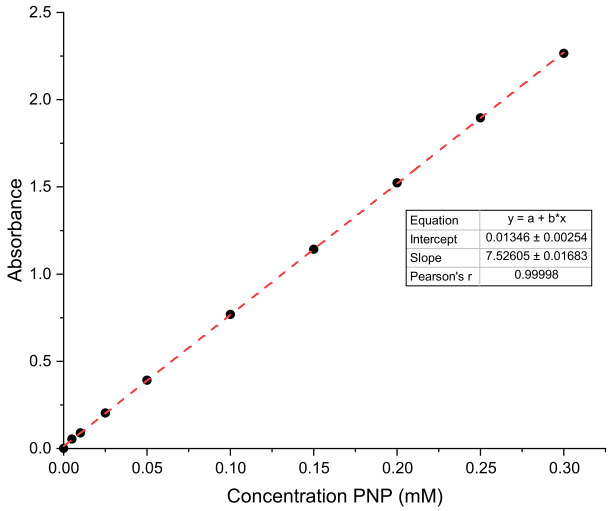

Figure 3.7: Calibration curve at 407 nm to determine the molar extinction coefficient of para-nitro phenol (PNP) in N-ethyl morpholine (NEM) buffer solution at pH 10.

3.5 Kinetics

Chemical kinetics are used as a measurement for how fast a reaction is occurring. Within catalysis, kinetics is a useful tool to determine catalytic performance of different materials and to determine the reaction rate.[5]

The reaction rate is defined as the measure of change in concentration of reactants or products per unit time [Equation 3.4].

$$\text{Rate} = \frac{\Delta\text{concentration}}{\Delta\text{time}} \tag{3.4}$$

For a reaction with reagents A and B and product C the rate can be expressed in terms of any of the components:

$$\text{Rate} = -\frac{\Delta[\text{A}]}{\Delta \text{t}} \tag{3.5}$$

$$\text{Rate} = -\frac{\Delta[\text{B}]}{\Delta \text{t}} \tag{3.6}$$

$$\text{Rate} = \frac{\Delta[\text{C}]}{\Delta \text{t}} \tag{3.7}$$

A rate law relates the rate of the reaction to a rate constant (k) and the concentrations of the reagents [Equation 3.8]. Many factors can influence the rate of a reaction including temperature, reagents, physical state of reagents, solvents, and the presence of a catalyst.

$$\text{Rate} = k[\text{A}]^{\text{x}}[\text{B}]^{\text{y}} \tag{3.8}$$

The reaction order is determined by the relationship between the rate and the concentration of the reagents. This can be calculated from the rate law by adding the exponential values of the species; from the equation above the reaction order would be x+y.

First-order reactions proceed at a rate that depends on only one reacting species. This rate can be described with a differential equation [Equation 3.9] with the rate (mols time^{-1}) depending on k, the reaction rate constant (time^{-1}).

$$\text{Rate} = -\frac{\text{d}[\text{A}]}{\text{dt}} = k[\text{A}]^{-1} = k[\text{A}] \tag{3.9}$$

This equation can be integrated to give an equation in the form of $y = mx + c$ which allows the rate constant of a reaction to be calculated from experimental data [Equation 3.10].

$$\ln[\mathrm{A}] = -k\mathrm{t} + \ln[\mathrm{A}]_0 \tag{3.10}$$

This can also be further simplified to Equation 3.11, which is used to calculated the concentration of a species during the reaction if the rate constant, k, and the time, t, is known.

$$[\mathrm{A}] = [\mathrm{A}]_0 \mathrm{e}^{-k\mathrm{t}} \tag{3.11}$$

The half life of a first-order reaction can easily be calculated if the rate constant, k, is known using Equation 3.12. This is derived from Equation 3.11 as we know when half the reagent has reacted then $[\mathrm{A}] = 0.5[\mathrm{A}]_0$.

$$\mathrm{t}_{\frac{1}{2}} = \frac{\ln 2}{k} \tag{3.12}$$

Second-order reactions have more complicated rate equations due to reaction rates being determined by multiple species. A summary of rate equations for zero-, first- and second-order reactions are given in Table 3.2.

Table 3.2: Rate laws for chemical reactions with various orders of reaction.

	Zero-order	**First-order**	**Second-order**
Rate Law	Rate = k	Rate = $k[\mathrm{A}]$	Rate = $k[\mathrm{A}]^2$
Integrated Rate Law	$[\mathrm{A}] = -k\mathrm{t} + [\mathrm{A}]_0$	$\ln[\mathrm{A}] = -k\mathrm{t} + \ln[\mathrm{A}]_0$	$\frac{1}{[\mathrm{A}]} = k\mathrm{t} + \frac{1}{[\mathrm{A}]_0}$

Plotting experimental data can give a good indication of the order of a reaction. If a concentration-time chart is linear, this indicates a zero-order reaction where the reaction is independent of reagent concentration. First and second order reactions are more difficult to determine from concentration time graphs therefore additional calculation is needed. Plotting ln[A] verses time will give a straight line if a first-order reaction has occurred. To identify a second-order reaction, a straight line is seen when plotting $1/[\mathrm{A}]$ verses time. In all of these charts the rate constant is calculated as the gradient of the line.

In this Thesis, initial reaction rates are calculated by assuming a first-order reaction has occurred for the catalytic hydrolysis of DMNP with calculations based on the generation of the product PNP. Initial rate calculations are based on previous literature,[6] and a reaction rate is calculated to allow comparison to published results.[7]

3.6 Nuclear Magnetic Resonance

Nuclear Magnetic Resonance (NMR) is a spectroscopy technique that allows for structural determination of small molecules. It is used for a wide range of applications such as in medicinal and organic chemistry, as well as within medicine.

NMR is a nuclei specific techniques that uses a large magnet to probe the intrinsic spin properties of atomic nuclei within a sample. The protons and neutrons that make up the nucleus of atoms contain a spin; nuclei with even numbers of protons and neutrons have net zero spin, but atoms with odd-numbers have a non-zero spin. Those molecules that contain a spin have a magnetic moment, μ, calculated by Equation 3.13, where **I** is the spin and γ the gyromagnetic ratio that is a proportionality constant between the magnetic dipole moment and angular momentum that is specific to each nucleus.

$$\mu = \gamma I \tag{3.13}$$

Within an NMR experiment an external magnetic field (B_0) is applied to the sample. This forces the nuclei to align either with or against the external magnetic field due to their magnetic moment forcing them to act as tiny bar magnets. There is a difference in energy between the nuclei that are aligned or non-aligned with B_0 and an NMR experiment measures the energy that is required to flip the nuclei between the two states.[8]

Due to the electrons that surround the nucleus, nuclear shielding occurs and allows for structural assignments. The local electronic environment around each nuclei changes the magnetic field felt by the nucleus by a small degree.

This changes the energy levels required to initiate a flip in spin and creates inequivalent nuclei. These signals are determined by Fourier transformation to different peaks within the NMR spectrum which allow structural determination of molecules.

Relaxation is used to refer to excited nuclei returning to a thermodynamically stable, and lower energy state, after excitement. This can occur via spin lattice relaxation or spin spin relaxation. Some nuclei, such as ^{1}H have a fast relaxation time which allows the subsequent peaks within the NMR spectra to be integrated to give the relative number of protons that cause the signal. For others nuclei, such as ^{13}C, the relaxation time is very long therefore cannot be used easily as a quantitative technique.

Within this Thesis, NMR spectroscopy was used to confirm the structure of MOF linkers, as well as to determine the ratios of linkers within digestive ^{1}H-NMR experiments. Experiments were submitted to either a 400 MHz Bruker AV II 400 or 500 MHz Bruker AV III 500 spectrometer. Acquired data was analysed using MestReNova 12.0.4 software.

3.7 References

[1] K. N. Pickworth Gluster, Jenny; Trueblood, *Crystal Structure Analysis: A Primer*, Oxford University Press, New York, 2010.

[2] W. H. Bragg and W. L. Bragg, *Proceedings of the Royal Society of London. Series A, Containing Papers of a Mathematical and Physical Character*, 1913, **88**, 428–438.

[3] W. Clegg, *Crystal Structure Determination*, Oxford University Press, 1998.

[4] J. D. Zhou W.; Apkarian R., Wang Z.L., in *Scanning Microscopy for Nanotechnology*, Springer, New York, NY, 2006, ch. Fundamentals of Scanning Electron Microscopy (SEM).

[5] I. N. Levine *et al.*, *Physical chemistry*, HIGHER EDUCATION, 2021.

[6] J. Casado, M. A. Lopez-Quintela and F. M. Lorenzo-Barral, *J. Chem. Educ.*, 1986, **63**, 450.

[7] J. M. Palomba, C. V. Credille, M. Kalaj, J. B. DeCoste, G. W. Peterson, T. M. Tovar and S. M. Cohen, *Chem. Commun.*, 2018, **54**, 5768–5771.

[8] T. Atta-Ur-Rahman, *Nuclear magnetic resonance: basic principles*, Springer Science & Business Media, 2012.

Chapter 4

Mixed-metal MOFs

4.1 Aims

The aim of this Chapter is to prepare and characterise mixed-metal MOFs. Subsequently these MOFs will be used as catalysts for the hydrolysis of the nerve agent simulant DMNP.

Mixed-metal analogues of well-known MOFs will be synthesised: UiO-66, NU-1000 and MOF-808. These Zr-MOFs are known to successfully catalyse the hydrolysis of nerve agents and simulants. The effects of the addition of Hf, and therefore the reduction of Lewis-acidity, on each MOF will be investigated.

All materials synthesised will be characterised through PXRD and EDS. With the catalytic testing carried out using either a high-throughput or in-house method with monitoring via in−situ UV-Vis. Further investigation will be carried out on materials presenting favourable catalytic properties and will be characterised by TGA, DLS and SEM to understand the factors behind successful catalysis.

4.2 Introduction

The major focus for MOFs for the catalytic destruction of warfare agents has centred around Zr-MOFs as they have given the best results to date.[1] This is mainly due to the strong Zr−O−Zr bonds and Lewis-acidity of the Zr_6 SBU, alongside pore size and SBU accessibility. Many studies have been carried out to prepare MOFs with optimum pore size and active site accessibility and the effects of these properties are well understood. However, very little work has been carried out on understanding the importance of the Lewis-acidity by replacing Zr with other Lewis-acidic metals.

One study that set out to understand the effect of the M_6 cluster on catalysis compared isostructural M-NU-1008 MOFs where M was Zr(IV), Hf(IV), Ce(IV) and Th(IV)[Figure 4.1].[2] When used as catalysts for the CO_2 fixation it was found that Ce-NU-1008 exhibited the fastest rates due to the ease of dissociation of water from the nodes, allowing greater access to the active site. It was also found that dehydrated Hf-NU-1008 performed well for this catalysis due to the availability of active sites within the framework.

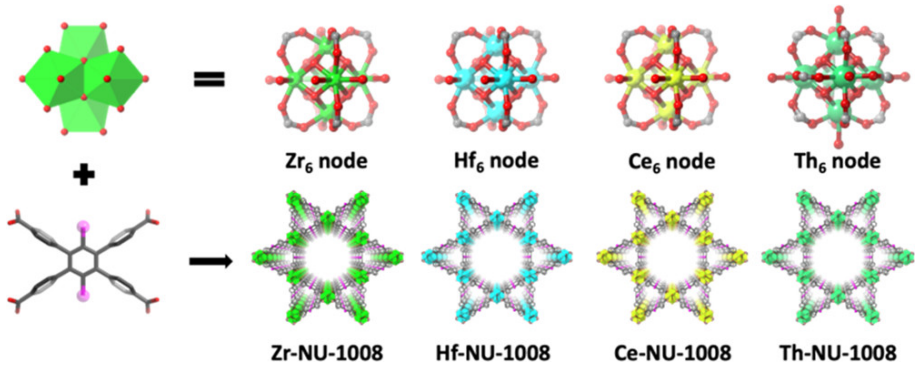

Figure 4.1: Illustration of the four isostructural M-NU-1008 MOFs formed from Group 4 metals. Figure taken from 2

Further studies have been carried out using other Lewis-acidic metals for the catalytic hydrolysis of nerve agents. In the case of UiO-66, isostructural materials have been synthesised with Hf(IV) and Ce(IV). The Hf-UiO-66 resulted in lower rates when compared to the Zr-analogue,[3] however in the case of Ce(IV) the catalytic rates observed where higher than in the for the Zr UiO-66.[4]

Few studies have looked into mixed-metal MOFs for the catalytic hydrolysis of nerve agents. In one, a series of Zr/Ce mixed metal MOFs were prepared,

including UiO-66 and MOF-808.[5] It was found that the introduction of Ce into the MOF framework resulted in higher catalytic rates; this was particularly prevalent in the MOF-808 mixed-metal materials with 20% Ce which observed the highest rate of the materials studied. It was however noted that the addition of Ce into MOF-808 resulted in a reduction of stability at high temperatures.

In this chapter we will investigate the effects of mixed-metal MOFs on the catalytic hydrolysis of nerve agents and simulant. The three well-known Zr-MOF catalysts were chosen: UiO-66, NU-1000 and MOF-808, to compare rates. Hafnium was chosen as the alternate metal to Zr as they exhibit similar properties; Hf lies one row below Zr on the periodic table, with Hf having a lower Lewis-acidity. Hf-MOFs have also been well studied for catalytic applications, and share the same M_6 SBU that is present in the chosen Zr MOFs.[6] Additionally the atomic radii of Zr^{4+} and Hf^{4+} cations are 0.79 and 0.78 Å respectively,[7] therefore a mixed SBU-node may be able to form within the synthesis, as seen previously for Zr/Ce MOFs.[8]

4.3 Experimental

Starting materials were purchased from Sigma-Aldrich or Alfa Aesar and used without further purification. Reactions involving bis(triphenylphosphine)palladium(II) dichloride were carried out under N_2 using standard Schlenk techniques. ^{1}H NMR spectra (400 MHz) were recorded in $CDCl_3-d$ or $DMSO-d_6$ at 298 K on a Bruker AV 400 spectrometer equipped with a BBFO probe. Chemical shifts (δ) are reported in ppm. Abbreviations used for multiplicity are as follows: s - singlet, d - doublet, m - multiplet.

PXRD data has been acquired on STOE STADIP capillary diffractometers using CuK radiation at room temperature. Diffractometers were operated in capillary Debye-Scherrer mode.

SEM images were collected on a Jeol JSM-5600 (tungsten filament) with a resolution of 3.5 nm using an acceleration voltage of 5 kV and a working distance of 10 mm.

Thermogravimetric analyses were carried out on a Stanton Redcroft STA-780 simultaneous TG-DTA in oxidising atmosphere (25 mL/min). Samples were heated to 700 °C at a heating ramp of 5 °C/min, with an isothermal step at 25 °C for 10 min.

4.3.1 MOFs

4.3.1.1 UiO-66

Mixed metal UiO-66(ZrXHfY)

$Zr(IV)Cl_4$ ($X/6 \cdot 122$ mg, 0.52 mmol), $Hf(IV)Cl_4$ ($Y/6 \cdot 166$ mg, 0.52 mmol), and terephthalic acid (86.0 mg, 0.52 mmol) were added to a solution of DMF (15 mL) and acetic acid (0.5 mL). The mixture was added to a Teflon lined autoclave and sonicated for 10 min. The resulting solution was placed in an oven at 120 °C for 24 h. After cooling to room temperature the resulting precipitate was collected by centrifugation (fixed-angle rotor, 6000 rpm, 15 min), washed with 3 x 10 mL portions of MeOH over 24 h, and 1 x 10 mL hexane. The product was activated under vacuum at 60 °C overnight.

4.3.1.2 NU-1000

NU-1000 linker

The following synthesis is adapted from reference Mondloch *et al.*[9].

1,3,6,8-Tetrakis(4-methoxycarbonyl)phenyl)pyrene (L1-Me)

A mixture of (4-methoxycarbonyl)phenyl boronic acid (3.61 g, 20.0 mmol), 1,3,6,8-tetrabromopyrene (1.73 g, 3.34 mmol), bis(triphenylphosphine)palladium(II) dichloride (0.12 g, 0.17 mmol), and potassium carbonate (8.00 g, 72.3 mmol) were stirred in dioxane (100 mL) under a nitrogen atmosphere. The reaction was heated to 130 °C for 72 hr. The reaction mixture was evaporated to dryness and the resulting solids were washed with water and extracted with chloroform (3 x 50 mL). The organic solution was filtered to remove impurities and the filtrate was evaporated to dryness. The resulting solid was boiled in THF for 2 hr to remove impurities. The resulting filtrate gave 1,3,6,8-tetrakis(4-methoxycarbonyl)phenyl)pyrene (**L1-Me**) (1.21 g, 49% yield). ^{1}H NMR ($CDCl_3-d$) δ/ppm: 8.23 (d, 8H), 8.15 (s, 4H), 8.01 (s, 2H), 7.75 (d, 8H), 3.99 (s, 12H).

1,3,6,8-Tetrakis(*p*-benzoic acid)pyrene (L1)

L1-Me (1.21 g, 1.64 mmol) was added to a solution of NaOH (3.15 g, 78.8 mmol) in THF/water (200 mL, ratio 1:1). The mixture was stirred overnight at 100 °C. After evaporating to dryness the resulting solid was dissolved in water (50mL) to give a yellow solution. This was stirred for 2 hr and the pH value was adjusted to 1 by addition of concentrated HCl. The resulting yellow solid was collected by filtration and washed with water. The product was dried under vacuum to give 1,3,6,8-tetrakis(*p*-benzoic acid)pyrene (**L1**) as a yellow powder (0.91 g, 81% yield). ^{1}H NMR ($DMSO-d_6$) δ/ppm: 8.15 (s, 4 H), 8.15 (d, 8H), 8.05 (s, 2H), 7.83 (d, 8H).

Mixed metal NU-1000(ZrX**Hf**Y**)**

$Zr(IV)Cl_4$ (X/6 * 140 mg, 0.60 mmol), $Hf(IV)Cl_4$ (Y/6 * 192 mg, 0.60 mmol) and benzoic acid (5.4 g, 44.2 mmol) were dissolved via sonication in DMF (15 mL). **L1** (0.040 g, 0.12 mmol) was added to the solution and sonicated for a further 20 minutes. The resulting yellow solution was heated in a sealed autoclave at 100 °C for 24 hr. After 24 h the cooled reaction mixture was centrifuged (6,000 r.p.m, 15 min) to separate the liquid and solid phases. The liquid was decanted and the resulting bright yellow solid was washed with 1 x 10 mL portions DMF, 2 x MeOH over 24

hr then centrifuged (6,000 r.p.m, 15 mins) to afford NU-1000(Zr) as a yellow solid.

4.3.1.3 MOF-808

Mixed metal MOF-808(ZrXHfY)

Zirconium (IV) chloride ($X/6 \cdot 233$ mg, 1.0 mmol), hafnium (IV) chloride ($Y/6 \cdot 320$ mg, 1.0 mmol), and 1,3,5-benzenetricarboxylic acid (70.6 mg, 0.34 mmol) were added to a solution of DMF (7.5 mL) and formic acid (7.5 mL). The mixture was added to a Teflon lined autoclave and sonicated for 10 min. The resulting solution was placed in an oven at 135 °C for 24 h. After cooling to room temperature the resulting precipitate was collected by centrifugation (fixed-angle rotor, 6000 rpm, 15 min), washed with 3 x 10 mL portions of MeOH over 24 h, and 1 x 10 mL hexane. The product was activated under vacuum at 120 °C overnight.

Mixed metal MOF-808(ZrXTiY)

Zirconium (IV) chloride ($X/6 \cdot 233$ mg, 1.0 mmol), titanium (IV) isopropoxide ($Y/6 \cdot 280$ mg, 1.0 mmol), and 1,3,5-benzenetricarboxylic acid (70.6 mg, 0.34 mmol) were added to a solution of DMF (7.5 mL) and formic acid (7.5 mL). The mixture was added to a Teflon lined autoclave and sonicated for 10 min. The resulting solution was placed in an oven at 120 °C for 36 h. After cooling to room temperature the resulting precipitate was collected by centrifugation (fixed-angle rotor, 10000 rpm, 10 min), washed with 3 x 10 mL portions of MeOH over 3 days, and 1 x 10 mL acetone overnight. The product was activated under vacuum at 120 °C overnight.

4.3.2 Catalytic Testing

4.3.2.1 High-throughput method

This method was carried out by Dr. J. Palomba at UCSD as outlined in Palomba *et al.*[3].

4.3.2.2 In-house UV-Vis

This procedure is based upon the reported method by Mondloch *et al.*[10]. A buffer solution of *N*-ethylmorpholine (100 mL, 0.45 M, pH 10) was prepared. A MOF-808 sample (3.0 mg, 6 mol%) was added to an aqueous solution of dimethyl *p*-nitrophenylphosphate (5 mL, 0.25 mM stock solution of DMNP in *N*-ethylmorpholine buffer (0.45 M, pH 10)). The rate of DMNP hydrolysis was measured using an *in-situ* UV-Vis probe monitoring the product *p*-nitrophenoxide absorbance at 407 nm.

4.3.3 Characterisation Methods

4.3.3.1 Thermogravimetric Analysis

Within this chapter TGA was carried out in order to understand the stability, alongside calculating the linker defects present. Using methodology based on previous work on UiO-66 the number of missing linkers in the synthesised MOFs can be calculate from normalised thermogravimetric analysis (TGA) and is detailed below.[11]

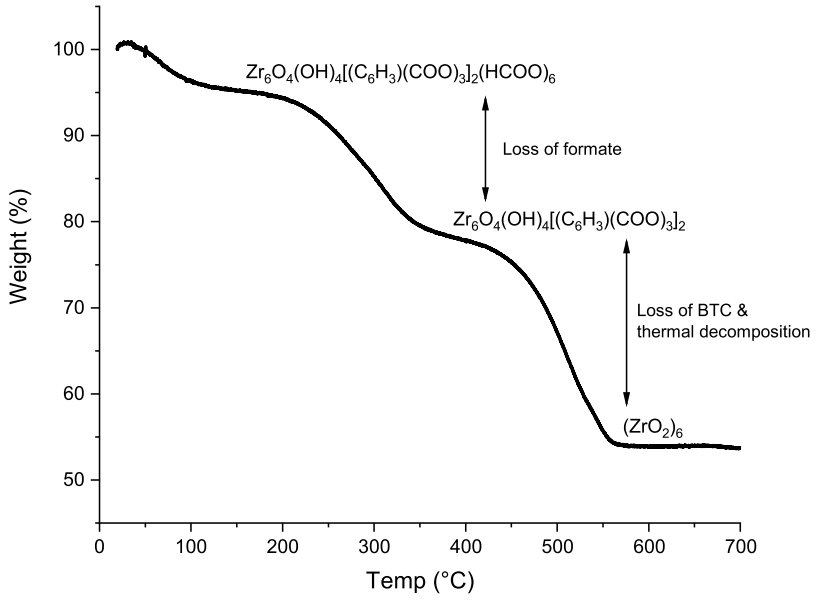

Figure 4.2: TGA trace of MOF-808-PR upon heating at a rate of 5 °C min^{-1} in air showing structural formula at each plateau.

All TGAs were measured under air from 25 °C to 700 °C, heating at a rate of 5 °C min^{-1}. Previously published data has identified degradation temperatures

of up to 100 °C for the loss of solvent (DMF, H_2O), 270 °C for coordinated formate and hydroxyls, and 425 °C for the loss of the BTC linker and the thermal decomposition of MOF-808 into ZrO_2.[12] An example of a pristine MOF-808 TGA trace is given in Figure 4.2 with the formula of the remaining material given at each plateau.

As we know the final residue is 6 moles of ZrO_2, with a molar mass of 739.34 g mol^{-1}, we can estimate the theoretical linker loss by normalising the TGA curve so the end weight is 100%. The molar mass of the MOF-808 structure after the loss of formate and hydroxyl ions, $Zr_6O_4(OH)_4[(C_6H_3)(COO)_3]_2$, is 1093.6 g mol^{-1}. This is a factor of 1.47 higher than the final ZrO_2 residue which gives a theoretical TGA plateau for that structure of 147%.

The final mass loss step in the MOF-808 TGA corresponds to the loss of the BTC linkers which, giving the above values (147% - 100%), corresponds to the BTC comprising of 47% of the structure. Using this information we can determine the percentage of linkers (PL) that are in the MOF-808 structure with the following equation:

$$\mathrm{PL} = \frac{(\mathrm{Plat}_{\mathrm{exp}} - 100)}{47} \cdot 100 \tag{4.1}$$

Where $\mathrm{Plat}_{\mathrm{exp}}$ is the plateau value in collected TGA which corresponds to the material in the form $Zr_6O_4(OH)_4[(C_6H_3)(COO)_3]_2$ and is typically taken in the temperature region ca. 425 °C.

An example of a normalised MOF-808 TGA curve is shown in Figure 4.3. We can calculate the percentage of linkers present in this structure using Equation 5.1 which gives a linker percentage of 96%. As this value is very close to 100% we can assume that all linkers are present in this structure and no linker defects are present. This method will be used to identify any materials with linker defects in this chapter.

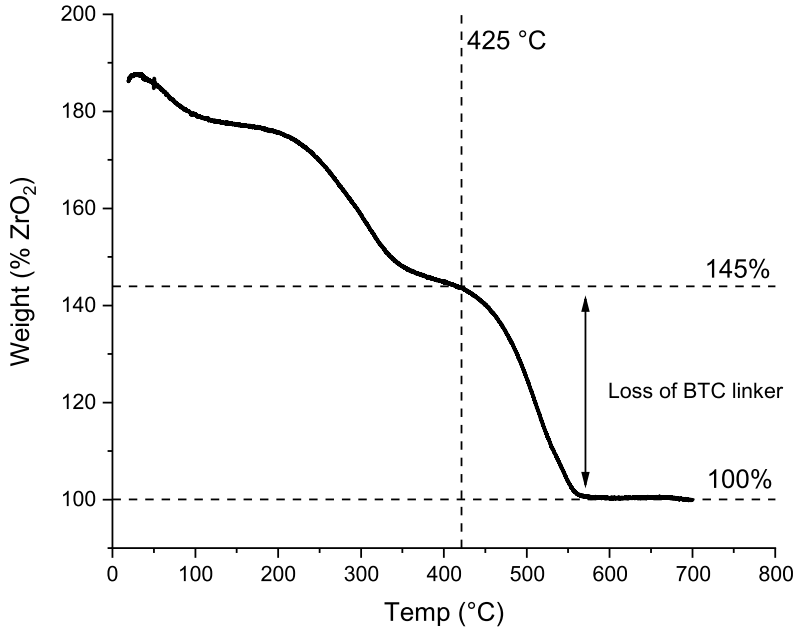

Figure 4.3: Normalised TGA trace of MOF-808-PR with respect to ZrO_2 showing percentage loss due to BTC linker.

4.3.4 Dynamic Light Scattering

Dynamic Light Scattering (DLS) was carried out in house by A. Edward on a Malvern Ultra Intrument using a glass cuvette (10 mm path length).

Multiple solvents were tested with MOF-808 to ensure that particles were stable in solution and did not aggregate. These included water, isopropanol, ethanol, methanol and dimethylformamide (DMF). From these studies it was found that the optimum solvent was isopropanol.

4.4 Results & Discussion

4.4.1 Mixed metal Zirconium and Hafnium MOFs

In order to investigate the role of Lewis acidity in the catalytic hydrolysis of nerve agents and simulants, a series of mixed metal UiO-66, NU-1000 and MOF-808 materials were prepared using zirconium and hafnium. The anticipated role of substituting Zr for Hf was to lower the Lewis-acidity throughout the series; one sixth Hf mol % was systematically introduced in the synthesis to replace a single Zr in the Zr_6 node which is present in all MOFs synthesised.

4.4.1.1 UiO-66

Samples of mixed metal UiO-66(Zr/Hf) were prepared as outlined in subsection 4.3.1 ranging from 100% Zr to 100% Hf in intervals of one sixth. These samples are referred to as MOF-808-ZrXHfY with X and Y denoting the amounts of Zr and Hf added to the synthesis.

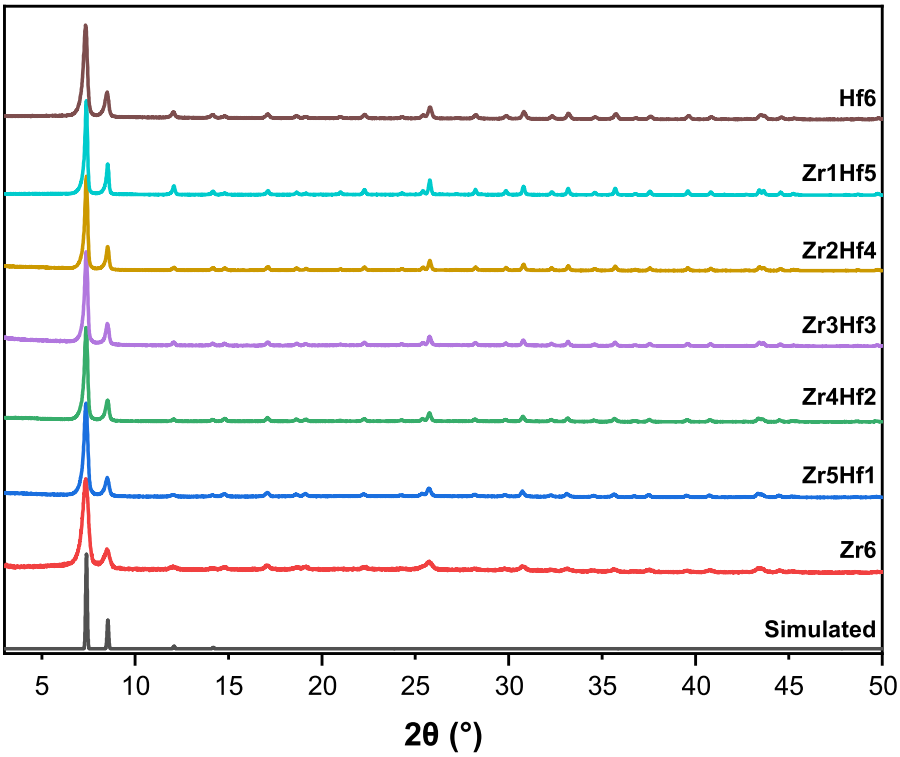

Figure 4.4: PXRD of mixed metal Zr/Hf-UiO-66 samples synthesised with the remaining percentage in the sample being Hf.

Following the synthesis, all materials were thoroughly washed to remove

any un-reacted starting materials. The bulk crystallinity of each sample was confirmed by PXRD [Figure 4.4]. All samples are in good agreement with the simulated UiO-66 PXRD pattern, with no substantial differences between each sample. This indicates that the addition of Hf does not effect the overall crystal structure; all samples are phase pure and no significant shift in d-spacing is observed across the samples. This is in agreement with previous studies which have shown that other Group 4 metals can be incorporated into the synthesis of UiO-66 to form isostructural materials.[13]

In order to confirm that both Zr and Hf are present in each mixed metal sample, and in the desired, energy-dispersive X-ray spectroscopy (EDS) was carried out. Measurements were taken over multiple crystallites within each sample to confirm that both Zr and Hf are present in all the mixed metal samples [Table 4.1]. Each UiO-66-Zr/Hf sample displays good agreement between the ratios of metal pre-cursor added to the synthesis and the final ratios within each sample. In the samples with high percentages of Zr, we see slightly less Zr incorporation than desired from the EDS results. Below 50% Zr, we see slightly higher levels than expected. However, all of the samples have low uncertainty values, therefore the ratios of metals are homogenous across each sample.

Table 4.1: EDS results for Zr/Hf-UiO-66 samples comparing the experimental target vs measured percentage of Zr in each sample. The remaining percentage is Hf.

Sample	Target Zr%	Measured Zr%
UiO-66 Zr5Hf1	83	84 $\pm$1.0
UiO-66 Zr4Hf2	67	62 $\pm$1.1
UiO-66 Zr3Hf3	50	44 $\pm$1.3
UiO-66 Zr2Hf4	33	34 $\pm$1.3
UiO-66 Zr1Hf5	17	18 $\pm$4.7

As the bulk crystallinity and mixed-metal ratio within each sample was confirmed, catalytic testing was carried out on all mixed metal UiO-66 samples. Each sample was tested multiple times using a high-throughput method previously reported.[3] From these results initial rates were calculated and given in Figure 4.5.

The highest initial rate observed is for the UiO-66-Zr sample. This is expected due to the higher Lewis-acidity for Zr, compared to Hf, being preferential in this catalysis. However, if Lewis-acidity was the only factor determining rate for

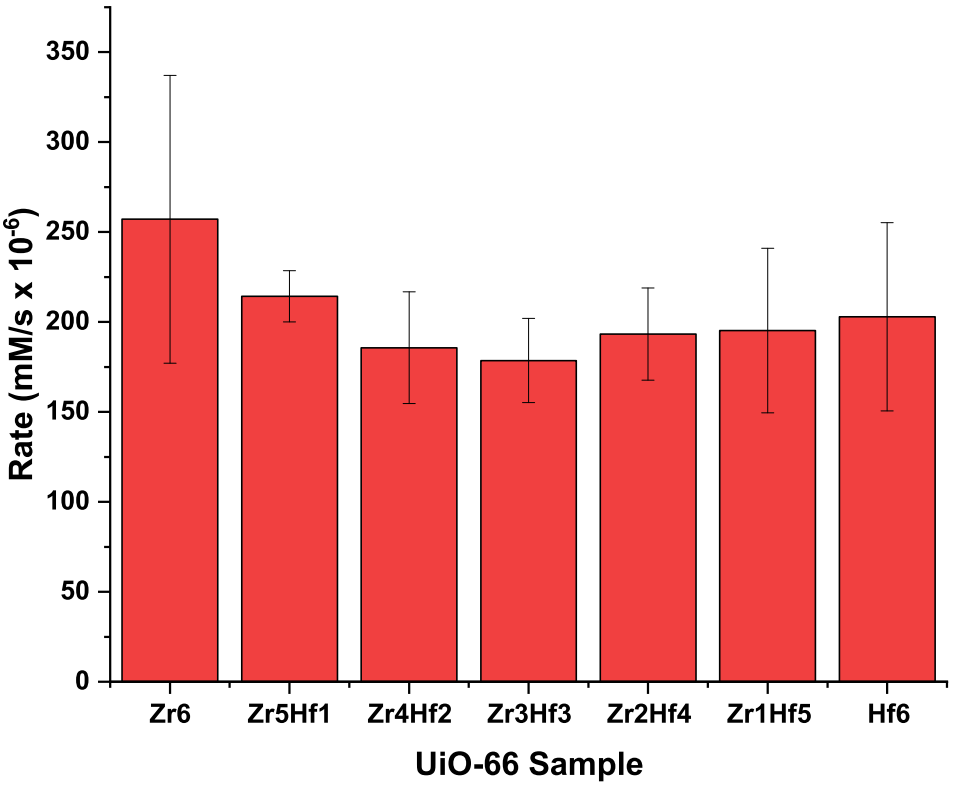

Figure 4.5: Catalytic rate of hydrolysis for mixed metal UiO-66 samples.

these materials, we would expect to see the lowest rate for UiO-66-Hf which is not the case. The sample with the lowest initial rate is UiO-66-Zr3Hf3, which from EDS measurements contains 44% Zr and 56% Hf. This sample is not strikingly lower than others within the series and it is clear than the catalytic activity does not linearly decrease with the addition of Hf.

Due to the pore size of UiO-66 being 6Å in diameter and therefore too small to allow DMNP to enter the pores in this case, catalysis takes place on the surface of the particle. The nerve agent simulant only comes into contact with the Lewis-acidic active sites on the surface of the UiO-66 particles, which has been calculated as only 0.75% of the total metal SBUs within the particle. Due to this, the composition of metals within the SBU is unlikely to have as large an affect on the catalytic rate as the particle size or the number of defects within the structure.

4.4.1.2 NU-1000

Following the lack of distinction between the catalytic rates of mixed-metal UiO-66 samples, possibly due to the small pore structure, a large pore MOF,

NU-1000, was investigated. Mixed-metal NU-1000 was synthesised in two parts. The linker for this MOF was synthesised in house as outlined in subsection 4.3.1 with a yield of 81%. This synthesis was successful as determined by NMR spectroscopy [Appendix Figure 4.19]. The MOF synthesis method differs from previous literature where a two-step process was used,[9] instead a one step synthesis method was successfully implemented as outlined above. The resulting solids were isolated, washed thoroughly to remove unreacted starting materials, and characterised through PXRD [Figure 4.6].

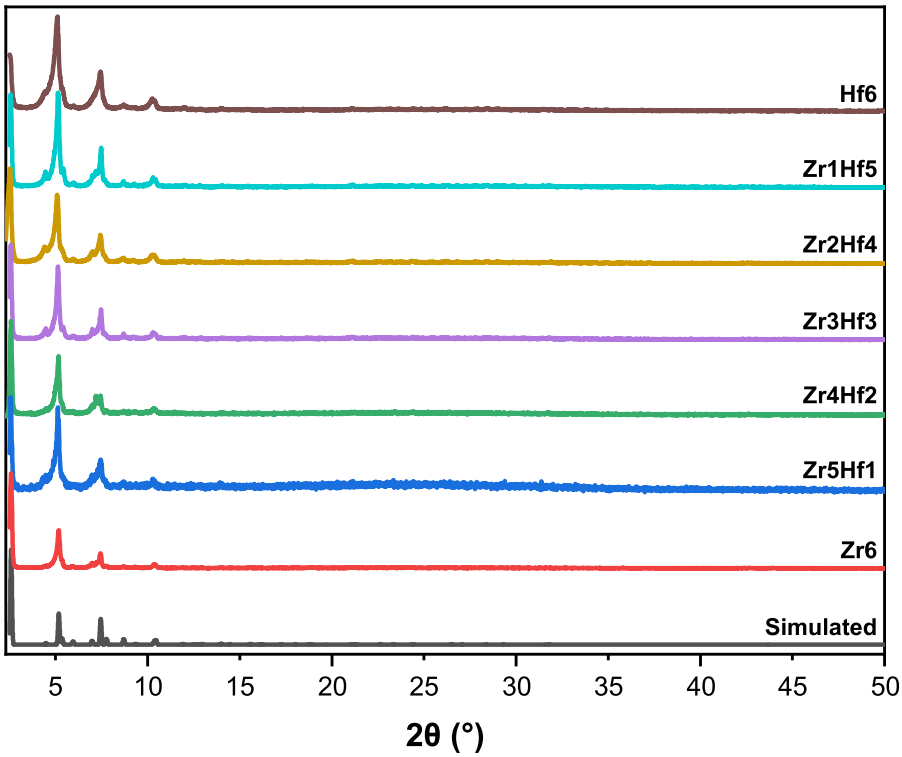

Figure 4.6: PXRD of mixed metal Zr/Hf-NU-1000 samples synthesised with the remaining percentage in the sample being Hf.

The PXRD for all samples is in agreement with the simulated 100% Zr NU-1000 literature pattern and confirms bulk crystallinity across the materials synthesised. This implies that the addition of Hf does not change the NU-1000 crystal structure, this is expected as previous studies have synthesised a purely Hf NU-1000 which is isostructural to the purely Zr NU-1000.[14]

As the bulk crystallinity of the samples were confirmed, the mixed-metal ratio of each sample was quantified through EDS measurements. For each sample, multiple NU-1000 crystallites were measured to calculate a Zr % for each sample given in Table 4.2. For all mixed-metal samples both Zr and Hf were detected by

EDS which confirms the successful synthesis of mixed-metal NU-1000.

Table 4.2: EDS results for Zr/Hf-NU-1000 samples comparing the experimental target vs measured percentage of Zr in each sample. The remaining percentage is Hf.

Sample	Target Zr%	Measured Zr%
NU-1000 Zr5Hf1	83	84 $\pm$3.4
NU-1000 Zr4Hf2	67	75 $\pm$7.4
NU-1000 Zr3Hf3	50	49 $\pm$2.9
NU-1000 Zr2Hf4	33	29 $\pm$1.1
NU-1000 Zr1Hf5	17	11 $\pm$0.6

The measured Zr% present in each sample as measured by EDS are generally in good agreement with the ratios of metal used in the synthesis. There are some outliers such as the NU-1000 Zr4Hf2 containing a higher percentage of Zr than intended. The standard deviation within the measurement is also relatively large which implies that the metal composition is not consistent across the sample, with some areas with a metal composition more similar to that of NU-1000 Zr5Hf1. The standard deviation in the EDS measurements throughout the rest of the samples are low, therefore have a uniform ratio of metals throughout.

Once the materials were successfully characterised and the ratio of metals quantified, catalytic testing was carried out to determine the effect of increasing Hf within the NU-1000 framework. All samples were activated under dynamic vacuum at 120°C before catalytic tests were carried out due to prior literature precedence.[10] The catalysis was carried out in-house using an *in-situ* UV-Vis probe as outlined in 4.3.2. It should be noted that the catalytic loading was higher for in-house measurements due to the scale of reaction, therefore direct comparisons between results from the in-house and the high-throughput method cannot be made. The initial rates calculated from repeat tests are given in Figure 4.7.

The highest initial rate observed was for the Zr 100% NU-1000 sample. This is followed by the general trend of reducing initial catalytic rate with increasing Hf%. This trend is expected as the lower Lewis-acidity of Hf compared to Zr is less favourable for the catalytic hydrolysis of nerve agents and simulants. There are some outliers to this trend: NU-1000 Zr5Hf1 has a lower rate than either Zr4Hf2 or Zr3Hf3 NU-1000. Yet, with the errors associated, these outlier may prove to be insignificant.

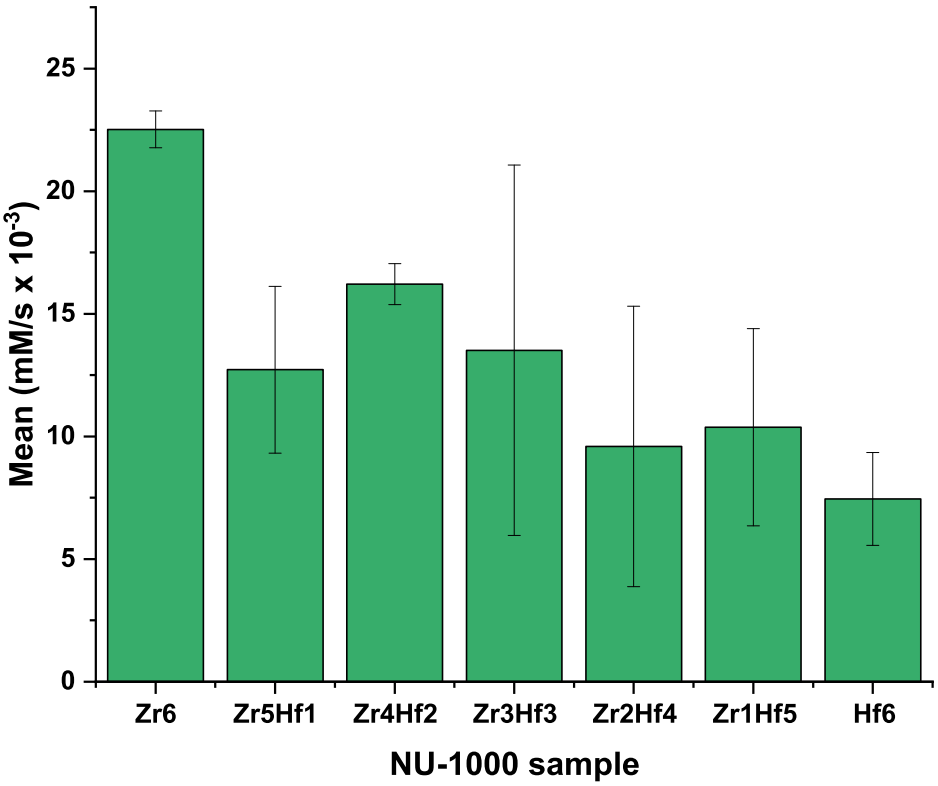

Figure 4.7: Catalytic rate of hydrolysis for mixed metal NU-1000 samples.

It should also be noted that the mixed-metal NU-1000 samples with a Zr incorporation of 50% and lower (Zr3Hf3 to Zr1Hf5) have a large standard error associated with the average initial rate value. This is interesting as the EDS measurements for these samples have the lowest associated standard deviation, therefore there may be other factors within these materials that are effecting the rate such as particle size or defects.

Overall, for NU-1000 the initial testing carried out on the mixed-metal samples show a decrease in initial catalytic rates as the percentage of Hf increases within the structure; the initial rate for Zr-NU-1000 is around 3 times higher than for Hf-NU-1000. This result is in agreement with a previous study on NU-1008, with the same 8-connected SBU as seen in NU-1000, where the catalytic activity of a Lewis-acidic promoted reaction decreased with Hf when compared to Zr.[2] It is therefore likely that for MOFs with 8-connected SBUs and a wide pore structure, the Lewis-acidity of the metals do influence the catalytic rate.

4.4.1.3 MOF-808

The final MOF chosen for investigation was MOF-808, this MOF has a pore size of 18 Å; between the small 6 Å diameter of UiO-66 and the large 31 Å diameter of NU-1000. MOF-808 also exhibits the lowest SBU connectivity of the three MOFs investigated with 6-connected linkers per M_6 SBU, which may allow greater accessibility to the active metal sites.

Mixed metal MOF-808 was synthesised as outlined in subsection 4.3.1 in a one-step synthesis containing a range of Zr and Hf ratios. The resulting precipitates were isolated and thoroughly washed to remove any unreacted starting materials then characterised by PXRD to confirm bulk crystallinity [Figure 4.8]. All samples synthesised are in good agreement with the simulated literature pattern of Zr 100% MOF-808 which indicates, as seen with other MOFs investigated, that the introduction of Hf into the framework does not disrupt the long-range structure.

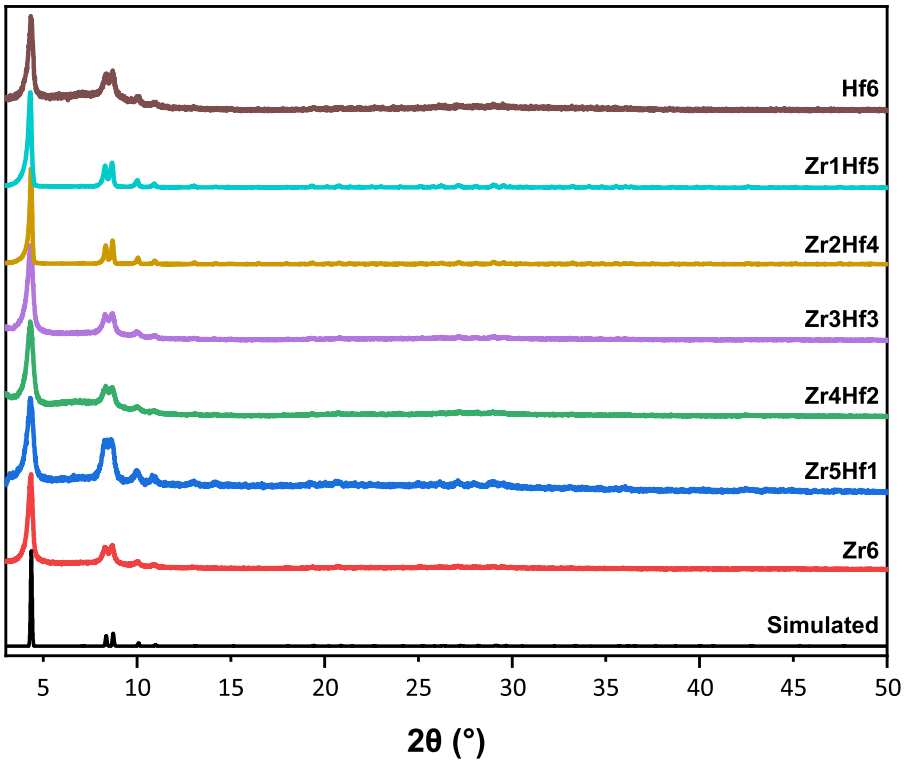

Figure 4.8: PXRD of mixed metal Zr/Hf-MOF-808 samples synthesised with the remaining percentage in the sample being Hf.

To ensure each mixed-metal sample has successfully incorporated both Zr and Hf, EDS measurements were carried out over with the calculated Zr% given in

Table 4.3. In all cases the mixed-metal samples have successfully incorporated both Zr and Hf, with excellent agreement between the target and measured Zr%. The standard deviation within the measurements is also relatively low, with the averages being calculated from over numerous measurements, signifying that the mixed-metal ratio is homogenous across each sample.

Table 4.3: EDS results for mixed-metal MOF-808 samples comparing the target vs measured Zr% in each sample. The remaining percentage being Hf.

Sample	Target Zr%	Measured Zr%
MOF-808 Zr5Hf1	83	81 $\pm$0.9
MOF-808 Zr4Hf2	67	66 $\pm$0.9
MOF-808 Zr3Hf3	50	49 $\pm$1.6
MOF-808 Zr2Hf4	33	34 $\pm$2.3
MOF-808 Zr1Hf5	17	16 $\pm$3.2

As the mixed-metal properties of each samples was successfully quantified, catalytic testing for the hydrolysis of the nerve agent simulant DMNP was carried out. These tests were carried out by Palomba *et al.* using the high-throughput method previously published.[3] From these tests, initial rates were calculated from multiple repeats and are given in Figure 4.9.

From these results, mixed-metal MOF-808 does not follow the trend seen in NU-1000, where the addition of Hf results in a reduction of initial rates. It is also unlike UiO-66 as there are clear differences between the rates of each sample. Instead, it is clear that there is no overall trend, with some mixed-metal MOFs outperforming both Zr 100% and Hf 100% samples. The most interesting result is for MOF-808 Zr2Hf4 which exhibits over an initial rate over twice as fast as any other sample. This rate of 1400 mM/s x 10^{-6} is one of the highest rates currently reported for MOF-808.[3]

All of these mixed-metal samples outperform the MOF-808 Zr6 sample, with the exception of MOF-808 Zr1Hf5, therefore it is clear that the catalytic rates for MOF-808 materials are not linearly correlated with Lewis-acidity. To ensure that these results are not due to a change in porosity across the series, BET analysis was carried out [Appendix Figure 4.20]. This shows that all materials are porous, but no correlation between the porosity and the catalytic rates is present.

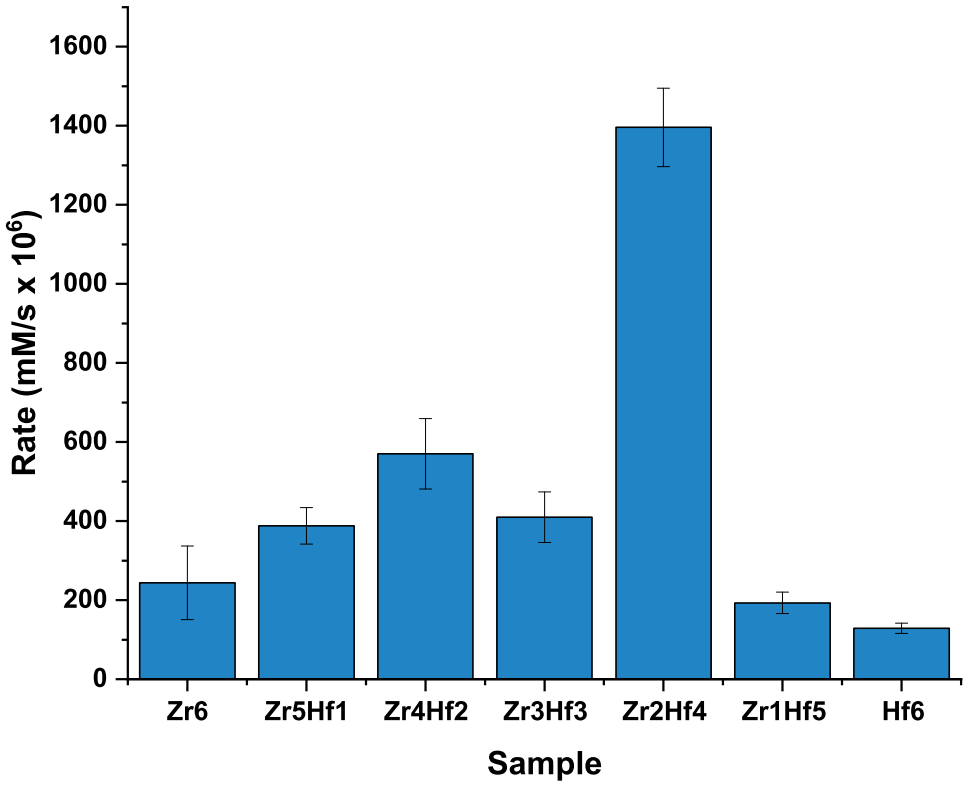

Figure 4.9: Catalytic rate of hydrolysis for mixed metal MOF-808 samples.

As these results did not follow the expected trend further mixed-metal MOF-808 materials were synthesised to check for reproducibility of catalytic activity, and to investigate other characteristics of the MOFs.

An additional two batches of the mixed-metal MOF-808 series were synthesised using the exact procedure as outlined above. All materials were thoroughly washed to remove unreacted starting materials. To ensure all materials show bulk crystallinity PXRD was carried out; all materials synthesised were in agreement with the simulated literature sample of MOF-808, with no change in the long-range crystalline structure and all three batches in agreement [Appendix Figure 4.21 & Figure 4.22].

As the bulk crystallinity of all samples were confirmed, the metal composition of each material was quantified by EDS. Multiple measurements were taken on different crystallites to calculate the Zr% in each sample, with results for batch 2 and batch 3 given in Table 4.4.

Table 4.4: EDS results for mixed-metal MOF-808 Batch 2 and 3 samples comparing the experimental target vs measured Zr% in each sample. The remaining percentage is Hf.

Sample	Target Zr%	Batch 2 Zr%	Batch 3 Zr%
MOF-808 Zr5Hf1	83	84 ±0.6	85 ±1.2
MOF-808 Zr4Hf2	67	65 ±1.7	66 ±1.0
MOF-808 Zr3Hf3	50	48 ±1.7	51 ±3.9
MOF-808 Zr2Hf4	33	32 ±2.3	35 ±9.3
MOF-808 Zr1Hf5	17	10 ±1.4	12 ±1.8

For all samples both Zr and Hf was detected, confirming that a range of mixed-metal compositions of MOF-808 can be reliably and reproducibly synthesised through a one-pot *in-situ* synthesis. As the mixed-metal nature of all samples were confirmed, catalytic testing was carried for the hydrolysis of DMNP using the previously published high-throughput method outlined in subsection 4.3.2. From these results initial rates were calculated and all mixed-metal MOF-808 initial rates are given in Figure 4.10.

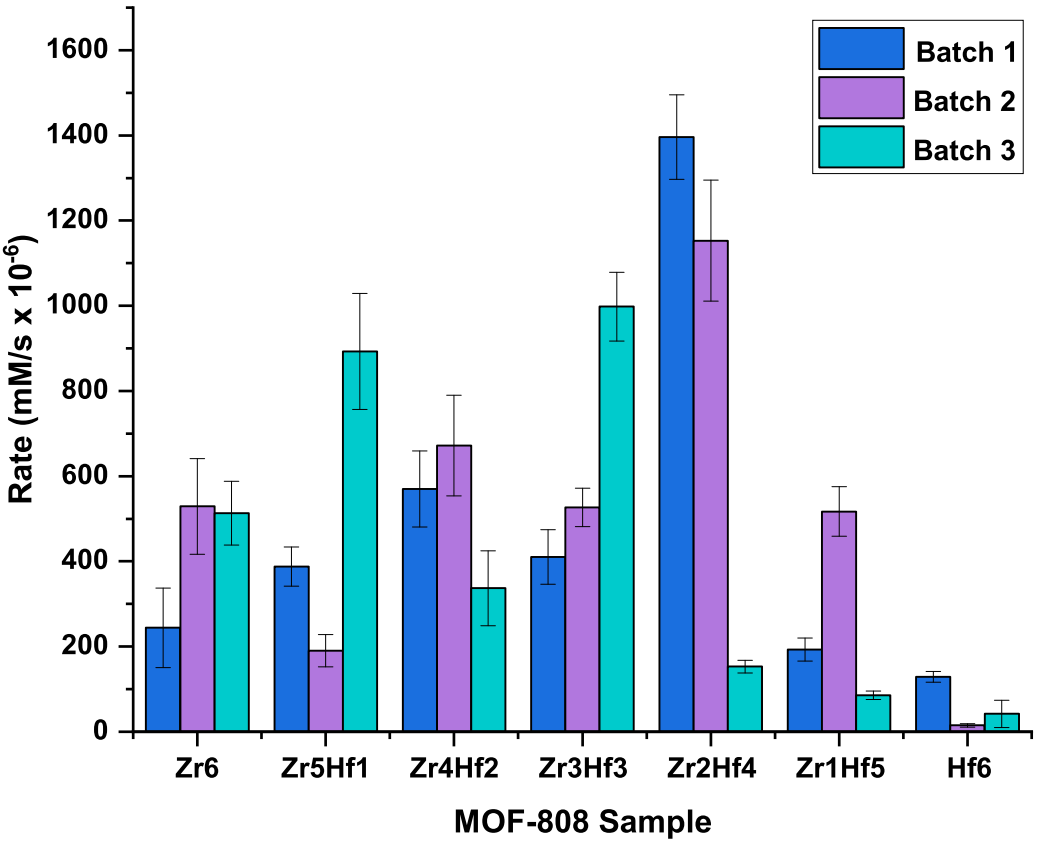

Figure 4.10: Catalytic rate of hydrolysis for Batch 1, 2 and 3 mixed metal MOF-808 samples.

The initial rates vary between batches , with no overall trend seen. However, it is clear that particular mixed-metal samples outperform MOF-808 Zr6 samples in all batches. For the three batches synthesised, the MOF-808 Hf6 sample displays the lowest catalytic rates which is in agreement with previous studies on Group 4 metal MOFs for this application.[2] However, the lack of studies into mixed-metal MOF-808 may have overlooked favourable catalytic properties of these materials.

Mixed-metal samples outperforming the MOF-808-Zr6 sample in Batch 2 include MOF-808 Zr4Hf2 and MOF-808 Zr2Hf4 with initial rates of 670 and 1150 mM/s x 10^{-6} respectively. As with Batch 1, MOF-808 Zr2Hf4 has the highest catalytic rate of all samples within Batch 2.

When comparing catalytic results for MOF-808 Batch 3, MOF-808 Zr6 is outperformed by mixed metal samples of the composition MOF-808 Zr5Hf1 and MOF-808 Zr3Hf3 with rates of 900 and 1000 mM/s x 10^{-6} respectively. We do not see the elevated rate for MOF-808 Zr2Hf4 as seen in Batch 1 and 2. For Batch 3 this sample only reports an initial rate of 150 mM/s x 10^{-6}, lower than many of the other samples, including MOF-808 Zr6, with the highest rate seen for MOF-808 Zr3Hf3.

These results are very interesting as immediately it is clear that Zr2Hf4 sample is the best performing catalyst for both Batch 1 and 2 over repeat measurements, with relatively low associated standard errors. However, the Zr2Hf4 sample synthesised in Batch 3 is one of the lowest performing catalysts. In order to understand this discrepancy further investigation has been carried out on all batches of MOF-808 Zr2Hf4 to identify properties of the materials that may effect the catalytic results, and to determine why this material exhibits the highest initial rate seen for this catalysis.[3] Other samples were also investigated such as MOF-808 Zr3Hf3 from Batch 3 as this material also exhibited unexpectedly high catalytic activity.

The EDS measurements carried out found good agreement between experimental Zr mol% and measured Zr mol% in the repeat samples [Table 4.4]. These measurements were carried out over 25 separate crystallites within each sample to ensure accurate reporting of ratios across the materials, therefore it can be reliably stated that all samples are mixed-metal in nature.

Looking closer at the EDS results of the three batches of MOF-808 Zr2Hf4 the average Zr mol% is in good agreement with the desired result of 33% with values of 34%, 32% and 35% for Batch 1, 2 and 3 respectively. However, when the error associated with these results is considered, for Batch 3 MOF-808 Zr2Hf4 a $\pm$ 9% is calculated. The spread of the EDS data collected for the Zr2Hf4 samples is illustrated in Figure 4.11 and shows that some crystallites measured within the batch 3 Zr2Hf4 sample contained as little as 10% Zr in some cases. This is likely to have effected the average catalytic rate as the samples with *ca.* 17% Zr (MOF-808 Zr1Hf5), displayed lower catalytic rates [Figure 4.10].

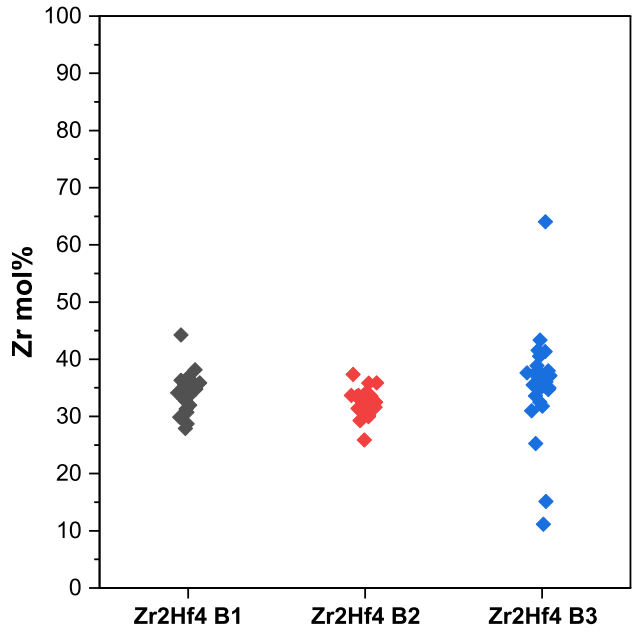

Figure 4.11: Spread of EDS results taken for 25 separate crystallites for Batch 1, 2 and 3 MOF-808-Zr2Hf4 samples .

Another structural property that may increase catalytic performance of MOF-808 Zr2Hf4 is increased accessibility to M_6-SBU active sites through the linker defects present in the structure. Thermogravimetric analysis (TGA) was carried out on all three batches of MOF-808-Zr2Hf4 to investigate stability of the three samples, and determine the presence of linker defects. The methodology for this calculation is described above in subsection 4.3.3.

For each sample the TGA data collected was normalised to the final weight following decomposition; for the mixed-metal samples this consists of the ratio of ZrO_2 and HfO_2 determined by the EDS measurements. Three characteristic mass-losses are observed in the TGA for all batches of MOF-808 Zr2Hf4 [Figure 4.12].

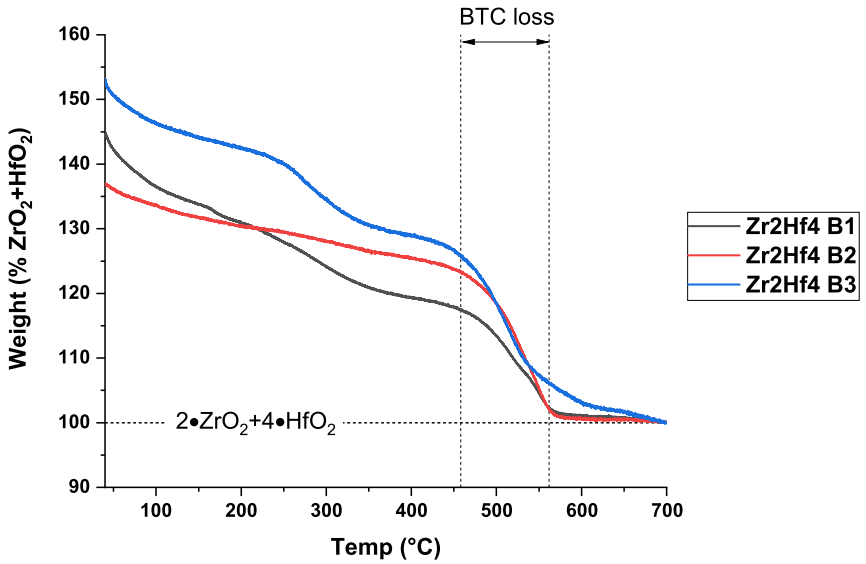

Figure 4.12: TGA analysis for Batch 1, 2 and 3 MOF-808-Zr2Hf4 samples with plots normalised to a $2ZrO_2 4HfO_2$.

The weight losses at 100°C, 270°C and 475°C can be attributed to loss of solvent (H2O, DMF), loss of formate, and loss of linker (1,3,5-benzenetricarboxylic acid) respectively.[12]

The TGA traces differ between each samples, indicating some inconsistencies within the structure between batches of MOF-808 Zr2Hf4. For batch 1 and 3 we see a pronounced mass loss around 270°C which corresponds to the loss of formate ions that coordinate to the SBU, and originate from the formic acid used as a modulator. This is not seen in batch 2, rather a longer plateau is observed, this suggests that fewer formate ions are coordinated to the hydrated structure. It should be noted that before each catalytic test the samples are activated at 120°C to give the dehydrated structure. However, this structure will still contain coordinated formate ions as they are not lost until 270°C; as the formate mass loss is largest for Zr2Hf4 batch 3, this sample contains the highest proportion of coordinated formate ions of the three samples. This may hinder access to the SBU active sites comparatively more than for batch 1 or 2, and could contribute to the lower catalytic rate observed.

All batches show a plateau corresponding to the dehydrated structure and a mass loss at the characteristic temperature of 475°C, corresponding to the loss of the BTC linker and the structure thermally decomposing. The overall stability is unchanged between batches and is therefore not a factor affecting the catalysis.

As each MOF-808 Zr2Hf4 sample displays a mass loss for BTC at the expected temperature, the number of linker defects within the structure can be quantified. It has been established for UiO-66 that the percentage weight lost for linker decomposition correlates to the number of defects in the framework.[11] Using this method we have estimated the percentage of linker defects within each MOF-808 Zr2Hf4 sample using Equation 5.1 given above.

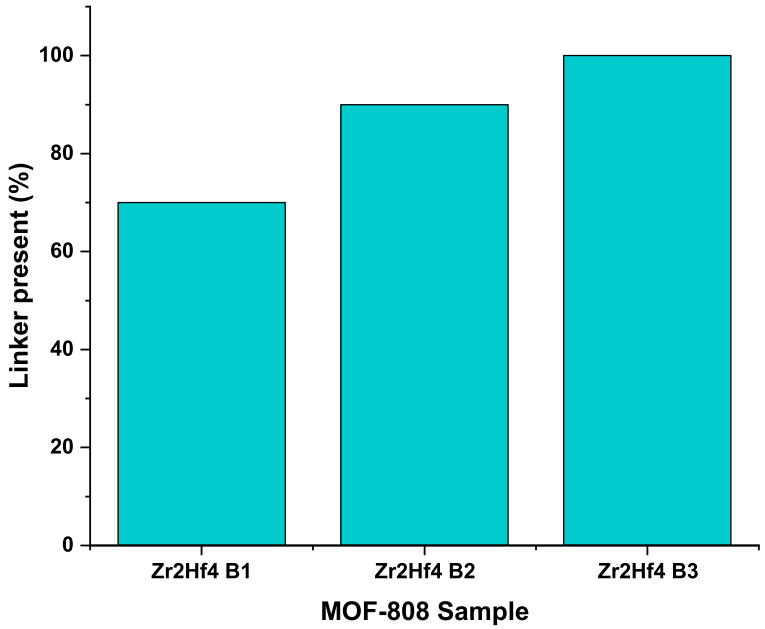

Figure 4.13: Percentage of linker present in MOF-808 Zr2Hf4 samples relative to a pristine MOF-808 structure calculated from normalised TGA.

The percentage of linker incorporated into each sample of MOF-808 Zr2Hf4 as calculated from TGA is given in Figure 4.13. The proportion of linker present in the structure, relative to a pristine MOF-808 structure, is 70%, 90% and 100% for Batch 1, 2 and 3 MOF-808 Zr2Hf4, respectively. These values reveal that linker defects are present in both batch 1 and 2, but not for batch 3 MOF-808 Zr2Hf4 as 100% of the expected linker incorporation is confirmed by TGA. This result indicates that a correlation exists between linker defects in the structure and the initial rate value. The sample containing the lowest percentage of linkers corresponds to the sample with the highest initial rate: batch 1 MOF-808 Zr2Hf4.

Higher catalytic rates are observed for samples with linker defects likely due to increased access to the catalytically active open metal sites created by fewer linkers coordinating to the M_6-SBU. Previous studies have observed this effect on highly coordinated SBU MOFs such as UiO-66, with a pristine crystal structure

containing a 12-connected SBU.[15] However, studies have not been carried out on defective MOF-808 structures for this catalysis, partially due to MOF-808 already consisting of a relatively low connected SBU in the pristine form: 6-coordinated.

As a trend between linker defects within the structure and the catalytic rate was found for the Zr2Hf4 samples, TGA was carried out on other mixed-metal samples to establish the role of defects on the catalysis across the mixed-metal series. The samples chosen were MOF-808 Zr6 and MOF-808 Hf6 from batch 1 and MOF-808 Zr3Hf3 from batch 3 in an attempt to gain understanding of the relationship between Lewis-acidity, linker defects and catalytic rates. The percentage linker present in these samples, calculated from TGA measurements, compared to initial catalytic rates is given in Figure 4.14.

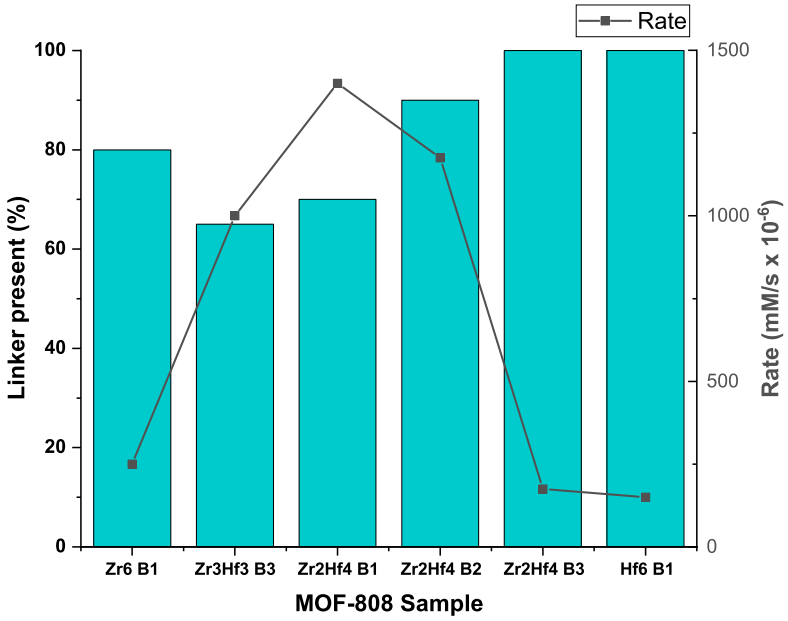

Figure 4.14: Linker present within mixed-metal MOF-808 samples relative to a pristine MOF-808 structure (blue bars, left axis) and catalytic rate observed (grey squares, right axis).

For the MOF-808 Zr6 and MOF-808 Hf6 samples, it was calculated that 80% and 100% of the expected linkers were present respectively. This correlates with a marginally higher rate for the Zr6 sample compared to the Hf6 which may be due to fewer linkers present, therefore higher accessibility to the active metal sites. Yet the rate for the Zr6 sample at 220 mM/s x 10^{-6} is much lower than the MOF-808 Zr2Hf4 sample at 1400 mM/s x 10^{-6} even though there are fewer linkers present in the Zr6 sample: 80% compared to 90%. This demonstrates that the mixed-metal MOF acts as a better catalyst despite it having more linkers

present in the structure, indicating changes in Lewis-acidity are factoring into the catalytic rates.

The calculated proportion of linker present in MOF-808 Zr3Hf3 batch 3 sample is 64%; the lowest percentage linker present for the samples chosen. Although this sample displays a high initial rate value, it is lower than MOF-808 Zr2Hf4 batch 1 or 2 initial rate values. This supports the conclusion that, although linker defects play a role, the Lewis-acidity has a greater effect on catalysis in this case; if rates were inversely correlated to the number of defects present we would observe, for the materials investigated, the highest initial rate for MOF-808 Zr3Hf3 batch 3.

Another important factor to consider in MOF catalysis is particle size. Previous studies on UiO-66 have shown that the smaller the particle size the better the catalytic activity due to higher surface area available for catalysis.[16] To date, studies on MOF-808 particle size have not been carried out for this application. This may be due to the pore size being large enough to accommodate nerve agents and simulants, therefore the particle surface area being a secondary considerations, however, this is also true for NU-1000 yet studies show surface area does have an effect.[17]

Investigations into the particle size of batch 1, 2 and 3 MOF-808 Zr2Hf4 samples were carried out through Dynamic Light Scattering (DLS). Measurements were carried out and average particle sizes for Zr2Hf4 samples were calculated and given in Figure 4.15.

It is clear that the particle size is not consistent between the three batches synthesised with particle sizes of 548 nm, 495 nm and 223 nm for batch 1, 2 and 3 respectively. These samples are stable within the isopropanol chosen as the DLS solvent and therefore display low errors in each measurement. Previously reported MOF-808 particles used in this catalysis range from 200 - 1200 nm.[18,19]

To further illustrate the differences in particles size SEM images were captured for the three MOF-808 Zr2Hf4 samples [Figure 4.16]. The topology between each sample is consistent with defined prism-like particles, with batch 1 clearly consisting of the larger particles, followed by batch 2, and then batch 3 with noticeably smaller crystallites. The difference in particle size is interesting as each batch was synthesised in identical conditions, using the same autoclave.

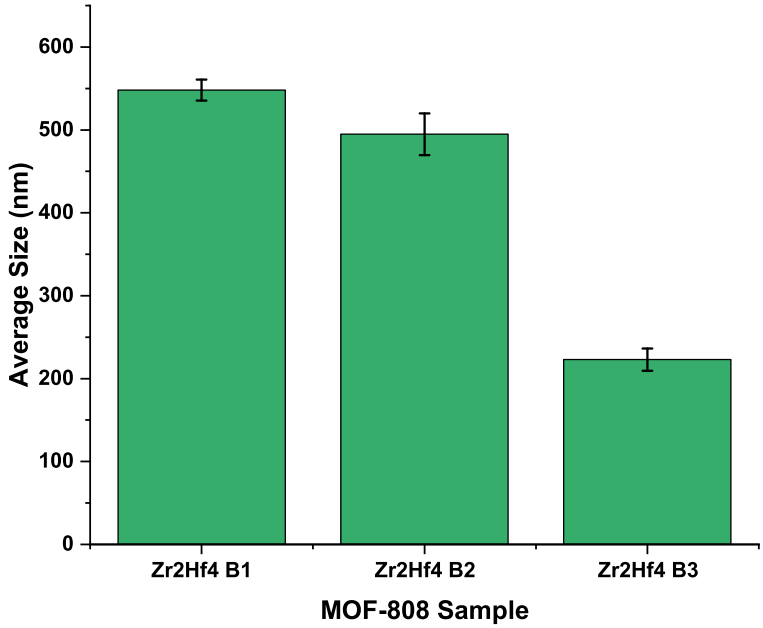

Figure 4.15: Average particle size of all MOF-808-Zr2Hf4 samples determined by Dynamic Light Scattering measurements.

Therefore the difference in particle size is unintentional and may be due to a variety of effects within the synthesis outwith our control. It is known that controlling particle size within solvothermal syntheses is challenging.[20]

When we compare the particle size to the initial rates observed for each of the MOF-808 Zr2Hf4 samples a trend is observed where the larger the particle size, the higher the initial rate. This is an unusual result as in previous studies a smaller particle size has been associated with an increase in rate due to higher surface area available for catalysis.[17] However, it should be noted that DLS measurements were carried out in isopropanol, whereas the catalysis is carried out in an aqueous solution. This may result in different average particle sizes being present in the reaction solution due to agglomeration.

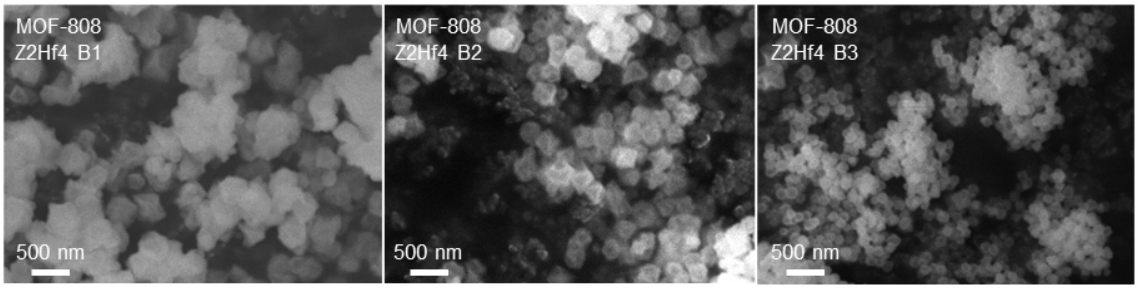

Figure 4.16: Images captured using SEM showing the difference in size between particles in each batch of MOF-808-Zr2Hf4.

To gain a greater understanding between particle size, Lewis-acidity and catalytic rates, further samples were analysed by DLS: MOF-808 Zr6 from batch 1 and MOF-808 Zr3Hf3 from batch 3. The observed average particle size and initial rate for each of the samples selected are given in Figure 4.17.

The inverse correlation between rate and particle size is also seen for MOF-808 Zr6 which has an average particle size of 286 nm and a lower catalytic rate similar to that of MOF-808 ZrHf4 batch 3. Comparable particle sizes are seen between MOF-808 Zr2Hf4 batch 1 and 2, and MOF-808 Zr3Hf3 batch 3 which also all gave high initial catalytic rates for the hydrolysis of DMNP. However, this trend is not entirely linear as the Zr3Hf3 sample with an average particle size of 540 nm is almost identical to batch 1 MOF-808 Zr2Hf4 with an average size of 548 nm; if particle size was the determining factor within this catalysis then MOF-808 Zr3Hf3 batch 3 would show a higher rate in line with the Zr2Hf4 batch 1 and 2 samples. Therefore the metal composition within the samples are contributing to high catalytic rates.

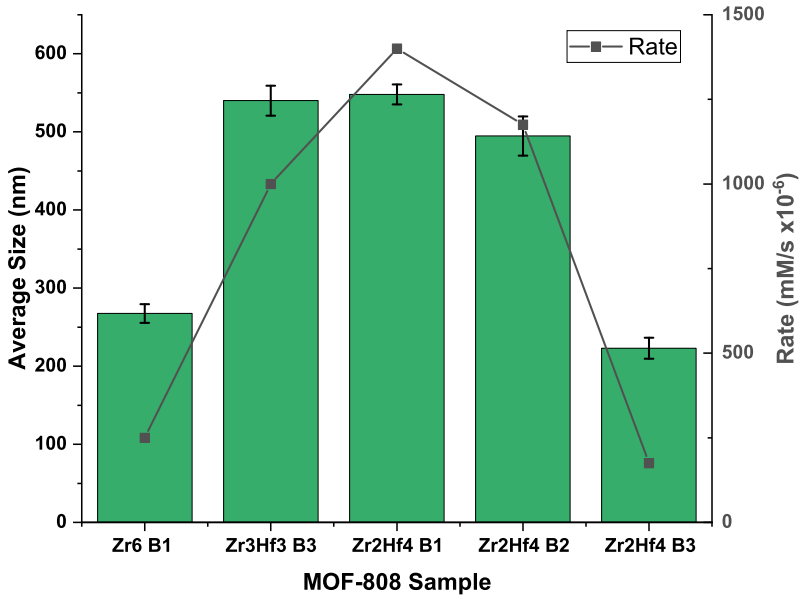

Figure 4.17: Average particle size of a selection of mixed-metal MOF-808 samples determined by DLS measurements (green bar, left axis) and catalytic rate (grey square, right axis).

Overall the catalytic results for mixed-metal MOF-808 are varied, with no clear trend emerging. However the MOF-808 Zr2Hf4 sample gave the highest recorded initial rates in two out of three batches synthesised. We can conclude from further characterisation data, that the batch 3 synthesis gave markedly

different structural properties than either batch 1 or 2; lower defects and small particle size. Although these factors contribute to the catalytic properties, it has been shown that the Lewis-acidity of the materials is the dominant factor and the particular metal composition of 33% Zr and 66% Hf seen in the Zr2Hf4 samples is favourable for the catalytic hydrolysis of DMNP.

4.5 Conclusions

This chapter has shown that mixed-metal Zr/Hf MOFs can be successfully synthesised in the case of UiO-66, NU-1000 and MOF-808 with no change or distortions to the underlying structure

In the case of UiO-66, the series of mixed-metal Hf/Zr MOFs were synthesised successfully using a solvothermal synthesis method previously reported for pure Zr UiO-66. The PXRD showed no deviation in the MOF structure across the series, and EDS measurements across multiple crystallites gave reliable percentages of Zr and Hf in the structure in good agreement with targeted mixed-metal ratios.

When the catalyic hydrolysis of DMNP over mixed-metal UiO-66 was carried out, using a high-throughput method, there was little difference between initial rates across the mixed-metal series. The UiO-66 Zr sample performed best within the catalysis, but there was no overall trend associated with the reducing Lewis-acidity. This suggests that the small pore size of UiO-66 prevents DMNP entering the structure, and therefore the Lewis-acidity of the SBU-active sites is not a dominant factor in this catalysis.

In the case of NU-1000, a simplified one-step synthesis was carried out to successfully form a series of mixed metal Zr/Hf MOFs. Using PXRD we confirmed that the structure was consistent across the series and in agreement with the literature structure. The EDS results showed good agreement between targeted and measured Zr and Hf proportions within the samples which were subsequently tested as catalysts.

The NU-1000 catalytic tests were carried out in-house and monitored using an *in-situ* UV-Vis probe. The NU-1000 Zr6 sample gave the highest initial rate measured in this study of 22.5 mM/s x 10^{-3}. However, as these materials were not tested using the high-throughput method used for UiO-66 and MOF-808, absolute comparisons would not be reliable as the catalytic loading is not equivalent. Across the mixed-metal series the initial catalytic rate of the hydrolysis of DMNP generally reduced as the proportion of Hf was increased in the MOF. This supports the hypothesis that Lewis-acidity does affect the catalysis in this case.

Finally, for MOF-808 three batches of a Zr/Hf mixed-metal series were synthesised successfully using a previously reported solvothermal synthesis method used for pure Zr MOF-808. Every sample, across each batch, had a structure consistent with MOF-808 Zr6 with no increase in d-spacing or missing characteristic peaks proving that the addition of Hf into the framework does not disrupt the long-range crystallinity. EDS was carried out on all samples which confirmed the mixed-metal nature of each with good agreement between targeted and measured Zr/Hf ratios.

When these materials were tested as catalysts for the hydrolysis of the nerve agent simulant DMNP, they presented very interesting results with no overall trend. Both batch 1 and 2 MOF-808 Zr2Hf4 exhibited the highest overall rates seen for these materials, indicating that this particular composition of 33% Zr and 66% Hf was having a highly beneficial rate on catalysis compared to the 100% Zr sample.

However, batch 3 MOF-808 Zr2Hf4 did not agree with this result so further analysis was carried out. It was found from EDS, TGA and DLS measurements and analysis that the batch 3 sample had a less accurate composition of Zr/Hf, contained fewer linker defects and a smaller particle size when compared to MOF-808 Zr2Hf4 batch 1 and 2 samples. For this reason, it can be said that the Lewis-acidity is effecting the catalytic activity of MOF-808, however, care must be taken to ensure other material characteristics of MOF-808 are controlled within the synthesis to give consistent materials for this catalysis.

Introducing Hf into MOF-808 to form mixed-metal Zr/Hf MOF-808 improves the catalytic rates of nerve agent hydrolysis when compared to MOF-808-Zr6. The initial rates recorded with Batch 1 and 2 MOF-808-Zr2 are some of the best for this catalysis. Yet, we see in Batch 3 MOF-808-Zr2 that this increased rate can be reduced if particle size and defectiveness is not controlled within mixed-metal MOF-808 samples. From this study we find that a combination of factors; particle size, defectiveness and metal composition, contribute to the catalysis rates reported for the hydrolysis of the nerve agent simulant DMNP.

4.6 References

[1] K. O. Kirlikovali, Z. Chen, T. Islamoglu, J. T. Hupp and O. K. Farha, *ACS Appl. Mater. Interfaces*, 2020, **12**, 14702–14720.

[2] J. Lyu, X. Zhang, P. Li, X. Wang, C. T. Buru, P. Bai, X. Guo and O. K. Farha, *Chem. Mater.*, 2019, **31**, 4166–4172.

[3] J. M. Palomba, S. M. Cohen, J. B. DeCoste, T. M. Tovar, C. V. Credille, M. Kalaj, G. W. Peterson, J. B. DeCoste, G. W. Peterson, T. M. Tovar and S. M. Cohen, *Chem. Commun.*, 2018, **54**, 5768–5771.

[4] T. Islamoglu, A. Atilgan, S.-Y. Moon, G. W. Peterson, J. B. DeCoste, M. Hall, J. T. Hupp and O. K. Farha, *Chem. Mater.*, 2017, **29**, 2672–2675.

[5] E. Geravand, F. Farzaneh, R. Gil-San-Millan, F. J. Carmona and J. A. R. Navarro, *Inorg. Chem.*, 2020, **59**, 16160–16167.

[6] M. Rimoldi, A. J. Howarth, M. R. DeStefano, L. Lin, S. Goswami, P. Li, J. T. Hupp and O. K. Farha, *ACS Catal.*, 2017, **7**, 997–1014.

[7] V. Bon, V. Senkovskyy, I. Senkovska and S. Kaskel, *Chem. Commun.*, 2012, **48**, 8407–8409.

[8] K. A. Lomachenko, J. Jacobsen, A. L. Bugaev, C. Atzori, F. Bonino, S. Bordiga, N. Stock and C. Lamberti, *J. Am. Chem. Soc.*, 2018, **140**, 17379–17383.

[9] J. E. Mondloch, W. Bury, D. Fairen-Jimenez, S. Kwon, E. J. Demarco, M. H. Weston, A. A. Sarjeant, S. T. Nguyen, P. C. Stair, R. Q. Snurr, O. K. Farha and J. T. Hupp, *J. Am. Chem. Soc.*, 2013, **135**, 10294–10297.

[10] J. E. Mondloch, M. J. Katz, W. C. Isley III, P. Ghosh, P. Liao, W. Bury, G. W. Wagner, M. G. Hall, J. B. DeCoste, G. W. Peterson, R. Q. Snurr, C. J. Cramer, J. T. Hupp and O. K. Farha, *Nat. Mater.*, 2015, **14**, 512–516.

[11] G. C. Shearer, S. Chavan, S. Bordiga, S. Svelle, U. Olsbye and K. P. Lillerud, *Chem. Mater.*, 2016, **28**, 3749–3761.

[12] E. Plessers, G. Fu, C. Tan, D. De Vos and M. Roeffaers, *Catalysts*, 2016, **6**, 104.

[13] V. R. Bakuru, S. R. Churipard, S. P. Maradur and S. B. Kalidindi, *Dalt. Trans.*, 2019, **48**, 843–847.

[14] H. Beyzavi, R. C. Klet, S. Tussupbayev, J. Borycz, N. A. Vermeulen, C. J. Cramer, J. F. Stoddart, J. T. Hupp and O. K. Farha, *J. Am. Chem. Soc.*, 2014, **136**, 15861–15864.

[15] G. W. Peterson, M. R. Destefano, S. J. Garibay, A. Ploskonka, M. McEntee, M. Hall, C. J. Karwacki, J. T. Hupp and O. K. Farha, *Chem. Eur. J.*, 2017, **23**, 15913–15916.

[16] K. Y. Cho, J. Y. Seo, H.-J. Kim, S. J. Pai, X. H. Do, H. G. Yoon, S. S. Hwang, S. S. Han and K.-Y. Baek, *Appl. Catal. B*, 2019, **245**, 635–647.

[17] P. Li, R. C. Klet, S. Y. Moon, T. C. Wang, P. Deria, A. W. Peters, B. M. Klahr, H. J. Park, S. S. Al-Juaid, J. T. Hupp and O. K. Farha, *Chem. Commun.*, 2015, **51**, 10925–10928.

[18] S.-Y. Moon, Y. Liu, J. T. Hupp and O. K. Farha, *Angew. Chemie., Int. Ed.*, 2015, **54**, 6795–6799.

[19] M. C. de Koning, M. van Grol and T. Breijaert, *Inorg. Chem.*, 2017, **56**, 11804–11809.

[20] S. Dai, C. Simms, I. Dovgaliuk, G. Patriarche, A. Tissot, T. N. Parac-Vogt and C. Serre, *Chem. Mater.*, 2021, **33**, 7057–7066.

4.7 Appendix

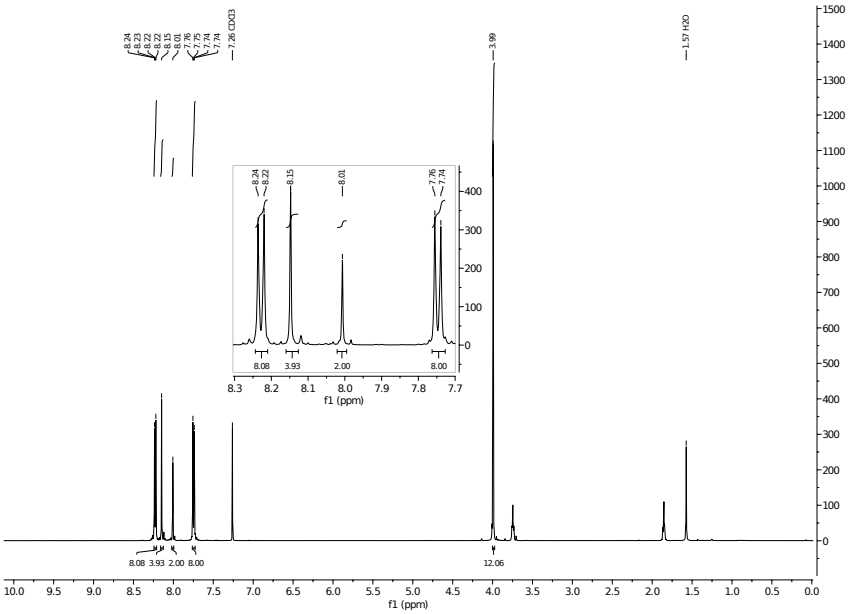

Figure 4.18: ^{1}H NMR of NU-1000 linker precursor (L1).

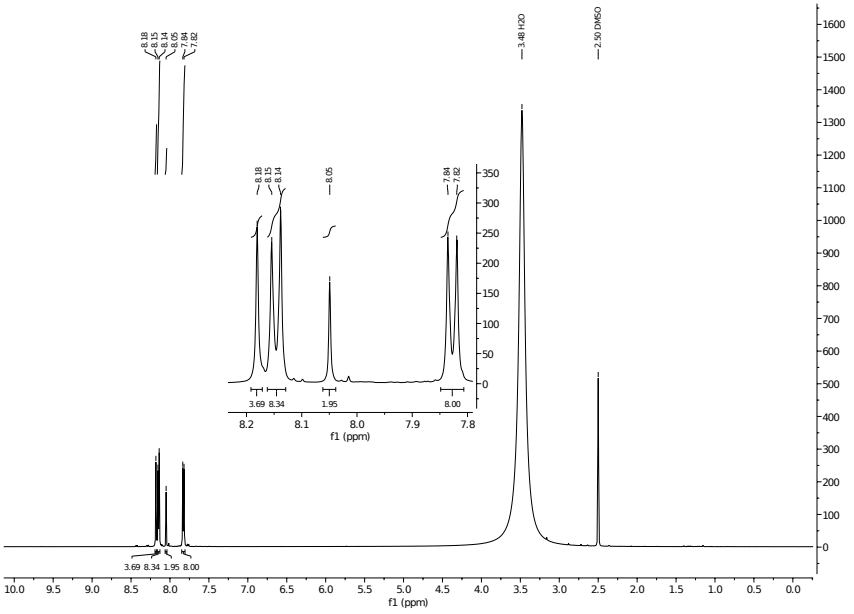

Figure 4.19: ^{1}H NMR of NU-1000 linker (L1).

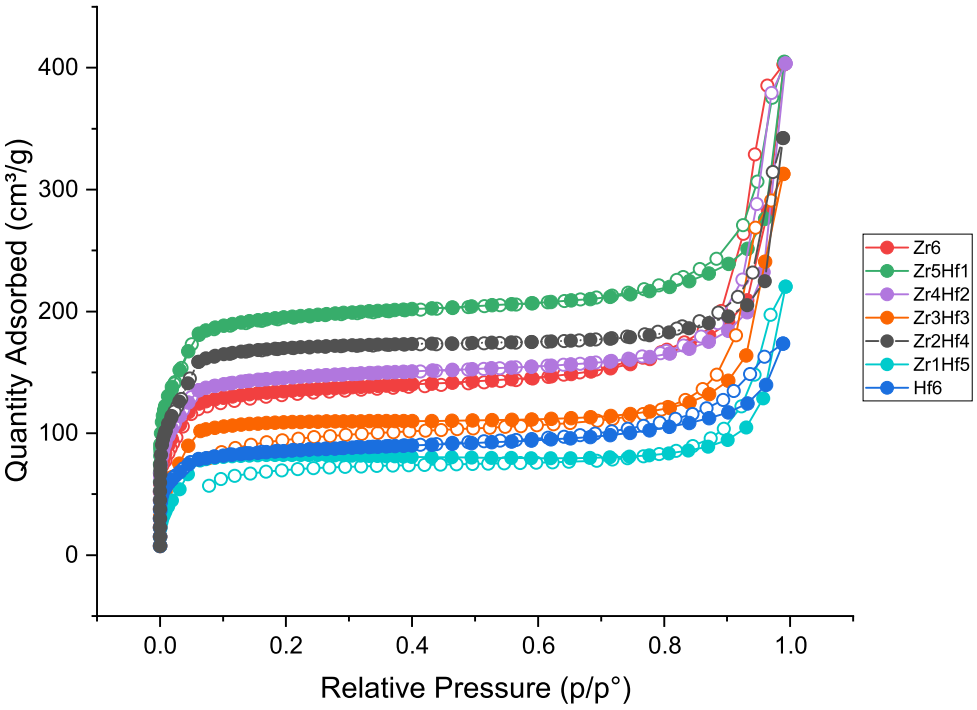

Figure 4.20: Nitrogen isotherms recorded at 77 K of mixed-metal MOF-808 Batch 1. Solid circles represent adsorption and outlined circles represent desorption.

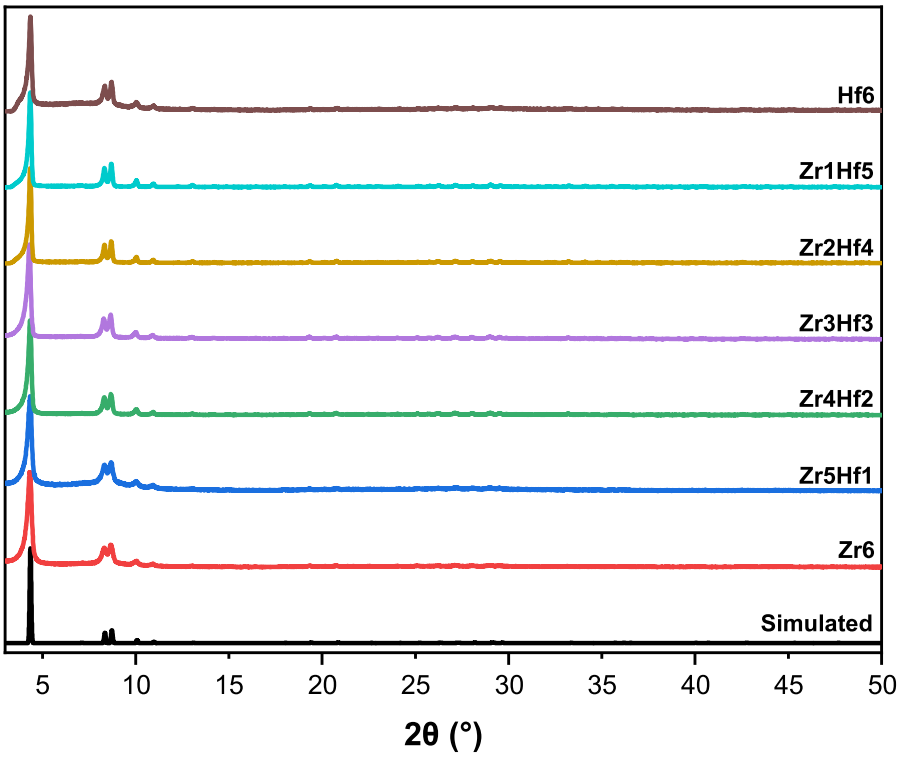

Figure 4.21: PXRD of mixed metal Zr/Hf-MOF-808 Batch 2 samples synthesised with the remaining percentage in the sample being Hf.

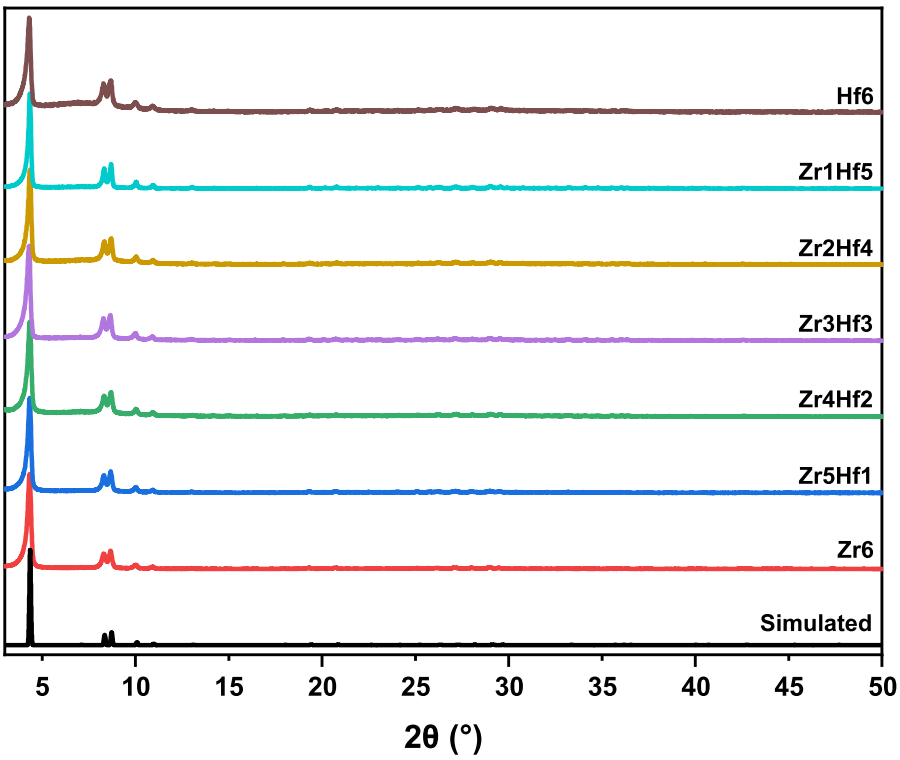

Figure 4.22: PXRD of mixed metal Zr/Hf-MOF-808 Batch 3 samples synthesised with the remaining percentage in the sample being Hf.

Chapter 5

Structure Modifications of MOF-808

5.1 Aims

The aim of the work in this Chapter is to modify the structure of MOF-808 by introducing different linkers into the synthesis. This will be done in order to identify characteristics that can improve the catalytic properties of MOF-808.

MOF-808 is known to be an effective catalyst for the hydrolysis of nerve agents and simulants. In Chapter 4 MOF-808 is altered by introducing other Group 4 metals to the framework and the resulting catalytic results were discussed. In this Chapter the MOF-808 structure will be modified by introducing additional linkers to the framework. These linkers are chosen with the intention of introducing additional functionality to the MOF-808 framework. Additionally, Chapter 4 results suggest that defects are an important factor to consider for this catalytic application. Therefore, as well as introducing functionality, these di-topic linkers are added into the structure in an attempt to engineer defects.

The materials synthesised will be characterised using powder X-ray diffraction, thermogravimetric analysis and quantitative-NMR spectroscopy, then tested as catalysts for the hydrolysis of a nerve agent simulant, DMNP.

5.2 Introduction

Zr-based MOFs for the catalytic hydrolysis of nerve agents and simulants have attracted much research in recent years. This can be attributed to the high chemical and thermal stability exhibited by strong Zr(IV)−O bonds, and the Lewis-acidity of the Zr(IV) sites within the MOF node that are required for the hydrolysis reaction.[1]

It has been previously reported that there is an inverse relationship between SBU connectivity and catalytic activity; the fewer linkers connected to the Zr(IV)-oxo cluster, the higher the rate of hydrolysis of nerve agents and simulants. This can be attributed to the greater proportion of open Zr(IV) sites and better accessibility to them in the node when fewer linkers are present. MOF-808 has shown some of the highest catalytic rates for this application in-part due to the low connectivity of 6 linkers for each SBU.[2]

In-order to increase this accessibilty further, defects can be incorperated into the MOF framework. This has been widely reported for UiO-66 MOFs due to the high 12-connectivity of the SBU in the pristine framework. Although linker defects may occur naturally, work has also been carried out to intentionally form these defects. One study introduced defects into UiO-66-NH_2 through the use of modulators and altering reaction temperatures. Roughly 0.6 to 1.3 missing linker sites per node could be introduced to the structure with high reproducibility. When tested as catalysts for the hydrolysis of nerve agents, a 20-fold increase in initial rate was observed for the high defect samples compared to the pristine structure.[3]

Limited research has been carried out on introducing defects to the larger pore, and lesser connected MOF-808. One study has been carried out by Mautschke *et al.*[4] introduced four di-topic linkers into the MOF-808 framework in an attempt to induce defects into the framework. The catalytic properties of the resulting materials were investigated and it was found that samples synthesised with additional linkers showed increased catalytic activity.

The introduction of additional linkers into MOFs to form mixed-linker materials has been investigated and implemented to form catalysts for the hydrolysis of nerve agents. Most work in this area has been carried out on UiO-66, where

functionalised derivatives of the BDC linker were added to the synthesis in a variety of combinations [Figure 5.1]. From high-throughput catalytic tests it was found that the combination of an amino ($-NH_2$) and bromo (-Br) functionalised linker resulted in the fastest rate.[5]

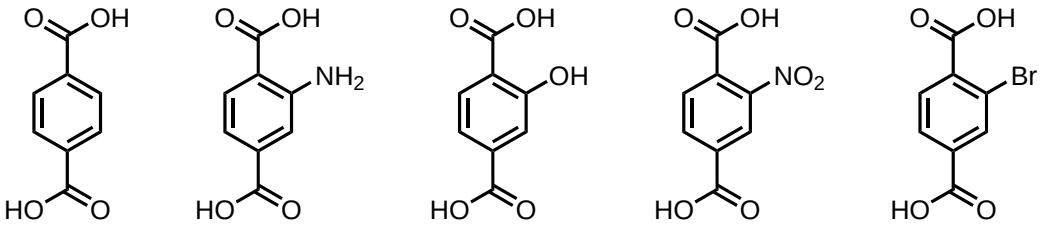

Figure 5.1: Structures of linkers used in mixed-linker UiO-66 syntheses.

In this chapter, mixed-linker MOF-808 will be synthesised with the intention of inducing defects into the structure, as well as investigating the effect of functionalisation of the linker on the resulting catalytic rates. Di-topic linkers will be used based upon 1,3-benzenedicarboxylic acid, containing one fewer carboxylic acid than the BTC linker, and additional functional groups. with the intention to form the MOF-808 structure with defined open metal sites [Figure 5.2]. The resulting products will be used as catalysts for the hydrolysis of nerve agents to probe the relationship between the MOF-808 structure and functionality, and the catalytic rate.

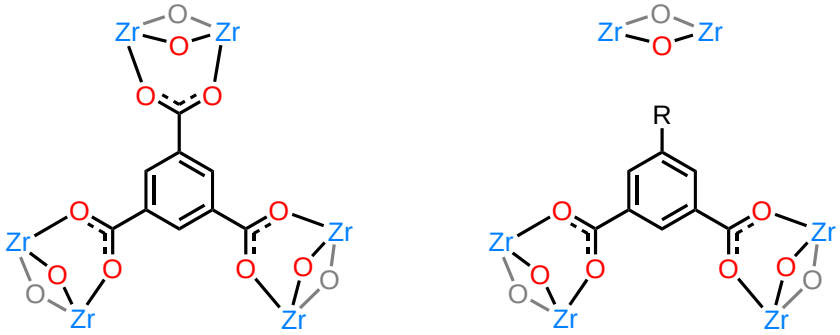

Figure 5.2: Binding mode of BTC (left) compared to the proposed binding of ditopic linkers used to prepare MOF-808-D samples (right).

5.3 Experimental

5.3.1 Pristine MOF-808

MOF-808-PR

Zirconium(IV) oxynitrate hydrate (0.24 g, 0.75 mmol) and 1,3,5-benzenetricarboxylic acid (105 mg, 0.50 mmol) were added to a solution of DMF (10 mL) and formic acid (10 mL). The mixture was added to a Teflon lined autoclave and sonicated for 10 min. The resulting solution was placed in an oven at 130 °C for 48 h. After cooling to room temperature the resulting precipitate was collected by centrifugation (fixed-angle rotor, 6000 rpm, 15 min), washed with DMF (1 x 10 mL) and methanol (2 x 10 mL) over 3 days. The product was activated under vacuum at 120 °C for 24 hr.

5.3.2 MOF-808-D 10% samples

MOF-808-D1-10

Zirconium (IV) oxynitrate hydrate (0.32 g, 1.00 mmol), 1,3,5-benzenetricarboxylic acid (95.0 mg, 0.45 mmol) and 5-amino isophthalic acid (9.10 mg, 0.05 mmol) were added to a solution of DMF (10 mL) and formic acid (10 mL). The mixture was added to a Teflon lined autoclave and sonicated for 10 min. The resulting solution was placed in an oven at 130 °C for 48 h. After cooling to room temperature the resulting precipitate was collected by centrifugation (fixed-angle rotor, 6000 rpm, 15 min), washed with DMF (1 x 10 mL) and methanol (2 x 10 mL) over 3 days. The product was activated under vacuum at 120 °C for 24 hr.

MOF-808-D2-10

Zirconium(IV) oxynitrate hydrate (0.32 g, 1.00 mmol), 1,3,5-benzenetricarboxylic acid (95.0 mg, 0.45 mmol) and 5-hydroxy isophthalic acid (9.10 mg, 0.05 mmol) were added to a solution of DMF (10 mL) and formic acid (10 mL). The mixture was added to a Teflon lined autoclave and sonicated for 10 min. The resulting solution was placed in an oven at 130 °C for 48 h. After cooling to room temperature the resulting precipitate was collected by centrifugation (fixed-angle rotor, 6000 rpm, 15 min), washed with DMF (1 x 10 mL) and methanol (2 x 10 mL) over 3 days. The product was activated under vacuum at 120 °C for 24 hr.

MOF-808-D3-10

Zirconium(IV) oxynitrate hydrate (0.32 g, 1.00 mmol), 1,3,5-benzenetricarboxylic acid (95.0 mg, 0.45 mmol) and isophthalic acid (8.30 mg, 0.05 mmol) were added to a solution of DMF (10 mL) and formic acid (10 mL). The mixture was added to a Teflon lined autoclave and sonicated for 10 min. The resulting solution was placed in an oven at 130 °C for 48 h. After cooling to room temperature the resulting precipitate was collected by centrifugation (fixed-angle rotor, 6000 rpm, 15 min), washed with DMF (1 x 10 mL) and methanol (2 x 10 mL) over 3 days. The product was activated under vacuum at 120 °C for 24 hr.

MOF-808-D4-10

Zirconium(IV) oxynitrate hydrate (0.32 g, 1.00 mmol), 1,3,5-benzenetricarboxylic acid (95.0 mg, 0.45 mmol) and pyridine-3,5-dicarboxylic acid (8.40 mg, 0.05 mmol) were added to a solution of DMF (10 mL) and formic acid (10 mL). The mixture was added to a Teflon lined autoclave and sonicated for 10 min. The resulting solution was placed in an oven at 130 °C for 48 h. After cooling to room temperature the resulting precipitate was collected by centrifugation (fixed-angle rotor, 6000 rpm, 15 min), washed with DMF (1 x 10 mL) and methanol (2 x 10 mL) over 3 days. The product was activated under vacuum at 120 °C for 24 hr.

5.3.3 MOF-808-D1 series

Zirconium(IV) oxynitrate hydrate (0.32 g, 1.00 mmol) was added to a solution of DMF (10 mL) and formic acid (10 mL) along with 1,3,5-benzenetricarboxylic acid (BTC) and 5-amino isophthalic acid (L1) [see Table 5.1] . The mixture was added to a Teflon lined autoclave and sonicated for 10 min. The resulting solution was placed in an oven at 130 °C for 48 h. After cooling to room temperature the resulting precipitate was collected by centrifugation (fixed-angle rotor, 6000 rpm, 15 min), washed with DMF (1 x 10 mL) and methanol (2 x 10 mL) over 3 days. The product was activated under vacuum at 120 °C for 24 hr.

Table 5.1: Quantities of 1,3,5-benzenetricarboxylic acid (BTC) and 5-amino isophthalic acid (L1) used in each synthesis for MOF-808-D1 series.

Sample	Terephthalic acid	5-amino isophthalic acid
MOF-808-D1-10	95.0 mg, 0.45 mmol	9.10 mg, 0.05 mmol
MOF-808-D1-20	84.0 mg, 0.40 mmol	18.2 mg, 0.10 mmol
MOF-808-D1-30	73.0 mg, 0.35 mmol	27.3 mg, 0.15 mmol
MOF-808-D1-40	63.3 mg, 0.30 mmol	36.4 mg, 0.20 mmol
MOF-808-D1-50	52.5 mg, 0.25 mmol	45.5 mg, 0.25 mmol
MOF-808-D1-60	42.1 mg, 0.20 mmol	54.3 mg, 0.30 mmol

5.3.4 Post-synthetic exchange MOF-808-D1

The following sample synthesis was carried out by G. Kudzin as part of a Chemistry BSc (Hons) project.

MOF-808-PR (0.30 g, 0.21 mmol) was added to methanol (20 mL) and 5-amino isophthalic acid (L1) was added [see Table 5.2] . The mixture was refluxed for 24 hr at 60 °C. After cooling to room temperature the resulting precipitate was collected by centrifugation (fixed-angle rotor, 6000 rpm, 15 min), washed with DMF (1 x 10 mL) and methanol (2 x 10 mL) over 3 days. The product was activated under vacuum at 120 °C for 24 hr.

Table 5.2: Quantities of 5-amino isophthalic acid (L1) used in each synthesis for MOF-808-PSE series.

Sample	5-amino isophthalic acid
MOF-808-PSE5	0.19 g, 1.05 mmol
MOF-808-PSE10	0.38 g, 2.10 mmol
MOF-808-PSE15	0.57 g, 3.15 mmol

5.3.5 Catalysis

Before catalysis measurements all materials were activated under vacuum at 120 °C for 24 hr and stored in flame-sealed vials until measurements were carried out.

Catalytic hydrolysis of dimethyl *p*-nitrophenylphosphate

This procedure is based upon the reported method by Mondloch *et al.*[6]. A buffer solution of *N*-ethylmorpholine (100 mL, 0.45 M, pH 10) was prepared.

A MOF-808 sample (3.0 mg) was added to an aqueous solution of dimethyl *p*-nitrophenylphosphate (5.00 mL, 0.25 mM stock solution of DMNP in *N*-ethylmorpholine buffer (0.45 M, pH 10)). The rate of DMNP hydrolysis was measured using an *in-situ* UV-Vis probe monitoring the product *p*-nitrophenoxide absorbance at 407 nm.

5.4 Characterisation Methods

5.4.1 Quantitative ^{1}H-NMR spectroscopy

Quantitative NMR spectroscopy is a useful technique that can be used to identify and quantify the amount of a substance within a sample. We use this method in order to calculate the ratio of linkers present in each sample of MOF-808. These calculations are based on previous work that uses acid digestion methods to investigate the components present in MOFs.[7]

The synthesised MOF-808 samples (5 mg) were dissolved in concentrated H_2SO_4 (30 µL) by sonicating for 10 min. To this DMSO$-d_6$ (1 mL) was added. ^{1}H-NMR spectroscopy was carried out on each sample. In the collected spectrum, the integrals for the BTC and defective linker peak were compared to give a ratio. This allowed a percentage value to be calculated for the defective linker present in the sample. This combination of acid and NMR solvent was chosen as no signals overlapped with the characteristic peaks for each defective linker, allowing easy integration [Figure 5.3].

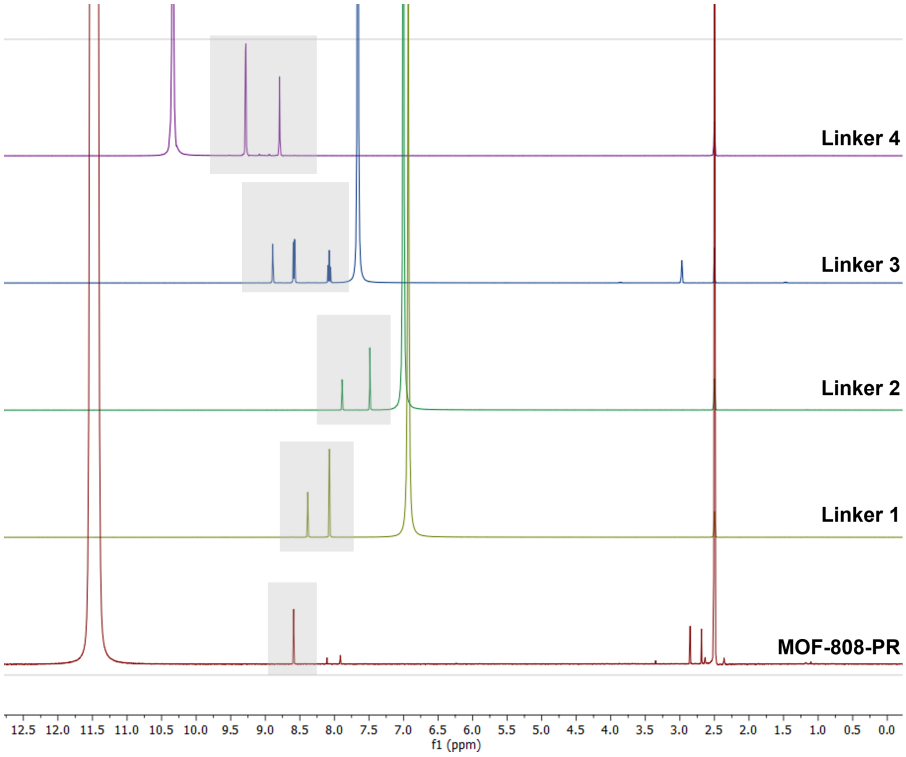

Figure 5.3: Stacked ^{1}H$-$NMR spectra of acid digested linkers and MOF-808-PR illustrating that characteristic peaks (grey boxes) can be easily distinguished and do not overlap.

5.4.2 Thermogravimetric Analysis

In this Chapter TGA will be used to determine the stability and the number of missing linkers in the synthesised MOFs, using a methodology previously reported.[8] This characterisation technique was used and described in detail previously in Chapter 4 but a brief explanation will be given below.

All TGAs were measured under air from 25 °C to 700 °C, heating at a rate of 5 °C min^{-1}. The final residue from decomposition of MOF-808 is 6 moles of ZrO_2, with a molar mass of 739.34 g mol^{-1}. From this we can estimate the theoretical linker loss by normalising the TGA curve so the end weight is 100%. The molar mass of the MOF-808 structure after the loss of formate and hydroxyl ions, $Zr_6O_4(OH)_4[(C_6H_3)(COO)_3]_2$, is 1093.6 g mol^{-1}. This is a factor of 1.47 higher than the final ZrO_2 residue which gives a theoretical TGA plateau for the dehydrated structure of 147%.

The final mass loss step in the MOF-808 TGA corresponds to the loss of the BTC linkers which, and in a pristine sample, corresponds to 47% of the structure. Using this information we can determine the percentage of linkers (PL) that are in the MOF-808 structure with the following equation:

$$\mathrm{PL} = \frac{(\mathrm{Plat_{exp}} - 100)}{47} \cdot 100 \tag{5.1}$$

Where $Plat_{exp}$ is the plateau value in collected TGA which corresponds to the material in the form $Zr_6O_4(OH)_4[(C_6H_3)(COO)_3]_2$ and is typically taken in the temperature region ca. 425 °C.

If this is 100%, or very close, we can assume that all linkers are present in this structure and no linker defects are present. Any value lower than this suggests that linker defects are present, and we can quantify how many. This method will be used to identify any materials with linker defects in this chapter.

5.5 Results & Discussion

5.5.1 Pristine MOF-808

Many solvothermal synthesis procedures have been reported for MOF-808 with the procedure chosen from Furukawa *et al.*[9]. This procedure was used in-order to synthesise a defect-free, or pristine sample, to compare with the mixed linker samples and will further be referred to as MOF-808-PR (PR standing for pristine).

MOF-808-PR was made as outlined in Section 5.3. Once synthesised the material was washed with DMF to remove any un-reacted starting material. Subsequently it was washed twice with methanol in order to remove any DMF coordinated to the framework. It has also been reported that washing with methanol can remove the bridging formate molecules that coordinate onto the Zr metal centre upon formation.[10] By removing these formate molecules, open sites are created on the metal centre which is advantageous for catalysis. Finally the washed product is dried under reduced pressure at 120 °C to remove unwanted material within the pores.

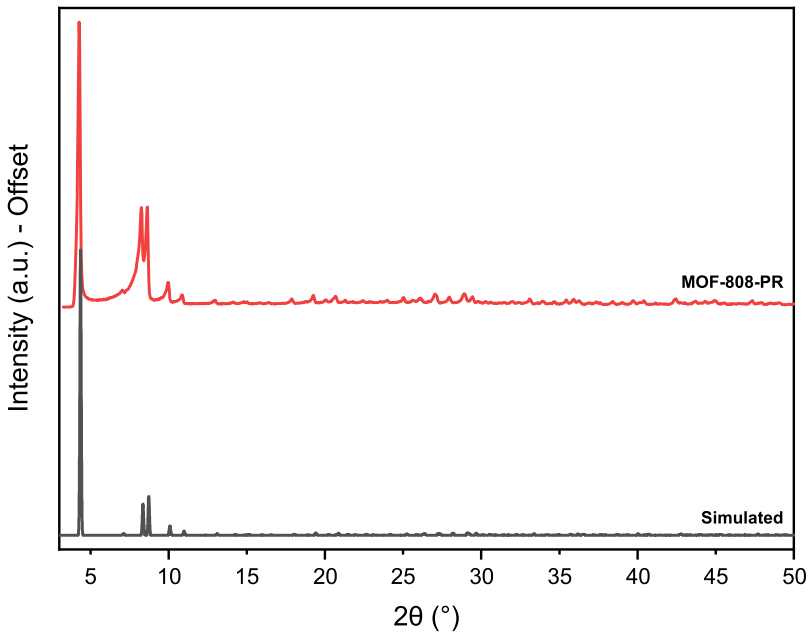

Figure 5.4: Comparison of experimental (red) and simulated (black) powder X-ray diffraction pattern of MOF-808.

MOF-808-PR was first characterised by PXRD to ensure bulk crystallinity throughout the structure. The PXRD collected was in agreement with the simulated pattern [Figure 5.4] which was found in literature.[9] This confirms that

the synthesis of MOF-808-PR was successful.

Once the structure of MOF-808-PR was confirmed, further material characterisation was carried out. TGA analysis allows the thermal stability of the MOF-808-PR structure to be investigated. The TGA analysis was carried out under air flow and is shown in Figure 5.5. The data collected is in agreement with previously published TGA data for MOF-808.[11]

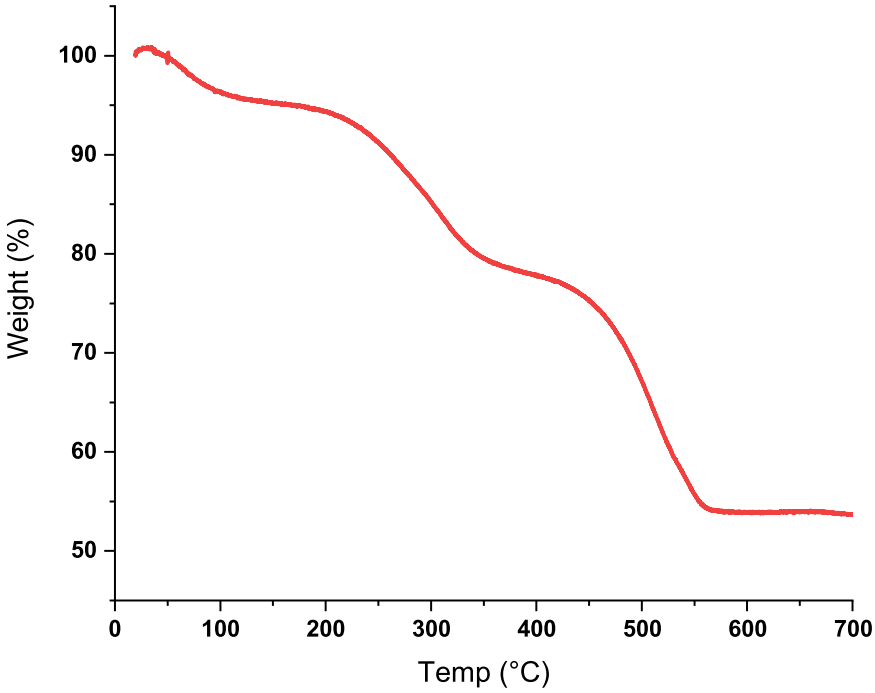

Figure 5.5: TGA trace of MOF-808-PR upon heating at a rate of 5 °C min^{-1} in air.

As can be seen in Figure 5.5 there is a loss of mass up to around 100 °C which can be attributed to the removal of water adsorbed on the external surface area of the MOF and any other solvents within the pores. The plateau present from around 100 - 200 °C gives the activated structure of MOF-808 with the formula $Zr_6O_4(OH)_4[(C_6H_3)(COO)_3]_2(HCOO)_6$. Formate linkers, from the formic acid used as a modulator, remain coordinated to the Zr-nodes, however, some studies suggest that the formate is replaced with water and hydroxyl ions to give the structural formula $Zr_6O_4(OH)_4[(C_6H_3)(COO)_3]_2(H_2O)_6(OH)_6$ therefore both structures are likely present here.[12]

The next mass loss from 200 - 350 °C is due to the loss of any remaining coordinated formate, water and hydroxyl ions. It has also been suggested that any

remaining DMF that was not exchanged in the washing steps is also removed at these temperatures.[11] After the removal of these species there is a clear plateau at around 400 °C which gives the dehydroxylated form of MOF-808-PR with the formula $Zr_6O_4(OH)_4[(C_6H_3)(COO)_3]_2$. The final mass loss starting at around 425 °C corresponds to the decomposition of the BTC linker and therefore the collapse of the MOF-808 structure to give a final residue of $(ZrO_2)_6$.

As the final mass can be assumed to be $(ZrO_2)_6$, the mass loss due to the BTC linker can be quantified and can give information on the number of linkers present in the structure. The methodology used to calculate the percentage of missing linkers in detailed in Section 5.4. With this method it was found that the percentage of linkers corresponded to 100% of the expected quantity given by the crystal structure [Figure 5.17]. This confirms that this material does not have quantifiable linker defects and can be used as a comparison to future samples.

5.5.2 Defect engineered MOF-808

Following the successful synthesis of MOF-808-PR, attempts to prepare mixed-linker MOF-808 samples were carried out with the aim to induce defects into the MOF-808 structure. These samples will be referred to as MOF-808-D (D denoting defects).

The linkers chosen were based on previous work where a mixed linker MOF gave improved catalytic results in comparison to the parent MOF.[4] The linkers chosen for the MOF-808-D samples are 5-amino isophthalic acid (1), 5-hydroxy isophthalic acid (2), isophthalic acid (3), and pyridine-3,5-dicarboxylic acid (4) [Figure 5.6]. These linkers posses a range of functional groups that may alter the catalytic properties of MOF-808. Additionally, all linkers chosen are di-carboxylic acids which, unlike BTC a tri-carboxylic acid, will only connect with two Zr-oxo clusters and leave an open metal site as illustrated in Figure 5.2. This open metal site, or linker defect site, may be advantageous to catalysis as seen in Chapter 4.

The mixed linker MOF-808 samples were prepared as outlined in Section 5.3. From this point these samples will be referred to as MOF-808-DX-Y, with the X denoting which additional linker was added to the synthesis as outlined in Figure 5.6, and Y denoting the mol% of linker that was added to the synthesis. The MOF-808-D samples were prepared using the identical solvothermal synthesis

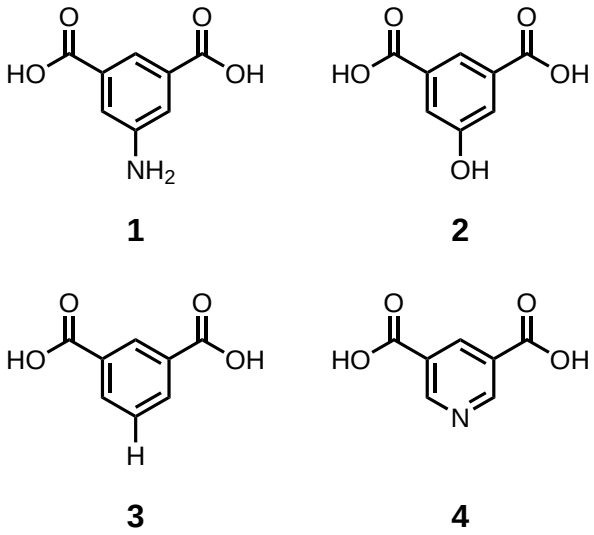

Figure 5.6: Linkers used in the preparation of DE-MOF-808.

method used for MOF-808-PR, except a mol% of the original benzene-1,3,5-tricarboxylate (BTC) linker is replaced with a di-topic linker.

Initially 10 mol% of defect-inducing linker was added to the MOF-808-D syntheses, replacing 10 mol% of BTC. The resulting products (MOF-808-D-10) were washed using the same procedure as for MOF-808-PR; 1 x DMF to remove un-reacted starting materials and 2 x methanol to remove unwanted DMF from the structure. Finally the materials were heated to 120 °C under reduced pressure to give the activated structure.

The resulting materials were first characterised with PXRD. As shown in Figure 5.7 all patterns collected match the MOF-808-PR recorded structure. As the MOF-808-PR structure is in agreement with the simulated MOF-808 pattern, the MOF-808-D samples have been successfully prepared. Between each MOF-808-D-10 sample there are no visible shifts in the 2θ values of the PXRD pattern. As expected, this indicates that all materials have the same unit cell with the additional linkers not changing the long-range MOF-808 crystal structure.

In order to confirm the reproducibility of these syntheses, two additional batches of 10 mol% MOF-808-D samples were prepared with the linkers shown in Figure 5.6. The PXRD patterns collected for these are given in Figure 5.18 and Figure 5.19. All PXRD patterns are in agreement with the simulated pattern for MOF-808, and show no shifts in 2θ values between batches or between MOF-808-D-10 samples.

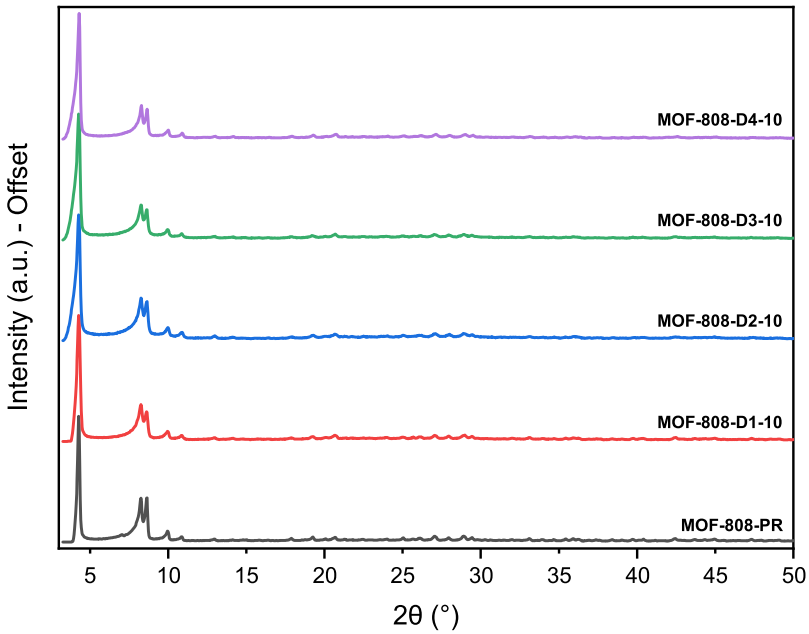

Figure 5.7: Powder X-ray diffraction of all 10% defect linker samples compared against MOF-808-PR.

As the bulk crystallinity of all the MOF-808-D-10 samples were confirmed, further analysis was carried out to determine if the defect inducing linkers had been incorporated into the structure, and to what extent. No change can be observed between samples in the PXRD patterns therefore other methods were implemented.

A method that has been used previously to determine the ratio of linkers within a MOF structure is quantitative-NMR (q-NMR) spectroscopy.[13] This method was implemented for all MOF-808-D-10 samples by dissolving a small amount of each sample in H_2SO_4 as outlined in Section 5.3. This method results in the MOF structure breaking down to leave the organic linkers in-tact, allowing detection by ^1H-NMR spectroscopy.

As this is a quantitative technique we can integrate the linkers peaks in each structure to determine the ratio of BTC to defective linker in the digested sample. From these values the percentage of defective linker incorporated into the MOF-808-D structure can be calculated. This method was used for all MOF-808-D-10 samples as the NMR peaks of BTC and all defect inducing linker are clearly distinguishable from each other [Figure 5.3].

The calculated percentage of defect inducing linker for all MOF-808-D-10 samples is given in Table 5.3, including Batches 2 and 3.

Table 5.3: Calculated defective-inducing linker percentages from digestion $^{1}H-NMR$ integrals. (*) denotes samples where no D-linker peak can be observed in $^{1}H-NMR$ spectroscopy.

Sample	Batch	D-linker (%)
MOF-808-D1-10	1	9.1
	2	8.0
	3	13.9
MOF-808-D2-10	1	5.9
	2	*
	3	8.3
MOF-808-D3-10	1	5.1
	2	10.8
	3	11.5
MOF-808-D4-10	1	19.4
	2	13.2
	3	11.3

From the table above the calculated percentages of additional linker incorporated varies between each sample. It is believed that the linker percentages given are from coordinated linkers within the structure, as the washing steps following the synthesis ensures all un-reacted starting materials, including the linkers, are removed from the pores.

In the case of MOF-808-D1-10, the $^{1}H-NMR$ spectrum confirms the presence of both the BTC linker coordinated alongside 5-amino isophthalic acid in the MOF structure [Figure 5.20 - Figure 5.22]. Integral ratios for all three batches show the defective linker has been successfully incorporated with an average of 10.3 $\pm$ 1.8% across the three batches. As 10 mol% of the D1 linker was added to this synthesis, the average value of 10% within the product is a very promising result as it suggest that the reagents have reacted in the targeted ratios. This, alongside the PXRD, shows the synthesis has been successful and is also reproducible.

For the MOF-808-D2-10 samples, less than the targeted 10% defective linker has been incorporated into the structure in all cases. Both B1 and B3 show the presence of 5-hydroxy isophthalic acid in the $^{1}H-NMR$ spectrum to give an average of 7.1 $\pm$ 0.9% incorporation into the product. In the case of Batch 2

only the BTC linker is identified in the product, with no 5-hydroxy isophthalic acid present in the $^{1}H-NMR$ [Figure 5.24]. As less than 10 % of the defective linker has been incorporated into the MOF-808 structure through this synthesis method, 5-hydroxy isophthalic acid is less easily incorporated into the MOF-808 structure as was the case for 5-amino isophthalic acid. The reproducibility for this synthesis is also less robust than for MOF-808-D1-10.

In the $^{1}H-NMR$ spectra for the batches of MOF-808-D3-10 the defective linker incorporated, isophthalic acid, is detected along with the BTC linker [Figure 5.26 - Figure 5.28]. The average percentage of isophthalic acid incorporation across the batches is $9.1 \pm 2.0\%$. This is statistically comparable to the target of 10% so can be considered a successful result. It should also be noted that there is greater agreement between B2 and B3, with only B1 showing a lesser extent of linker incorporation. This suggests that the synthesis is generally reproducible. As this linker is the least sterically hindered of all the defect inducing linkers used, the lower extent of incorporation into the structure is surprising. We expected that lower steric hindrance may be beneficial when trying to include additional linkers into a MOF structure.

For the synthesised MOF-808-D4-10 samples, the $^{1}H-NMR$ spectra for all batches show peaks for both the BTC and pyridine-3,5-dicarboxylic acid [Figure 5.29 - Figure 5.31]. The percentages calculated from the integrals give values of more than 10% incorporation in all cases; the average percentage of defective linker is $14.7 \pm 2.4\%$ across the three batches. This suggests that the defective inducing linker, pyridine-3,5-dicarboxylic acid, may be more preferentially coordinated within the MOF-808 structure than the BTC linker to give a higher proportion of pyridine-3,5-dicarboxylic than expected. It is unlikely that the elevated value is due to additional linkers within the pores of the MOF-808-D4-10 as each sample is washed thoroughly within the synthesis procedure.

Overall, we have successfully incorporated the chosen defect inducing linkers into the MOF-808 structure with an in-situ synthesis method. Using quantitative $^{1}H-NMR$ spectroscopy calculations the incorporation shows good agreement between batches and within the target region of 10% defective linker.

As the defect inducing linkers have been confirmed within the structure, TGA was carried out to test the stability of the material and to determine if we

have been successful in promoting missing linker defects within the MOF-808 structure. The TGAs recorded for all MOF-808-D-10 materials are shown in Figure 5.8.

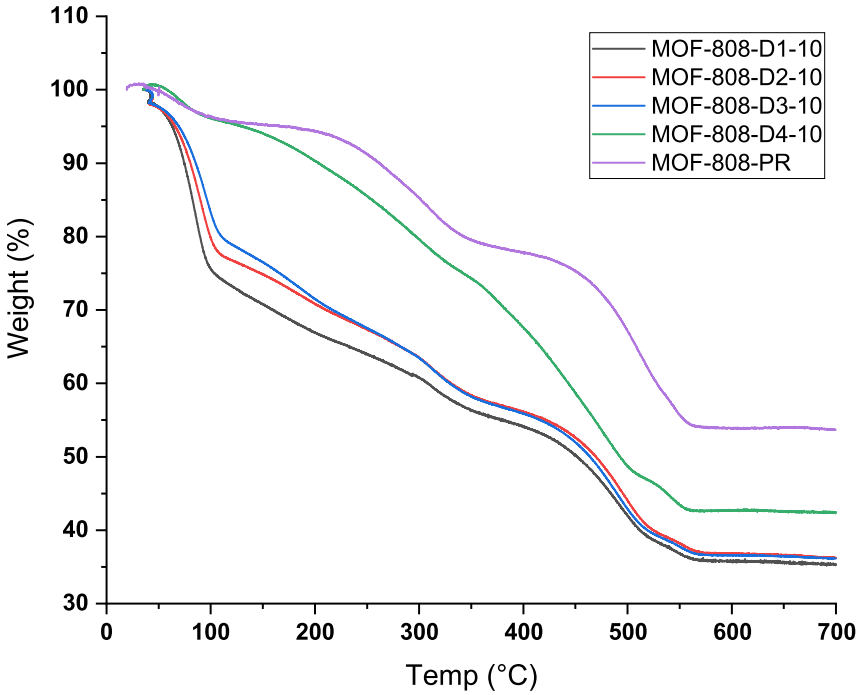

Figure 5.8: TGA traces for all MOF-808-D-10 samples collected with heating at a rate of 5°C min^{-1} in air.

It is clear that the TGA traces for all MOF-808-D-10 samples deviate from the thermal decomposition exhibited by the MOF-808-PR sample [Figure 5.8, purple trace]. The initial mass loss up to 100°C is much larger in the defective samples, however, this is likely due to water adsorption within the MOF-808-D-10 structure occurring in the time between activation and the TGA data being collected.

The data beyond 100°C is more interesting and gives greater insight into the thermal stability of the samples. It is clear from Figure 5.8 that the stable first plateau observed at 150°C for MOF-808-PR is not present in any of the MOF-808-D-10 samples. This constant mass loss is likely due to the removal of water, hydroxyls and formate ions that were present in the synthesis and also gives an indication that the activated structure seen in MOF-808-PR, $Zr_6O_4(OH)_4[(C_6H_3)(COO)_3]_2(HCOO)_6$, has a narrower stability range in the defective additional linker samples.

In the case of MOF808-D1-10, MOF808-D2-10 and MOF808-D3-10 there is a

plateau at 350 - 450°C. This, as in the case of MOF-808-PR, corresponds to the structure without formate or hydroxyl ions coordinated and only linkers remaining. As both BTC and the di-topic linkers are present in the MOF-808-D-10 samples, the exact structural formula is unknown for this plateau. This results indicates that the stability for the activated MOF is mostly unchanged with the addition of di-topic linkers which is a promising result for use in catalysis applications.

For MOF808-D4-10 there is only a very narrow plateau, with the activated sample thermally decomposing at a lower temperature (*ca.* 350°C) than all other samples. This sample also has the highest calculated incorporation of di-topic linker within the structure. Due to the increase in di-topic linker, and therefore reduction in tri-topic linkages, a reduction in stability may occur for the crystalline structure.

There is little difference between the decomposition of the MOF808-D1-10, MOF808-D2-10 and MOF808-D3-10 samples above 400°C . This suggests that, although the addition of a di-topic linker does effect the stability compared to the pristine sample, we do not see a difference in stability between these defective samples.

Using the TGA traces collected, any missing linker defects present in the materials can be quantified. This is carried out as discussed in Section 5.4 where the TGA curve is normalised with respect to ZrO_2 and the percentage of linker present in the sample can be calculated. Although additional linkers will be present in each structure changing the molecular weight of the product, the calculations use the parent MOF-808 structure as the di-topic linkers are only present in small quantities. The percentage of linkers present in each sample as calculated by TGA is given in Table 5.4.

Interestingly, from the TGA calculations we find that the materials are, in all but one case, free from linker defects. This is not the expected result as it was believed that some di-topic linkers would not be incorporated into the MOF-808 structure and leave free metal sites.

In most cases more than 100% linker incorporation has been calculated from the TGAs. This suggests that the di-topic linkers have been fully integrated into the

Table 5.4: Percentage of linker present in MOF-808-D samples relative to a pristine MOF-808 structure calculated from normalised TGA.. (∗) this value could not be calculated due to the lack of stability within the structure of the sample.

Sample	Batch	Linker (%)
MOF-808-D1-10	1	103.2
	2	104.0
	3	104.9
MOF-808-D2-10	1	109.6
	2	106.6
	3	86.8
MOF-808-D3-10	1	108.5
	2	108.3
	3	104.3
MOF-808-D4-10	1	*
	2	111.3
	3	100.6

MOF-808 structure. Although full linker defects have not been identified in these samples, as illustrated in Figure 5.2, for each di-topic linker within the structure there will be one more open metal site compared to the tri-topic BTC coordinated metal nodes.

The samples of MOF-808-D-10 with a calculated linker percentage of over 100% suggest that metal defects exist within the structure. These defects may have occurred due to the lesser connectivity of the di-carboxylic acid linkers. During the synthesis, these linkers may orientate in a way so there is an absence of carboxylic acids coordinating groups in order to form the Zr-node.

We cannot quantify the number of missing metal defects using this method as the calculations assume the correct number of Zr atoms within the structure. As all calculated values are close to 100% it is believed that the number of metal defects are small, and unlikely to have a major affect on the synthesised materials.

All MOF-808-D-10 materials have been successfully synthesised and characterised using a range of techniques. Although these materials are not significantly defective, as determined by TGA, they will be tested as catalysts for the hydrolysis of the nerve agent simulant DMNP. The initial rate of hydrolysis will be determined for each sample to determine the effect of additional linker has on the catalytic performance of MOF-808.

5.5.3 Defect engineered MOF-808 with 5-amino isophthalic acid

The above section discussed the successful synthesis and characterisation of mixed linker MOF-808 using 10% of an additional di-topic linker. This section will investigate if larger percentages of di-topic linker can be incorporated into MOF-808. We have selected 5-amino isophthalic acid (Linker 1) for these studies as it showed promise when incorporating 10%. Literature has also reported that the amino group has beneficial properties when included in Zr-MOFs for the catalytic hydrolysis of nerve agents and simulants.[14]

5.5.3.1 In-situ synthesis

Mixed linker MOF-808 samples with 5-amino isophthalic acid were prepared as outlined in Section 5.3. These samples will be referred to as MOF-808-D1-Y with Y denoting the mol% of linker that was added to the synthesis, the D1 stands for the di-topic linker being used: Linker 1 from Figure 5.6. The MOF-808-D1 samples were prepared using a solvothermal synthesis method as in the case for MOF-808-PR, with a mol% of the original benzene-1,3,5-tricarboxylate (BTC) linker replaced with 5-amino isophthalic acid in intervals of 10 from 10% to 70%.

The resulting MOF-808-D1 materials were first characterised by PXRD to determine bulk crystallinity. The PXRD patterns collected are shown in Figure 5.9. For samples MOF808-D1-10 to MOF808-D1-60, the PXRD matches the MOF-808-PR sample, and therefore the simulated MOF-808 pattern. This confirms the addition of increasing mol% of 5-amino isophthalic acid does not disrupt the long-range MOF-808 crystal structure.

For the sample MOF-808-D1-70 there are many sharp peaks visible correlating with the correct 2θ for the MOF-808 structure, however, there is a large broad peak visible at low 2θ. This is present after the washing steps, therefore this sample does not have long range crystallinity that is observed for the other samples. For this reason only samples up to MOF-808-D1-60 will be characterised further. Samples with 5-amino isophthalic mol% above 70% did not successfully form MOF-808. This indicates that the upper limit of additional linker that can be added to form MOF-808 is 60%.

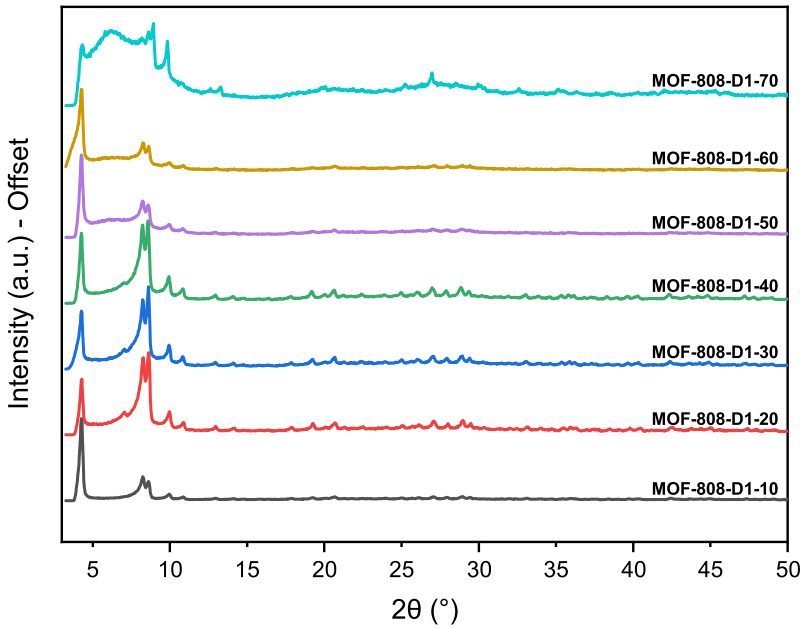

Figure 5.9: PXRD of MOF-808-D1-series.

Once the structure of each sample was identified by PXRD, the amount of 5-amino isophthalic linker within the synthesised samples was quantified. As outlined above in Section 5.4 digestion q-NMR spectroscopy was utilised. Each sample was dissolved in a small amount of concentrated sulphuric acid, breaking down the MOF structure whilst leaving the linkers in-tact and possible to detect through ^{1}H-NMR spectroscopy. The calculated loadings for all samples are given in Table 5.5.

Table 5.5: Calculated defective linker percentages of MOF-808-D1 samples from digestion ^{1}H−NMR integrals.

Sample	D-linker (%)
MOF-808-D1-10	9.1
MOF-808-D1-20	13.4
MOF-808-D1-30	19.6
MOF-808-D1-40	20.7
MOF-808-D1-50	24.9
MOF-808-D1-60	25.4

From the q-NMR spectroscopy data the incorperation of the 5-amino isophthalic acid linker has been successful in all samples. However, the amount detected

in the final product does not accurately correlate with the mol% added to the synthesis, with all samples containing less defect linker than added to the synthesis. This is seen throughout the series; the 20 mol% L1 synthesis only contains 13.5% defective linker in the sample, and the highest defective linker synthesis containing 60 mol% L1 only contains 25.4% in the sample. This indicates that a maximum amount of *ca.* 25% additional linker is possible to incorporate into the MOF-808 structure.

With the percentage of di-topic linker within the MOF successfully quantified, TGA was carried out for each sample in order to compare thermal stability [Figure 5.10].

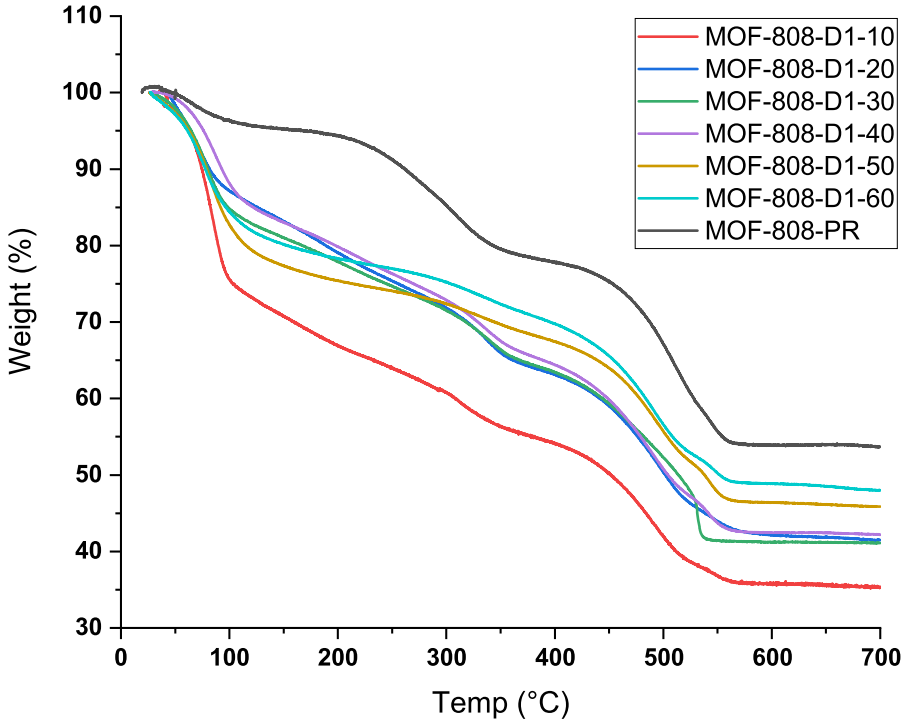

Figure 5.10: TGA traces for all MOF-808-D-10 samples collected with heating at a rate of 5°C min^{-1} in air.

The TGA traces for all MOF-808-D1 samples show the characteristic mass losses seen for MOF-808-PR. Up to 100°C the loss of water and other solvents can clearly be seen, giving the dehydrated structure. Interestingly, a clear plateau is only seen for MOF-808-D1-50 and MOF-808-D1-60 at this temperature. As both of these samples have a calculated defective linker incorporation of 25% the similarity of the TGA is expected. For all other samples no plateau is observed for the dehydrated structure, instead a steady decrease in mass is seen, this is likely due to constant loss of solvent over these temperatures and lack of stability

in the dehydrated structure.

For all samples there is a visible plateau at 350°C, this suggests all materials have lost the coordinated hydroxy and formate ions and in this range exhibit similar stability. The range of stability seems to decrease as the percentage of defect linker increases, with MOF-808-D1-60 exhibiting a very short plateau, before beginning to thermally collapse before the other samples. The parent MOF-808-PR structure shows the highest range of stability up to 425°C, whereas all other samples have begun to decompose at this temperature. This final mass decrease which occurs at 425°C corresponds to the loss of the BTC and 5-amino isophthalic linkers, giving a final plateau consisting of ZrO_2 for all samples.

As discussed previously, the addition of di-topic linkers may promote the occurrance of linker defects within the synthesised MOF. We can attempt to quantify linker defects using TGA, as discussed in Section 5.4. The percentage of linkers present in each samples can be calculated from the normalised TGA data [Figure 5.38] and are given in Table 5.6.

Table 5.6: Percentage of linker present in MOF-808-D1 samples relative to a pristine MOF-808 structure calculated from normalised TGA.

Sample	Linker (%)
MOF-808-D1-10	103.2
MOF-808-D1-20	103.4
MOF-808-D1-30	107.9
MOF-808-D1-40	103.6
MOF-808-D1-50	93.2
MOF-808-D1-60	88.7

As for the MOF-808-DX-10 samples, many MOF-808-D1 samples have percentage linker values of over 100%. All samples from MOF-808-D1-10 to MOF-808-D1-40 do not show any linker defects within the structure as the linker incorporation value calculated is above 100%. The highest value is calculated for MOF-808-D1-30 where 108% linker is present. This suggest that these samples are lacking in Zr metal, with some potentially missing Zr-clusters. This lack of metal may be due to the orientation of the di-topic linkers not being favourable for the formation of Zr-oxo clusters due to the lack of a carboxylic acid group. Another reason for the high linker percentage may be additional di-topic linker within the pores, however, the washing procedure is thorough and should prevent this.

For the higher percentage samples, MOF-808-D1-50 and MOF-808-D1-60, the calculations give a lower linker percentage than 100% which indicates the presence of linker defects within the samples. These samples are therefore likely to have a greater proportion of open metal sites which may be advantageous to the catalytic properties. The reduction in the percentage of linkers present within the structure may also cause the reduction in stability seen within the TGA data.

Using *in-situ* solvothermal synthesis we have successfully incorporated up to 25 mol% of 5-amino isophthalic acid into the MOF-808 structure whilst retaining the long range crystalline structure. A reduction in thermal stability can be observed as the mol% of di-topic linker is introduced to the structure as shown by the TGA data. We have also successfully introduced linker defects into MOF-808-D1-50 and MOF-808-D1-60 samples as calculated by normalised TGA data. All MOF-808-D1 samples will be tested as catalysts for the hydrolysis of DMNP in order to investigate the effect of increasing di-topic linker in MOF-808 on the catalytic performance.

5.5.3.2 Post-synthetic Exchange Samples

In order to introduce higher amounts of di-topic linker into the structure than the 25% observed for the in-situ solvothermal synthesis, post-synthetic exchange (PSE) was attempted. Both metal and linker PSE has been widely utilised to introduce additional functionality to MOFs for a range of applications.[15] In an attempt to synthesise a mixed linker MOF-808 through PSE, a pre-prepared MOF-808-PR sample will be stirred with 5-amino isophthalic acid.

The PSE exchange was carried out on MOF-808-PR samples with the addition of high molar equivalents of di-topic linker; values of 5, 10 and 15 molar equivalents of 5-amino isopthalic acid to MOF-808-PR were used. These samples will be referred to as MOF-808-PSE-5, MOF-808-PSE-10, and MOF-808-PSE-15, respectively. The synthesis was carried out as detailed in Section 5.3 where a MOF-808-PR was stirred in a solution of 5-amino isophthalic acid in methanol. Subsequently, the same washing procedure as for the solvothermal synthesis samples was carried out in order to remove any uncoordinated linker from the sample.

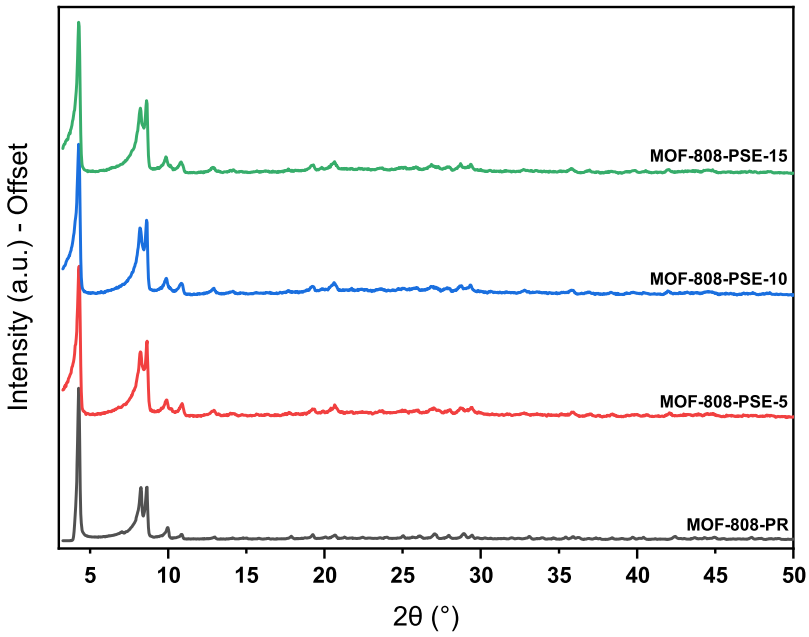

Figure 5.11: PXRD of MOF-808-PSE series.

Once the samples were collected and washed, PXRD was carried out to confirm that the bulk crystallinity of the MOF-808-PR had been preserved. As can be seen in Figure 5.11 the three MOF-808-PSE samples have all retained the bulk crystallinity, and the PSE reaction has not caused a shift in any 2θ values throughout the series. This is an expected result as MOF-808 is known to be stable at room temperature in methanol. This is also in line with the other samples discussed above, with the MOF-808 parent structure being preserved upon the addition of a di-topic linker.

As the bulk crystallinity of the samples has been confirmed, digestion q-NMR spectroscopy was carried out to identify if the PSE exchange was successful in exchanging the BTC linker with 5-amino isophthalic acid. From the values in Table 5.7 we can see the PSE reaction has been successful, and large proportions of our di-topic linker have been introduced into the MOF-808 structure than previously seen.

It is interesting that although the molar equvalents of 5-amino isopthalic acid used in the synthesis increased three-fold over the samples, the resulting di-topic linker percentage detected within the MOFs do not vary between samples. It is also clear that using PSE allows more linker to be incorperated into the structure than in the case of in-situ solvothermal synthesis. However, both methods show that there is a limit to the proportion of di-topic linker that can be integrated into

Table 5.7: Percentages of 5-amino isopthalic linker within mixed-linker MOF-808 samples synthesised through PSE and calculated from q-NMR spectroscopy.

Sample	D1-Linker (%)
MOF-808-PSE5	51.5
MOF-808-PSE10	54.4
MOF-808-PSE15	56.8

the structure: in-situ giving a limit of close to 25% and PSE giving around 50%.

TGA was carried out on all MOF-808-PSE samples and can be seen in Figure 5.12. These samples give an interesting TGA as although all mass losses expected of a MOF-808 structure are present, the percentage mass loss and the temperature where they occur differ.

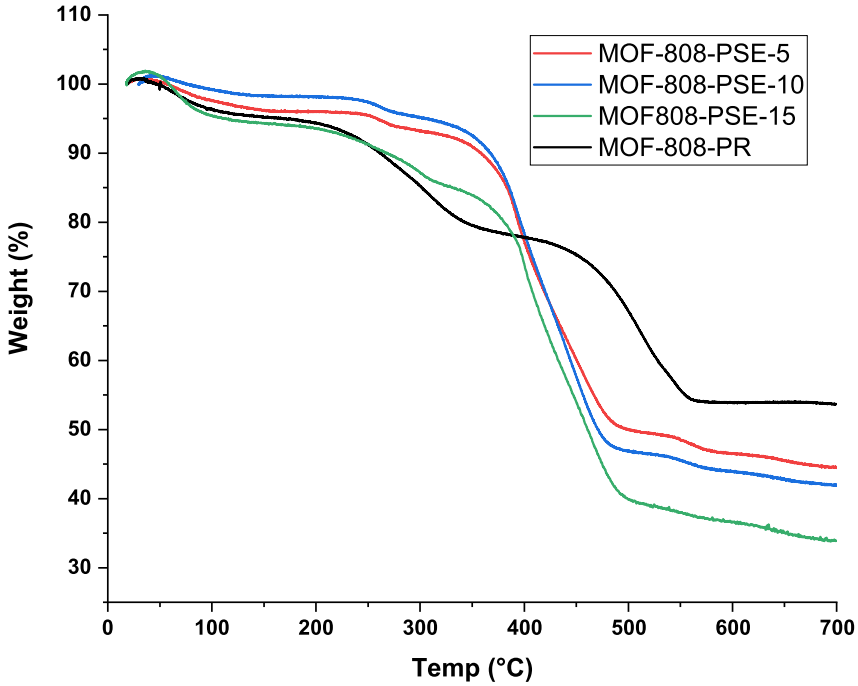

Figure 5.12: TGA traces of MOF-808-PSE series upon heating at a rate of 5 °C min^{-1} in air.

The difference between the MOF-808 and PSE samples is seen first at the mass loss which typically occurs around 250 °C. In the MOF-808-PSE samples this mass loss occurs at a higher temperature and exhibits a much smaller percentage drop. This mass loss is attributed to the loss of coordinated formate and hydroxyl ions, therefore in the MOF-808-PSE samples fewer are present. This is expected as the pre-synthesised MOF808-PR sample has been washed previously, and the

additional washing in methanol during the PSE reaction may further decrease the bridging formate ions as previously reported.[10] However, this mass loss may also be due to increased linker coordination to the Zr_6 nodes; the 5-amino isophthalic acid may replace the formate ions which reside in open metal sites. This will reduce the active sites available for the catalytic hydrolysis.

The other large difference between the pristine and PSE samples is the final mass loss associated with the loss of linkers. The stability of the MOF-808 has been decreased through PSE as the mass loss begins at a lower temperature than the 425°C observed for the parent MOF-808 structure, in-fact the lower temperature of 350°C is closer to the decomposition temperature of 5-isophthalic acid. The MOF-808-PSE samples also exhibit a much higher proportion of mass loss due to the loss of linker than for the MOF-808-PR. This also supports the conclusion that rather than replacing the BTC linkers, the 5-amino isophthalic acid has coordinated to open metal sites within the structure.

As the di-topic linker in the structure is present in such high quantities [Table 5.7] and the TGA trace for the PSE samples shows a clear difference from MOF-808-PR, the linker composition within the MOF-808 structure has clearly been altered by this process. For all other samples the TGA has been used to quantify the linker defects within the structure, this is not possible for these samples as the structure has been changed so greatly. However, we can hypothesise from the above data that the PSE structures are unlikely to have created linker defects due to the vast amount of 5-amino isopthalic acid that has been added to the structure. Due to the lesser stability and lack of information regarding the structure of the PSE samples, they will not be tested as catalysts.

In this section successfully synthesis has been carried out for a series of MOF-808 mixed linker samples with a range of 5-amino isophthalic acid percentages, using both an in-situ solvothermal synthesis and a PSE. The in-situ samples are all crystalline and show similar stability to MOF-808-PR. The di-topic linker incorporation has been calculated throughout and varies widely over the samples, with few samples presenting linker defects. All in-situ synthesis samples will be tested as catalysts for the hydrolysis of a nerve agent simulant DMNP in Section 5.6. The link between increasing the percentage of di-topic linker within the synthesis and the catalytic rate will be discussed below.

5.6 Catalytic testing

Following the synthesis and characterisation of all mixed linker MOF-808 samples, catalytic testing was carried out. As discussed in *Reference introduction*, live nerve agents cannot be used therefore, nerve agent simulants are used instead. For these tests the nerve agent simulant dimethyl 4-nitrophenylphosphate (DMNP) was chosen due to previously reported catalytic results closely correlating with sarin.[16] The reaction is monitored by observing the evolution of the hydrolysis product *para*-nitrophenol (PNP) through UV-Vis spectroscopy.

The catalytic hydrolysis was carried out as outlined in subsection 5.3.5. For each test a 3.0 mg (6 mol% Zr) sample was used. Due to acidic byproducts of the reaction, the catalysis is carried out in the presence of the buffer *N*-Ethylmorpholine (NEM) at pH 10. Previous stability studies have shown that MOF-808 is stable at pH 10 therefore we assume the MOF samples do not break down in solution.[17] Each sample was tested multiple times.

Catalytic rates were calculated by converting absorption values to PNP concentrations using a molar absorption coefficient, ε, from an in-house calibration curve. Using the method of initial rates an initial rate of hydrolysis can be calculated for each material.[18]

5.6.1 10% Di-topic linker samples

For each MOF-808-D-10 sample, multiple catalytic tests were carried out for all batches (1, 2 and 3). All samples showed catalytic activity for the hydrolysis of DMNP. The initial rates calculated for each sample are shown in Figure 5.13, with each bar being the average of multiple repeats. The conversion profiles for all tests are given in Figure 5.43 - Figure 5.46.

The conversion profiles for the catalytic tests on MOF-808-D1-10 samples can be seen in Figure 5.43. For all samples the conversion achieved is at least 80% and agreement for each batch is high. The majority of samples achieve 100% conversion over the 15 minute monitoring time. The samples which do not achieve this have yet to plateau and would reach 100% if longer times were monitored. The sample with the lowest conversion is the Batch 3 MOF-808-D1-10 sample which in one case exhibited a final conversion of 80%, this sample exhibits the highest di-topic linker percent of the three batches.

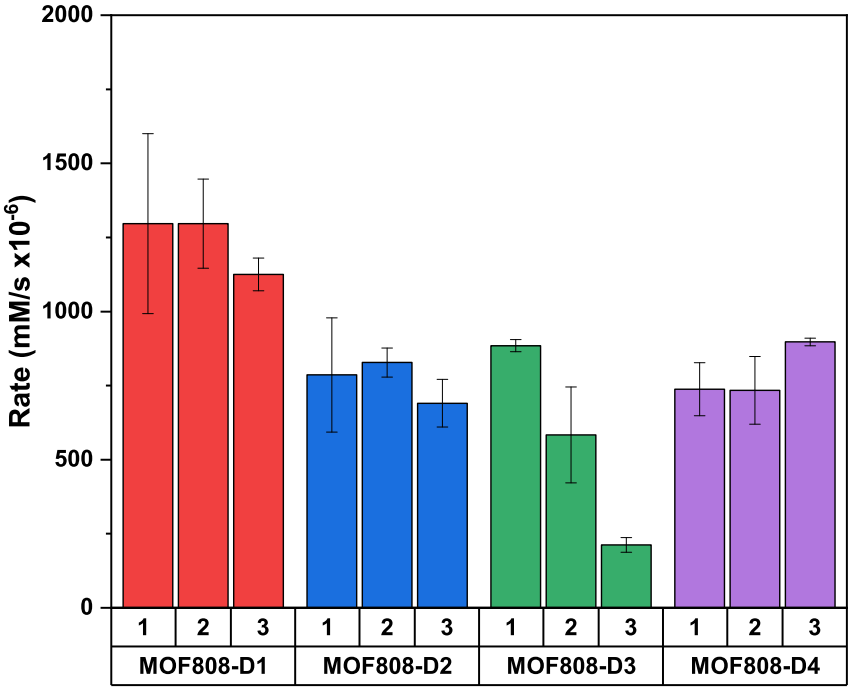

Figure 5.13: Initial rate of catalysis for the hydrolysis of DMNP using defective samples with 10% defective linker. Numbers on x axis denote Batch of each sample.

When comparing the initial rates, the MOF-808-D1-10 samples show the highest average initial rates of all di-topic linker samples tested [red bars, Figure 5.13]. Each repeat batch show good agreement, with Batch 3 showing a slightly reduced rate. This correlates with the di-topic linker percentages that are present in the samples; the Batch 3 sample has a di-topic linker incorporation of 13.9% and a lower initial rate, compared to 9.1% and 8.0% for Batch 1 and Batch 2 which both show higher rates.

The negative correlation between rates and di-topic linker incorporation suggests that the additional linker is not having the intended consequence and may in-fact be hindering the reaction due to steric hindrance. There is no correlation between the overall percentage linker within the structure as calculated from the TGA and the rates calculated which supports the conclusion that no defects have been incorporated and therefore are not having any effect on this application.

Although all MOF-808-D1-10 initial rates are close to the determined MOF-808-PR rate of 1400 mM/s $x\,10^{-6}$, the addition of the di-topic linker has not improved the rate. Some higher rates were observed in the individual tests for the Batch 1

sample, which results in more uncertainty in the average rate, yet is promising for further study.

For MOF-808-D2-10, the conversion profiles are not in agreement across the three batches [Appendix Figure 5.44]. Batch 2 successfully achieves 100% conversion within 15 minutes for all repeats. This is not the case for either batch 1 or 3, with the range of conversions achieved between 40% - 70%. With longer reaction times the conversion may increase, however, it is clear that batch 1 and 3 are not as successful in hydrolysing DMNP, with the MOF-808 samples losing the catalytic ability overtime. If we compare these results to the calculated percentage of 5-hydroxy isophthalic acid from q-NMR spectroscopy, batch 2 MOF-808-D2-10 is the only sample that did not contain any additional linker. This strongly indicates that the addition of this linker is negatively impacting the catalysis.

The initial rates calculated for MOF-808-D2-10 are lower than those for the MOF-808-D1-10 samples [Figure 5.13]. Similar percentages of 5-hydroxyl isophthalic acid were recorded as in the 5-amino isophthalic case, therefore the addition of the hydroxy functional group is hindering the catalysis. It is also interesting to note than within batch 2 there is an absence of di-topic linker detected, yet the average rate for this batch is higher than the others. This also supports the conclusion that the addition of 5-hydroxy isophthalic acid to MOF-808 is not advantageous to this application. Previous studies have also reported that the addition of an hydroxy functional group into the structure of UiO-66 reduces the initial rate for this reaction.[19]

It is also interesting to note that the MOF-808-D2-10 batch 3 was the only sample that we calculated to include linker defects within the structure [Table 5.4]. Yet this is the sample that exhibits the lowest conversion after 15 mins and the lowest average initial rate of the three batches synthesised. These results clearly indicate that having lower percentage of linkers within the structure does not positively impact the catalytic performance for MOF-808. As the parent MOF-808-PR structure is already only 6-connected leaving open-metal sites within the structure, any additional sites clearly do not impact this application.

The catalytic results for MOF-808-D3-10 are the most varied of all the samples. The conversion profiles vary widely between batches [Figure 5.45]. The best conversion result is for Batch 1 with 90% - 100% conversion over 15 minutes,

this is followed by Batch 2 which achieves around 70% conversion. The least successful conversion is seen for MOF-808-D3-10 Batch 3, this sample only achieves 25% conversion after 15 minutes. Within each batch, the agreement between repeats is high. As with previous samples, the batch with the best results correlate with the least di-topic linker being present as calculated by q-NMR spectroscopy [Table 5.3].

The initial rates calculated for MOF-808-D3-10 also vary widely between batches [Figure 5.13]. The Batch 1 sample shows an initial rate of 885 mM/s $x\,10^{-6}$, this is higher than all initial rates calculated for MOF-808-D2-10. The batch 1 sample also displays the least isophthalic acid of the three batches with 5.1%. The average initial rates for batch 2 and batch 3 are both lower than all other samples measured, with MOF-808-D3-10 Batch 3 having the lowest calculated rate of all samples with 212 mM/s $x\,10^{-6}$. These results clearly indicate that the addition of isophthalic acid does not increase the rate of catalysis, and the increased percentage of this di-topic linker seems to inhibit catalytic activity. This may be due to this linker coordinating to open metal sites within the MOF-808 structure, creating steric hindrance at the active site.

For the final 10% sample, MOF-808-D4-10, each batch is in generally good agreement when the conversion profiles are compared [Figure 5.13]. All samples achieve over 80% conversion with repeat results in good agreement, with the exception of one batch 3 repeat which only achieves 55%. This sample looks to be plateauing after 15 minutes so is unlikely to achieve the 100% conversion in this reaction. There is little difference between the conversion profiles, yet there is a wide range of pyridine-3,5-carboxylic acid calculated by q-NMR spectroscopy to be within the MOF-808 structure. From these results the addition of this linker does not seem to effect the total conversion achieved.

The initial rates calculated for MOF-808-D4-10 show good agreement between batches and have similar rates to MOF-808-D2-10. These samples overall have a higher percentage of di-topic linker within the structure than seen in the other samples. This has not inhibited the catalysis to as great an extent as other samples; with 19% pyridine-3,5-carboxylic acid within the MOF-808 structure, the initial rate is similar to the MOF-808-D2-10 sample which exhibits 6% 5-hydroxy isophthalic acid. A reason this linker may not effect the catalysis is due to the reduced steric hindrance as there is a lack of functional

group on the ring compared to 5-amino isophthalic or 5-hydroxy isophthalic acid.

Overall, the 10% di-topic linker samples show a range of catalytic rates, but all were successful for this application. However, none of the samples tested gave an average initial rate higher than the 1400 mM/s $x\,10^{-6}$ reported for MOF-808-PR. All samples which incorporated di-topic linkers show decreased initial rates and lower reaction conversions over the 15 minutes. It is likely that the additional di-topic linkers do not cause linker defects, resulting in additional active Zr_6 sites within the structure, as initially hypothesised. Instead, it is likely that they are coordinating to previously uncoordinated sites within the MOF-808 node, reducing the availability of these active sites, and decreasing the rate and conversion for this catalysis.

An interesting result was obtained for the 5-amino isophthalic samples which showed the highest initial rates of all samples tested. A reason for this may be that although active sites are being sterically hindered as in the other cases, the NH_2 functional group is having a beneficial effect on this catalysis, counteracting the negative steric effect. This has been the case in other reported materials, where the addition of 2-amino terephthalic acid to the structure of UiO-66 has enhanced the catalysis of nerve agents and simulants.[20]

5.6.2 5-amino isophthalic containing MOF-808

Following the catalytic results seen when *ca.* 10% of 5-amino isophthalic acid was incorporated into MOF-808, the samples prepared with increasing percentages of 5-amino isophthalic were tested as catalysts for the hydrolysis of DMNP. Each sample was tested multiple times and conversion profiles are given in Figure 5.47 - Figure 5.51.

Across the series, as the percentage of 5-amino isophthalic acid increases, the conversion achieved declines from 100% for MOF-808-D1-10 to 50% for MOF-808-D1-60. This reduction is likely due to the lack of active sites available within the MOF as the percentage of 5-amino isophthalic acid is added to the structure and causes steric hindrance. It is interesting to note that there is little difference between the MOF-808-D1-10 [Figure 5.43] and MOF-808-D1-20 [Figure 5.47] conversion profiles; both samples achieve close to 100% conversion for all repeats with di-topic linker percentages of 9.1% and 13.9% respectively.

For MOF-808-D1-30 and MOF-808-D1-40 the conversion achieved drops to *ca.* 75% [Figure 5.48 & Figure 5.49]. Both of these samples also exhibit a similar 5-amino isophthalic acid incorporation of 19.6% and 20.7%. Following the same trend, the samples MOF-808-D1-50 and MOF-808-D1-60 with 5-amino isophthalic acid percentages of 24.9% and 25.4%, have a reduced conversion percentage of *ca.* 60%. This clearly indicates that increasing the proportion of 5-amino isophthalic within the MOF results in lower percentage conversion.

Initial rates were calculated for all samples [Figure 5.14]. The highest average initial rate reported is 1560 mM/s $x\,10^{-6}$ for MOF-808-D1-20, which surpasses the MOF-808-PR initial rate of 1400 mM/s $x\,10^{-6}$. This is a really interesting result as the remaining samples with increasing 5-amino isophthalic acid exhibit reduced rates compared to MOF-808-PR.

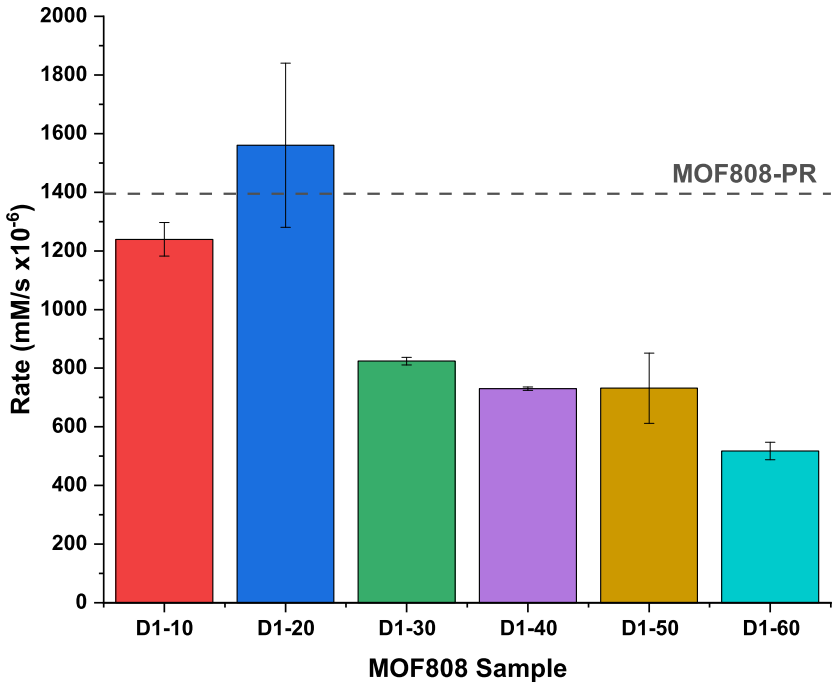

Figure 5.14: Initial rate of catalysis for the hydrolysis of DMNP using defective samples with a range of amino linker % in the sample.

The total linker percentages that were calculated from normalised TGA are almost identical for MOF-808-D1-10 to MOF-808-D1-40, with no linker defects being observed [Table 5.6]. The two samples, MOF-808-D1-50 and MOF-808-D1-60, where linker defects were calculated show the lowest overall rates. Therefore, as was the case for the 10% samples above, the increased rates are not due to defect linker sites allowing more access to the active Zr_6 sites as is the case with

other Zr-MOFs used in this catalysis.[3]

If we compare rates to the percentage of di-topic linker that has been incorporated into the structure we can see a negative correlation overall [Figure 5.14]. The lowest rate recorded is 520 mM/s $x\,10^{-6}$ for MOF-808-D1-60 which also has the highest linker incorporation. However, the MOF-808-D1-20 sample does not follow this trend; the di-topic linker value of 13.9% is higher than the 9.1% value calculated for the MOF-808-D1-10 sample. The addition of slightly more 5-amino-isophthalic acid may be having a positive effect on the hydrolysis reaction. This has not been the case with any other samples so we hypothesise that this value is a balance between steric hindrance and the positive effect the NH_2 functionality has for this reaction. Once beyond the *ca.* 14% 5-amino isophthalic acid incorporation, the steric hindrance effects may take over.

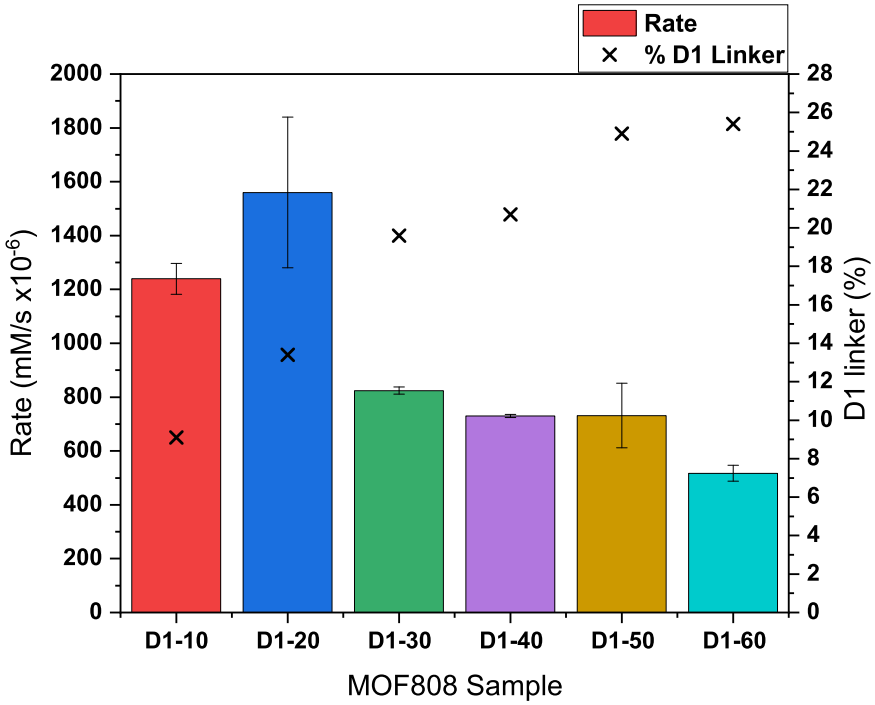

Figure 5.15: Initial rate of catalysis for the hydrolysis of DMNP using defective samples with a range of amino linker % in the sample (left axis) percentage of D1 linker incoorperated into the structure (right axis).

Overall, the MOF-808 samples containing 5-amino isophthalic acid were successful for the catalytic hydrolysis of DMNP with an enhanced rate shown by MOF-808-D1-20 compared to MOF-808-PR. We hypothesise that an ideal percentage of 5-amino isophthalic acid has been achieved in the synthesis to

create a balance between negative steric effects and beneficial effects from the NH_2 functionality. We should also consider the effect the 5-amino isophthalic acid may having within the *in-situ* synthesis upon the overall MOF structure. Although the PXRD of all samples are identical, the TGAs differ with some samples clearly less stable than others. Particle size studies should be considered for the MOF-808-D1 samples as that is reported to have an effect on this catalytic hydrolysis.[21]

5.7 Conclusions

Within this chapter we have successfully incorporated four di-topic linkers into the structure of MOF-808: 5-amino isophthalic acid, 5-hydroxy isophthalic acid, isophthalic acid, and pyridine-3,5-dicarboxylic acid.

In the first instance *ca.* 10% of each linker was successfully added and showed high reproducibility over 3 batches. Using TGA analysis we found that the di-topic linkers did not result in linker defects within the structure, and in most cases over 100% linker was calculated to be present in each MOF-808 structure. We were therefore, unsuccessful in initiating linker defects within MOF-808.

The 10% linker samples all showed catalytic activity of the hydrolysis of DMNP, however, no sample out-performed MOF-808-PR. The sample containing 5-amino isophthalic acid showed the most promise, and had the highest rate over all batches out of all di-topic linker containing samples.

Further investigations were carried out in an attempt to incorporate more 5-amino isophthalic acid into the MOF-808 structure using both in-situ and post-synthetic exchange synthesis methods. The in-situ synthesis proved successful in incorporating up to 25% 5-amino isophthalic acid into the MOF-808 structure as determined by q-NMR spectroscopy. The PSE syntheses were less successful, as although the q-NMR spectroscopy determined that 50% of the linkers within the structure were 5-amino isophthalic acid, the TGA showed reduced stability and too great a proportion of linker to metal for a MOF-808 structure. Therefore, only the in-situ samples were tested as catalysts for the hydrolysis of DMNP.

All 5-amino isophthalic acid samples showed catalytic activity for this application. The most successful sample was MOF-808-D1-20 which displayed an average initial rate of 1560 mM/s $x\,10^{-6}$, a value higher than that of MOF-808-PR. All other samples showed a decreased activity with higher incorporation of di-topic linker within the structure.

Overall, the results in this chapter have shown that additional linkers can be added to the structure of MOF-808 without compromising the overall crystal structure. The proportion of di-topic linker can be calculated using digestion-NMR spectroscopy techniques and showed consistent results across multiple

samples. Although linker defects have not been produced by the addition of di-topic linkers, additional functional groups have been incorporated into the structure. In particular we have shown the successful incorporation of an amino group into the MOF-808 structure, and in specific proportions, can out-perform the parent MOF-808 as a catalysis for the hydrolysis of DMNP.

5.8 References

[1] K. O. Kirlikovali, Z. Chen, T. Islamoglu, J. T. Hupp and O. K. Farha, *ACS Appl. Mater. Interfaces*, 2020, **12**, 14702–14720.

[2] S.-Y. Moon, Y. Liu, J. T. Hupp and O. K. Farha, *Angew. Chemie., Int. Ed.*, 2015, **54**, 6795–6799.

[3] G. W. Peterson, M. R. Destefano, S. J. Garibay, A. Ploskonka, M. McEntee, M. Hall, C. J. Karwacki, J. T. Hupp and O. K. Farha, *Chem. Eur. J.*, 2017, **23**, 15913–15916.

[4] H. Mautschke, F. Drache, I. Senkovska, S. Kaskel and F. X. Llabrés i Xamena, *Catal. Sci. Technol.*, 2018, **8**, 3610–3616.

[5] M. Kalaj, J. M. Palomba, K. C. Bentz and S. M. Cohen, *Chem. Commun.*, 2019, **55**, 5367–5370.

[6] J. E. Mondloch, M. J. Katz, W. C. Isley III, P. Ghosh, P. Liao, W. Bury, G. W. Wagner, M. G. Hall, J. B. DeCoste, G. W. Peterson, R. Q. Snurr, C. J. Cramer, J. T. Hupp and O. K. Farha, *Nat. Mater.*, 2015, **14**, 512–516.

[7] A. J. Howarth, A. W. Peters, N. A. Vermeulen, T. C. Wang, J. T. Hupp and O. K. Farha, *Chem. Mater.*, 2017, **29**, 26–39.

[8] G. C. Shearer, S. Chavan, S. Bordiga, S. Svelle, U. Olsbye and K. P. Lillerud, *Chem. Mater.*, 2016, **28**, 3749–3761.

[9] H. Furukawa, F. Gándara, Y.-B. Zhang, J. Jiang, W. L. Queen, M. R. Hudson and O. M. Yaghi, *J. Am. Chem. Soc.*, 2014, **136**, 4369–4381.

[10] G. Fu, B. Bueken and D. De Vos, *Small Methods*, 2018, **2**, 1800203.

[11] E. Plessers, G. Fu, C. Tan, D. De Vos and M. Roeffaers, *Catalysts*, 2016, **6**, 104.

[12] R. Hardian, S. Dissegna, A. Ullrich, P. L. Llewellyn, M. Coulet and R. A. Fischer, *Chem. Eur. J.*, 2021, **27**, 6804–6814.

[13] W. Liang, R. Babarao, T. L. Church and D. M. D'Alessandro, *Chem. Commun.*, 2015, **51**, 11286–11289.

[14] T. Islamoglu, M. A. Ortuño, E. Proussaloglou, A. J. Howarth, N. A. Vermeulen, A. Atilgan, A. M. Asiri, C. J. Cramer and O. K. Farha, *Angew. Chemie., Int. Ed.*, 2018, **57**, 1949–1953.

[15] T. Islamoglu, S. Goswami, Z. Li, A. J. Howarth, O. K. Farha and J. T. Hupp, *Acc. Chem. Res.*, 2017, **50**, 805–813.

[16] Y. Liu, A. J. Howarth, N. A. Vermeulen, S. Y. Moon, J. T. Hupp and O. K. Farha, *Coord. Chem. Rev.*, 2017, **346**, 101–111.

[17] H.-Q. Zheng, C.-Y. Liu, X.-Y. Zeng, J. Chen, J. Lü, R.-G. Lin, R. Cao, Z.-J. Lin and J.-W. Su, *Inorg. Chem.*, 2018, **57**, 9096–9104.

[18] J. Casado, M. A. Lopez-Quintela and F. M. Lorenzo-Barral, *J. Chem. Educ.*, 1986, **63**, 450.

[19] J. M. Palomba, S. M. Cohen, J. B. DeCoste, T. M. Tovar, C. V. Credille, M. Kalaj, G. W. Peterson, J. B. DeCoste, G. W. Peterson, T. M. Tovar and S. M. Cohen, *Chem. Commun.*, 2018, **54**, 5768–5771.

[20] M. J. Katz, S.-Y. Moon, J. E. Mondloch, M. H. Beyzavi, C. J. Stephenson, J. T. Hupp and O. K. Farha, *Chem. Sci.*, 2015, **6**, 2286–2291.

[21] P. Li, R. C. Klet, S.-Y. Moon, T. C. Wang, P. Deria, A. W. Peters, B. M. Klahr, H.-J. Park, S. S. Al-Juaid, J. T. Hupp and O. K. Farha, *Chem. Commun.*, 2015, **51**, 10925–10928.

5.9 Appendix

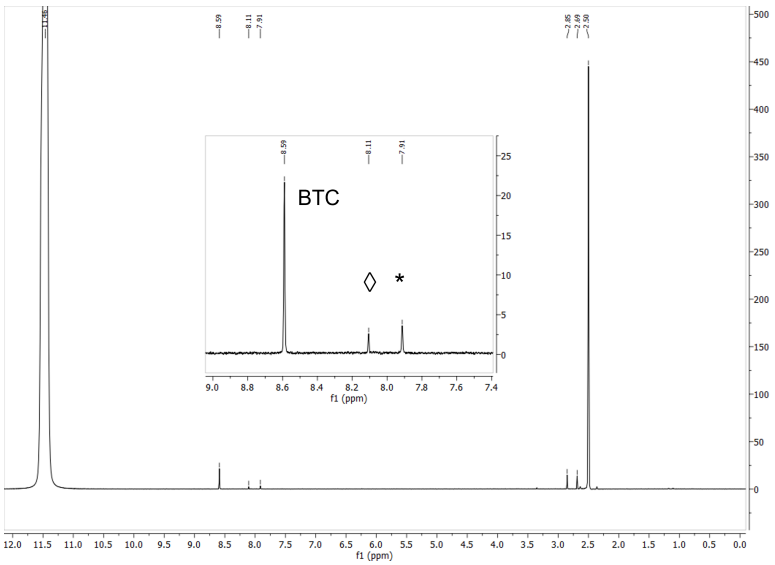

Figure 5.16: ^{1}H−NMR of acid digested MOF-808-PR sample with BTC peak labelled. Also present are solvent impurities of formic acid (◊) and DMF (∗).

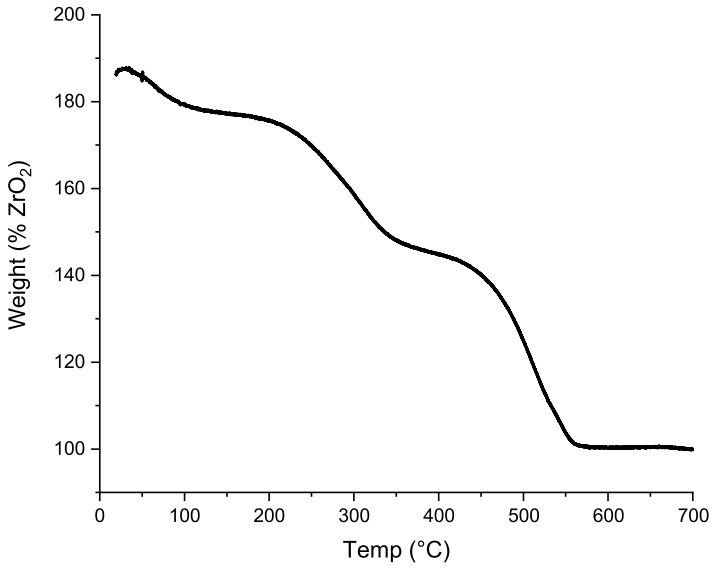

Figure 5.17: Normalised TGA data for MOF-808-PR to give percentage of linkers in the structure.

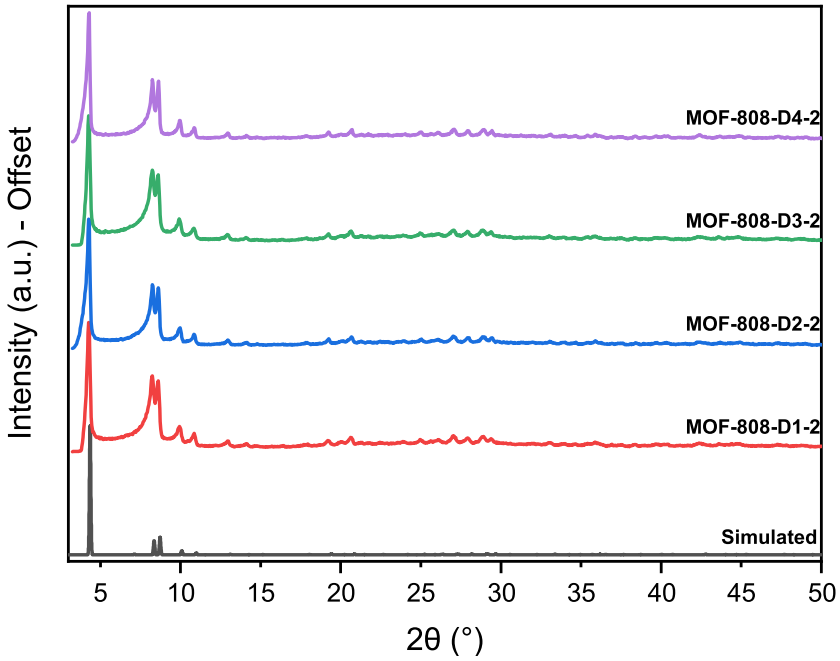

Figure 5.18: Powder X-ray diffraction of all 10% defect linker Batch 2 samples compared against MOF-808-PR.

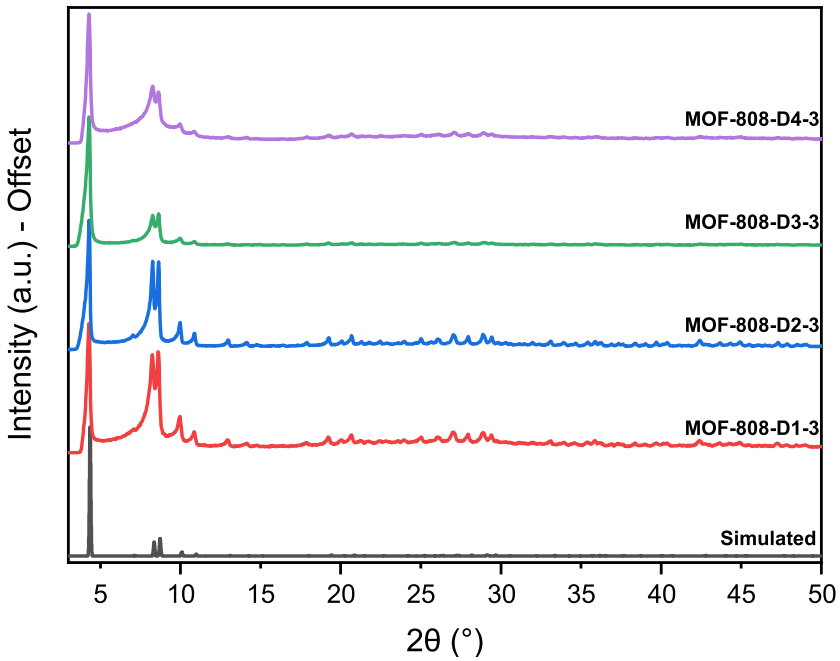

Figure 5.19: Powder X-ray diffraction of all 10% defect linker Batch 3 samples compared against MOF-808-PR.

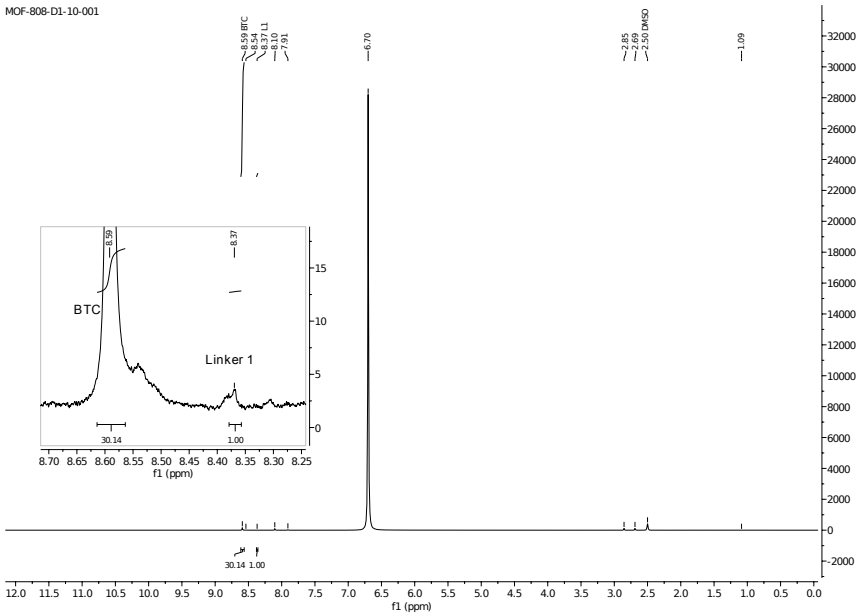

Figure 5.20: ^{1}H−NMR of acid digested MOF-808-D1-10 Batch 1 sample. Inset shows BTC and Linker 1 integral.

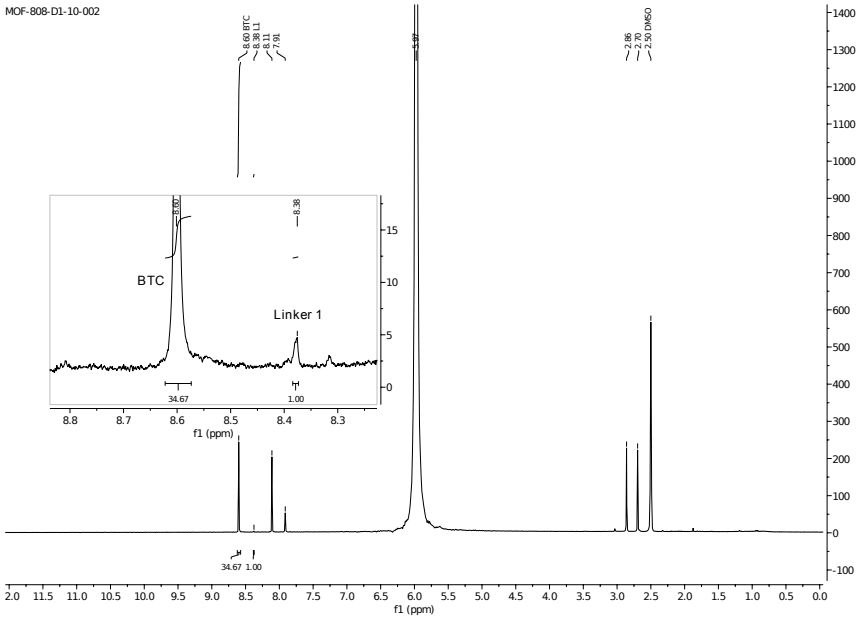

Figure 5.21: ^{1}H−NMR of acid digested MOF-808-D1-10 Batch 2 sample. Inset shows BTC and Linker 1 integral.

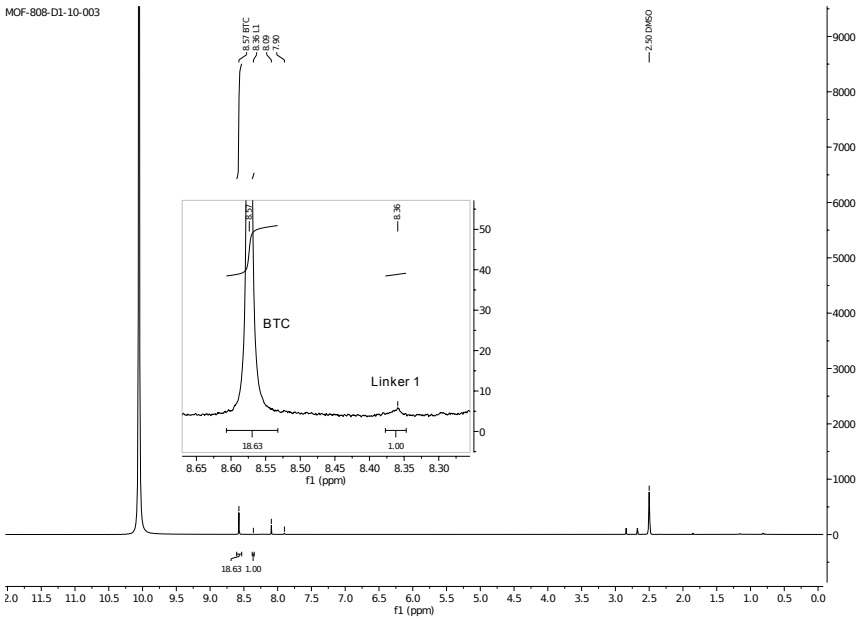

Figure 5.22: ^{1}H – NMR of acid digested MOF-808-D1-10 Batch 3 sample. Inset shows BTC and Linker 1 integral.

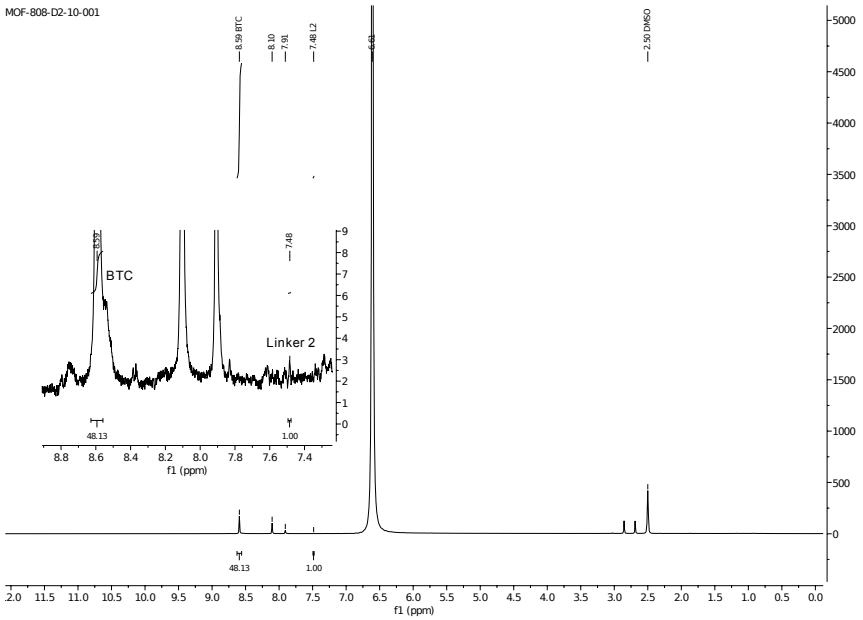

Figure 5.23: ^{1}H – NMR of acid digested MOF-808-D2-10 Batch 1 sample. Inset shows BTC and Linker 2 integral.

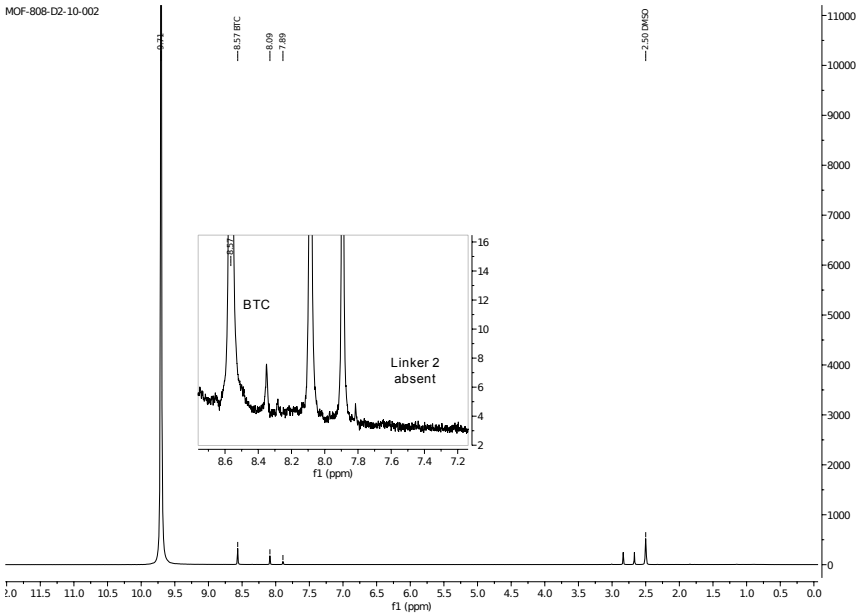

Figure 5.24: ^{1}H−NMR of acid digested MOF-808-D2-10 Batch 2 sample. Inset shows BTC and Linker 2 integral.

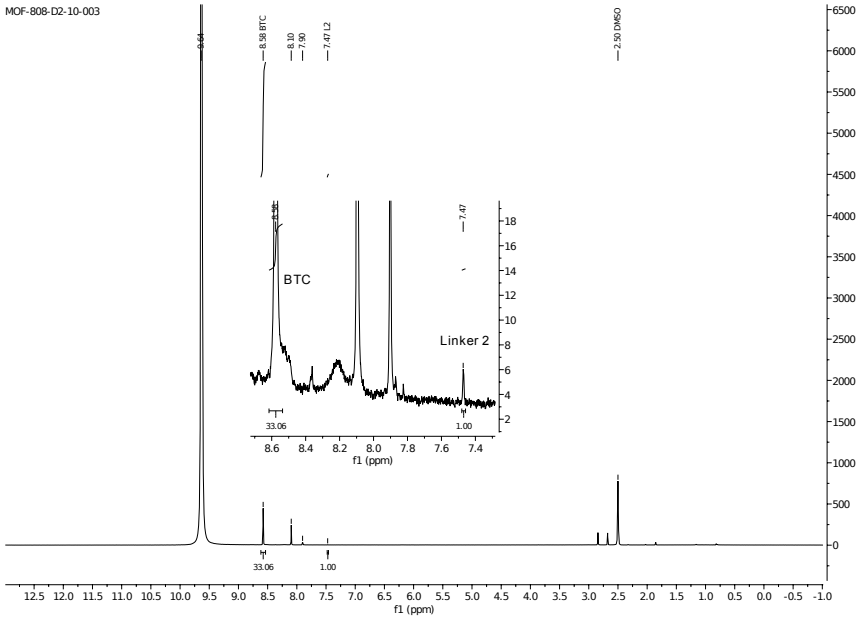

Figure 5.25: ^{1}H−NMR of acid digested MOF-808-D2-10 Batch 3 sample. Inset shows BTC and Linker 2 integral.

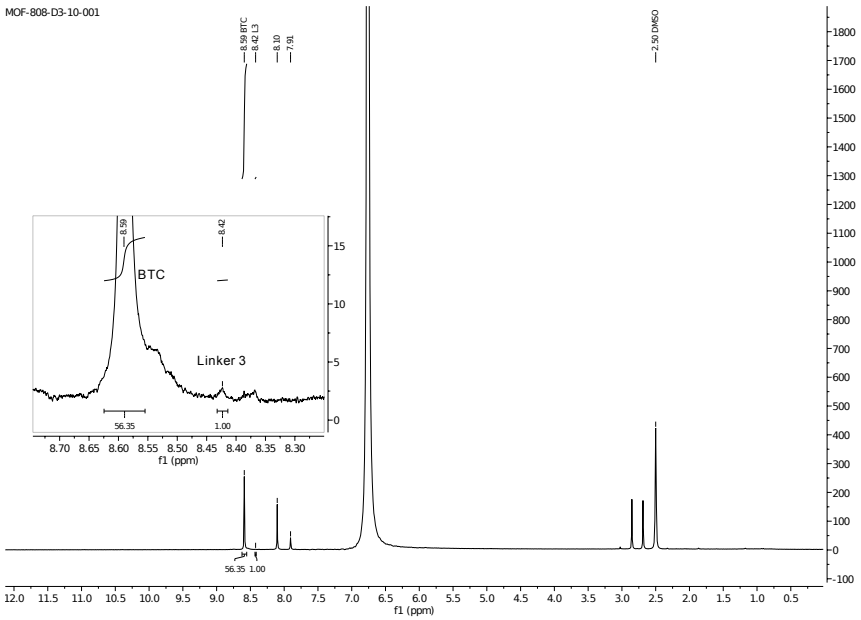

Figure 5.26: ^{1}H – NMR of acid digested MOF-808-D3-10 Batch 1 sample. Inset shows BTC and Linker 3 integral.

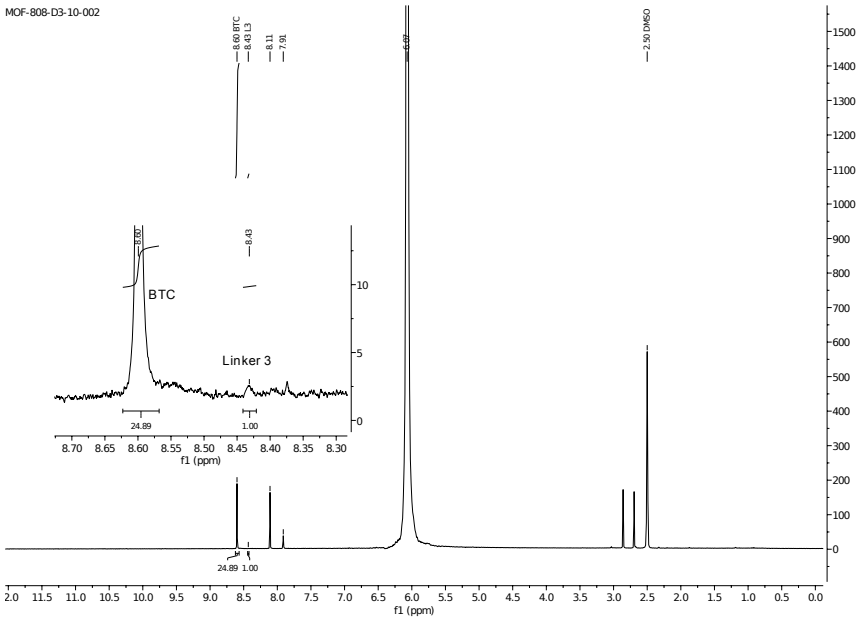

Figure 5.27: ^{1}H – NMR of acid digested MOF-808-D3-10 Batch 2 sample. Inset shows BTC and Linker 3 integral.

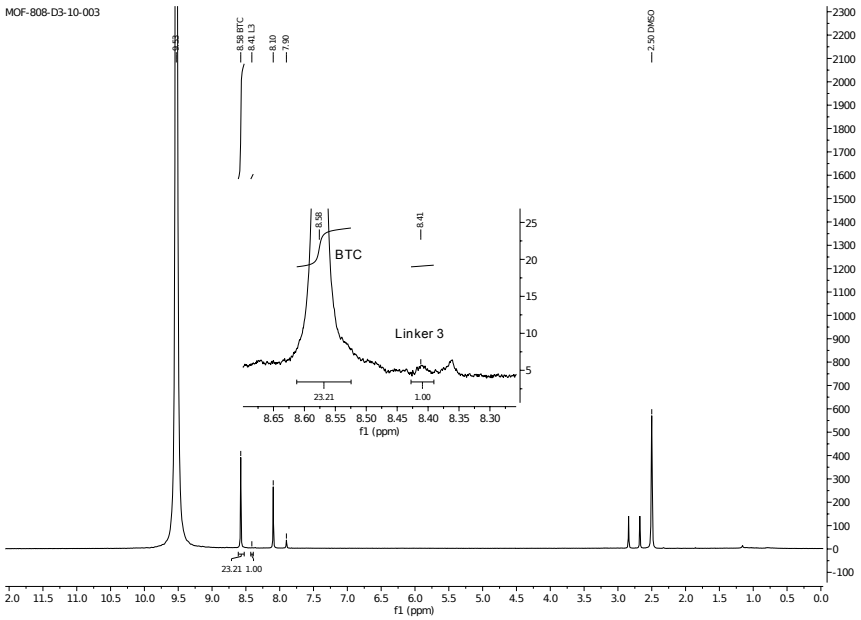

Figure 5.28: ^{1}H – NMR of acid digested MOF-808-D3-10 Batch 3 sample. Inset shows BTC and Linker 3 integral.

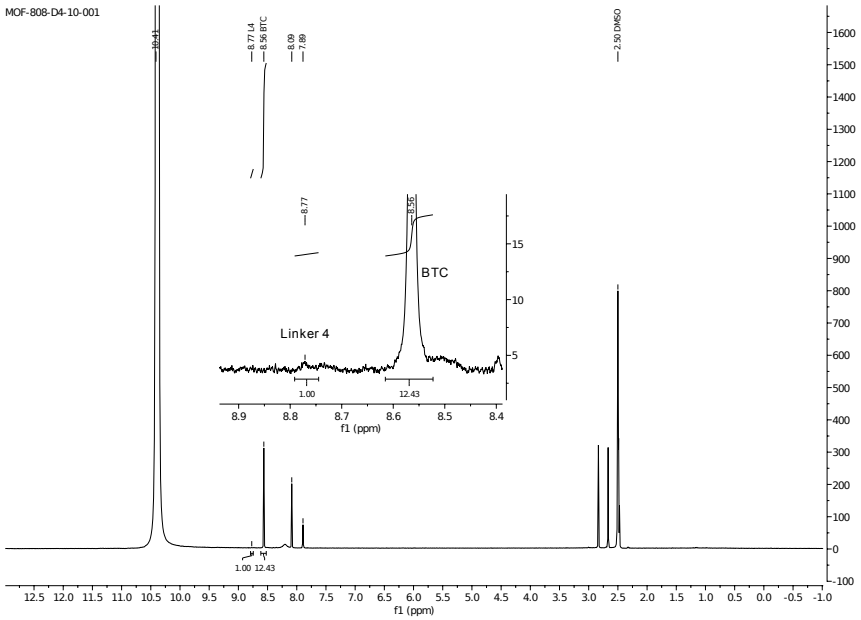

Figure 5.29: ^{1}H – NMR of acid digested MOF-808-D4-10 Batch 1 sample. Inset shows BTC and Linker 4 integral.

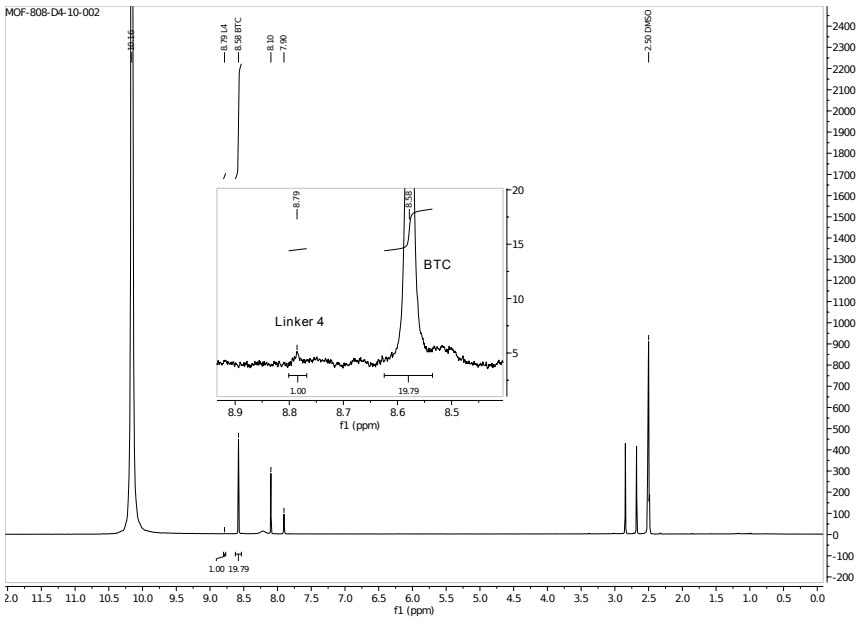

Figure 5.30: ^{1}H – NMR of acid digested MOF-808-D4-10 Batch 2 sample. Inset shows BTC and Linker 4 integral.

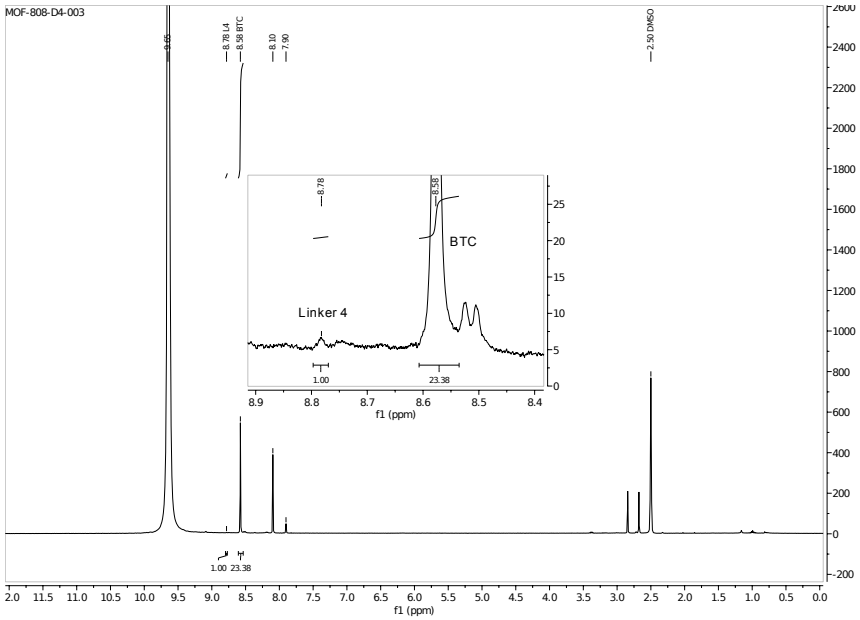

Figure 5.31: ^{1}H – NMR of acid digested MOF-808-D4-10 Batch 3 sample. Inset shows BTC and Linker 4 integral.

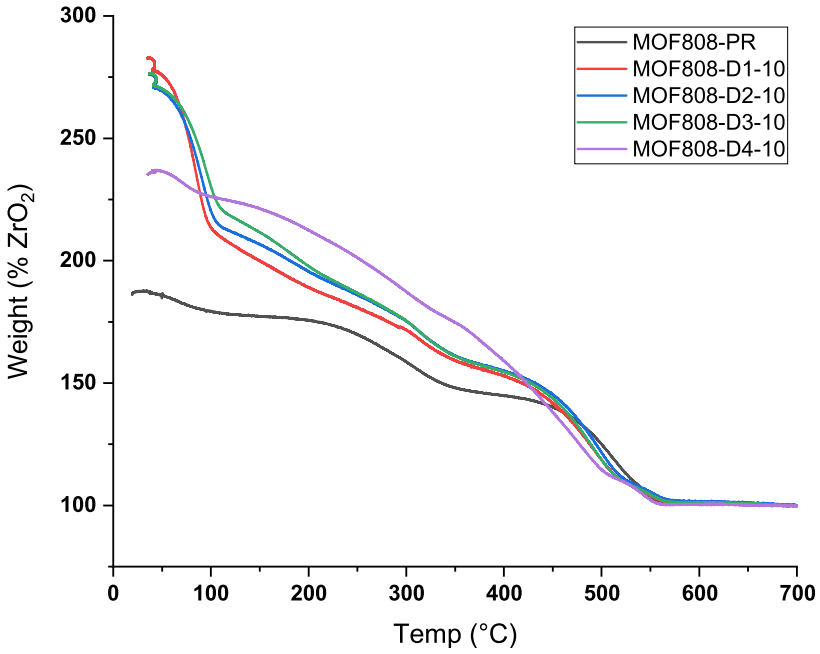

Figure 5.32: Normalised TGA data for all MOF-808-D-10 samples. Used to calculate percentage of linkers in the structure.

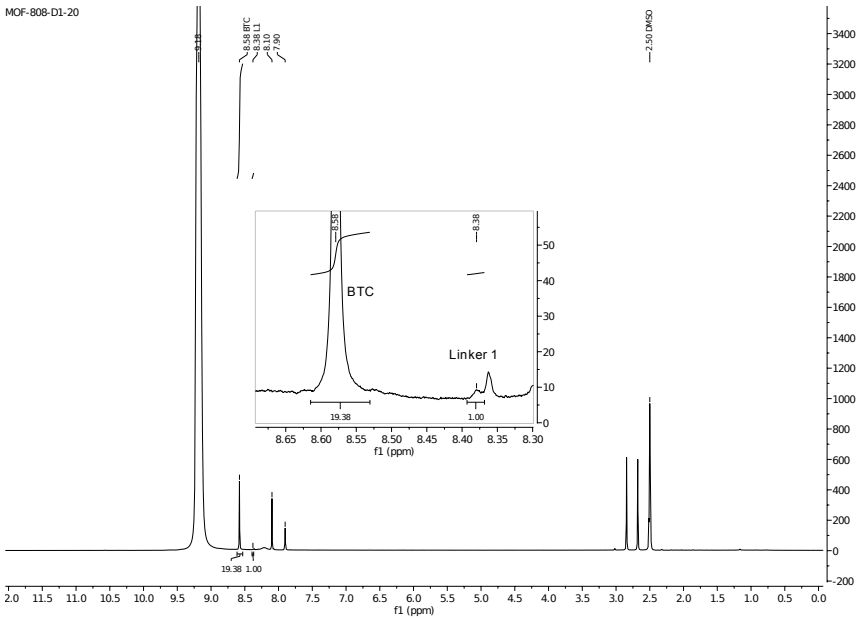

Figure 5.33: ^{1}H – NMR of acid digested MOF-808-D1-20 sample. Inset shows BTC and Linker 1 integral.

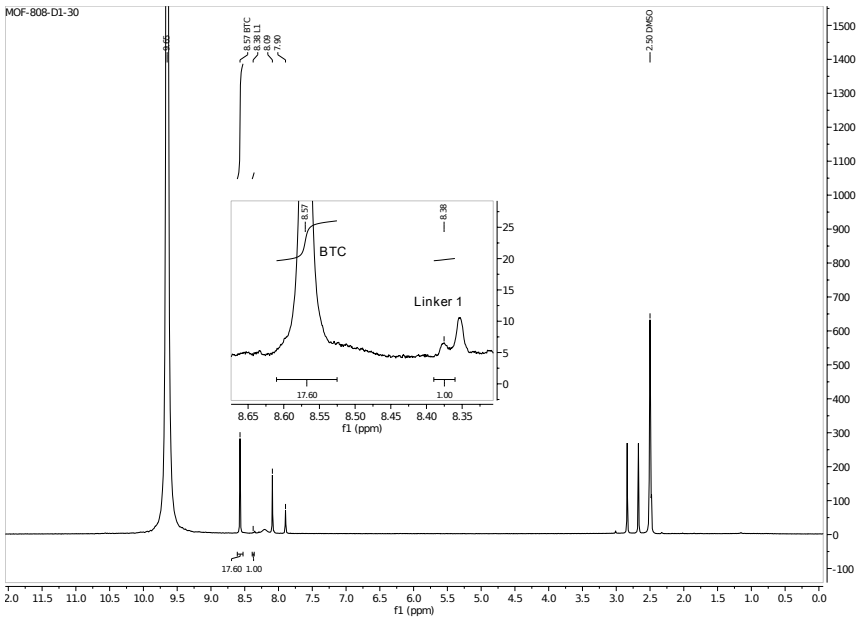

Figure 5.34: ^{1}H – NMR of acid digested MOF-808-D1-30 sample. Inset shows BTC and Linker 1 integral.

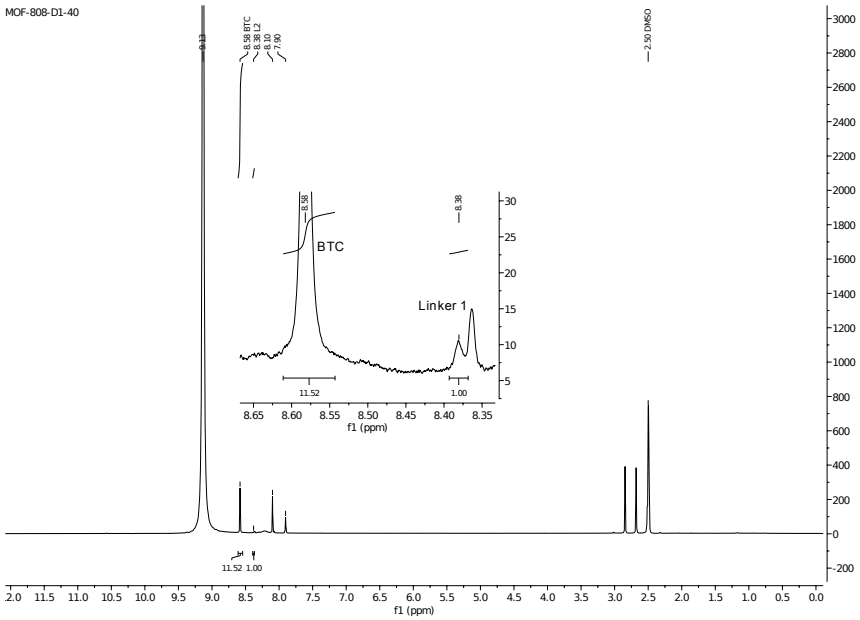

Figure 5.35: ^{1}H – NMR of acid digested MOF-808-D1-40 sample. Inset shows BTC and Linker 1 integral.

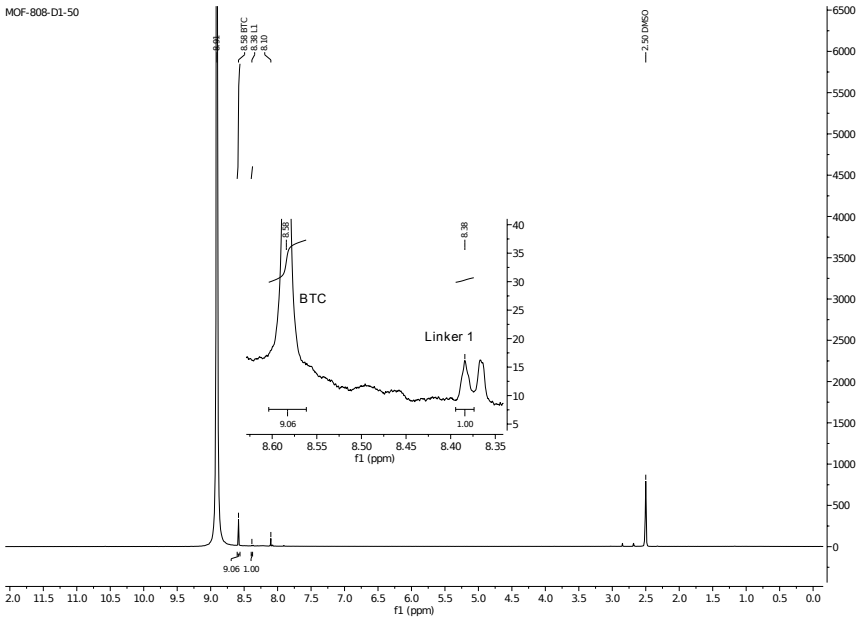

Figure 5.36: ^{1}H – NMR of acid digested MOF-808-D1-50 sample. Inset shows BTC and Linker 1 integral.

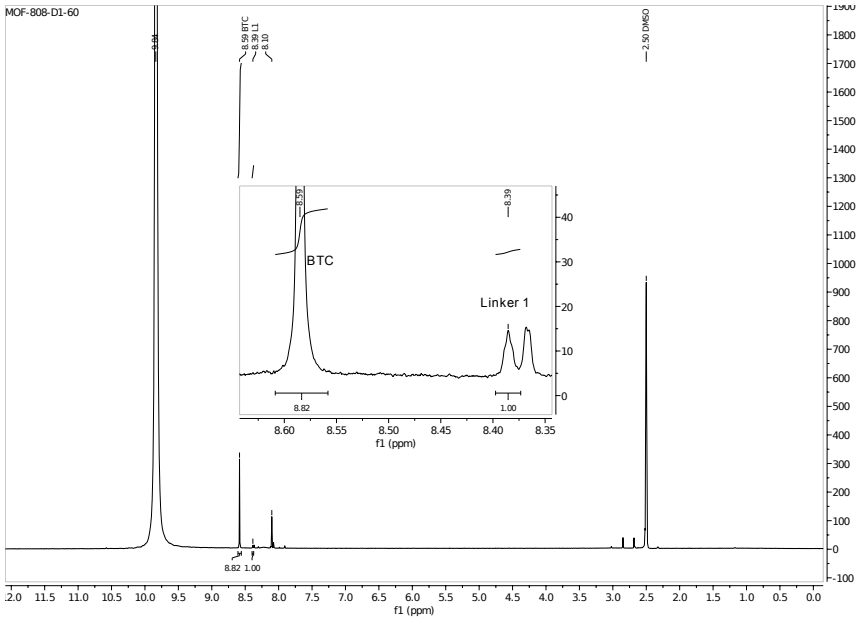

Figure 5.37: ^{1}H – NMR of acid digested MOF-808-D1-60 sample. Inset shows BTC and Linker 1 integral.

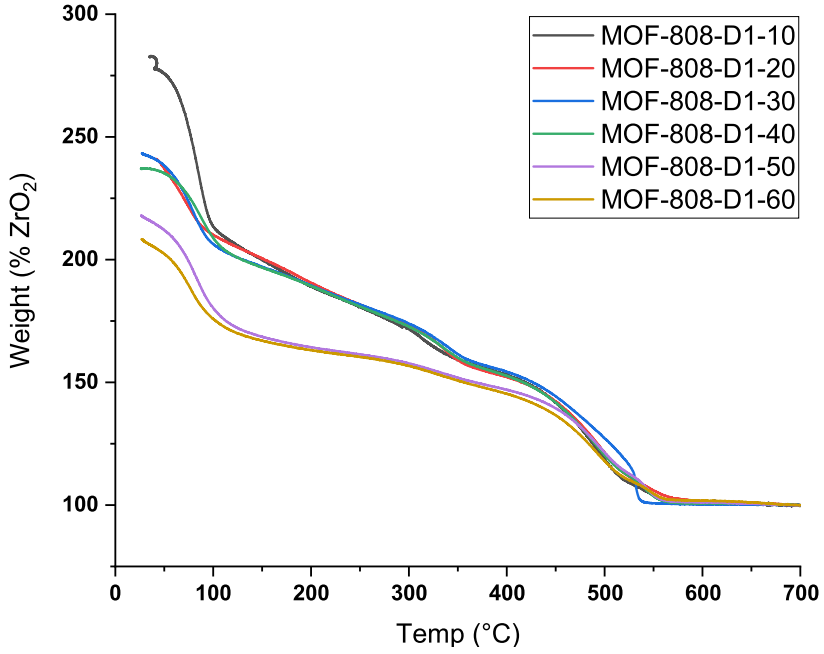

Figure 5.38: Normalised TGA data for the MOF-808-D1 series. Used to calculate percentage of linkers in the structure.

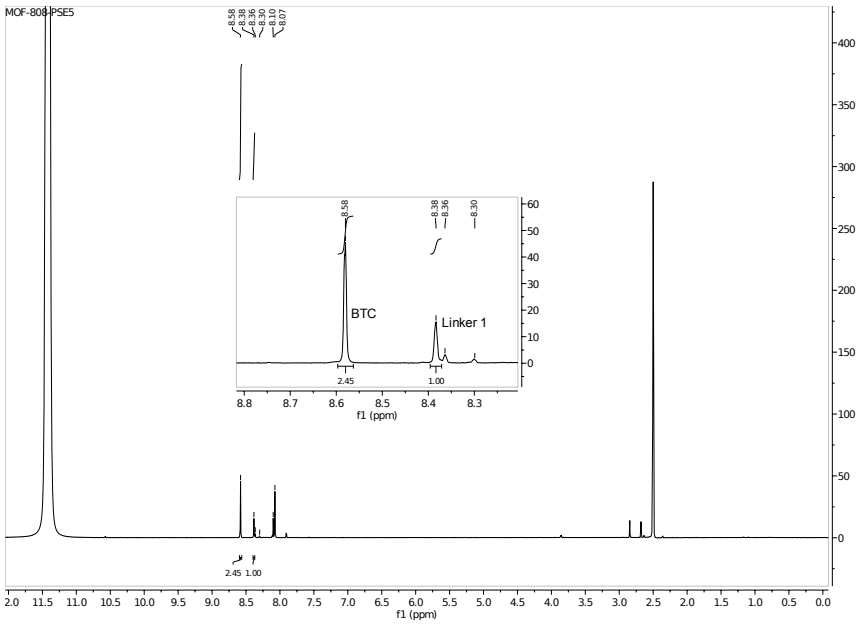

Figure 5.39: $^{1}H-NMR$ of acid digested MOF-808-PSE5 sample. Inset shows BTC and Linker 1 integral.

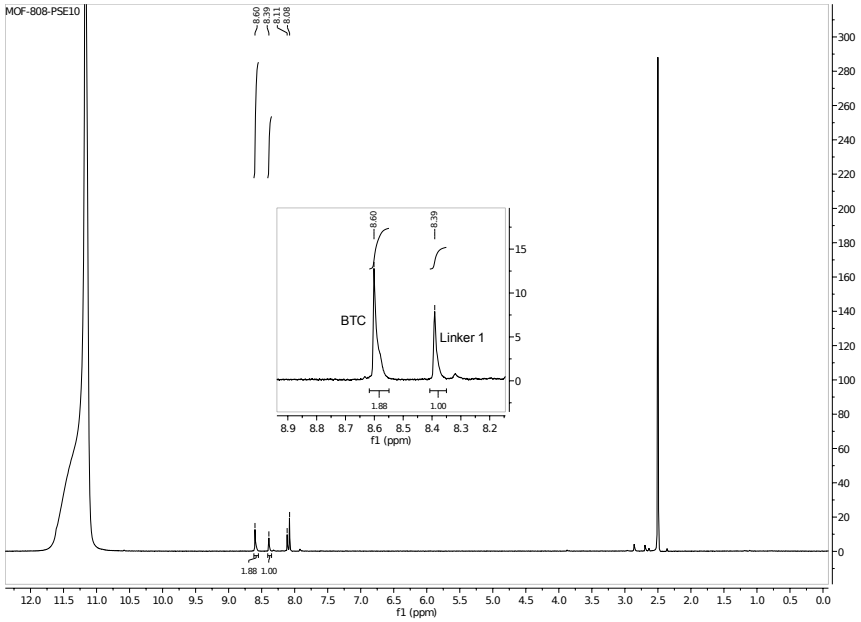

Figure 5.40: ^{1}H−NMR of acid digested MOF-808-PSE10 sample. Inset shows BTC and Linker 1 integral.

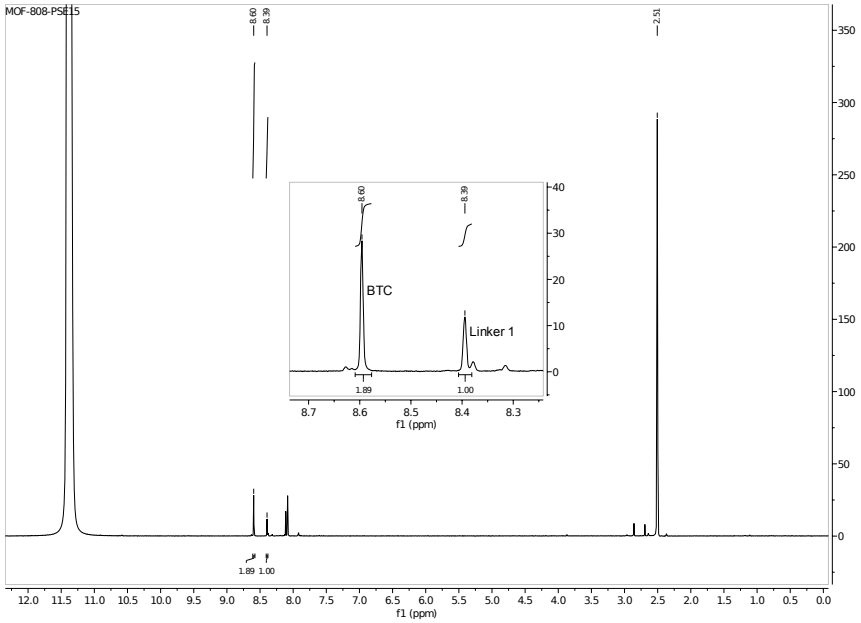

Figure 5.41: ^{1}H−NMR of acid digested MOF-808-PSE15 sample. Inset shows BTC and Linker 1 integral.

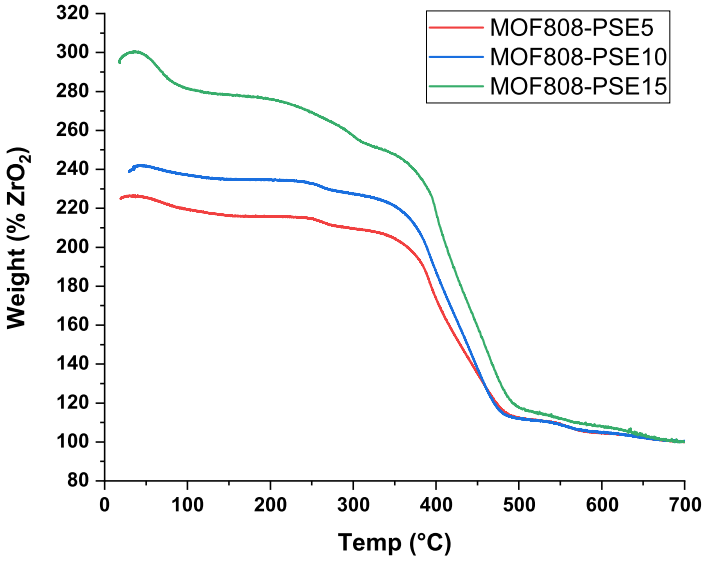

Figure 5.42: Normalised TGA data for the MOF-808-PSE series. Used to calculate percentage of linkers in the structure.

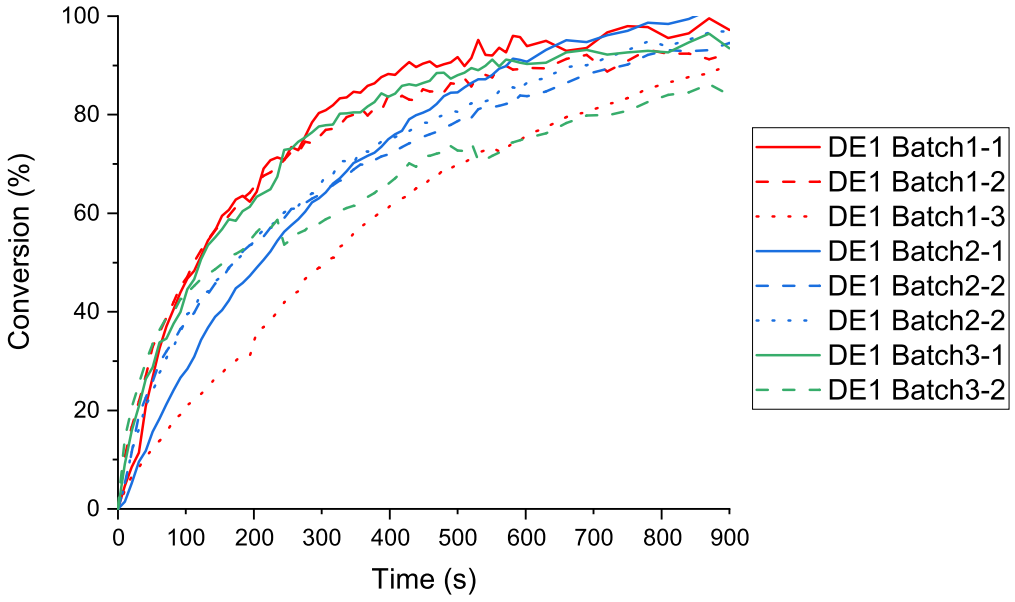

Figure 5.43: Conversion over time for all MOF808-D1 samples.

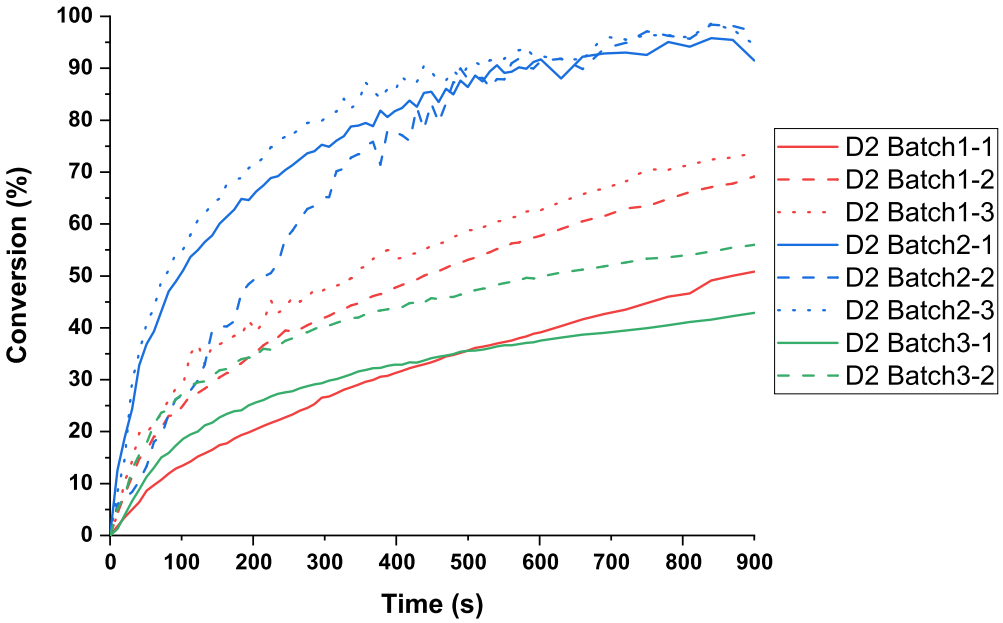

Figure 5.44: Conversion over time for all MOF808-D2 samples.

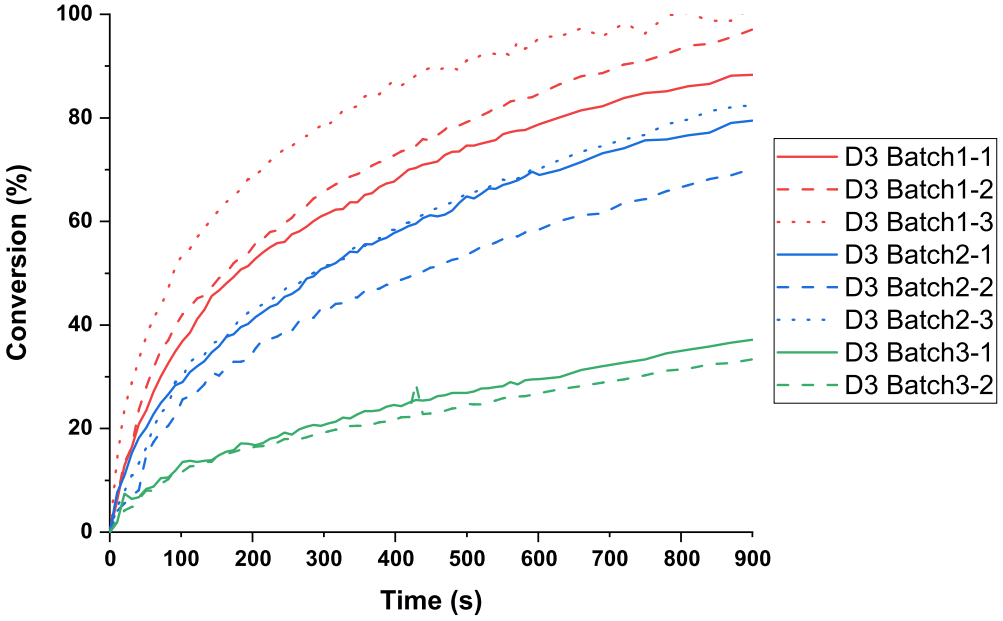

Figure 5.45: Conversion over time for all MOF808-D3 samples.

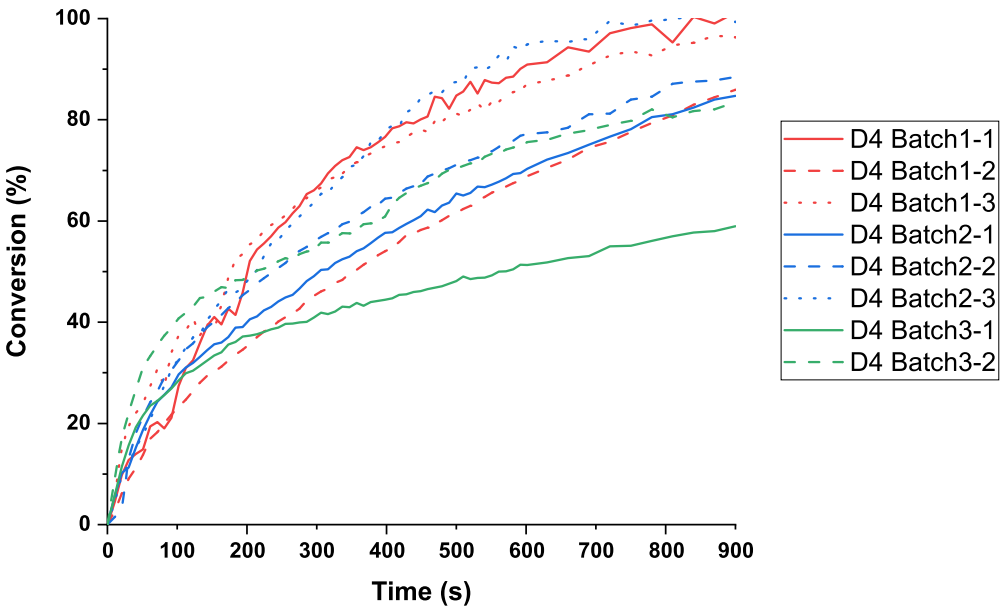

Figure 5.46: Conversion over time for all MOF808-D4 samples.

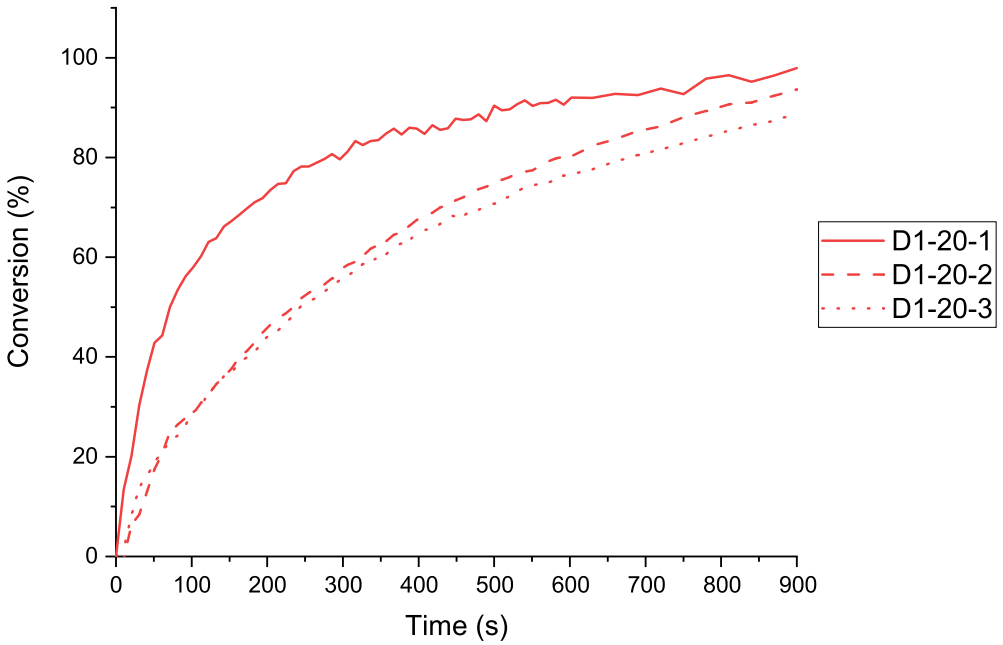

Figure 5.47: Conversion over time for MOF-808-D1-20.

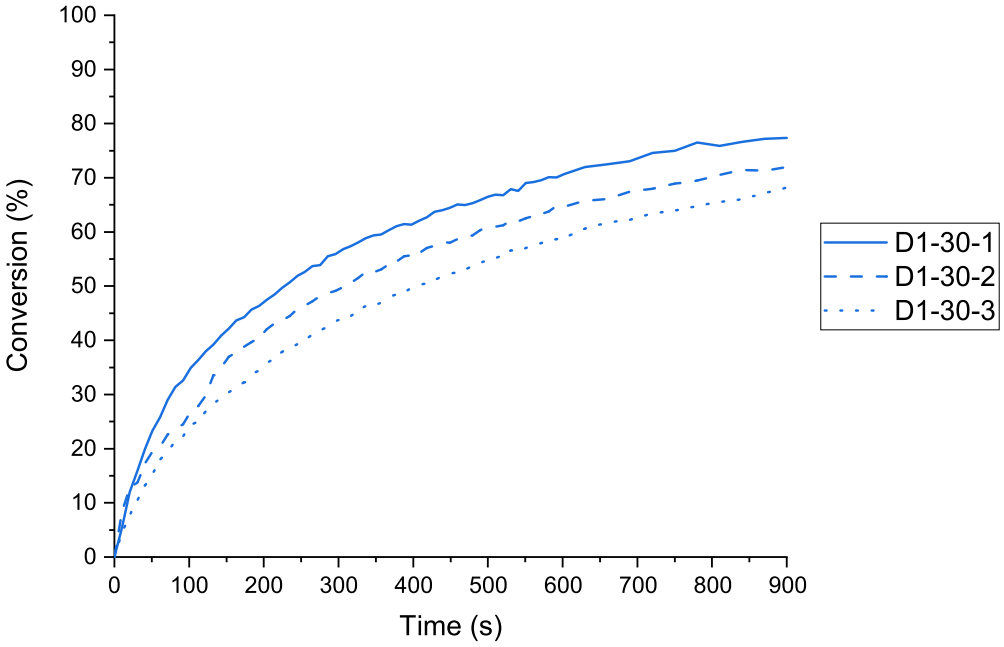

Figure 5.48: Conversion over time for MOF-808-D1-30.

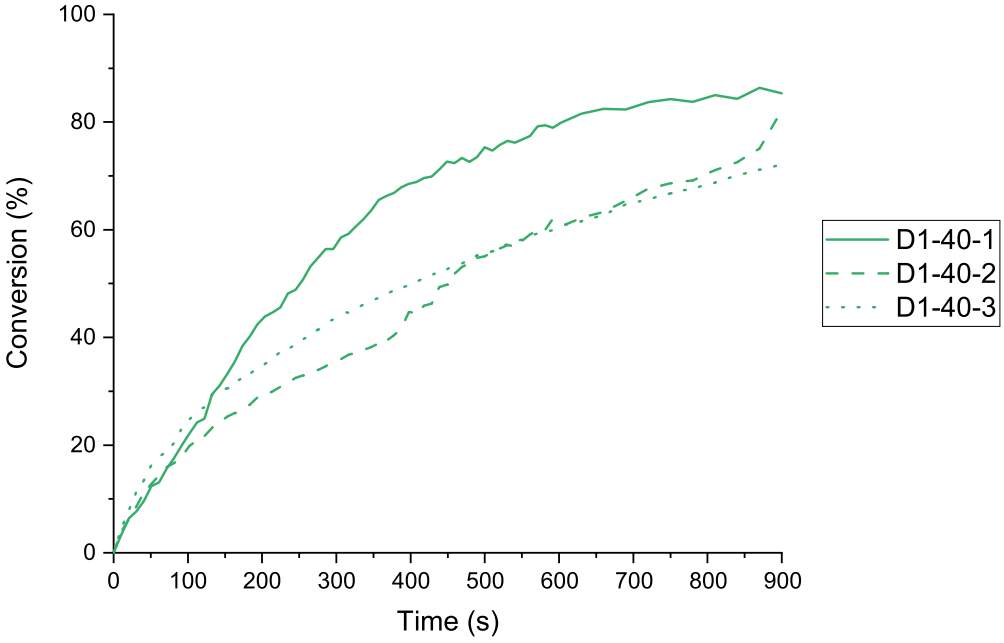

Figure 5.49: Conversion over time for MOF-808-D1-40.

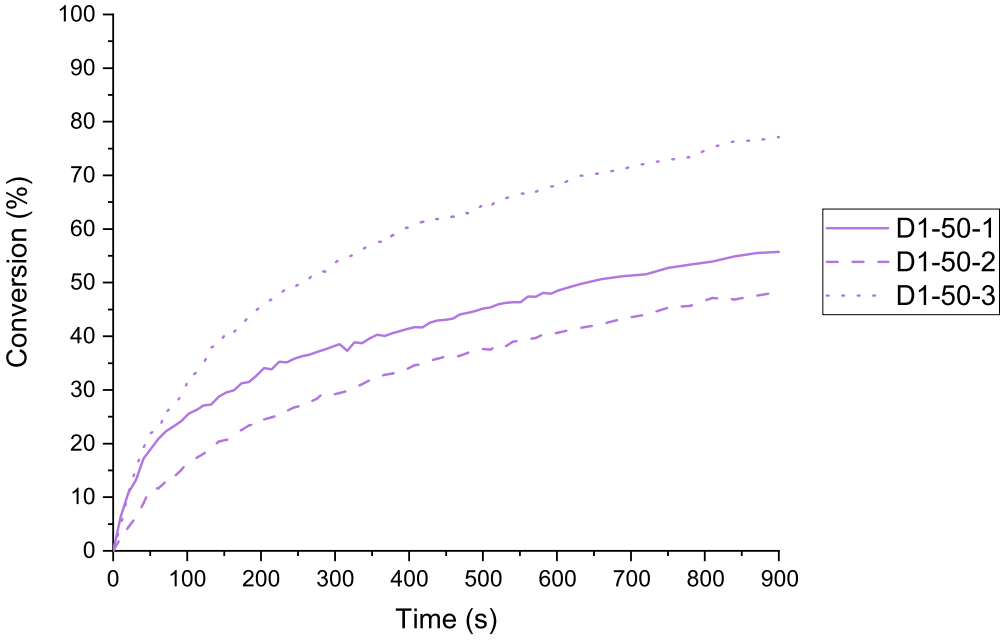

Figure 5.50: Conversion over time for MOF-808-D1-50.

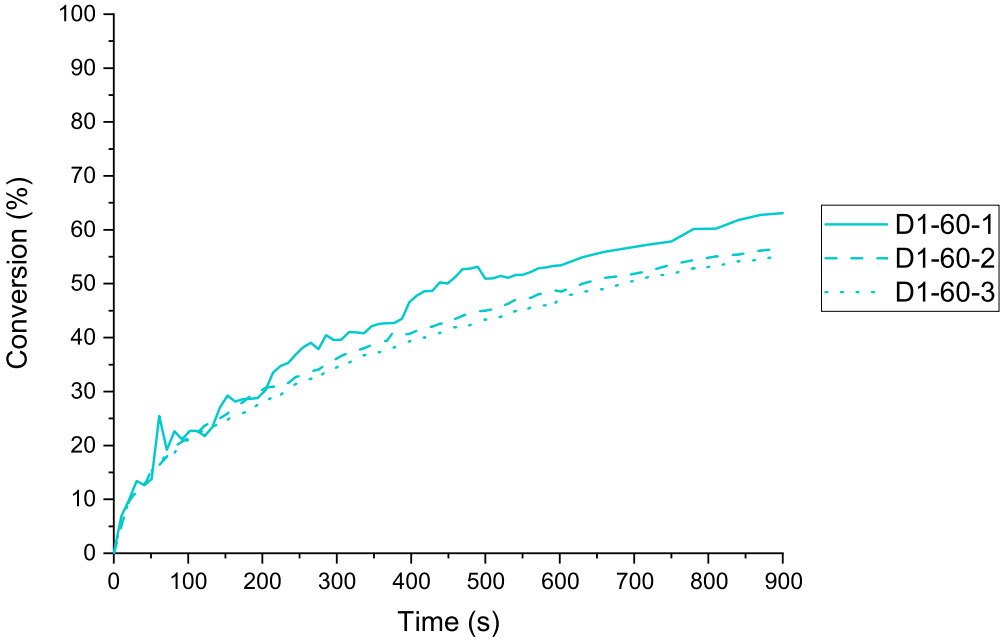

Figure 5.51: Conversion over time for MOF-808-D1-60.

Chapter 6

MOF-composite materials

6.1 Aims

The aim of this Chapter is to prepare MOF-composite materials that retain catalytic properties to successfully hydrolyse the nerve agents simulant DMNP.

MOF-808 is chosen for this study as it is a well known MOF, easy to synthesise, and shows one of the fastest catalytic rates for the catalytic hydrolysis of nerve agents and simulants. The fabrics chosen for investigation include polyethylene terephthalate (PET), polypropylene, cotton, silk and nylon.

Multiple synthesis routes will be investigated: solvothermal, room temperature, sono-chemical and silane coupling, in order to identify the most promising approach to forming successful MOF-composite catalysts. These will be evaluated through MOF loading, stability and catalytic performance. All composite materials will be characterised through PXRD, q-NMR spectroscopy and SEM. Catalysis will be carried out in-house in the solution state and monitored by *in-situ* UV-Vis.

6.2 Introduction

Zr-MOFs have shown great promise as catalysts for the hydrolysis of nerve agents and simulants, however, using MOF powders is only suitable for stockpile destruction. In order for MOFs to find success in protective equipment such as uniforms and masks they must be integrated into fabrics and polymers, whilst retaining adsorptive and catalytic properties.

Several methods have been investigated for the preparation of MOF-composites with the aim to integrate the MOF into the fabric or polymer with good adhesion and without aggregation. Atomic layer deposition (ALD) has been widely used to coat nano-fibres with a thin metal oxide layer that acts as a nucleation site for MOF growth.[1–3] This method has been used successfully to coat polypropylene with a dense, uniform layer of UiO-66-NH_2 which demonstrated catalytic activity for the hydrolysis of DMNP.[4]

Another method used in the preparation of MOF-composite materials is electrospinning where MOF particles are incorporated within fibres and spun to form large mat structures.[5–7] This method has also been successful in incorporating UiO-66 into polymers, which can be used as a protective layer and catalyst against the nerve agent simulant DFP.[8] Both of these methods produce catalytically active materials successfully, however, alternative methods that are simpler, and more environmentally and economically friendly are continued to be sought after.

One focus in this area is on finding synthesis routes that do not incorporate binders, as many are not stable within the catalysis conditions, or hinder the rate. One study synthesised a MOF-nylon composite through postsynthetic polymerisation; UiO-66-NH_2 was incorporated into PA-66 fibres as the polymer formed through amide bond formation between the amine on the MOF and the carbonyl on the monomer. This material showed catalytic activity for the hydrolysis of DMNP.[9] Another, more economical method has recently been reported, where a solution-based, template-free synthesis method successfully incorporated MOF-808 into polyester fibres. This material showed the highest catalytic activity for the hydrolysis of DMNP and soman seen for to-date for these composite materials.[10]

A lesser studied technique to form MOF-composite materials is the use of silane agents as a binder between the MOF and the chosen material. This method is widely used to link inorganic and organic materials such as polymers to glass or to create mixed-metal membranes with MOFs.[11–13] Structures of silane agents that have been used to bind inorganic materials to polymers are found in Figure 6.1.[14]

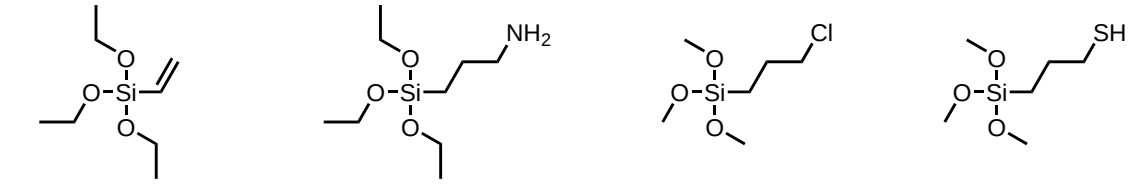

Figure 6.1: Structures of silanes used as binders in the preparation of fibre/polymer composites.

The silanes work by binding to SBUs within the MOF structure through alkoxy groups on the silane to form strong M−O−Si bonds. The remaining functional group on the silane can then interact with a material of choice through covalent or hydrogen bonding.[13] This method has been used to form Zr-MOF composite materials by immersing UiO-66-NH_2 treated with 3-chloropropyltrimethoxy silane in solution with silk. This material displayed an impressive uptake of As(III) compared to the MOF or fabric.[15]

The majority of research on MOF-composite materials for the catalytic degradation of nerve agents has focused on UiO-66 derivatives introduced into polymers such as poly(methylmethacrylate), polyacrylonitrile and polyvinylpyrrolidone.[5,16,17] The use of polyethylene terephthalate (PET) has also been investigated with MOF-808 as well as UiO-66.[10] The use of fabrics for this application have also been investigated such as silk, cotton and nylon with a range of Zr-MOFs.[9,18–20]

In this study the materials PET, cotton, silk and nylon were chosen alongside MOF-808 to form a range of MOF-composite materials. These fabrics were chosen due to the range of structures and functionality present within each material [Figure 6.2]. A range of synthesis routes were chosen: solvothermal, sonochemical and silane coupling, in order to determine if the structure of each

material has an optimum synthesis method for this application.

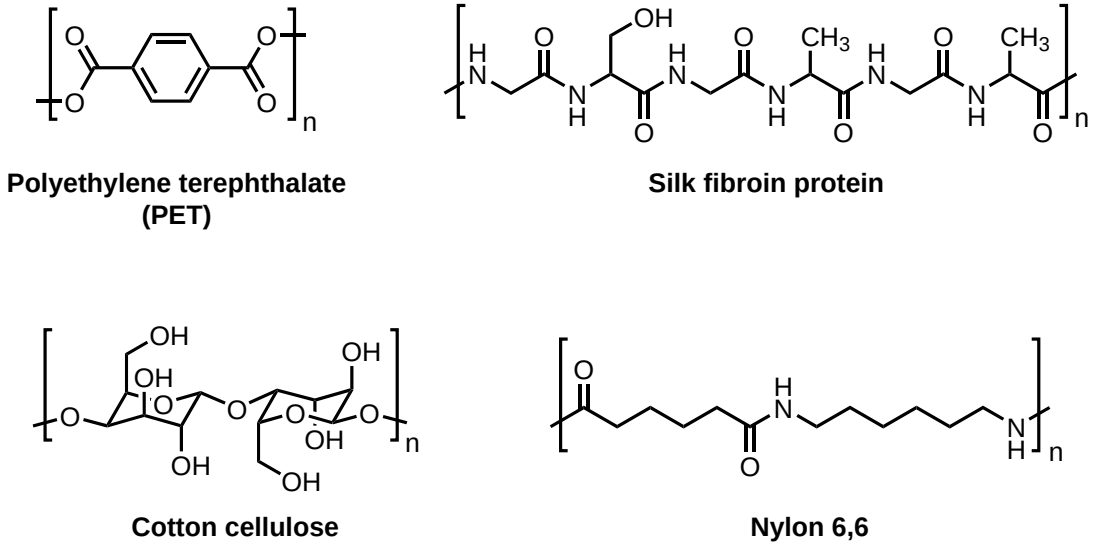

Figure 6.2: Chemical structures of materials chosen for the preparation of MOF-composite samples.

6.3 Experimental

6.3.1 MOFs

MOF-808-AA

Zirconium(IV) oxynitrate hydrate (0.40 g, 1.50 mmol) and 1,3,5-benzenetricarboxylic acid (0.16 g, 0.75 mmol) were suspended in a solution of water (6 mL) and glacial acetic acid (12 mL). The resulting solution was sonicated for 5 mins and then refluxed for 48 hr. The precipitate was washed with 2 x 15 mL portions ethanol over 2 days then collected via centrifugation (8000 rpm, 10 mins) to give a white solid. The product was activated under vacuum at 120 °C for 24 hr.

MOF-808-FA

Zirconium(IV) oxynitrate hydrate (0.40 g, 1.50 mmol) and 1,3,5-benzenetricarboxylic acid (0.16 g, 0.75 mmol) were suspended in a solution of water (6 mL) and formic acid (12 mL). The resulting solution was sonicated for 5 mins and then refluxed for 48 hr. The precipitate was washed with ethanol (2 x 15 mL) over 2 days then collected via centrifugation (8000 rpm, 10 mins) to give a white solid. The product was activated under vacuum at 120 °C for 24 hr.

Zr_6-oxo cluster

Zirconium(IV) chloride (2.00 g, 8.40 mmol) was dissolved in a mixture of acetic acid (15 mL) and isopropanol (25 mL). The solution was refluxed at 120 °C for 1 hr. The precipitate was washed with acetone (2 x 10 mL) and dried at 60 °C overnight to afford the product as a white solid.

MOF-808-RT

Pre-prepared Zr_6-oxo cluster (0.60 g, 0.43 mmol) was dissolved in formic acid (3 mL). A solution of 1,3,5-benzenetricarboxylic acid (0.15 g, 0.71 mmol) and water (5 mL) was added and stirred at room temperature for 48 hr. The resulting precipitate was washed with water (1 x 40 mL) and ethanol (2 x ethanol) over 3 days. The product was collected via centrifugation (8000 rpm, 10 mins) to give the product as a white solid. The product was activated under vacuum at 120 °C for 24 hr.

6.3.2 Composite materials

The following composite materials synthesis was carried out by A. Franchi as part of a Chemistry MChem (Hons) project.

Pre-treatment of all fabrics was carried out by washing thoroughly in de-ionised water and dried at 60 °C overnight.

For the silk fabric a de-gumming process was carried out based on the procedure by Feng *et al.*[21]. The silk fabric was submerged in a solution of aqueous sodium carbonate (0.05% w/w) and heated to 90 °C for 30 min. The silk was then washed with de-ionised water. This process was repeated three times. The fabric was dried overnight at 50 °C.

FABRIC-MOF808-TFA

This procedure is based upon the reported method by Ma *et al.*[10]. Zirconyl(IV) chloride octahydrate (1.45 g, 4.50 mmol), 1,3,5-benzenetricarboxylic acid (0.42 g, 2.00 mmol) and trifluoroacetic acid (10 mL), water (20 mL) and the chosen fabric (0.10 g) was added to a Teflon-lined autoclave. After sonication for 30 min the autoclave was placed in an oven at 100 °C for 2 hr. Once cooled, the fabric was transferred to a hydrochloric acid/acetone solution (100 mL, 1:99 v/v) and heated to 50 °C for 24 hr. The fabric was subsequently washed with water (2 x 50 mL), acetone (3 x 50 mL) then activated under vacuum at 100 °C for 24 hr.

FABRIC-MOF808-RT

Pre-prepared Zr_6-oxo clusters (0.6 g, 0.43 mmol) were dissolved in formic acid (3 mL). To this solution, water (5 mL), 1,3,5-benzenetricarboxylic acid (0.15 g, 0.71 mmol) and the chosen fabric (0.20 g) was added. The mixture was stirred at room temperature for 48 hr. The fabric was washed with water (1 x 40 mL) and ethanol (2 x 40 mL) then dried at 50 °C overnight.

FABRIC-MOF808-SC

Pre-prepared Zr_6-oxo clusters (0.6 g, 0.43 mmol) were dissolved in formic acid (3 mL). To this solution, water (5 mL), 1,3,5-benzenetricarboxylic acid (0.15 g, 0.71 mmol) and the chosen fabric (0.20 g) was added. The mixture was sonicated in an ultrasound bath for between 1 and 60 min. The fabric was washed with water (1 x 40 mL) and ethanol (2 x 40 mL) then dried at 50 °C overnight.

SLK-MOF808-Si(MOF)

Pre-prepared MOF-808-RT (0.10 g, 0.07 mmol) was added to methanol (100 mL) and sonicated for 15 min. 3-aminopropyltriethoxy silane (0.46 μL, 0.02 mmol) was added and the mixture was refluxed at 90 °C for 48 hr. Silk (0.20 g) was soaked in ethanol (50 mL) for 1 hr then both silk and ethanol was added to the cooled MOF/silane solution. The resulting solution was refluxed at 90 °C for 48 hr. Once cooled, the silk was washed with methanol (1 x 20 mL), ethanol (1 x 20 mL) and diethyl ether (1 x 20 mL). The fabric was then dried at 60 °C for 24 hr.

FABRIC-MOF808-Si

The chosen fabric (0.20 g) was soaked in ethanol (50 mL) for 1 hr. Methanol (50 mL) and 3-aminopropyltriethoxy silane (0.46 μL, 0.02 mmol) was added and the mixture was refluxed at 90 °C for 48 hr. Pre-prepared MOF-808-RT (0.10 g, 0.07 mmol) was added to methanol (50 mL) and sonicated for 15 min. This solution was added to the fabric/silane solution and refluxed at 90 °C for 48 hr. Once cooled, the fabric was washed with methanol (1 x 20 mL), ethanol (1 x 20 mL) and diethyl ether (1 x 20 mL). The fabric was then dried at 60 °C for 24 hr.

6.3.3 Catalysis

Before catalysis measurements all materials were activated under vacuum at 120 °C for 24 hr and stored in flame-sealed vials until measurements were carried out.

Catalytic hydrolysis of dimethyl *p*-nitrophenylphosphate

This procedure is based upon the reported method by Mondloch *et al.*[22]. A buffer solution of *N*-ethylmorpholine (100 mL, 0.45 M, pH 10) was prepared. A sample of composite material (0.10 g) was added to an aqueous solution of dimethyl *p*-nitrophenylphosphate (5 mL, 0.25 mM stock solution of DMNP in *N*-ethylmorpholine buffer (0.45 M, pH 10)). The rate of DMNP hydrolysis was measured using an *in-situ* UV-Vis probe monitoring the product *p*-nitrophenoxide absorbance at 407 nm.

6.4 Characterisation Methods

6.4.1 Quantitative ^{1}H-NMR spectroscopy

Quantitative NMR spectroscopy is a useful technique that can be used to identify and quantify the amount of a substance within a sample. We use this method in order to calculate the amount of MOF-808 present within prepared MOF-composites. These calculations are based on previous work that uses the same methods to calculate the purity of a sample.[23]

Quantitative ^{1}H-NMR spectroscopy was carried out to determine the loadings of each synthesised composite sample using an internal standard of maleic acid. An internal standard is needed in this case as the acid-digested materials (PET, cotton, silk, nylon) produce many signals in the ^{1}H-NMR and cannot be used for comparison. Maleic acid is chosen for this application as the proton peak exhibited does not overlap with any fabric peaks, or the BTC peak we are interested in that is representative of the MOF-808 in the sample. The samples were prepared for ^{1}H-NMR analysis as follows.

The synthesised MOF-composite sample (5 mg) was dissolved in concentrated H_2SO_4 (30 μL) by stirring for 16 hrs. To this DMSO$-d_6$ (600 μL) and maleic acid (1 M, 30 μL) were added.

From the BTC and maleic acid ^{1}H-NMR spectroscopy data the loadings can be calculated using Equation 6.1.

$$\mathrm{BTC}[\%] = \frac{n_{IS} \cdot \mathrm{Int}_t \cdot \mathrm{MW}_t \cdot m_{IS}}{n_t \cdot \mathrm{Int}_{IS} \cdot \mathrm{MW}_{IS} \cdot m_S} \cdot P_{IS} \tag{6.1}$$

Where n is the number of protons, Int is the integral value, MW is molecular weight, m is the mass, IS is the internal standard, t is the target species, and P is the purity.

As we can calculate the percentage of the linker BTC that is present in the NMR, we can then calculate the percentage of MOF-808 present. The assumption is made that all BTC present is due to MOF-808 rather than unreacted starting material and the MOF-808 is present in the pristine hydrated form $Zr_6O_4(OH)_4(HCOO)_6[(C_6H_3)(COO)_3]_2$.

6.5 Results & Discussion

6.5.1 MOF-808 synthesis

We discuss here a robust synthesis method for MOF-808 that will be able to work with the materials chosen. Due to the nature of the materials, solvents commonly used for the synthesis of MOF-808 such as DMF are not suitable. Therefore, synthesis methods with less harsh solvents must be found. The most ideal synthesis would be to use solvents such as ethanol or water. Some hydrothermal syntheses have been reported for Zr(IV) MOFs in literature, however, these are mainly focused on UiO-66.[24]

Attempts to develop a one-step hydrothermal synthesis of MOF-808 was carried out using a higher mol ratio of Zr to linker and using a large amount of modulator such as acetic acid or formic acid. The Zr source was also changed from $ZrCl_4$ to $ZrO(NO_3)_2$ as this has been more widely reported in the hydrothermal synthesis of UiO-66.[24] Many of these attempts were unsuccessful.

One synthesis, using a large excess of acetic acid as modulator in a water based synthesis, did result in a crystalline white power with a PXRD pattern that was in good agreement with the MOF-808 simulated pattern [Figure 6.3].

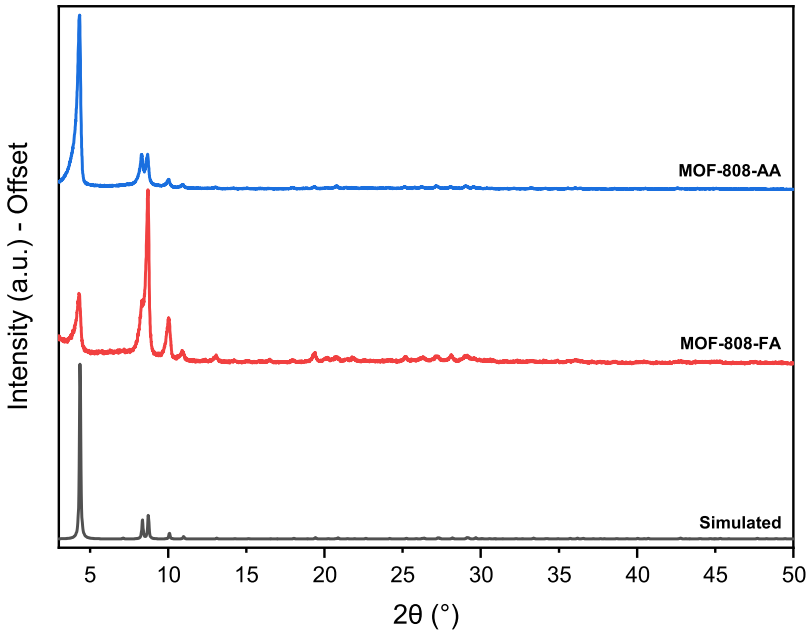

Figure 6.3: PXRD of MOF-808 samples synthesised through hydrothermal synthesis methods.

This synthesis was repeated using the same conditions but formic acid as the modulator instead of acetic acid. This synthesis also produced a PXRD pattern with peaks matching the simulated MOF-808. However, some broadening of the peaks in comparison to the acetic acid synthesis can be observed.

Another method that has been reported for the hydrothermal synthesis of MOF-808 is using a two-step method where pre-prepared Zr-oxo clusters are reacted with the linker in an aqueous solution.[25] Zr-oxo clusters were prepared as outlined above in Section 6.3. Confirming the identy of these clusters can be challenging as each cluster is relatively small when compared to a MOF structure, and this tends to give broad PXRD peaks. The PXRD for the synthesised Zr-oxo cluster does show one sharp peak and is distinguishable from the $ZrCl_4$ starting material therefore it was taken forward for MOF synthesis.

The pre-prepared Zr-oxo clusters were then added to a solution containing the BTC linker and stirred at room temperature for 7 days. This synthesis method was successful and resulted in the MOF-808-RT product [Figure 6.4].

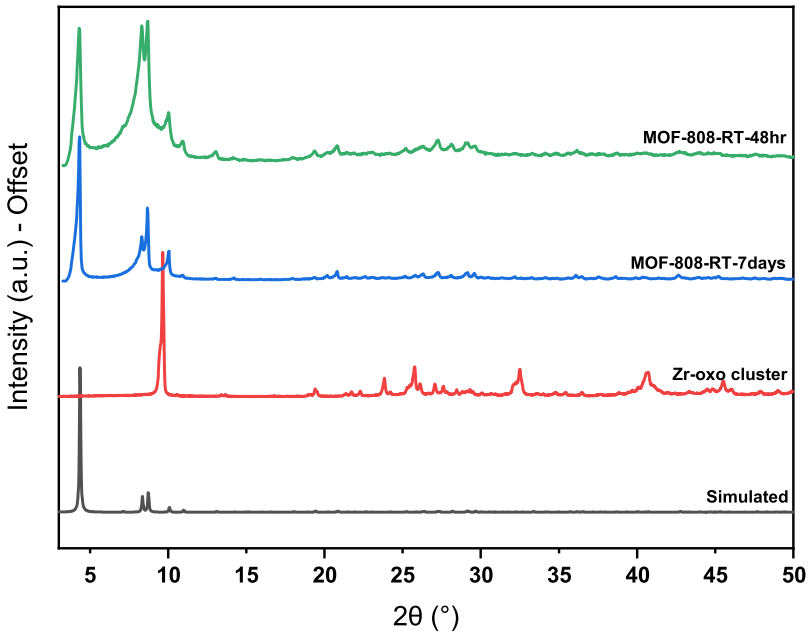

Figure 6.4: PXRD of MOF-808 samples synthesised through hydrothermal synthesis methods.

This synthesis is also easily scalable as tens of grams of the Zr-oxo cluster can be synthesised in one batch. This method is also preferable from the one-step process as it is carried out at room temperature so there are no further concerns

about selected fabrics not withstanding high temperatures.

As the room temperature synthesis of MOF-808, with water as the solvent, was successful and easy to scale this MOF-808 synthesis was chosen to be used in the MOF-composite synthesis where appropriate.

6.5.2 MOF composite synthesis

Upon successful synthesis of MOF-808 using methods that are compatible with the materials chosen, MOF-composites synthesis methods were investigated. The materials chosen to form the composites were polyethylene terephthalate (PET), polypropylene (PP), cotton, silk, and nylon. The polymers PET and PPE have previously been investigated for this application.[10] The other fabrics chosen are already used widely in clothing which may prove beneficial for the application of MOF-composites as protective clothing. To date, there is little work in the literature using cotton, nylon or silk for MOF-composite materials.[26]

6.5.2.1 Hydrothermal synthesis

The first synthesis method explored is hydrothermal synthesis. This method is commonly seen in the preparation of MOFs and MOF-composites as it is a straightforward synthesis and without harsh solvents, should not damage the fabrics chosen.

In order to compare synthesis methods, a literature procedure was carried out as reported by Ma *et al.*[10] and is outlined in subsection 6.3.2. This synthesis method is carried out with water as the solvent and trifluoroacetic acid (TFA) as the modulating agent. PET and PP were used as the composite materials for the initial attempts.

Both polymers were intact following the reaction and subsequent washing steps. PXRD was carried out in order to confirm the presence of MOF-808 on the fabrics. It can be seen in Figure 6.5 that for the sample PET-MOF808-TFA there are two small peaks indicated by (*) that align with the expected peaks for MOF-808 and are not present in the PET-blank samples. This suggests the experiment was successful as in the original literature.[10]

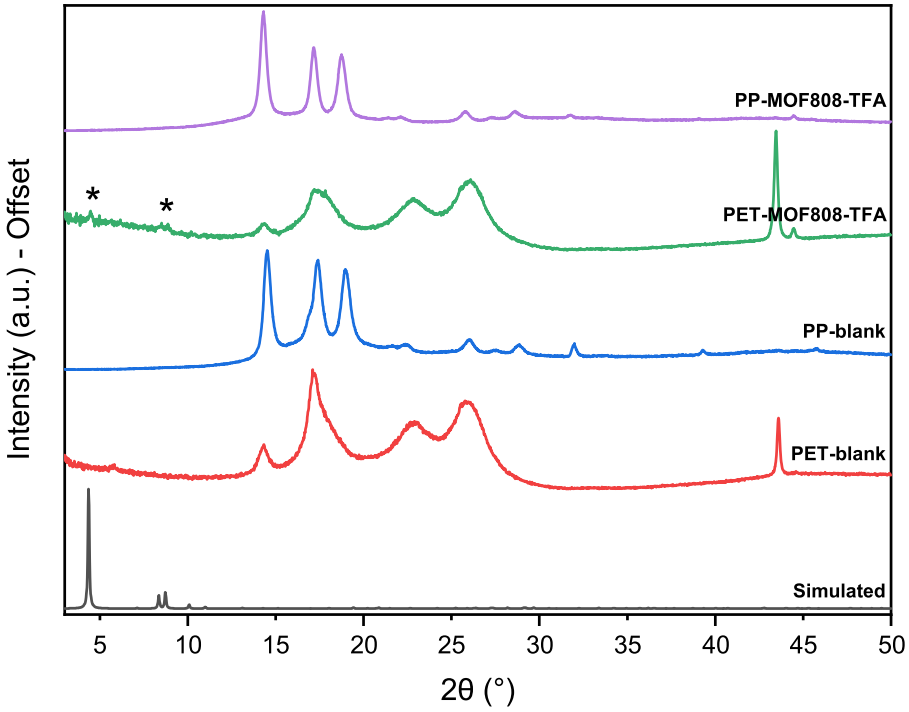

Figure 6.5: PXRD of polymer-MOF-808 samples synthesised through hydrothermal synthesis methods.

The characteristic MOF-808 peaks are not present in the PXRD of PP-MOF808-TFA and no additional peaks are present when compared to the PP-blank sample. This suggests that no MOF has been synthesised on this polymer. The difference in the chemical structures of the polymers may explain the difference in reactivity. PET is made of repeating $C_{10}H_8O_4$ units whereas PP is formed of repeating C_3H_6 units. The lack of any functional groups in the case of PP may prevent the MOF-808 from forming, whereas in the PET case, the carboxylic groups may help the formation of the MOF structure. For this reason PP was no longer used in further syntheses. Instead the polymer nylon was chosen as an alternative as it contains peptide bonds which may encourage MOF synthesis and incorporation onto the surface.

Following the success of the PET sample with this synthesis method, other fabrics were chosen for the formation of the MOF-808-composite. Cotton (CTN), silk (SLK) and nylon (NYL) were all used for this synthesis method with the same procedure carried out as for PET in Section 6.3. Following the synthesis the cotton sample became brittle and torn. A PXRD pattern was collected for the CTN-MOF808-TFA sample [Appendix Figure 6.53]. No MOF-808 peaks can be seen in the PXRD pattern, and due to the lack of durability of the sample, this

sample was not deemed a success.

The silk and nylon fabric samples both dissolved within the synthesis, therefore no sample was obtained and no further analysis could be carried out for the TFA synthesis. The lack of success with these materials is likely due to the high temperature and the use of a large amount of TFA in the synthesis. Due to these issues, the room temperature synthesis that was designed for the MOF-808 synthesis as outlined above, was used for further hydrothermal syntheses.

The fabrics PET, cotton, silk and nylon were used in the room temperature synthesis method outlined in subsection 6.5.1. This synthesis uses pre-prepared Zr-oxo clusters which are then added to a solution of BTC and acetic acid. To this solution a swatch of material was added. Upon completion of the synthesis all samples remained in-tact and some MOF formation was seen in solution for all samples. A PXRD was collected for each sample [Figure 6.6].

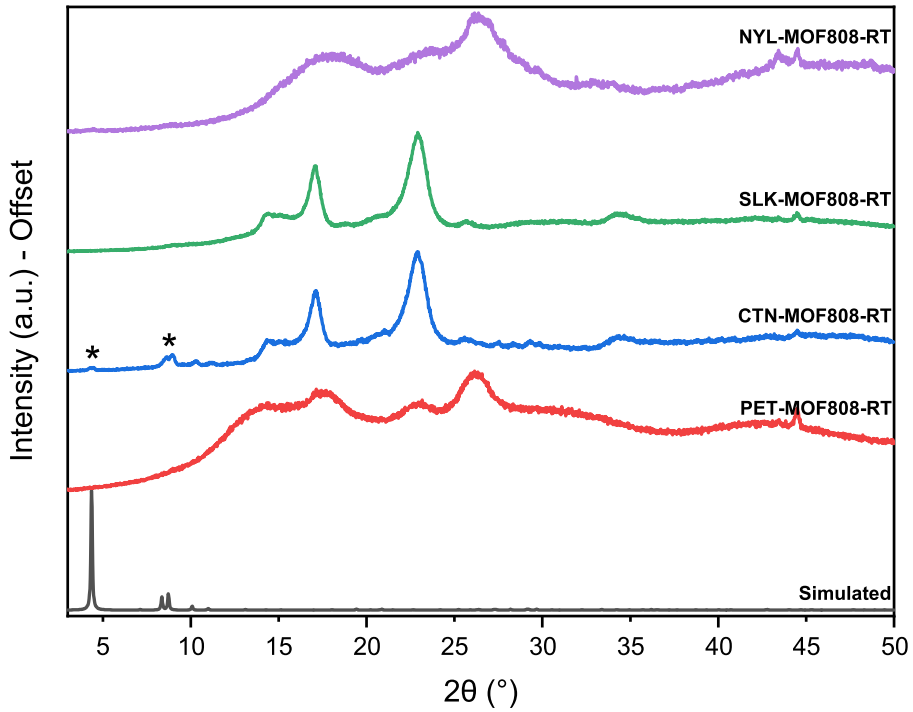

Figure 6.6: PXRD of polymer-MOF-808 samples synthesised through room temperature synthesis methods.

From the PXRD, CTN-MOF808-RT is the only sample that exhibits the characteristic MOF-808 peaks, indicated by (*). This gives evidence that this synthesis method is successful for this material. However, the absence of MOF-808 peaks in the PXRD may also be due to only very small particles, in small quantities

in relation to the amount of fabric being deposited on the materials. Other characterisation techniques such as IR and SEM can be used to identify if any MOF-808 has been successfully synthesised on the the other fabrics.

IR spectroscopy is a useful technique for these materials as we can easily identify the characteristic MOF-808 O-H bend at 1370 cm^{-1} [Figure 6.7, grey bar]. This peak is prominent in all samples that have undergone the room temperature synthesis. For the blank fabric samples this peak is not present, indicating that the MOF-808 structure is only present after the synthesis, even if it cannot be identified through PXRD.

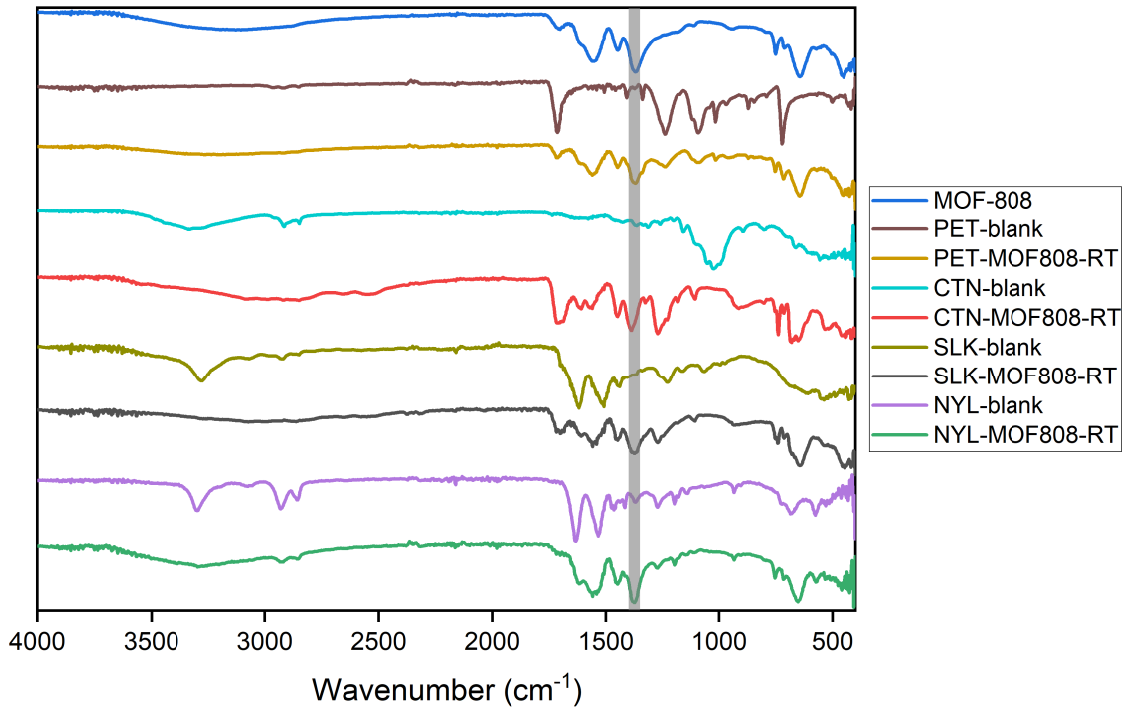

Figure 6.7: IR spectra of all MOF808-RT samples compared to blank samples. MOF-808 O-H bend highlighted with grey bar.

SEM images were collected in order to compare the visible difference between blank and room temperature synthesis samples. Images in Figure 6.8 highlight differences between the blank fabric samples and the MOF808-RT composite samples.

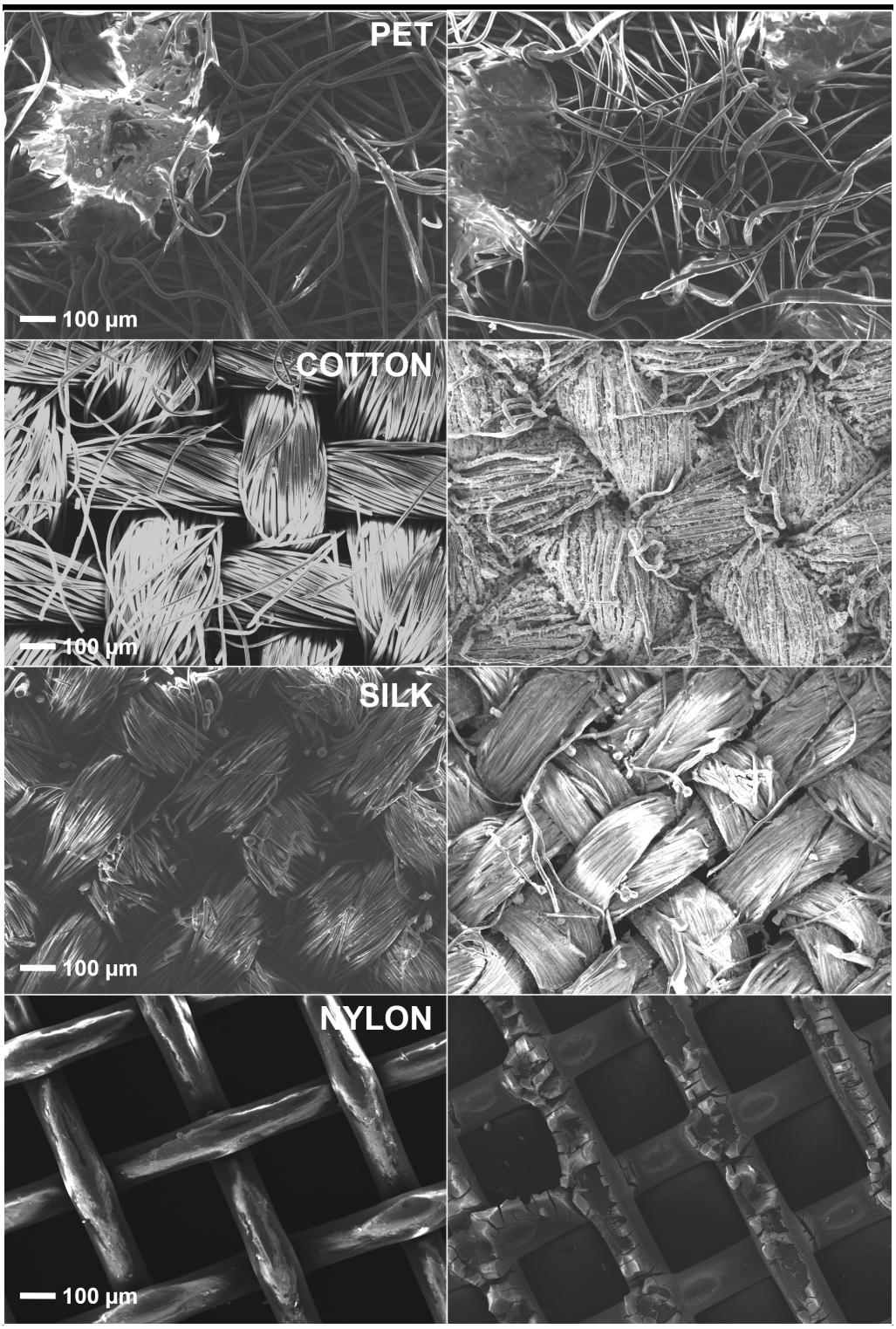

Figure 6.8: SEM image of all materials before and after rt synthesis. In order from top, left to right: PET-blank, PET-MOF808-RT, CTN-blank, CTN-MOF808-RT, SLK-blank, SLK-MOF808-RT, NYL-blank, NYL-MOF808-RT.

In the case of CTN-MOF808-RT and NYL-MOF808-RT that there is a clear difference in the SEM images compared to the respective blank samples. Both show compositional changes to the surface which suggest deposition of MOF-808 has occurred. These differences are less apparent for the PET-MOF808-RT and SLK-MOF808-RT samples, however, bright areas on the samples due to charging is likely due to Zr metal being present.

Further SEM images, using the back-scattered secondary electron (BSE) detector, were captured in order to better determine compositional change. The PET-MOF808-RT sample shows small particles deposited across the sample [Figure 6.9]. It is clear that there is compositional change when looking at individual fibres of the PET as there is a clear difference between the light and dark areas in the images. Although particles have been deposited, there are not of uniform size and are not spread across the sample in a homogenous manner.

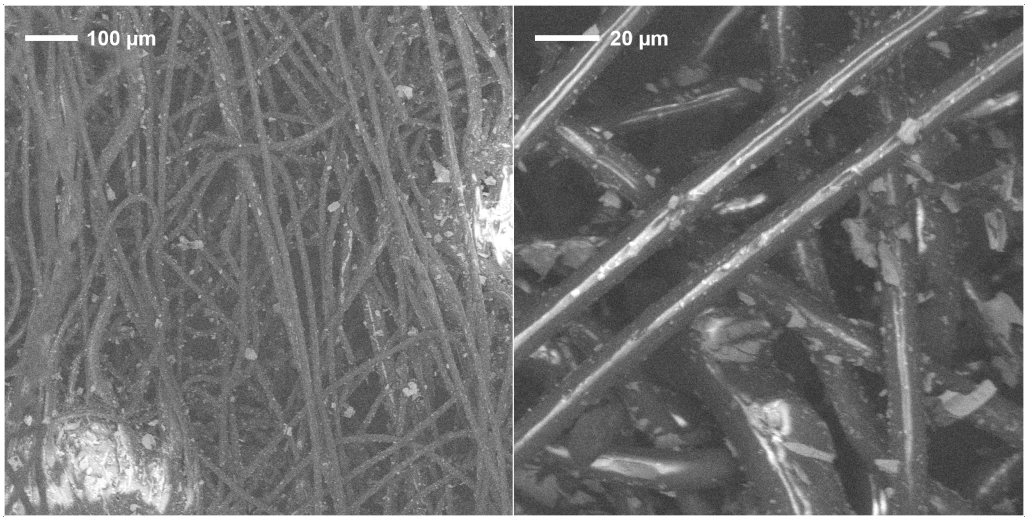

Figure 6.9: SEM image of PET-MOF808-RT sample using back scattered detector to show compositional change between the fabric and MOF-808.

To determine if the particles shown in the SEM images are MOF-808, EDS mapping was carried out. It can be seen in Figure 6.10 that Zr is present in the sample, and looks to be focused in small particles across the PET as suggested by the BSE images. There are also areas where no Zr or O are present in the sample which suggests that only the outer strands of the PET shows deposition of MOF-808.

Using the BSE detector to examine compositional change for the CTN-MOF808-

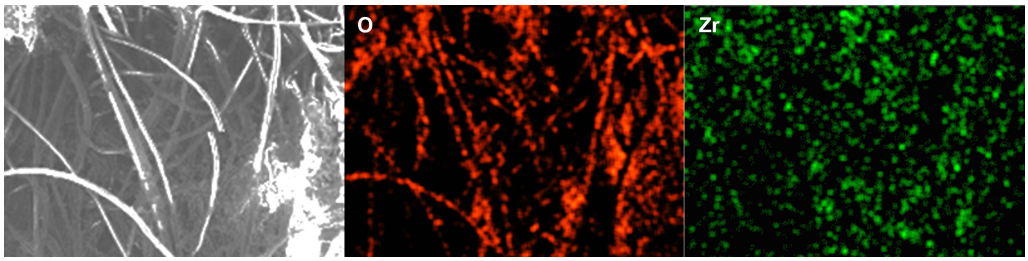

Figure 6.10: EDS mapping of PET-MOF808-RT sample showing the presence of Zr across the sample.

RT sample, there is clearly material deposited across the strands of the material [Figure 6.11]. When focusing on a single strand of the cotton material, small clusters of agglomerated MOF has been deposited. Some smaller particles are also visible across the sample.

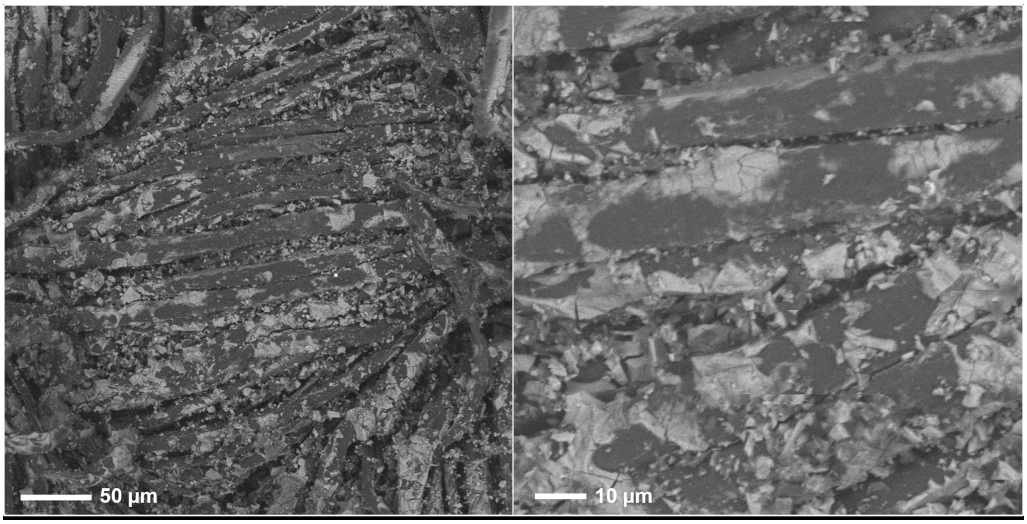

Figure 6.11: SEM image of CTN-MOF808-RT sample using back scattered detector to show compositional change between the fabric and MOF-808.

Using EDS to map the surface elemental composition of CTN-MOF808-RT, it can be seen the all the constituent elements of MOF-808 are present [Figure 6.12]. It also confirms that MOF-808 has been well dispersed across the samples. The darker areas are likely due to the woven nature of the fabric not allowing the deposition of MOF-808 less accessible areas. When comparing to the PET-MOF808-RT sample we look to have a greater dispersion of Zr across the entire sample.

The SLK-MOF808-RT sample has a similar fabric structure to the CTN-MOF808-RT samples, however we seen a more homogenous coverage of the material

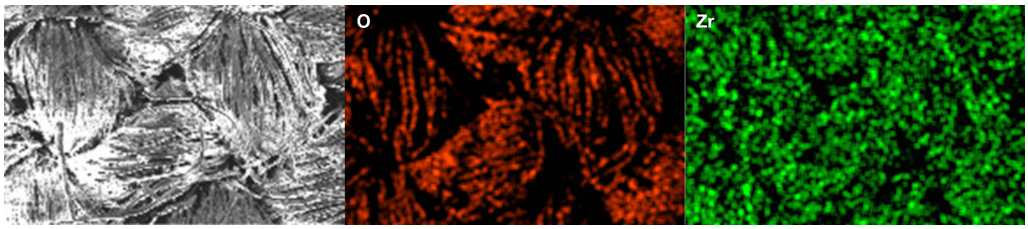

Figure 6.12: EDS mapping of CTN-MOF808-RT sample showing the presence of Zr across the sample.

in the BSE images [Figure 6.13]. There is little compositional difference across the fibres of the silk which suggests any individual particles seeming to have agglomerated to form a consistent layer of MOF-808.

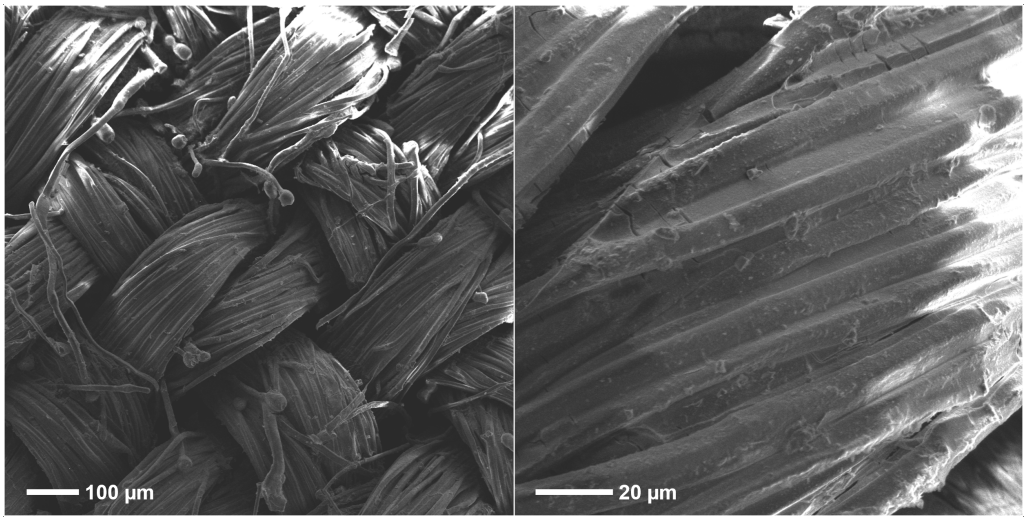

Figure 6.13: SEM image of SLK-MOF808-RT sample using back scattered detector to show compositional change between the fabric and MOF-808.

Using EDS mapping we can determine the elemental composition of the layer deposited in the SLK-MOF808-RT sample. The presence of Zr is confirmed across the sample, with some absences around the woven areas [Figure 6.14].

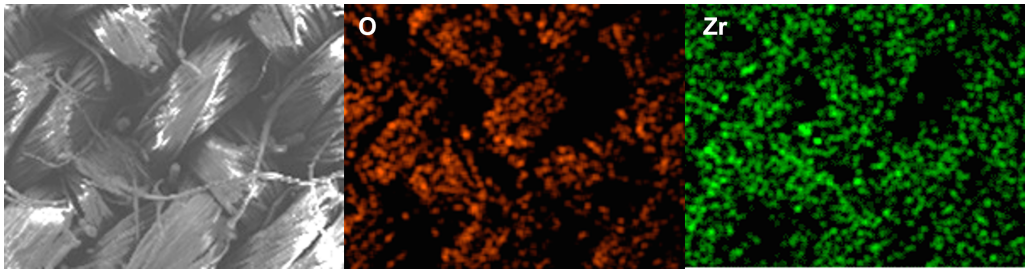

Figure 6.14: EDS mapping of SLK-MOF808-RT sample showing the presence of Zr across the sample.

Interestingly, the EDS shows the Zr areas are more disperse than they appear from the SEM-BSE images. This suggests that some of the layer present in not MOF-808, but instead other reagents not fully removed by the washing steps.

In the case of the NYL-MOF808-RT sample, the SEM images show that the structure of the nylon is very different to that of the silk and cotton [Figure 6.15]. The coverage of the MOF-808 deposition seems to be uniform across the fabric. Yet, if we look at the areas where the strands overlap, there are large areas free of MOF-808 coverage, this is likely due to loss of product when the material is folded and handled. These deposits on the strands are mostly agglomerates that form these large block-like areas.

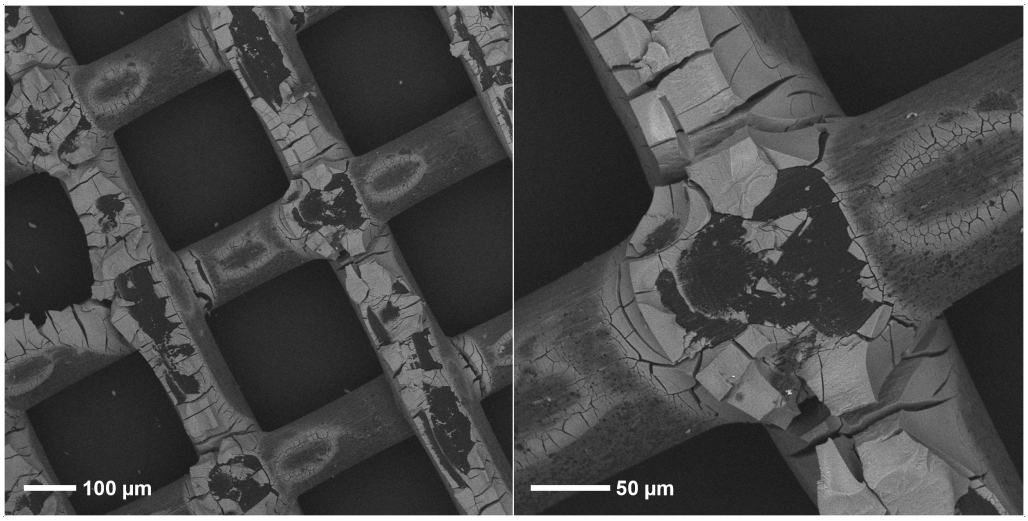

Figure 6.15: SEM image of NYL-MOF808-RT sample using back scattered detector to show compositional change between the fabric and MOF-808.

The EDS mapping of NYL-MOF808-RT proves that Zr is present across the material [Figure 6.16]. The distribution of the Zr also confirms the block-like structures are formed of agglomerated particles as the Zr has been detected in small particles across the strands. As in the case of the other fabric, there are darker regions where the material weaves below the other strands. This indicates that the MOF-808 is formed preferentially on the very surface of the materials.

Overall the SEM images confirm that MOF-808 has been deposited on all materials that were used in for the room temperature synthesis. From the combination of SEM and BSE images, and the EDS mapping, the PET-MOF808-RT sample seems to be the least successful using this method. Interestingly, PET is the

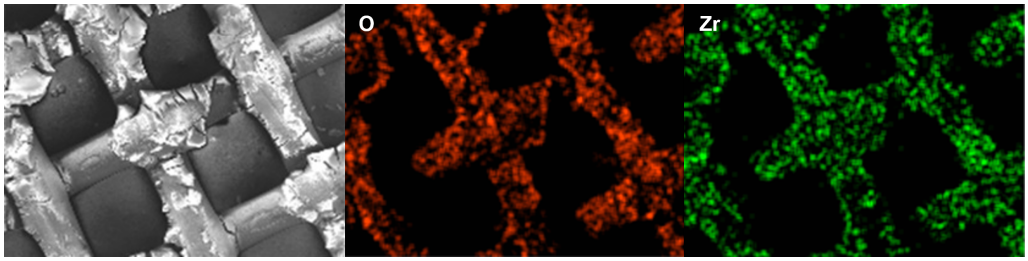

Figure 6.16: EDS mapping of NYL-MOF808-RT sample showing the presence of Zr across the sample.

only material that remained in-tact using the TFA room temperature method, therefore the addition of a stronger acid may be needed for more MOF-808 formation on this material. However, the nature of the strands being thin and non-uniformly woven throughout the sample may be the limiting factor in this synthesis.

IR and SEM can assist in identifying the presence of MOF-808, however, it cannot quantify the amount that has been deposited on the fabric; an important value to know for catalytic applications. Attempts to determine loadings were initially carried out using TGA. This method was not successful as the thermal decomposition of MOF-808 cannot be distinguished from the thermal decomposition of the materials both start decomposition at similar temperatures and the fabrics chosen do not fully decompose.

Quantitative-NMR (q-NMR) spectroscopy was instead used in an attempt to determine the loading of the room temperature MOF composite samples. The method used is outlined above in subsection 6.4.1, where the MOF-composite was dissolved in acid and an internal standard of maleic acid added. The integrals of the MOF-808 linker (BTC) to maleic acid peaks were used to determine the concentration of MOF in solution, and therefore the loading relative to the weight of the fabric. The loadings calculated for the RT-samples are given in Table 6.1.

The loadings calculated vary widely between materials. The PET-MOF808-RT has the highest loading at around 30 %, followed by SLK-MOF808-RT at abour 20 % loading. The other samples do not show as high a loading which is surprising given the amount of coverage seen from the SEM images, especially in the case of the NYL-MOF808-RT. One reason for this may be due to the Zr-oxo cluster having been deposited onto the fabric instead of the MOF being formed; this also

Table 6.1: Calculated loadings from q-NMR spectroscopy.

Sample	Loading (%)
PET-MOF808-RT	29.4
CTN-MOF808-RT	4.1
SLK-MOF808-RT	19.7
NYL-MOF808-RT	9.8

explains why the EDS shows the Zr present across the sample. This is also true in the case of the CTN-MOF808-RT sample which has the lowest loading of 4.1% despite the SEM shows substantial coverage across the material.

Due to the relatively low loadings that have been achieved using the room temperature synthesis, other methods were investigated in an attempt to increase this loading of MOF-808 on the chosen materials.

6.5.2.2 Sonochemical synthesis

Sonochemical synthesis was chosen as an alternative synthesis route as it is a fast and efficient method to form MOFs. It also has advantages of being environmentally friendly as the reaction is carried out at room temperature using water as the solvent. Sonochemical synthesis was carried out on all materials: PET, cotton, silk and nylon, in an attempt to deposit MOF-808 on the materials with shorter reaction time and higher loading when compared to the room temperature synthesis method.

Initially tests were carried out on silk to optimise the reaction time of this sonochemical synthesis. Silk was chosen as it showed relatively high loading in the RT-synthesis method discussed above, but it is more prone to damage during the synthesis than PET. Previously reported reaction times for sonochemical MOF syntheses tend to be on the order of minutes,[27] therefore to find the optimal reaction time the reaction was carried out as outlined in 6.3.2 with the time varied between 10 seconds to 1 hour.

Following the washing and drying procedures PXRD was carried out on all samples. The PXRD is generally inconclusive [Appendix Figure 6.54] so IR was instead used to identify MOF-808 on the silk [Figure 6.17].

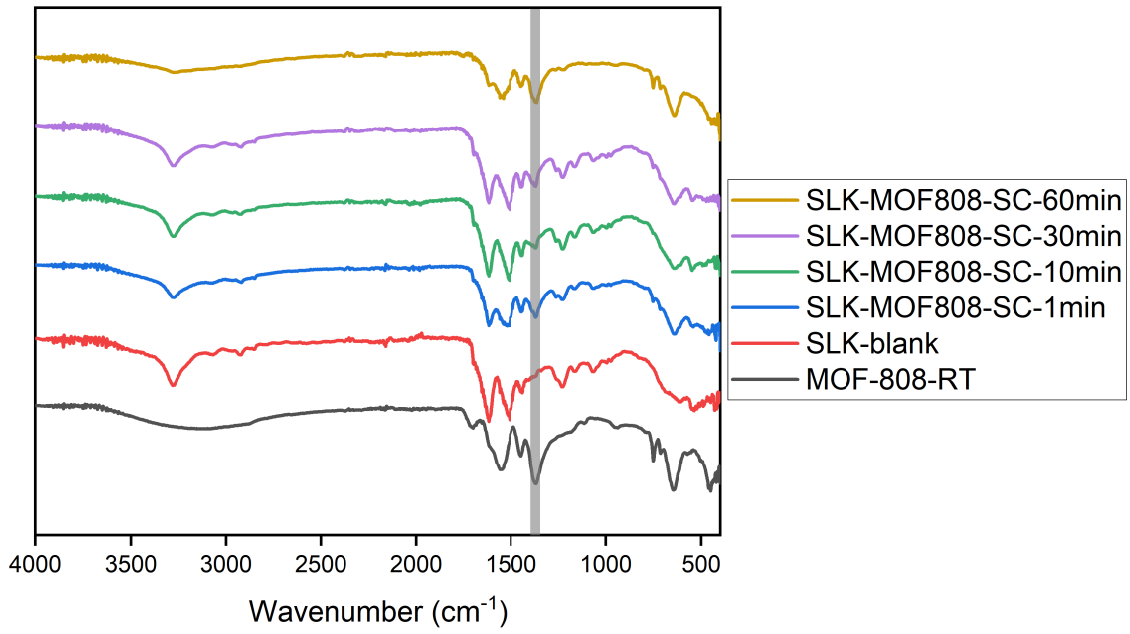

Figure 6.17: IR of SLK-MOF808-SC samples with various reaction times. MOF-808 O-H bend highlighted with grey bar.

From the IR presented we can see the emergence of the MOF-808 O-H bend in all of the samples [Figure 6.17, grey bar]. The characteristic signal is not present in the SLK-blank sample. The IR suggests that at all reaction times MOF-808 has been formed.

To determine the optimum reaction time we can estimate the loadings of the samples by weighing samples before and after the reaction has proceeded. All samples were thoroughly dried before being weighed and the calculated loadings are given in Table 6.2.

Table 6.2: Loadings estimated by weighing SLK-MOF808-SC samples before and after synthesis.

Reaction time (min)	Loading (%)
1	22.0
10	28.9
30	23.6
60	27.2

From the estimated loadings there is little deviation between 10 minutes, 30 minutes and 1 hour. However, we can see that samples with a reaction time of 1 minute or less have a marginally lower loading. As there is little difference between the higher reaction time loadings, 10 minutes was chosen as the optimum

reaction time for further composite material synthesis.

As the reaction time is relatively short, the reusability of the reaction solution was also investigated. In this case, after the inital 10 minutes, the silk fabric sample was removed and another blank silk samples was placed into the same solution. Using IR to identify the characteristic IR peak we can see the formation of MOF-808 after 8 swatches of silk have been reacted in the solution [Appendix Figure 6.55]. This is an important result for the potential scale up of this method as many samples can be prepared from one reaction solution.

Following the investigation of the sonochemical reaction using silk, the optimised synthesis was carried out using PET, cotton and nylon. All fabrics were in-tact after the sonochemical synthesis and no MOF-808 formation was observed within the synthesis solution; a benefit when compared to the room temperature synthesise discussed above.

The PXRD collected does not show the characteristic MOF-808 peaks for any of the samples so cannot be used to confirm the formation of MOF-808 [Appendix Figure 6.56]. As before, this is inconclusive as the MOF-808 may be present in quantities that cannot be detected with PXRD.

Instead IR can be used to establish if the MOF-808 O-H bend is present in the SC-samples. From Figure 6.18 the grey band shows that in all cases the MOF-808 is present. However, it should be noted that the peak is weaker for the PET sample which might suggest that less MOF-808 has been formed on the PET compared to the other materials used.

To further confirm that MOF-808 has been deposited through the sono-chemical synthesis, SEM images were captured to determine compositional changes to the fabric compared to the blank samples [Figure 6.20]. All materials are in tact after the synthesis, but the changes to the surface of the materials vary using the sonochemical synthesis method. At the scale shown in Figure 6.20 the PET-MOF808-SC and CTN-MOF808-SC samples both show a visible difference between the blank and MOF-808 sample. Some brighter areas in the SLK-MOF808-SC sample suggest some charging which is indicative of Zr present and suggests MOF-808 may have been formed. However, the NYL-MOF808-SC sample shows no discernable change from the blank sample.

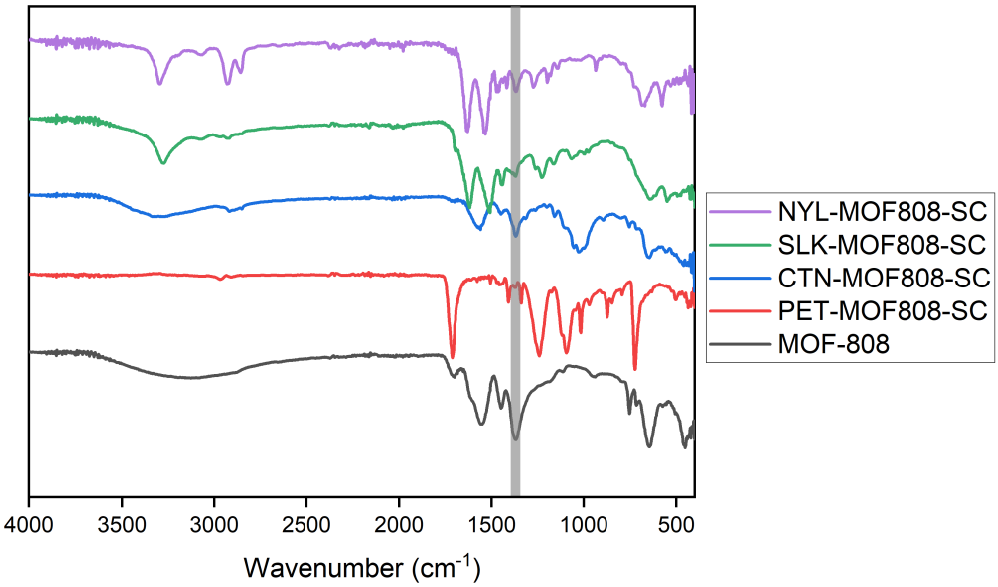

Figure 6.18: IR of SC-reactions carried out on all materials. MOF-808 O-H bend highlighted with grey bar.

The change in composition of these materials can be investigated using BSE images. For the PET-MOF808-SC sample there is no visible change between regions on the fabric [Figure 6.19]. This suggests that the material that has been deposited across the entire sample rather than particles in some regions. We can also see block-like structures across the sample, with some areas indistinguishable from the PET fibres. This differs drastically from the PET-MOF808-RT sample where we see small particles across the sample and on the fibres.

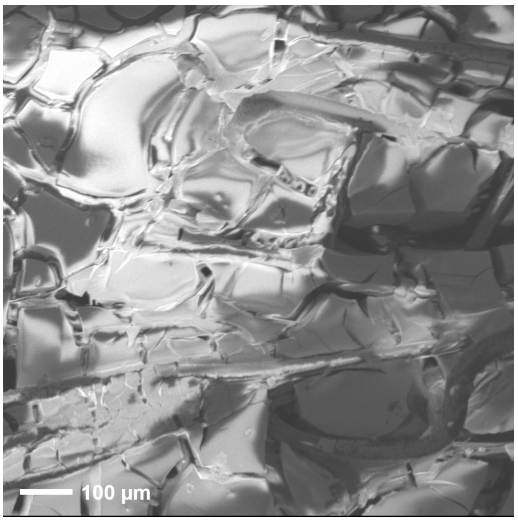

Figure 6.19: SEM image of PET-MOF808-SC sample using back scattered detector to show compositional change between the fabric and MOF-808.

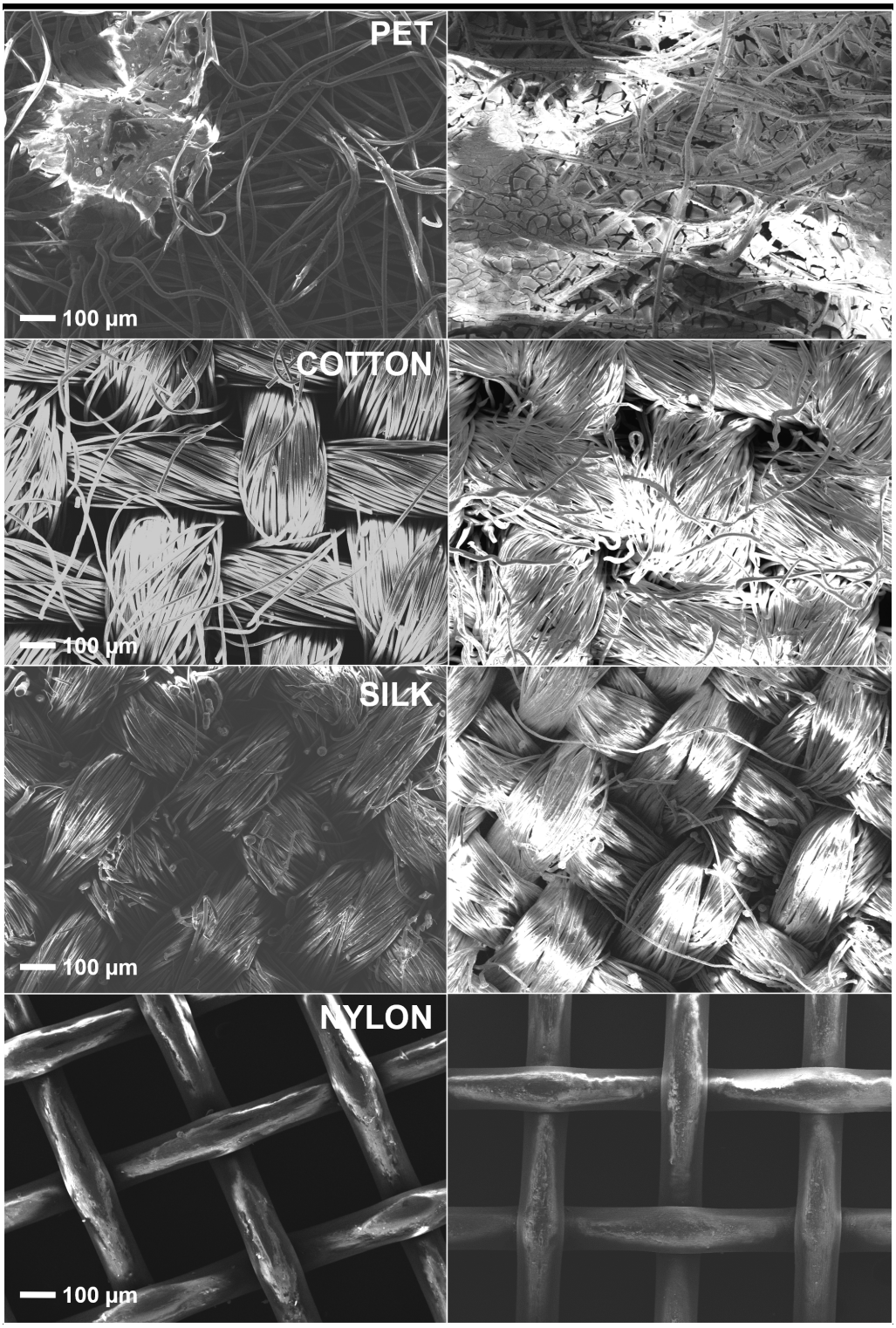

Figure 6.20: SEM image of all materials before and after sonochemical synthesis. In order from top, left to right: PET-blank, PET-MOF808-SC, CTN-blank, CTN-MOF808-SC, SLK-blank, SLK-MOF808-SC, NYL-blank, NYL-MOF808-SC.

EDS mapping carried out to investigate the elemental composition of the PET-MOF808-SC sample confirmed the presence of Zr in the sample [Figure 6.21]. However, unlike the SEM images, the Zr is present in particles across the material rather than in large black-like agglomerates. This suggests that the material deposited is not solely MOF-808, nor is it the Zr-oxo nodes that are present in the synthesis. The most likely identity of the material is the linker BTC which has not been entirely removed in the washing steps of the synthesis.

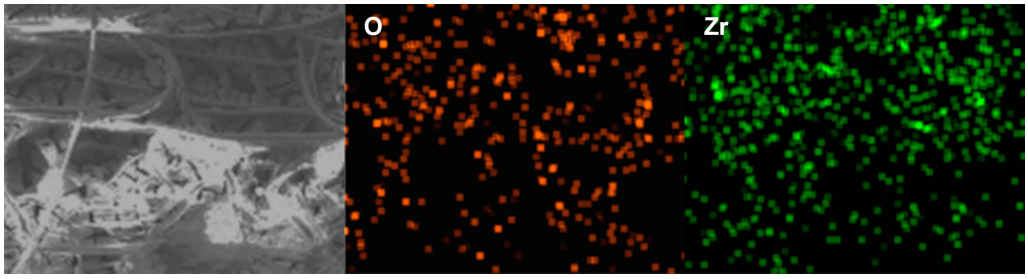

Figure 6.21: EDS mapping of PET-MOF808-SC sample showing the presence of Zr and O elements across the sample.

The BSE image captured of the CTN-MOF808-SC sample shows small particles have been deposited across the material [Figure 6.22]. As the BSE image captures compositional change, these particles are likely MOF-808 as they contrast starkly with the fabric.

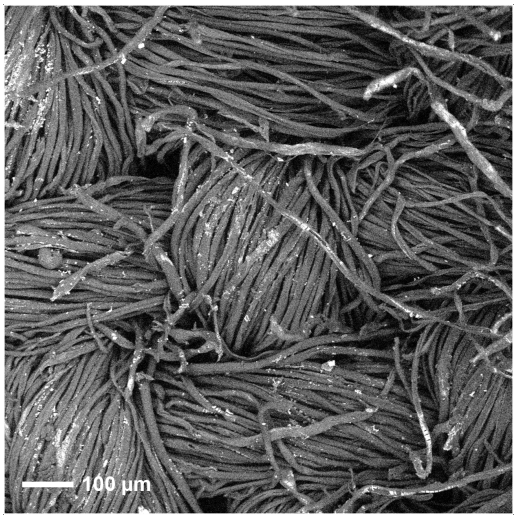

Figure 6.22: SEM image of CTN-MOF808-SC sample using back scattered detector to show compositional change between the fabric and MOF-808.

The size of the particles, and the low distribution across the sample is likely why they were not identified in the above SEM image. When compared to

the CTN-MOF808-RT sample, this sample shows less MOF-808 present on the material, suggesting a higher loading has not been achieved.

The elemental composition of CTN-MOF808-SC was investigated using EDS. The presence of Zr is confirmed across the sample, and is in good agreement with the BSE images; small particles with a low distribution across the cotton [Figure 6.23].

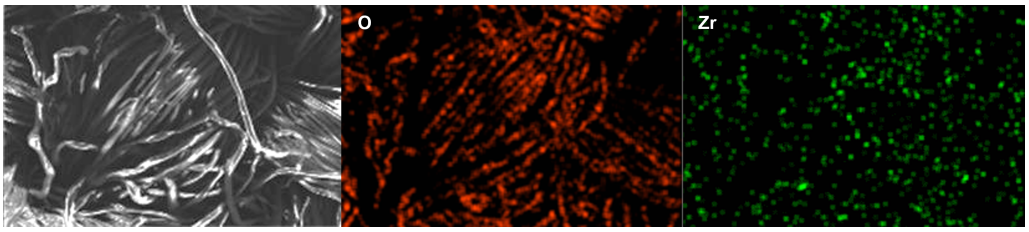

Figure 6.23: EDS mapping of CTN-MOF808-SC sample showing the presence of Zr across the sample.

In the case of the SLK-MOF808-SC sample, the BSE images give us more information than the SEM alone. We can see smaller particles on individual strands of the silk material, some of which have agglomerated in certain regions. This is different from the SLK-MOF808-SC in Figure 6.13 where the entire sample is covered in a layer of MOF-808.

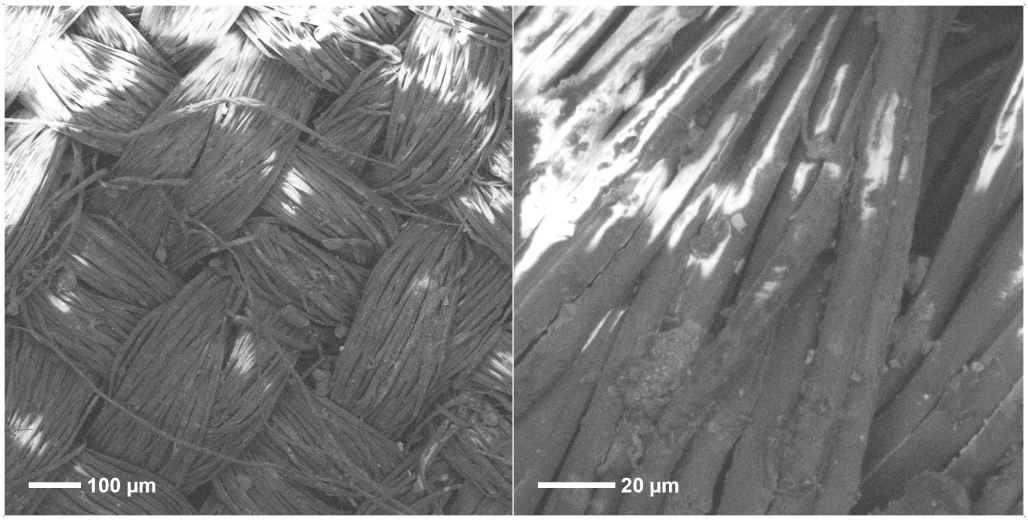

Figure 6.24: SEM image of SLK-MOF808-SC sample using back scattered detector to show compositional change between the fabric and MOF-808.

The EDS mapping carried out on SLK-MOF808-SC confirms the presence of Zr in the sample which implies MOF-808 has been formed. The distribution of the

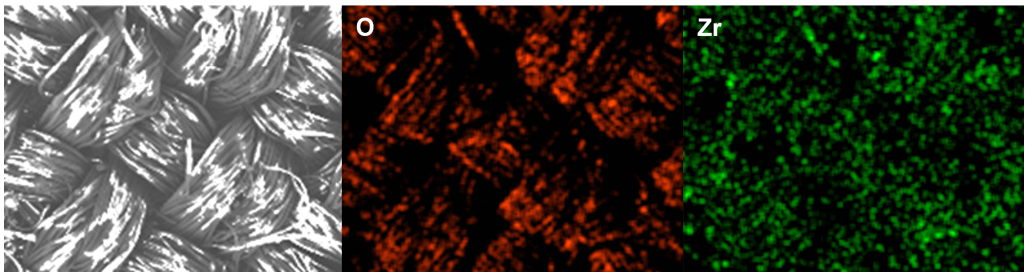

Figure 6.25: EDS mapping of SLK-MOF808-SC sample showing the presence of Zr across the sample.

Zr across the entire sample within small clusters, is in agreement with the BSE images. As is the case for the other woven fabrics, there are darker patches in the EDS map where no Zr is detected as the MOF-808 cannot form on the underlying strands, only on the surface.

The NYL-MOF808-SC sample is interesting as the SEM images show little difference from the blank nylon sample. However using the BSE detector to determine compositional change lighter areas are present in the centre of the nylon strands. This is indicative of MOF-808 being present; albeit in small particles with a very low distribution across the sample. This is markedly different from the NYL-MOF808-RT in Figure 6.15 were large block like structures of deposited material can be seen.

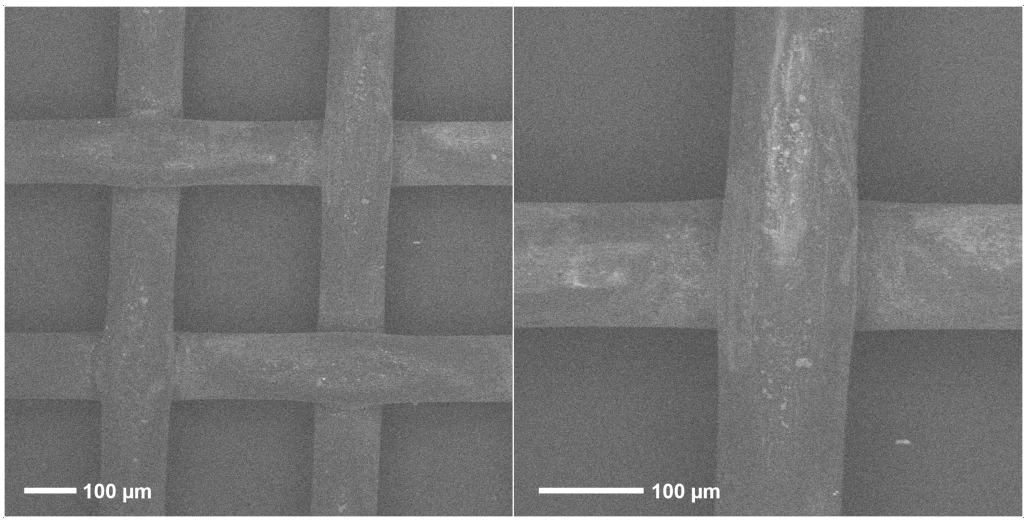

Figure 6.26: SEM image of NYL-MOF808-SC sample using back scattered detector to show compositional change between the fabric and MOF-808.

The EDS mapping also supports the BSE images for NYL-MOF808-SC as Zr is detected in small particles across the strands of nylon. These particles tend to

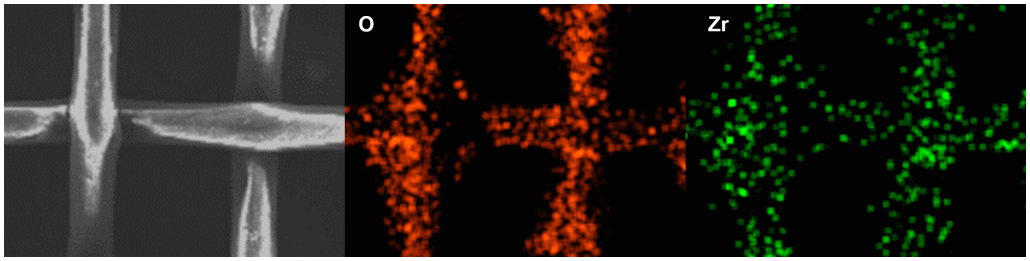

Figure 6.27: EDS mapping of NYL-MOF808-SC sample showing the presence of Zr across the sample.

be seen in the centre of the strands in a non-continuous area. This sample also shows much lower Zr detection when compared to the EDS mapping of the room temperature sample NYL-MOF808-RT.

Overall the combination of SEM, BSE and EDS techniques provides evidence that MOF-808 has been successfully prepared upon all materials to a certain degree. From the images the PET-MOF808-SC synthesis seems the most promising. However, when using the EDS mapping we cannot confirm the material is all MOF-808. In the NYL-MOF808-SC sample very little deposition of any material can be seen therefore there is unlikely to be a catalytic application for this sample.

To further confirm that MOF-808 has been formed on these materials, and to what extent, MOF-808 loadings can be calculated using q-NMR spectroscopy. The calculations are carried out as discussed in subsection 6.4.1 and the loadings for each sample are recorded in Table 6.3.

Table 6.3: Percentage loadings calculated from q-NMR spectroscopy for samples synthesised through the sonochemical method.

Sample	Loading (%)
PET-MOF808-SC	72.4
CTN-MOF808-SC	0.8
SLK-MOF808-SC	3.5
NYL-MOF808-SC	2.1

The loadings calculated show poor loadings across the CTN-MOF808-SC, SLK-MOF808-SC and NYL-MOF808-SC materials with none achieving a loading value above 4%. This supports the conclusion from the SEM images where little deposited material is visible on these samples. The presence of Zr within all the EDS maps may also be caused by unreacted Zr-oxo clusters present on the

surface of the material which have not fully reacted to make MOF-808 and have not been removed with washing.

The PET-MOF808-SC sample shows a very high loading calculated from the BTC present in the sample. This value is not entirely surprising given the amount of material observed in the SEM images. However, it must be considered that some of the material may be the unreacted linker, BTC, not fully removed during the washing steps, resulting in larger integral in the q-NMR and an inflated value for the MOF-808 loading. This is also supported when looking at the EDS mapping where the Zr signal is present in dispersed particles rather than the blocks seen in the images.

Using the sonochemical method to synthesise MOF-composite materials did not result in higher MOF-808 loadings compared to the room temperature synthesis: with the potential exception of PET-MOF808-SC. However, the short reaction time and reusability of the reaction solution with sono-chemical synthesis has the potential to be a useful method in the future.

6.5.2.3 Silane coupling

The final method used to synthesis MOF-composite materials is based upon work by Georgiou *et al.* where 3-chloropropyltriethoxy silane was used to combine a UiO-66 based framework with silk.[15] For our study aminopropytrimethoxysilane was chosen due to availability and preferential interaction with fabrics when compared to other silanes.[14] Silane coupling MOF-808 to fabrics has not been reported to date, therefore it was investigated as an alternative synthesis route for composite materials for this catalytic application.

Silane coupled experiments in the literature are typically carried out by treating the catalyst with silane and then adding in the polymer or material.[15] However, other papers treat the material first and then add in the catalyst (MOF or metal oxide etc.).[28] Due to the lack of agreement, initial experiments were carried out using both methods; treating the silk with the silane then introducing the MOF, and the reverse, to form the products SLK-MOF808-Si(silk) and SLK-MOF808-Si(MOF) respectively. Both materials were characterised using PXRD, IR and q-NMR spectroscopy to determine which method was optimal.

Following the synthesis, PXRD was carried out for both materials. In contrast to previous PXRD measurements where no MOF-808 peaks can be distinguished, the SLK-MOF808-Si(silk) sample has two characteristic MOF-808 peaks clearly visible [(*) in Figure 6.28]. This suggests that larger particles of MOF-808 have been deposited, or a significant increase in loading has been achieved compared to the other samples.

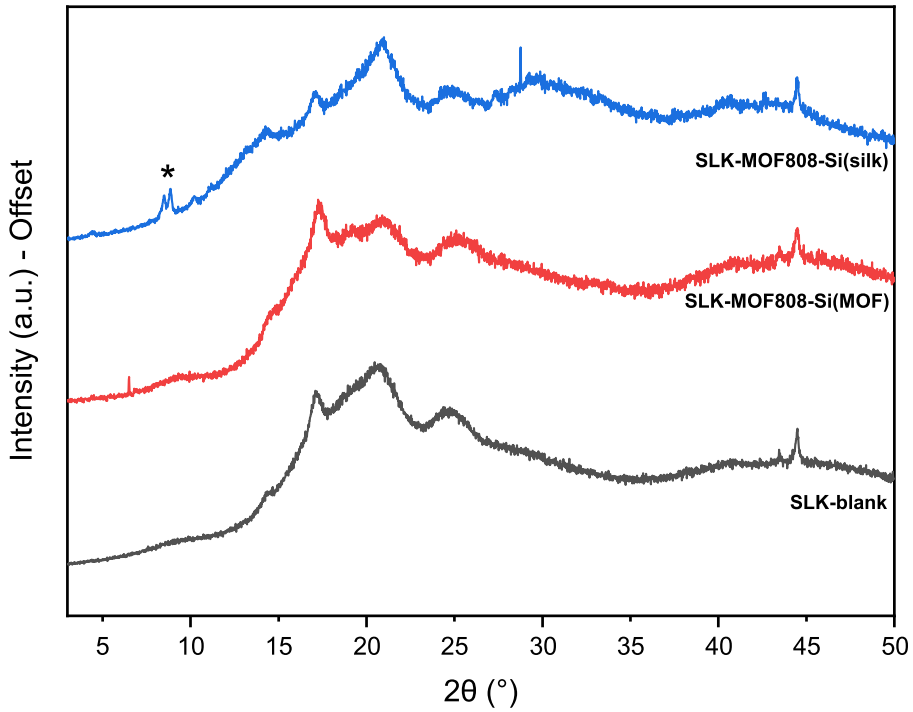

Figure 6.28: PXRD showing comparison of samples synthesised through silane coupling where either the MOF or fabric is treated first. The (*) denotes characteristic MOF-808 peaks.

Although no characteristic MOF-808 peaks are present for the SLK-MOF808-Si(MOF) in the PXRD this does not prove the absence of MOF-808 on the material. In order to establish if MOF-808 has been deposited on both structures, IR spectroscopy measurements were carried out. As shown in Figure 6.29 both samples show the MOF-808 O-H band at 1300 cm^{-1}, whereas no such peak is present in the SLK-blank sample. It can be seen that the SLK-MOF808-Si(silk) sample has a stronger signal in the IR than the SLK-MOF808-Si(MOF) sample which further supports that a greater quantity of MOF-808 has been deposited on the sample where the silk was treated with the silane agent first.

To determine which sample has a greater MOF-808 loading q-NMR spectroscopy was carried out on both samples. For this synthesis method the calculations

should be more accurate as the MOF-808 is pre-synthesised before addition in the synthesis, therefore there is unlikely to be any unreacted BTC linker that may alter the loading calculations. The MOF-808 loadings for both synthesis methods are given in Table 6.4.

Table 6.4: Percentage loadings calculated from q-NMR spectroscopy for samples synthesised through silane coupling with either the silk or MOF being treated first.

Sample	Loading (%)
SLK-MOF808-Si(silk)	9.1
SLK-MOF808-Si(MOF)	1.7

The calculated loadings show a clear difference between the two synthesis methods, with around a 5 times increase in the loading for the SLK-MOF808-Si(silk) sample compared to SLK-MOF808-Si(MOF). When considering all of the characterisation carried out on the two samples, it is clear that the method where the silk is first treated with the silane leads to a higher MOF loading, which is desired for this application.

Further composite syntheses were carried out with the materials PET, cotton, and nylon using the optimised silane synthesis method: the fabric is first treated

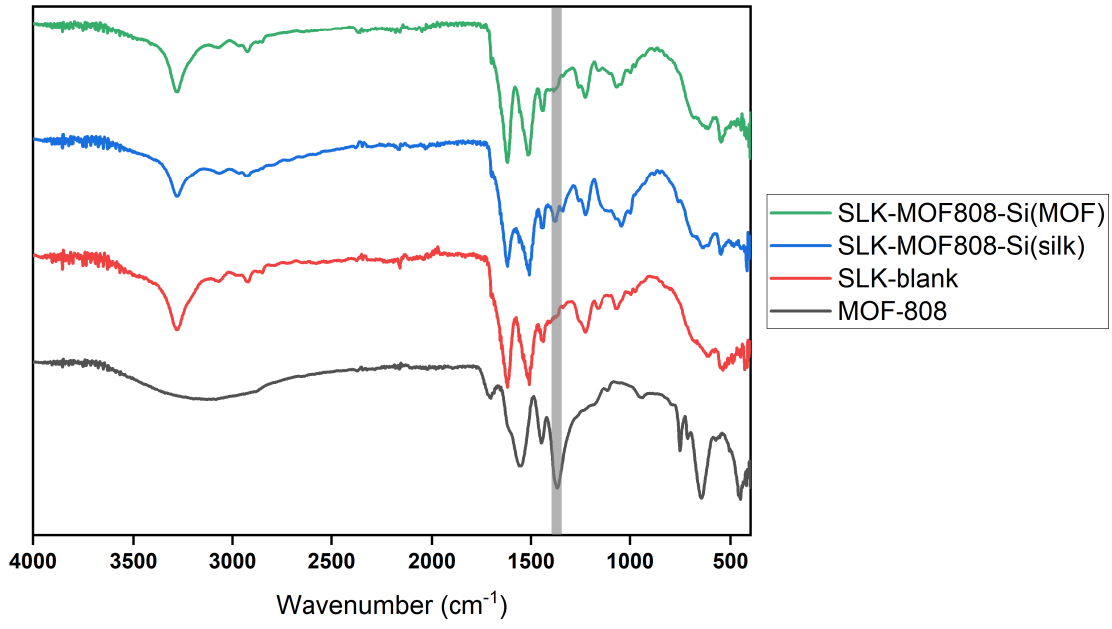

Figure 6.29: IR showing comparison of samples synthesised through silane coupling where either the MOF or fabric is treated first.

with 3-aminopropyltriethoxy silane, then the pre-synthesised MOF-808 is added as discussed in Section 6.3.

Following the synthesis all materials were in-tact and were characterised by PXRD in an attempt to identify characteristic MOF-808 peaks. In Appendix Figure 6.57 only the SLK-MOF808-Si sample showed the characteristic MOF-808 peaks, with all other samples only shown peaks associated with the chosen fabric.

Due to the absence of MOF-808 peaks in the PXRD for most of the samples, IR spectroscopy was carried out. The data collected for the samples clearly show the MOF-808 O-H bend at 1300 cm^{-1} for NYL-MOF808-Si, SLK-MOF808-Si and CTN-MOF808-Si [Figure 6.30, grey band]. For the PET-MOF808-Si sample this signal is very weak, suggesting that there is very little MOF-808 on this sample.

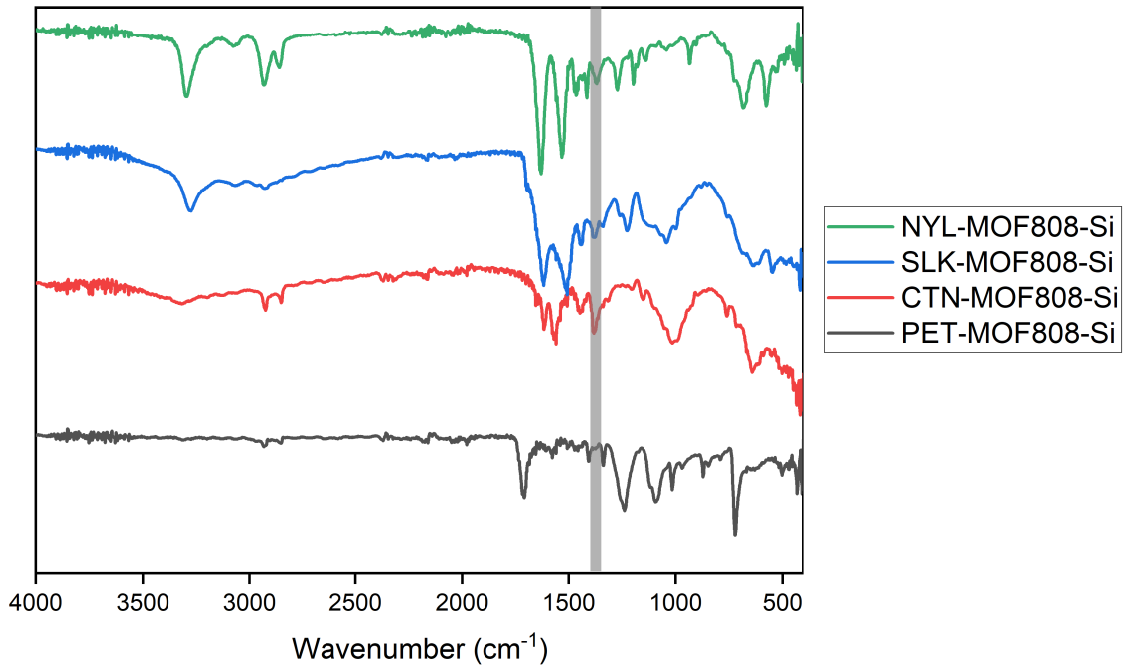

Figure 6.30: IR showing comparison of all samples synthesised through silane coupling where the fabric is treated first. Grey bar indicates where MOF-808 O-H stretch appears.

To further confirm the presence of MOF-808, and to investigate the topology of the silane-coupled composite materials, SEM was carried out [Figure 6.31]. When comparing the captured images for the MOF808-Si samples to the original blank materials there is little compositional difference, with the exception of CTN-MOF808-Si where a layer has been deposited on the surface of the cotton.

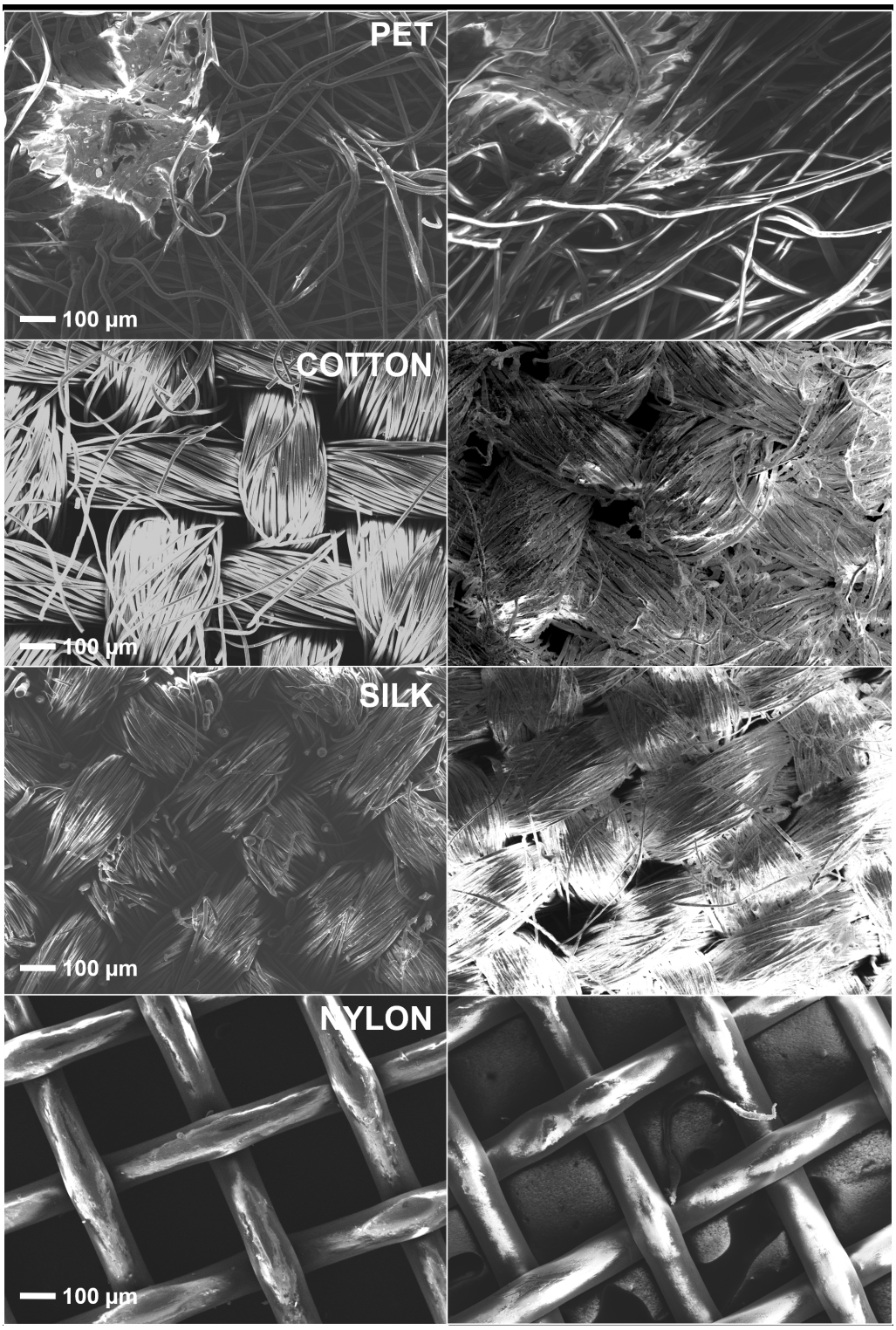

Figure 6.31: SEM image of all materials before and after sonochemical synthesis. In order from top, left to right: PET-blank, PET-MOF808-Si, CTN-blank, CTN-MOF808-Si, SLK-blank, SLK-MOF808-Si, NYL-blank, NYL-MOF808-Si.

Further images were captured at a smaller scale with the BSE detector to clearly distinguish compositional change [Figure 6.32]. For the PET sample there is clearly compositional change that is not visible in the SEM comparison images which may indicate a deposition of MOF. Very little coverage of the deposited material is observed and, unlike the room temperature and sono-chemical syntheses, there is partial coating of the material on the PET strands rather than particles.

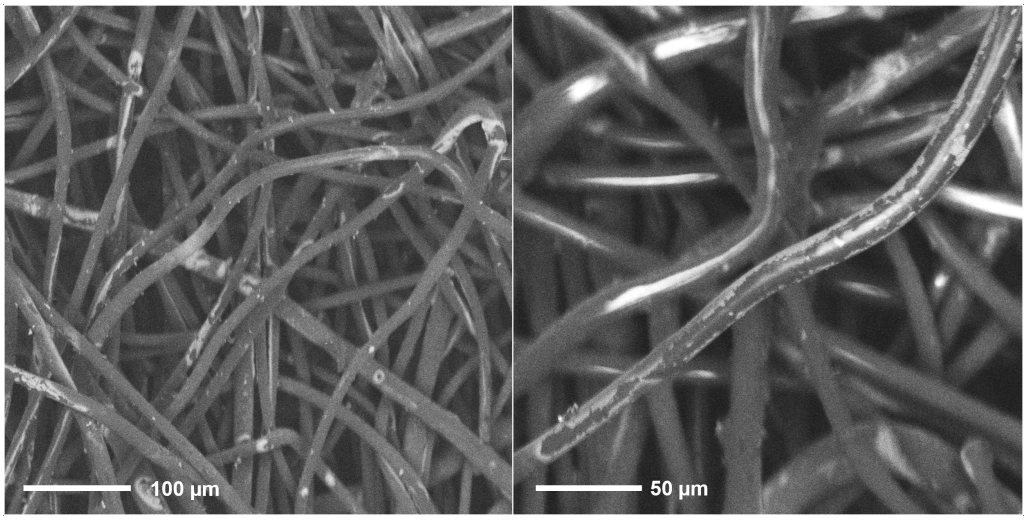

Figure 6.32: SEM image of PET-MOF808-Si sample using back scattered detector to show compositional change between the fabric and MOF-808.

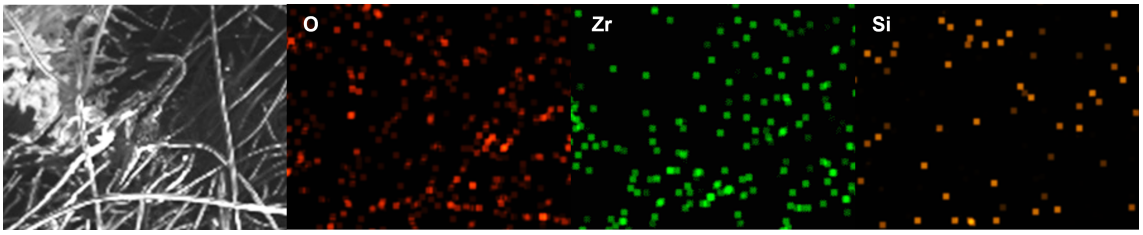

Figure 6.33: EDS mapping of PET-MOF808-Si sample showing the presence of O, Zr and Si elements across the sample.

The EDS carried out on the PET-MOF808-Si sample shows little Zr is present in the sample, the signal for Si is also measured to identify if the silane is also present on the sample Figure 6.33. The combination of BSE images and EDS confirms that although some MOF may have been deposited, it is in small quantities and results in poor coverage of the PET material.

The BSE images captured for the CTN-MOF808-Si sample shows more clearly that a layer of material has been deposited onto the cotton strands [Figure 6.34]. It also shows small agglomerates of particles in some areas across the sample which is indicative of MOF deposition. This is similar to the CTN-MOF808-SC but clearly different to the CTN-MOF808-RT sample where more material was deposited upon the cotton.

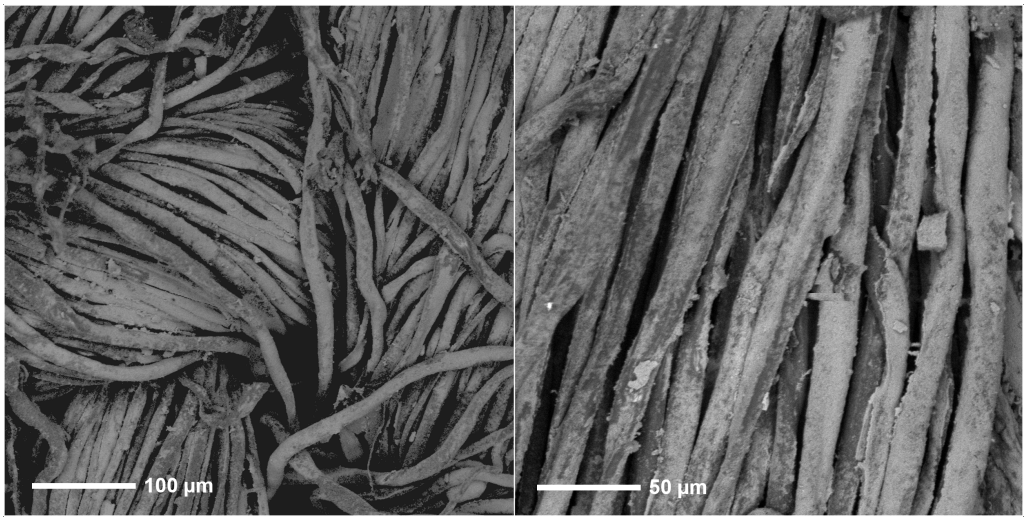

Figure 6.34: SEM image of CTN-MOF808-Si sample using back scattered detector to show compositional change between the fabric and MOF-808.

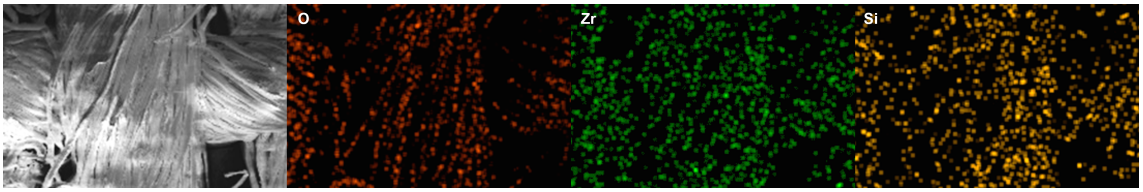

Figure 6.35: EDS mapping of CTN-MOF808-Si sample showing the presence of O, Zr and Si elements across the sample.

The EDS mapping for the CTN-MOF808-Si sample indicates that Zr is present on the surface of the sample therefore MOF-808 has been deposited [Figure 6.34]. The presence of Si also suggests that the silane coupling agent is present on the sample with the overlap between the Si and Zr regions indicating that it is in fact the silane linking the material and MOF-808 to form a composite, rather than deposition of just MOF-808 onto the surface.

The BSE images of the SLK-MOF808-Si sample show small particles within the sample which are likely MOF-808 [Figure 6.36]. When compared to the other

synthesis methods, this sample shows more distinct particles than for either the room temperature or sono-chemical synthesis. It does show less overall coverage than in the case of SLK-MOF808-RT.

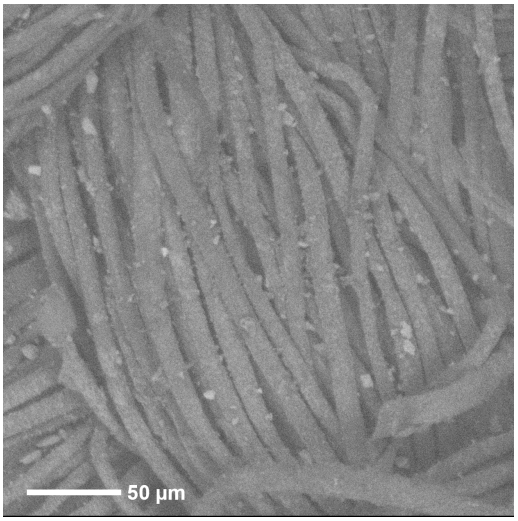

Figure 6.36: SEM image of SLK-MOF808-Si sample using back scattered detector to show compositional change between the fabric and MOF-808.

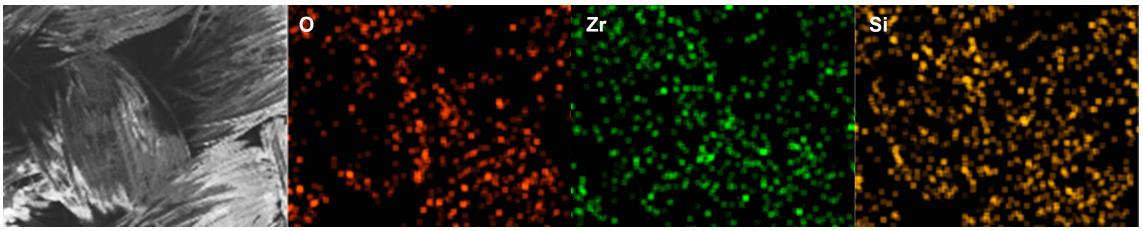

Figure 6.37: EDS mapping of SLK-MOF808-Si sample showing the presence of O, Zr and Si elements across the sample.

To confirm the particles seen in the BSE are of MOF-808, EDS was carried out on the SLK-MOF808-Si sample [Figure 6.37]. As Zr is present in small clusters across the sample, this suggests that the particles seen in the EDS image of SLK-MOF808-Si are MOF-808. The elemental composition is similar to the cotton sample synthesised through the same method; the Si and Zr present in the sample are overlapping which suggests the silane is coupling the MOF to the silk fabric.

The nylon BSE images do not give a strong indication that anything has been deposited, however there may be some material deposited around the overlapping areas of the strands [Figure 6.38]. Using EDS gives a better indication that

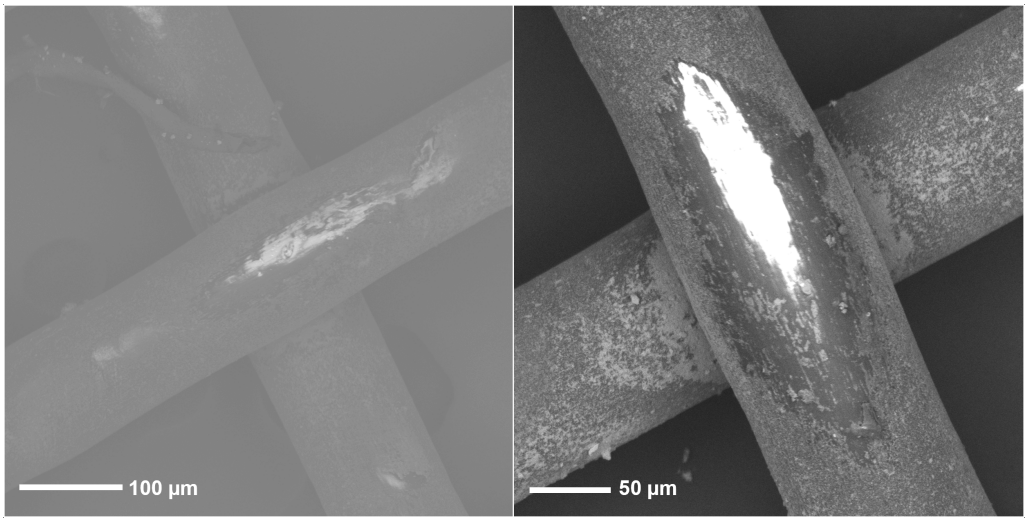

Figure 6.38: SEM image of NYL-MOF808-Si sample using back scattered detector to show compositional change between the fabric and MOF-808.

MOF-808 has been deposited as there is Zr and Si present in the sample and in overlapping areas, suggesting that the silane coupling mechanism has been successful [Figure 6.39]. From the SEM images for all of the nylon samples, only the room temperate synthesis method shows distinct changes in the topology of the material.

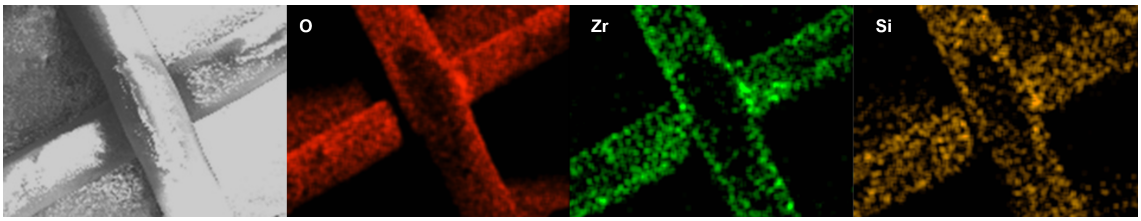

Figure 6.39: EDS mapping of NYL-MOF808-Si sample showing the presence of O, Zr and Si elements across the sample.

Whilst SEM and EDS imaging can confirm the presence of MOF-808 in the sample, in order to identify the amount of MOF-808 successfully deposited onto the materals, q-NMR spectroscopy was carried out as outlined in Section 6.3. The calculated MOF-808 loadings are given in Table 6.5.

From the calculated loadings, the silane coupling method has been the least successful across the three methods chosen. The highest loading values are seen for PET-MOF808-Si and SLK-MOF808-Si with values of 10.6% and 9.1% respectively. Both the CTN-MOF808-Si and NYL-MOF808-Si samples show negligible loadings for MOF-808. Although the SEM and EDS images indicated that MOF-808

Table 6.5: Percentage loadings calculated from q-NMR spectroscopy for samples synthesised through the silane coupling method.

Sample	Loading (%)
PET-MOF808-Si	10.6
CTN-MOF808-Si	0.9
SLK-MOF808-Si	9.1
NYL-MOF808-Si	1.8

is present on these materials, it is likely that it has low dispersion across the entire sample which leads to the low loadings calculated from q-NMR spectroscopy.

6.5.3 Catalytic testing

Following the synthesis and characterisation of the composite materials, catalytic testing was carried out. As discussed in Section 6.3, due to safety considerations live nerve agents cannot be used. Instead the nerve agent simulant dimethyl 4-nitrophenylphosphate (DMNP) was chosen due to previously reported catalytic results closely correlating with sarin.[29] The reaction is monitored by observing the evolution of the hydrolysis product *para*-nitrophenol (PNP) through UV-Vis spectroscopy.

Due to acidic byproducts of the reaction, the catalysis is carried out in the presence of the buffer *N*-Ethylmorpholine (NEM) at pH 10. To ensure all materials are suitable for this catalysis stability tests were carried out at pH 10 in NEM to ensure the MOF-808 remained on the materials. A sample of all materials were left overnight in the NEM buffer solution. The appearance of all materials can be seen in Appendix Figure 6.58 - Figure 6.61. All materials remained in-tact and no leaching of MOF from the fabric was observed. Previous studies have shown that MOF-808 is stable at pH 10.[30]

The catalytic hydrolysis was carried out as outlined in subsection 6.3.3. For each test a 100 mg sample of composite material was used, with the reaction carried out at pH 10 in a buffered solution. Each material was tested twice using a separate cutting of the same sample, this was to test for discrepancy in the MOF-808 coverage across the sample.

Catalytic rates were calculated by converting absorption values to PNP concen-

trations using a molar absorption coefficient, ε, from an in-house calibration curve. Using the method of initial rates an initial rate of hydrolysis can be calculated for each material.[31] The catalytic results will be grouped by material in order to compare the success of different composite synthesis methods.

6.5.3.1 PET

All synthesised PET-MOF808 composite materials show catalytic activity for the hydrolysis of DMNP [Figure 6.40]. These results support the conclusion, gained from characterisation of these materials, that MOF-808 is present in all samples. For comparison the PET-blank sample shows negligible catalytic activity over the same time-frame [Figure 6.40, black line].

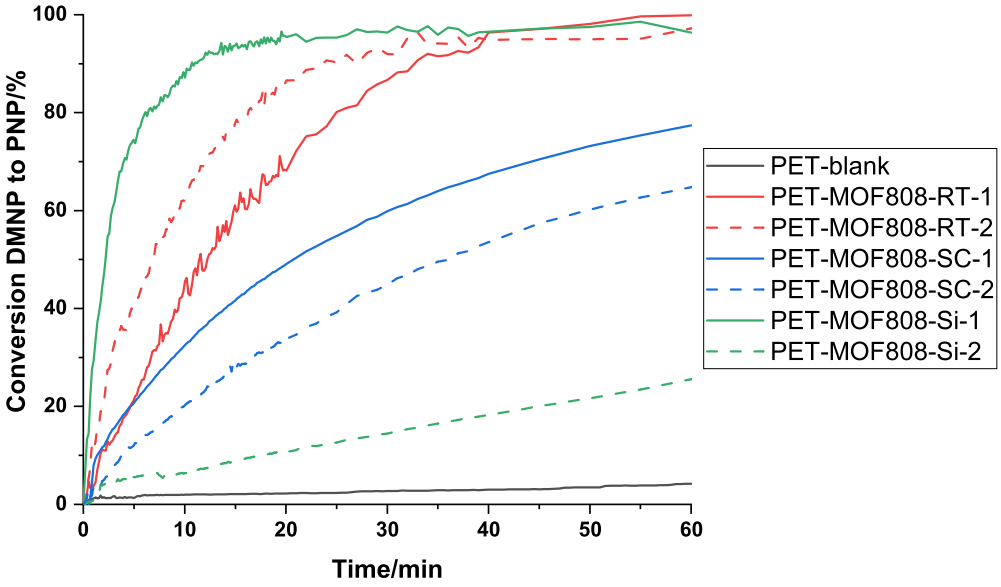

Figure 6.40: Conversion of DMNP to PNP over PET-MOF808 composite samples.

Three samples show 100% conversion within 1 hour: PET-MOF808-RT-1, PET-MOF808-RT-2 and PET-MOF808-Si-1. This is an important result as complete conversion over short time frames is necessary for these materials to be implemented in protective clothing. The other PET samples do not achieve complete conversion within this time frame, but have not plateaued, suggesting with longer reaction times all samples may achieve 100% conversion.

As each sample was tested twice, the conversion profiles can be compared. For PET-MOF808-RT and PET-MOF808-SC, the results are in good agreement, with

the room temperature synthesis samples performing best. The sono-chemical samples both achieve a conversion of around 60 - 70% within 1 hour which are good initial results for MOF-composite materials. For these two samples, the agreement in conversion profiles indicate that the MOF loading is consistent across the entire sample.

For the PET-MOF808-Si samples, the two tests from the same synthesis batch are not in agreement. The first test shows a very quick catalysis of the reaction and achieves 100% within 10 minutes, yet the second only shows 20% conversion after 1 hour. One explanation for such different results is that the coverage of MOF-808 is not uniform across the sample therefore the first sample has a greater loading of MOF-808 than the second sample. The loading calculated from q-NMR spectroscopy is 10.9 %, however this may not be uniformly distributed across the sample. The image of PET-MOF808-Si in Figure 6.49 supports this theory as there appears to be lighter areas on the sample where there may be less MOF-808 deposited.

Another consideration is the leaching of MOF-808 into the reaction solution in the first test. Although the stability test on PET-MOF808-Si shows no leaching of MOF-808 into the NEM buffer [Figure 6.61], when the DMNP begins to be hydrolysed the solution became cloudy. This is likely due to the acidic products of the hydrolysis reaction breaking the bonds between the PET, silane and MOF-808, causing leaching into solution. This has not happened with either the room-temperature or sono-chemical composite materials, indicating that the silane-coupling mechanism may not be as stable a process. When MOF-808 is free in solution, the initial rate and conversion is much higher than when bonded to the fabric.

In order to more accurately compare between samples initial rates were calculated and shown in Figure 6.41. When compared to the measured rate for unbound MOF-808 of 1400 mM/s $x\,10^{-6}$, these composite samples do not perform as well. The fact PET-MOF808-Si1 has a rate of 950 mM/s $x\,10^{-6}$ supports the hypothesis that MOF-808 has leached into the solution, therefore a fair comparison to other materials is not possible for this sample.

For the other composite samples the highest rate is seen for PET-MOF808-RT with an average initial rate of 557 mM/s $x\,10^{-6}$ and an average half-life of 6.8

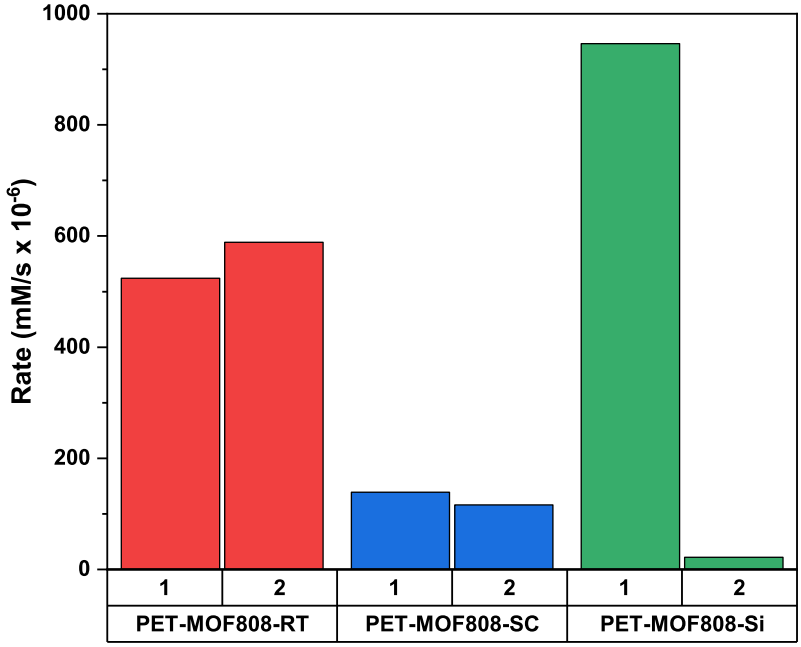

Figure 6.41: Initial rate of catalysis for the hydrolysis of DMNP using PET-MOF808 composite samples.

min. The best performance for a MOF808-PET composite with similar loading (22 %) is a half-life of 3 min.[10] Our result is promising as our synthesis method does not use TFA, a harmful chemical, yet achieving similar results with initial tests.

We also see relatively good activity for the PET-MOF808-SC sample with an average initial rate of 128 mM/s $x\,10^{-6}$. Although this rate is lower than for the room-temperature synthesis, the reaction time for the sono-chemical synthesis is much quicker than for room-temperature: 10 mins compared to 48 hours. Therefore, the sono-chemical synthesis shows potential for this application.

Table 6.6: Percentage loadings calculated from q-NMR spectroscopy for all PET samples.

Sample	Loading (%)
PET-MOF808-RT	29.0
PET-MOF808-SC	72.4
PET-MOF808-Si	10.6

As a standard weight of 100 mg was used for each test, the MOF-808 loadings should be considered. Table 6.6 gives the calculated loadings for the PET composites. It is clear that a higher loading does not result in higher initial rates

as PET-MOF808-RT outperforms PET-MOF808-SC at a lower loading. This result is not entirely unexpected as previous studies have shown that a lower loading results in better catalytic results as the accessibility of the Zr_6 node active sites is improved.[10]

However, the extent of the difference between initial rates between the RT and SC samples puts the loading calculated for the PET-MOF808-SC sample into doubt. The large loading value of 72 % may be partly un-reacted BTC linker that has coordinated to the surface of the fabric and has not been removed through the washing procedure.

Overall, the PET composite materials have shown successful catalysis of a nerve agent simulant and opened up quicker synthesis routes for composite materials that show great potential.

6.5.3.2 Cotton

The results for the cotton composite materials show that all synthesised materials successful catalyse the hydrolysis of DMNP [Figure 6.42]. The blank cotton sample shows negligible catalytic activity, supporting the conclusion from the characterisation data that MOF-808 has been deposited on the surface of the cotton in all synthesis procedures.

The sample CTN-MOF808-RT achieves 100% conversion for both repeats. This is a very promising result as few studies have shown a successful CTN-MOF808 catalyst.[20] This sample takes 1 hour to achieve complete conversion, slower than for the PET-MOF808-RT samples which achieved 100% conversion after 20 minutes. Yet, this result indicates that the catalytic activity of MOF-808 is not hindered when bonded to the cotton.

Neither CTN-MOF808-SC or CTN-MOF808-Si achieved 100% conversion over the monitored time. However, as in the case of the PET-MOF808 composites, neither of the samples show a plateau which shows they may achieve full conversion over longer time frames. The CTN-MOF808-Si samples show higher conversion than the CTN-MOF808-SC sample, suggesting the silane sample may have more accessible Zr_6 node active sites than in the sono-chemical sample.

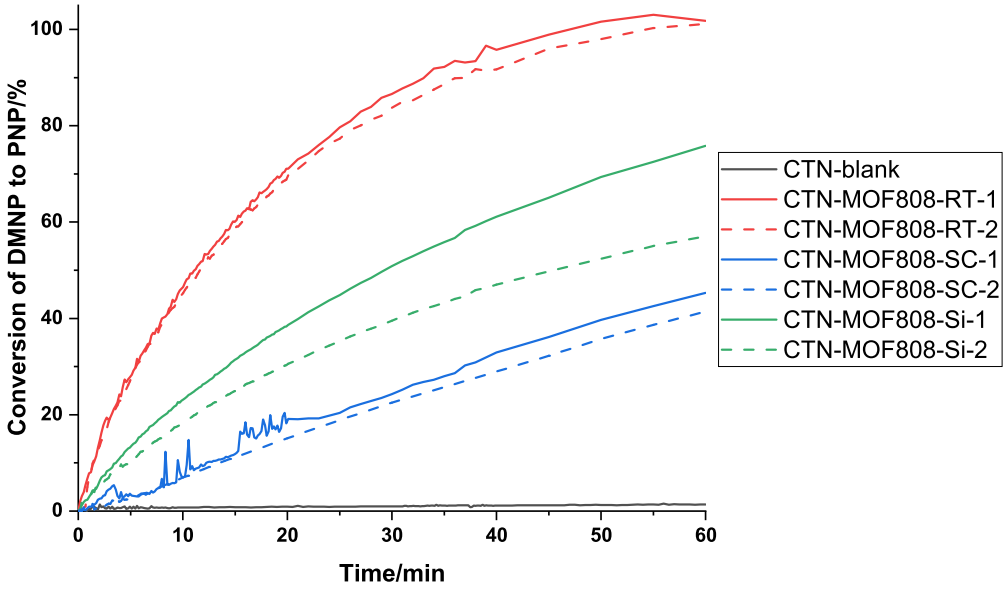

Figure 6.42: Conversion of DMNP to PNP over CTN-MOF808 composite samples.

For all CTN-composite materials tested, the repeat tests of each sample are in good agreement. This indicates that the material has a homogeneous loading of MOF-808 across the fabric. This can be further evidenced in Figure 6.50 where the CTN-MOF808 samples are clearly uniform in appearance. When compared to the PET samples there is more agreement between repeat tests and less variation in the composite appearance. It is also unlikely that any leaching of MOF-808 powder into the reaction has occurred as none of the CTN-MOF808 samples have a conversion profile similar to that of MOF-808.

To compare the kinetics of each sample, initial rates are calculated and shown in Figure 6.43. The highest rate calculated for the CTN-composites the room temperature synthesis sample, CTN-MOF808-RT, with an average initial rate of 337 mM/s $x\,10^{-6}$ and a calculated half-life of 9.3 min. This is a better result that previously published for CTN-MOF808 composites which found a half life of 24 mins, however that reaction was carried out in 50% relative humidity rather than in solution.[20] The other CTN-composite materials tested gave average initial rates of 101 mM/s $x\,10^{-6}$ and 43 mM/s $x\,10^{-6}$ for CTN-MOF808-Si and CTN-MOF808-SC respectively.

The initial rates can be compared to the MOF-808 loading values, previously calculated from q-NMR spectroscopy [Table 6.7]. For the CTN-composites, a trend is observed where the initial rates increase as the loadings increase.

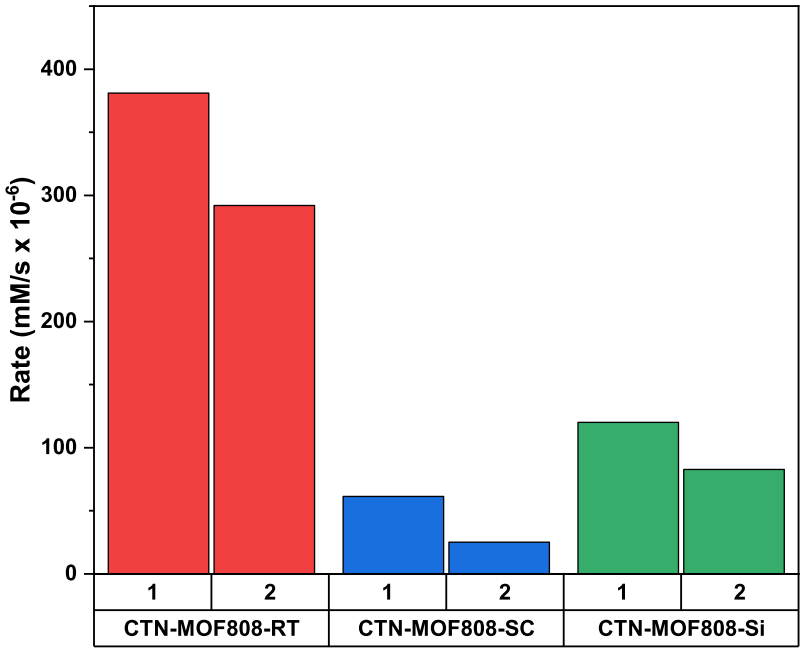

Figure 6.43: Initial rate of catalysis for the hydrolysis of DMNP using CTN-MOF808 composite samples.

The difference in loading between the sono-chemical and silane-coupled CTN-composites are negligible, yet there is a considerable difference in the initial rate. This indicates that factors other than loading need to be considered to increase the activity of these catalysts such as the availability of active sites. However, these results demonstrate that even with very low MOF-808 loading catalytic activity is achieved.

Table 6.7: Percentage loadings calculated from q-NMR spectroscopy for all CTN samples.

Sample	Loading (%)
CTN-MOF808-RT	4.1
CTN-MOF808-SC	0.8
CTN-MOF808-Si	0.9

The loading calculated for the CTN-MOF808-RT sample of 4% make the 100% conversion over 1 hour more impressive. If higher loadings can be achieved for CTN-composites the time for complete conversion may be decreased. All of the CTN-MOF808 catalytic results are very promising as all samples are catalytically active, whilst no observable leaching is detected, all whilst on a material that is extremely versatile.

6.5.3.3 Silk

All prepared SLK-composite samples were tested as catalysts for the hydrolysis of the nerve agent simulant DMNP and conversion time charts were plotted [Figure 6.44]. All SLK-MOF808 composite materials show some level of catalytic activity compared to the SLK-blank sample, supporting the conclusion that MOF-808 has been successfully deposited on all materials.

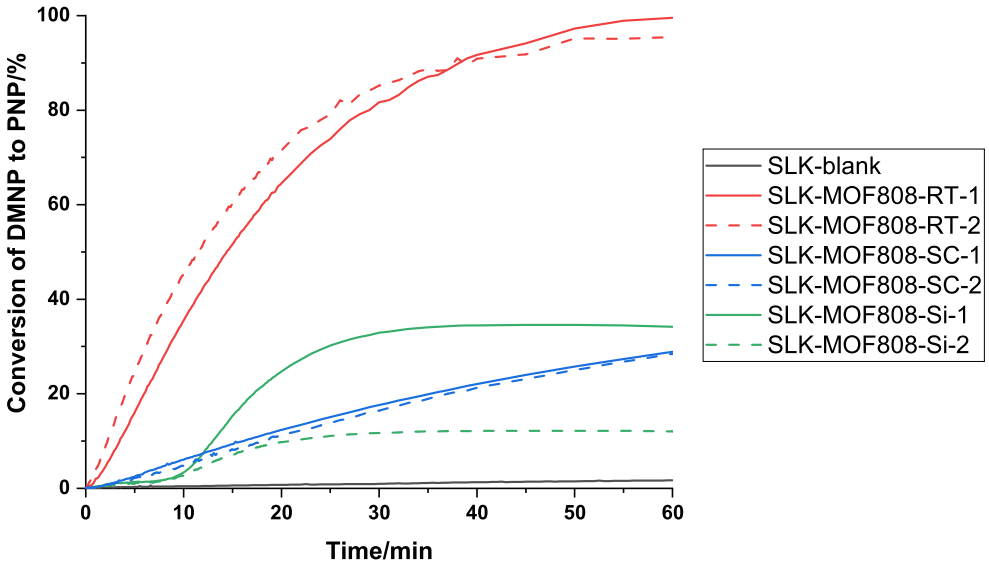

Figure 6.44: Conversion of DMNP to PNP over SLK-MOF808 composite samples.

The conversion profiles for the silk samples vary substantially between different synthesis methods. As we have previously seen for PET and cotton, the room-temperature synthesis sample, SLK-MOF808-RT, shows the highest conversion, with 100% conversion achieved within an hour. The two repeat tests for this sample are in good agreement, suggesting homogenous coverage of MOF-808 across the entire SLK-MOF808-RT sample. The SLK-MOF808-SC is less successful and only achieves a 20% conversion after 1 hour, it also looks to be plateauing around this value and is unlikely to reach 100% conversion.

The more interesting profile is seen for SLK-MOF808-Si; at first there looks to be negligible catalytic activity in-line with blank silk. However, after *ca.* 10 minutes there is a jump in rate which continues until it quickly plateaus with a conversion of 30% after 20 minutes of activity. This is mirrored by the second SLK-MOF808-Si sample but with a lower conversion of 10% achieved after 20 minutes.

Both of these results suggest that after a short period in the solution the MOF-808 is becoming detached from the silk, leaching into solution and acting as a catalyst, hence the higher rate displayed. The difference in the conversion achieved between the two samples of SLK-MOF808-Si is likely due to the difference of MOF loading, suggesting that the amount of MOF-808 deposited across the sample is not uniform. It is also interesting that, unlike the PET-MOF808-Si sample, there is a period of time that the MOF-808 stays bound to the silk before becoming detached. This suggests that the silk-silane bonds are stronger than PET-silane bonds.

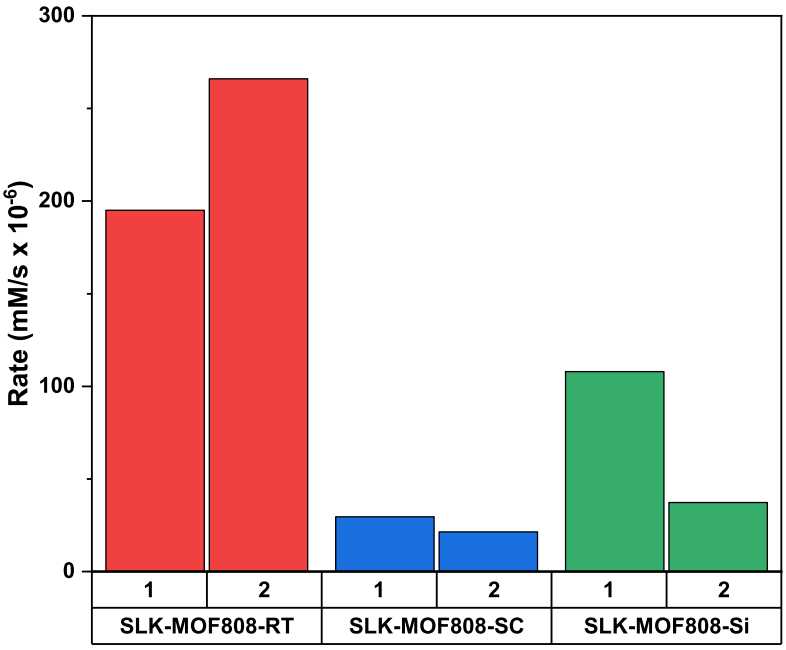

Figure 6.45: Initial rate of catalysis for the hydrolysis of DMNP using SLK-MOF808 composite samples.

Initial rates were calculated for all tested silk samples [Figure 6.45]. As with the other materials the highest initial rate is reported for the room temperature synthesis sample SLK-MOF808-RT with an average rate of 231 mM/s $x\,10^{-6}$. This is followed by SLK-MOF808-Si with 73 mM/s $x\,10^{-6}$ and finally SLK-MOF808-SC with an initial rate of 26 mM/s $x\,10^{-6}$. The initial rates calculated for SLK-MOF808-Si are based on the reaction occurring above 10 minutes so cannot be used to accurately compare results. The initial rate is negligible in the time-frame where we assume the MOF-808 is still coupled to the silk fabric.

When the loadings of each sample are taken into consideration, the rates and

conversion profiles correlate with a higher loading leading to better catalytic rates. The SLK-MOF808-SC sample has the lowest loading of the three synthesis methods of 3.5% which may explain the poor catalytic results. When comparing between materials using the sono-chemical synthesis method, the cotton sample CTN-MOF808-SC has a lower loading of 1% yet a higher initial rate. This suggests that the loading value may not be accurate for the silk sample, and the BTC signal measured in the q-NMR spectroscopy to calculate this value was due to unreacted starting material. It may also indicate than some synthesis methods are preferential on different fabrics, as although the SLK-MOF808-SC synthesis results in a relatively good loading, the active sites may be less accessible than in the cotton composite.

Table 6.8: Percentage loadings calculated from q-NMR spectroscopy for all SLK samples.

Sample	Loading (%)
SLK-MOF808-RT	19.7
SLK-MOF808-SC	3.5
SLK-MOF808-Si	9.1

The catalytic results for the silk show that the SLK-MOF808-RT sample has been the most successful in both MOF-808 loading achieved and catalytic rate. The other samples do show potential, however, more investigation into the silane-coupling synthesis is needed to understand why MOF-808 is becoming detached from the fabric after a period of time.

6.5.3.4 Nylon

The catalytic results for all nylon-composite materials for the hydrolysis of DMNP are shown in Figure 6.46. A blank nylon sample was also tested; negligable catalytic activity was detected for NYL-blank therefore any catalytic activity on the composite samples is due to the MOF-808 present in the sample.

From Figure 6.46 is it clear that both NYL-MOF808-RT and NYL-MOF808-SC show catalytic activity for the hydrolysis of DMNP. However, neither have achieved 100% conversion over the 1 hour monitoring. NYL-MOF808-RT has a higher conversion of 80%, compared to NYL-MOF808-SC at 30%. The final sample, NYL-MOF808-Si, has the same conversion profile as NYL-blank which

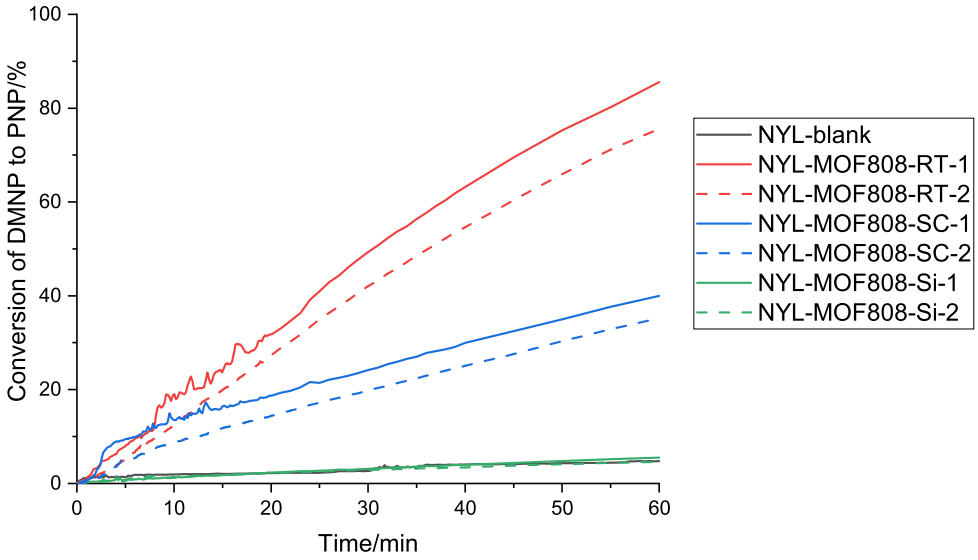

Figure 6.46: Conversion of DMNP to PNP over NYL-MOF808 composite samples.

suggests that negligible MOF-808 has been deposited on the nylon using this synthesis method or that all active sites are inaccessible on the material.

These results are supported by the appearance of NYL samples as shown in Figure 6.52 where there are visible areas of MOF-808 deposited on NYL-MOF808-RT, some small areas of deposited MOF-808 on NYL-MOF808-SC, whereas NYL-MOF808-Si is indistinguishable from NYL-blank.

In order to better compare samples, initial catalytic rates were calculated for each sample tested [Figure 6.47]. Repeat tests on the same sample are in good agreement for both the conversion plots and initial rates which suggest that MOF-808 has been deposited uniformly across the sample. The NYL-MOF808-RT sample exhibits the highest initial rate with an average of 71.6 mM/s $x\,10^{-6}$, followed by NYL-MOF808-SC with an initial rate of 37.8 mM/s $x\,10^{-6}$. These results are the lowest overall when compared to the results of other composite materials discussed above and are far from the initial rate calculated for MOF-808 of 1400 mM/s $x\,10^{-6}$.

When comparing the initial rates to the loadings calculated through q-NMR spectroscopy it is unsurprising that NYL-MOF808-RT has the better catalytic result as it shows the highest loading of the three samples by over 4 times. It is interesting to note that NYL-MOF808-SC and NYL-MOF808-Si have similar calculated loadings but different catalytic results. It is unlikely that the loading

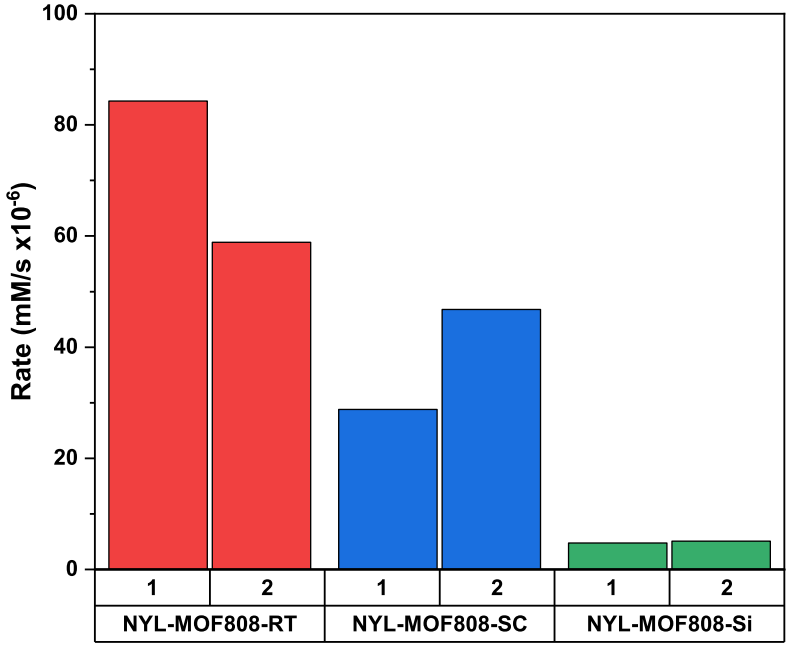

Figure 6.47: Initial rate of catalysis for the hydrolysis of DMNP using NYL-MOF808 composite samples.

value for NYL-MOF808-Si is incorrect as pre-prepared MOF-808 is used in this synthesis method, therefore the BTC peak detected can only be from MOF-808, rather than unreacted starting materials. Therefore, these results suggest that the accessibility of the active site, Zr_6 node, is restricted for the silane-coupling synthesis, possibly due to the silane.

Table 6.9: Percentage loadings calculated from q-NMR spectroscopy for all NYL samples.

Sample	Loading (%)
NYL-MOF808-RT	9.8
NYL-MOF808-SC	2.1
NYL-MOF808-Si	1.8

Overall the results for NYL-MOF808 composites are not as successful as other materials. However, this study shows promise as it is the first that has used nylon for this application and both the room temperature and sono-chemical synthesis methods have been successful at depositing MOF-808 onto this material. Although the conversion and initial rates are still far from the quickest recorded in literature, nylon is an extremely versatile materials that with more research could show promise for this catalysis.

6.6 Conclusions

In this chapter four materials, PET, cotton, silk and nylon, have been used to synthesise MOF-808 composite materials using three different synthesis methods; in-situ room-temperature, sono-chemical and silane-coupling. The most successful synthesis method has been in-situ room temperature which resulted in the highest catalytic results for each material [Figure 6.48].

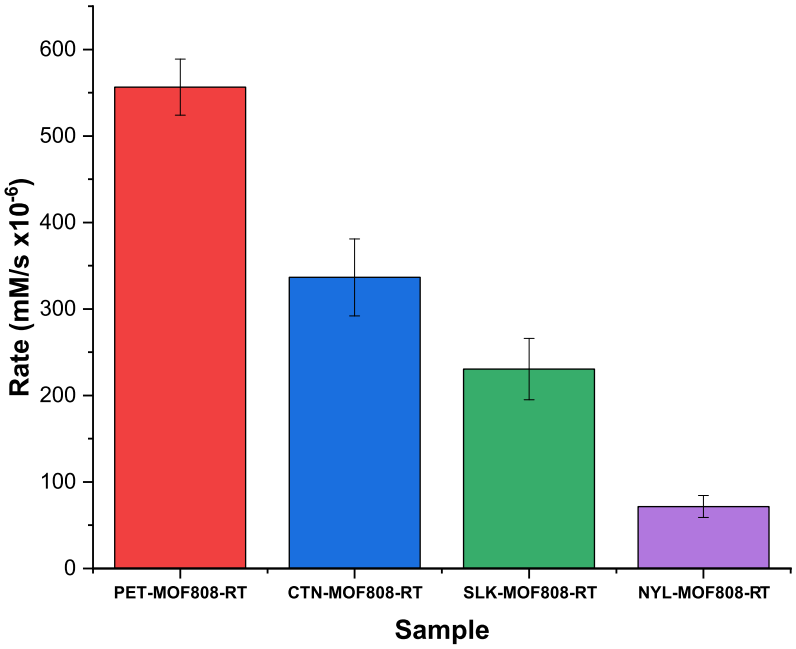

Figure 6.48: Initial rate of catalysis for the hydrolysis of DMNP using composite samples that have been prepared through the room-temperature synthesis.

Of all the synthesised composites the most successful for the catalytic hydrolysis of DMNP was PET-MOF808-RT, with an initial rate value of 557 mM/s $x\,10^{-6}$ with a MOF-808 loading calculated at 29%. Previous work has been carried out on PET fabrics, however, the method here is the most environmentally friendly as no harsh chemicals such as DMF or TFA are used in the synthesis, allowing the scale-up of this process to be more facile than previously reported methods.[10]

All other materials synthesised through the room temperature method have shown a range of success as hydrolysis catalysts. The cotton sample is particularly promising as a loading value of just 4.1% was calculated yet it displayed the second highest initial rate for this catalysis.

The sono-chemical synthesis method was also successful as all samples prepared using this method showed catalytic activity. Although this method achieved low loadings of MOF-808 on all samples, the reaction time used was only 10 mins. When compared to the room-temperature synthesis method which has a reaction time of 48 hours, the sono-chemical method has much potential for this application.

The silane-coupled synthesis method was the least successful of the three synthesis methods. The CTN-MOF808-Si sample showed the most promise as it out-performed the sono-chemical sample and was generally reproducible over the two repeat catalytic tests. In all other materials the silane-couple method exhibited poor reproducibility between repeat samples, and varying conversion plots. This was mostly down to poor loading and leaching of MOF-808 into the reaction solution after varying times.

Overall this chapter has shown that MOF-808 can be successfully loaded onto a variety of materials using a range of synthesis methods. Characterisation through PXRD, IR spectroscopy, and SEM proves the presence of MOF-808 and q-NMR spectroscopy calculations allow a estimation of loading which is vital for catalytic applications. All samples out-perform the blank materials for the catalytic hydrolysis of DMNP, with the exception of one, which gives further evidence that MOF-808 is present on these composites. The range of materials that we have shown to be successful for this catalysis show great potential for us as protective clothing for the destruction of chemical warfare agents.

6.7 References

[1] J. Zhao, M. D. Losego, P. C. Lemaire, P. S. Williams, B. Gong, S. E. Atanasov, T. M. Blevins, C. J. Oldham, H. J. Walls, S. D. Shepherd, M. A. Browe, G. W. Peterson and G. N. Parsons, *Adv. Mater. Interfaces*, 2014, **1**, 1400040.

[2] J. Zhao, D. T. Lee, R. W. Yaga, M. G. Hall, H. F. Barton, I. R. Woodward, C. J. Oldham, H. J. Walls, G. W. Peterson and G. N. Parsons, *Angew. Chemie., Int. Ed.*, 2016, **55**, 13224–13228.

[3] D. T. Lee, J. Zhao, C. J. Oldham, G. W. Peterson and G. N. Parsons, *ACS Appl. Mater. Interfaces*, 2017, **9**, 44847–44855.

[4] D. T. Lee, J. Zhao, G. W. Peterson and G. N. Parsons, *Chem. Mater.*, 2017, **29**, 4894–4903.

[5] D. L. McCarthy, J. Liu, D. B. Dwyer, J. L. Troiano, S. M. Boyer, J. B. DeCoste, W. E. Bernier and W. E. Jones, Jr, *New J. Chem.*, 2017, **41**, 8748–8753.

[6] M. Bechelany, M. Drobek, C. Vallicari, A. Abou Chaaya, A. Julbe and P. Miele, *Nanoscale*, 2015, **7**, 5794–5802.

[7] G. W. Peterson, A. X. Lu and T. H. I. Epps, *ACS Appl. Mater. Interfaces*, 2017, **9**, 32248–32254.

[8] D. B. Dwyer, N. Dugan, N. Hoffman, D. J. Cooke, M. G. Hall, T. M. Tovar, W. E. Bernier, J. DeCoste, N. L. Pomerantz and W. E. J. Jones, *ACS Appl. Mater. Interfaces*, 2018, **10**, 34585–34591.

[9] M. Kalaj, M. S. Denny Jr., K. C. Bentz, J. M. Palomba and S. M. Cohen, *Angew. Chemie., Int. Ed.*, 2019, **58**, 2336–2340.

[10] K. Ma, T. Islamoglu, Z. Chen, P. Li, M. C. Wasson, Y. Chen, Y. Wang, G. W. Peterson, J. H. Xin and O. K. Farha, *J. Am. Chem. Soc.*, 2019, **141**, 15626–15633.

[11] S. Sterman and J. G. Marsden, *J. Ind. Eng. Chem*, 1966, **58**, 33–37.

[12] S. Mallakpour and A. Barati, *Prog. Org. Coat.*, 2011, **71**, 391–398.

[13] S. Ahmadipouya, F. Ahmadijokani, H. Molavi, M. Rezakazemi and M. Arjmand, *Chem Eng Res Des*, 2021, **176**, 49–59.

[14] S. Shokoohi, A. Arefazar and R. Khosrokhavar, *J. Reinf. Plast.*, 2008, **27**, 473–485.

[15] Y. Georgiou, S. Rapti, A. Mavrogiorgou, G. Armatas, M. J. Manos, M. Louloudi and Y. Deligiannakis, *Sci. Rep.*, 2020, **10**, 9358.

[16] A. Yao, X. Jiao, D. Chen and C. Li, *ACS Appl. Mater. Interfaces*, 2019, **11**, 7927–7935.

[17] H. Liang, A. Yao, X. Jiao, C. Li and D. Chen, *ACS Appl. Mater. Interfaces*, 2018, **10**, 20396–20403.

[18] E. López-Maya, C. Montoro, L. M. Rodríguez-Albelo, S. D. AznarCervantes, A. A. Lozano-Pérez, J. L. Cenís, E. Barea and J. A. R. Navarro, *Angew. Chemie., Int. Ed.*, 2015, **54**, 6790–6794.

[19] M. A. Bunge, A. B. Davis, K. N. West, C. W. West and T. G. Glover, *J. Ind. Eng. Chem*, 2018, **57**, 9151–9161.

[20] Z. Chen, K. Ma, J. J. Mahle, H. Wang, Z. H. Syed, A. Atilgan, Y. Chen, J. H. Xin, T. Islamoglu, G. W. Peterson and O. K. Farha, *J. Am. Chem. Soc.*, 2019, **141**, 20016–20021.

[21] Y. Feng, J. Lin, L. Niu, Y. Wang, Z. Cheng, X. Sun and M. Li, *Polymer*, 2020, **12**, 2105.

[22] J. E. Mondloch, M. J. Katz, W. C. Isley III, P. Ghosh, P. Liao, W. Bury, G. W. Wagner, M. G. Hall, J. B. DeCoste, G. W. Peterson, R. Q. Snurr, C. J. Cramer, J. T. Hupp and O. K. Farha, *Nat. Mater.*, 2015, **14**, 512–516.

[23] G. F. Pauli, S. N. Chen, C. Simmler, D. C. Lankin, T. Gödecke, B. U. Jaki, J. B. Friesen, J. B. McAlpine and J. G. Napolitano, *J. Med. Chem.*, 2015, **58**, 9061.

[24] Z. Hu, Y. Peng, Z. Kang, Y. Qian and D. Zhao, *Inorg. Chem.*, 2015, **54**, 4862–4868.

[25] S. Dai, C. Simms, I. Dovgaliuk, G. Patriarche, A. Tissot, T. N. Parac-Vogt and C. Serre, *Chem. Mater.*, 2021, **33**, 7057–7066.

[26] M. Kalaj, K. C. Bentz, S. Ayala, J. M. Palomba, K. S. Barcus, Y. Katayama and S. M. Cohen, *Chem. Rev.*, 2020, **120**, 8267–8302.

[27] N. Stock and S. Biswas, *Chem. Rev.*, 2012, **112**, 933–969.

[28] Long, Park, Chae, Lee, Bae and Shin, *Polymer*, 2019, **11**, 1298.

[29] Y. Liu, A. J. Howarth, N. A. Vermeulen, S. Y. Moon, J. T. Hupp and O. K. Farha, *Coord. Chem. Rev.*, 2017, **346**, 101–111.

[30] H.-Q. Zheng, C.-Y. Liu, X.-Y. Zeng, J. Chen, J. Lü, R.-G. Lin, R. Cao, Z.-J. Lin and J.-W. Su, *Inorg. Chem.*, 2018, **57**, 9096–9104.

[31] J. Casado, M. A. Lopez-Quintela and F. M. Lorenzo-Barral, *J. Chem. Educ.*, 1986, **63**, 450.

6.8 Appendix

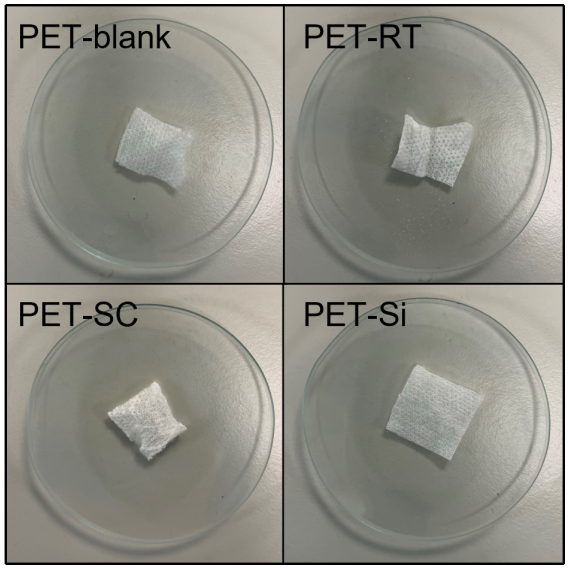

Figure 6.49: Appearance of PET fabrics before and after composite synthesis has taken place.

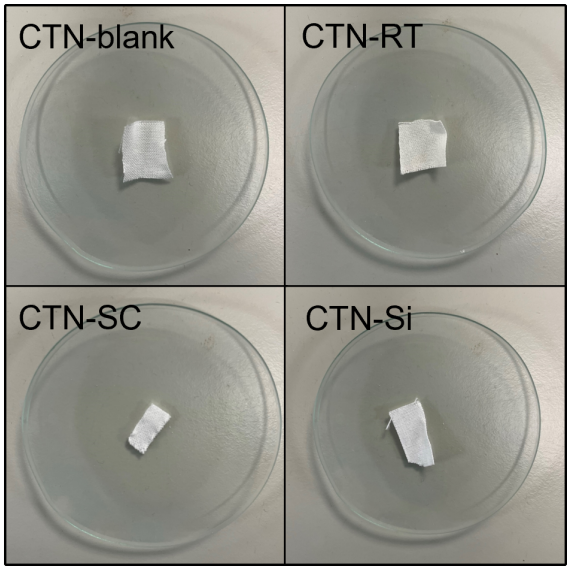

Figure 6.50: Appearance of cotton fabrics before and after composite synthesis has taken place.

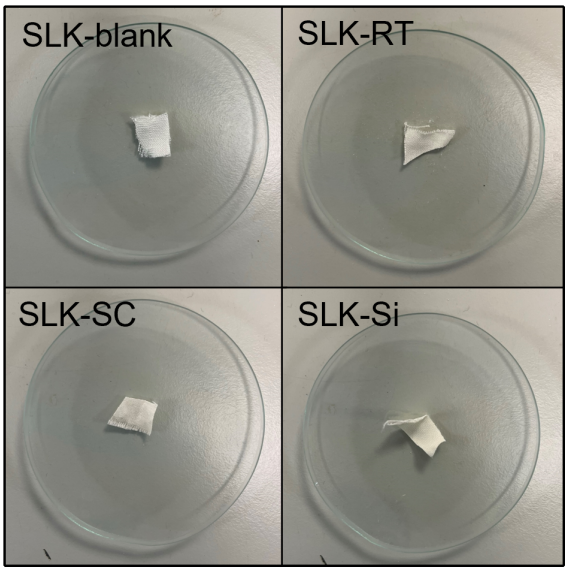

Figure 6.51: Appearance of silk fabrics before and after composite synthesis has taken place.

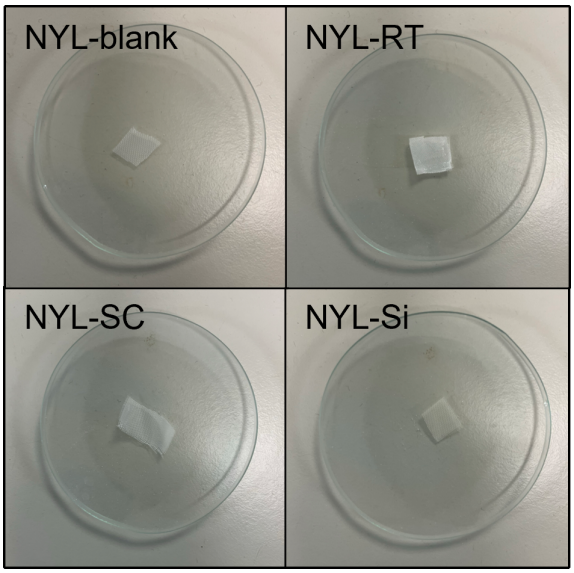

Figure 6.52: Appearance of nylon fabrics before and after composite synthesis has taken place.

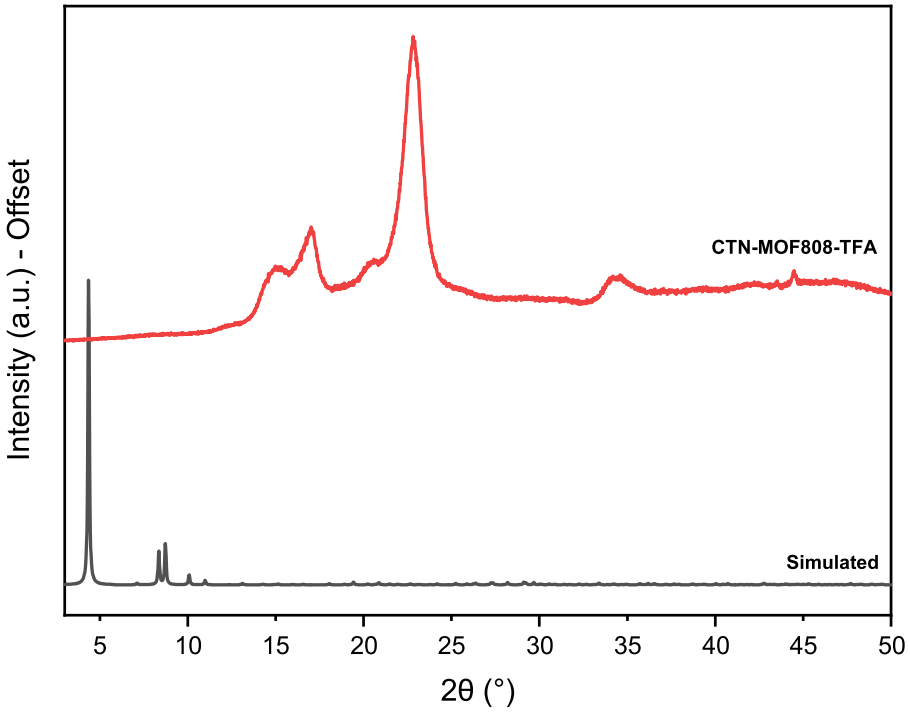

Figure 6.53: PXRD of polymer-MOF-808 samples synthesised through hydrothermal synthesis methods.

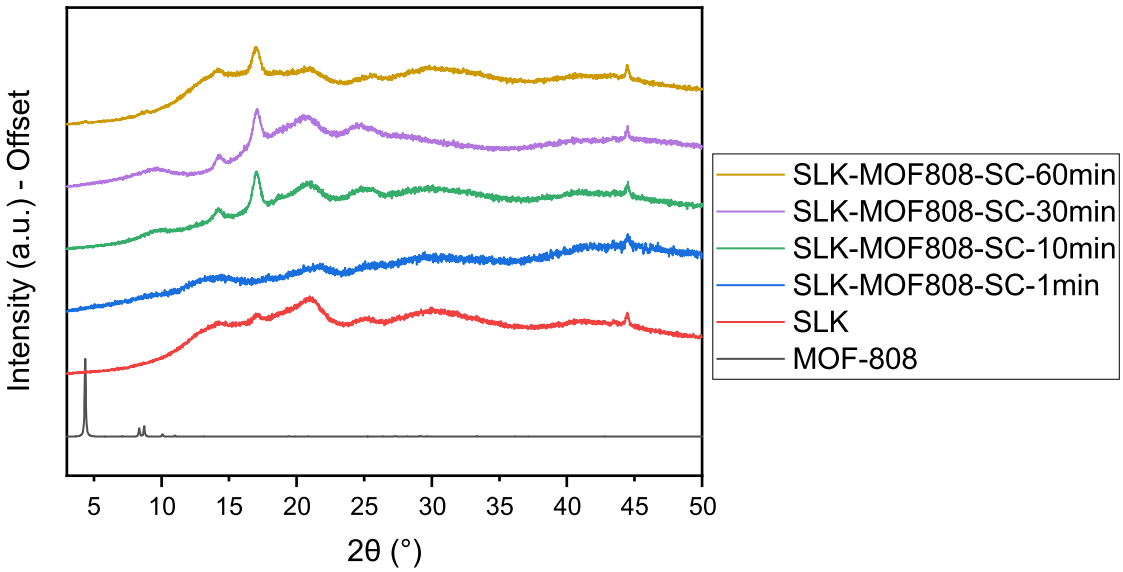

Figure 6.54: PXRD of SLK-MOF808-SC samples prepared at different reaction times.

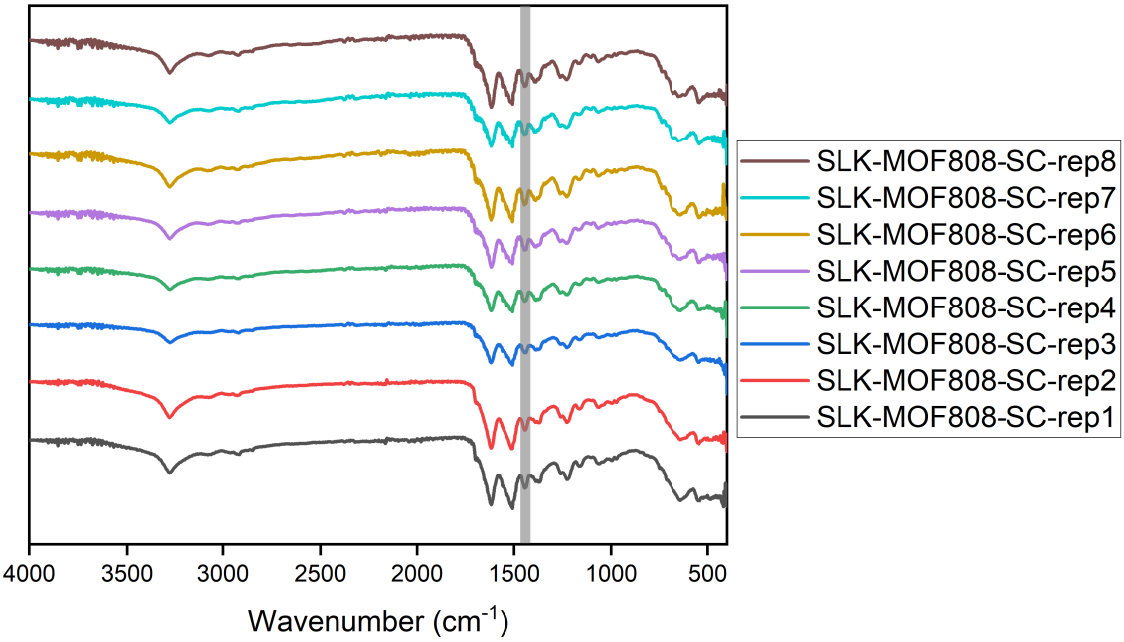

Figure 6.55: IR of SLK-MOF808-SC samples from synthesis repeated within the same solution. MOF-808 O-H bend highlighted with grey bar.

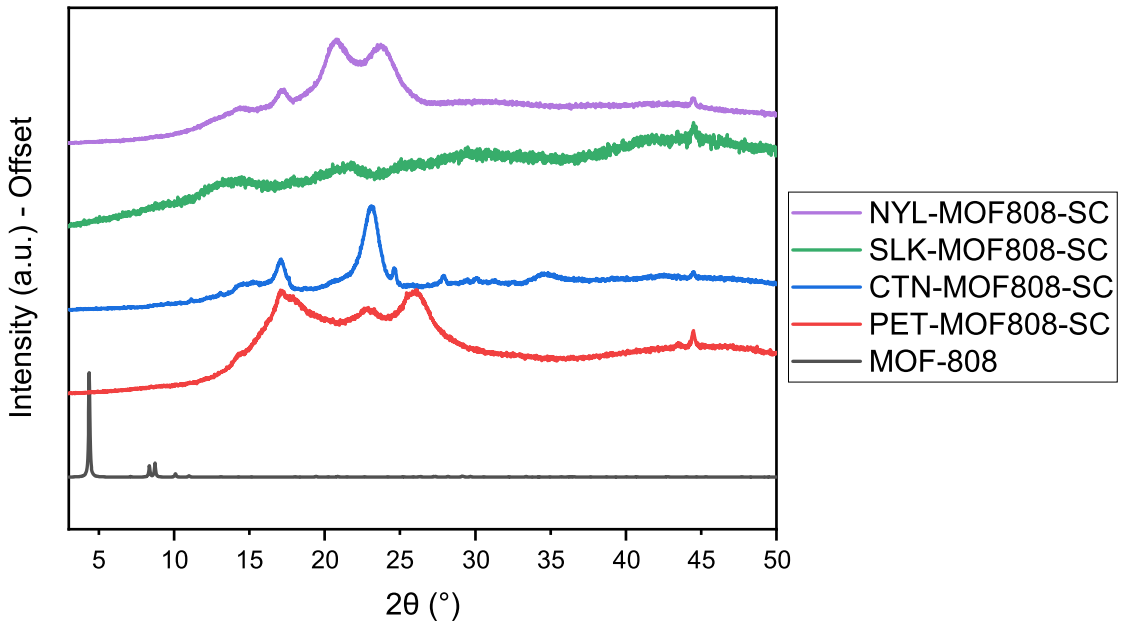

Figure 6.56: PXRD of sonochemical (SC) samples prepared on different fabrics.

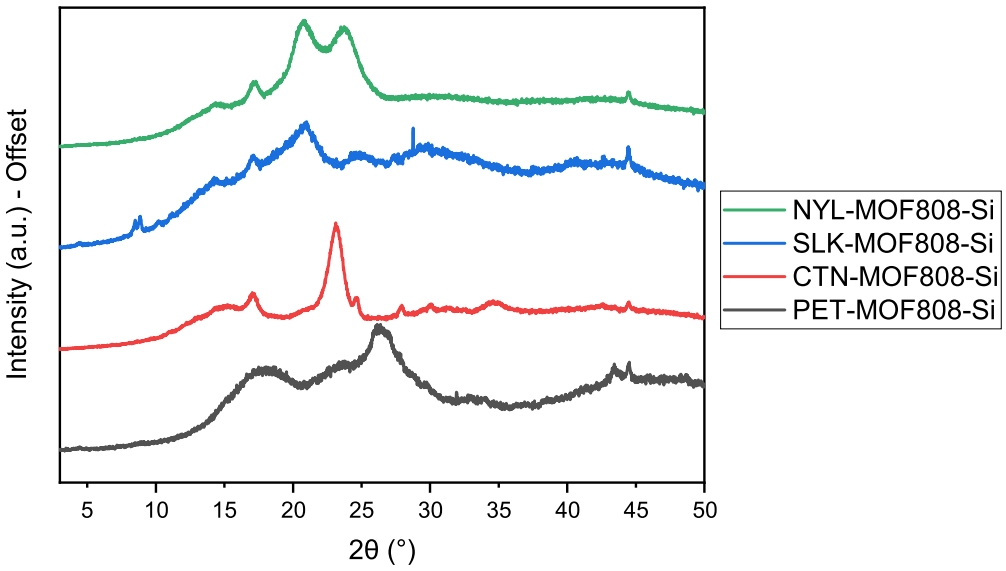

Figure 6.57: PXRD showing all samples synthesised through silane coupling.

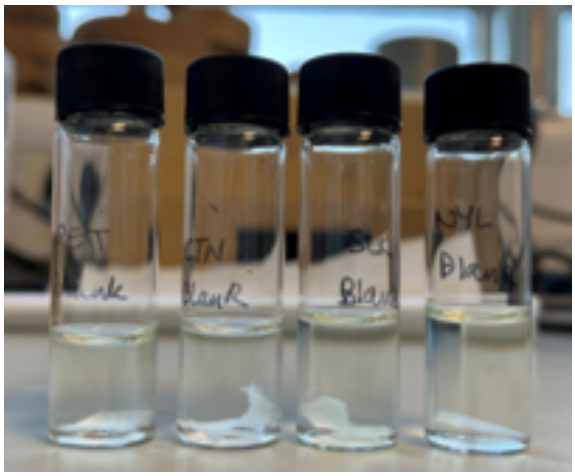

Figure 6.58: Appearance of blank fabrics after 24 hrs in NEM buffer solution, pH 10.

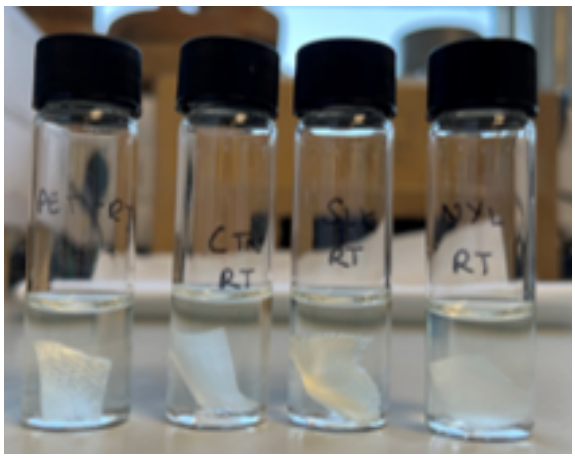

Figure 6.59: Appearance of all RT samples after 24 hrs in NEM buffer solution, pH 10.

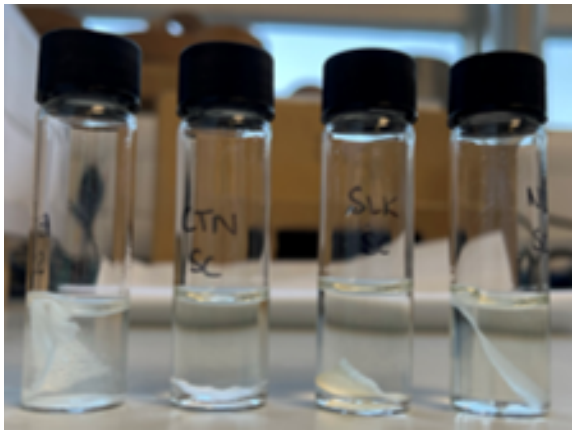

Figure 6.60: Appearance of sono-chemical samples after 24 hrs in NEM buffer solution, pH 10.

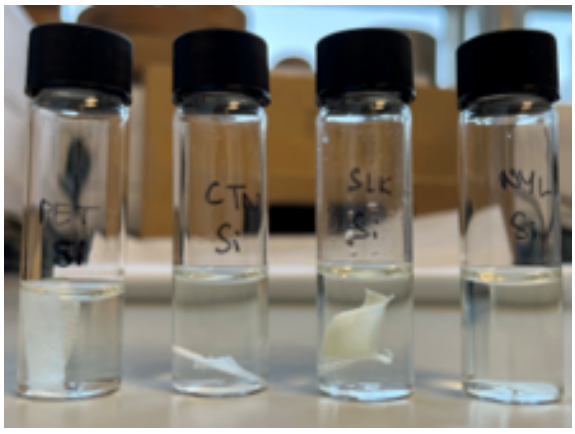

Figure 6.61: Appearance of silane coupled samples after 24 hrs in NEM buffer solution, pH 10.

Chapter 7

Conclusions and Outlook

The overarching aim for this Thesis was to prepare and investigate MOF catalysts for the destruction of nerve agents and simulants. A particular focus was to improve the catalytic performance of known Zr-MOFs by systematically altering the metal-nodes or linkers, and to incorporate Zr-MOFs into fabrics whilst retaining the catalytic properties.

7.1 Mixed-metal MOFs

In Chapter 4 a series of mixed-metal Hf/Zr-MOFs were successfully synthesised for the known MOFs, UiO-66, NU-1000 and MOF-808. Hf was added into each framework in 16% ($\frac{1}{6}^{\text{th}}$) intervals in order to lower the Lewis-acidity across the series. All materials were characterised with PXRD and EDS, then used as catalysts for the hydrolysis of the nerve agent simulant DMNP.

The mixed-metal UiO-66 series showed no change to the crystal structure upon the addition of Hf into the framework as determined by PXRD. The mixed-metal nature of the materials was confirmed by EDS measurements which confirmed that there was good agreement between targeted and resulting Zr/Hf percentages for each sample. The catalytic results for the UiO-66 samples were gathered using a high-throughput method carried out by Dr. J. Palomba. For the mixed-metal UiO-66 series there was no clear trend established between initial catalytic rates and Lewis-acidity, however, the 100% Zr UiO-66 sample gave the highest initial rate of the UiO-66 samples tested.

For the mixed-metal NU-1000 samples, a simplified synthesis method was implemented compared to literature,[1] which resulted in the successful preparation of the Zr/Hf NU-1000 series. As expected, the PXRD carried out showed no changes to the long-range crystal structure across the series as Hf is incorporated. EDS measurements were carried out and confirmed that each mixed-metal sample comprised of both Zr and Hf within the targeted percentages. The catalytic testing of these samples were carried out in-house using an *in situ* UV-Vis probe. The overall trend seen for mixed-metal NU-1000 supported the hypothesis as the increase in Hf into the framework, and therefore the decrease in Lewis-acidity, resulted in a decrease in rate across the series.

The final mixed-metal MOF series tested was Zr/Hf-MOF-808. For this material

three batches of the mixed-metal series was prepared. The PXRD carried out on all samples confirmed that all structures were consistent with literature, between both mixed-metal samples and batches. To ensure that both metals have been incorporated into each sample EDS was carried out. For all batches, and samples, the EDS measurements were in good agreement with the targeted percentages of Zr and Hf. Catalytic testing was carried out for the mixed-metal MOF-808 samples using a high-throughput method carried out by Dr. J. Palomba, and the calculated rates gave very interesting results with no overall trend being observed.

The catalytic results for batch 1 and 2 of the mixed-metal MOF-808 samples gave the highest initial rate value for the samples containing 33% Zr and 66% Hf. This indicates that this mixed-metal composition is having a beneficial effect on the catalysis when compared the 100% Zr, or other mixed-metal compositions. However, this result was not repeated in the Batch 3 mixed-metal MOF-808 samples, where the 50% Zr and 50% Hf sample gave the highest overall initial rate.

These samples were subject to further characterisation in an attempt to understand the differences in rate. Using EDS, TGA and DLS measurements the composition, stability and particle size of select samples was investigated. It was found for the 33% Zr and 66% Hf MOF-808 samples that batch 3 had a less accurate mixed-metal composition, fewer linker defects and a smaller particle size when compared to batch 1 and 2. These results indicate that Lewis-acidity does effect the catalytic activity of MOF-808, however other characteristics of the materials must be carefully controlled through the synthesis to ensure consistent catalytic results.

The introduction of Hf into the framework has a range of effects on catalytic performance of the MOFs tested. In the case of UiO-66 the difference in Lewis-acidity has little impact on the catalysis, for NU-1000 there is a positive correlation between increasing Lewis-acidity and initial rates, and finally there is a non-linear impact between Lewis-acidity and initial catalytic rates for mixed-metal MOF-808 materials.

To gain a better understanding of the relationship between Lewis-acidity in MOF-808 and initial catalytic rates, efforts could be made to control the struc-

tural properties during the synthesis. This could include preparing the samples with controlled particle size and defects. With all other variables constant, the change in rate with Hf percentage may be more clear. However, controlling MOF syntheses to prepare particles of a particular size, or controlling the quantity of defects is not a facile process, with many reported studies attempting this.[2,3]

In order to gain a better understanding of the mixed-metal nature of these materials, further investigations into the exact composition and structure could be carried out in a number of ways. Initially additional EDS measurements could be taken to give a elemental mapping image of each sample to ensure both metals are fully distributed across the sample.

More in-depth analysis could be carried out using solid-state NMR spectroscopy; previous reports have focused on using this technique for investigating mixed-metal materials.[4] This could be achieved through the enrichment of the mixed metal MOF-808 samples with ^{17}O post-synthetically through steaming experiments. Upon successful enrichment, NMR spectroscopy could be carried out in order to investigate the metal-oxygen linkages present in each sample. It may be possible to distinguish between Zr-O-Zr, Hf-O-Hf, and Zr-O-Hf bonds, allowing the SBUs within the mixed-metal MOFs to be identified. With this information, a correlation to the catalytic rates measured may be observed.

Another method that may be used to determine the elements within a mixed-metal SBU is with energy-dispersive X-ray spectroscopy. This has previously been used to successfully determine the positions of Ce and Zr atoms within a mixed-metal UiO-66 structure.[5]

To expand the scope of this work, other Lewis-acidic elements, such as Ti and Ce could be added to existing MOF frameworks to form mixed-metal MOFs. There is precedence for this, as both mixed-metal Zr/Ti and Zr/Ce MOFs have been prepared.[6,7] Catalytic testing, combined with in-depth structural investigations, could advance performance of known MOFs for this application.

7.2 Mixed-linker MOF-808

Owing to the successful results gained in Chapter 4 for mixed-metal MOFs, our attention turned to mixed-linker MOFs. In Chapter 5 four di-topic linkers were chosen to incorporate into the framework of MOF-808 alongside the standard BTC linker. The linkers chosen were 5-amino isophthalic acid, 5-hydroxy isophthalic acid, isophthalic acid, and pyridine-3,5-dicarboxylic acid.

Initial samples were prepared using 10 mol% of each di-topic linker in the place of the BTC linker within the solvothermal MOF-808 synthesis. The successful incorporation of each linker was determined by q-NMR spectroscopy. The percentages of di-topic linker in the resulting structures were in good agreement with the targeted 10%. The mixed-linker samples did not display any distortion or structural change as indicated by PXRD. The syntheses of each sample was repeated three times, and in each case there was good agreement for PXRD and q-NMR spectroscopy results, indicating high reproducibility in the 10% mixed-linker samples.

TGA analysis suggests that the addition of a di-topic linker to MOF-808 does not induce defects into the structure. All mixed-linker samples had a linker incorporation of *ca.* 100% relative to a perfect crystal structure. The TGA did show that all mixed-linker samples had a lower stability when compared to the parent MOF-808 structure, with the sample containing pyridine-3,5-dicarboxylic acid the least stable.

Further studies were carried out to incorporate a larger proportion of 5-amino isophthalic acid into the MOF-808 structure due to previously reported beneficial properties in amine functionalised MOFs for this application.[8] It was found that a MOF-808 structure can be successfully prepared with up to 60% di-topic linker within the synthesis. However, using q-NMR spectroscopy, the percentage of 5-amino isophthalic acid incorporated into the structure plateaus at 25%.

Post-synthetic linker exchange was also attempted to increase the percentage of 5-amino isophthalic acid in the MOF-808. These samples were determined through q-NMR spectroscopy to contain 50% di-topic linkers. However, TGA measurements showed these samples were much less stable than MOF-808.

The 10% samples, alongside the 5-amino isophthalic acid series samples were tested as catalysts for the hydrolysis of DMNP. All samples showed catalytic activity compared to a blank reference test. For the 10% samples, catalytic rates were slower in all cases when compared to pristine MOF-808. The 5-amino isophthalic acid samples gave interesting results as the 20% 5-amino isophthalic acid sample outperforming pristine MOF-808 and all other mixed-linker samples.

Overall, Chapter 5 results show that mixed-linker MOF-808 samples can be reproducibly synthesised in a one-step process with a range of di-topic linkers. The ratio of linkers can be determined by digestion q-NMR spectroscopy techniques and the overall proportion of linkers within the structure determined by TGA. Although additional functional groups have been added to the MOF-808 structure, defects have not been induced by the addition of a di-topic linker. The catalytic testing has shown that in specific proportions, addition of 5-amino isophthalic acid can out-perform pristine MOF-808 as a catalysis for the hydrolysis of DMNP.

In order to gain a greater understanding of the increased catalytic rates seen for the amine-functionalised samples, further material characterisation should be carried out. Using DLS, the average particle size of each sample may be determined. It would be interesting to learn if there is a correlation between particle size and proportion of di-topic linker, as the particle size also has an effect on this catalysis.[9]

Further investigation into functionalising MOF-808 would be beneficial, as other known Zr-MOFs such as NU-1000 and UiO-66 have shown improved catalytic rates when an amine group is present on the linker.[8] Rather than a mixed-linker approach, the functionalisation of the BTC linker could be attempted. This may allow a greater proportion of functional groups throughout the structure, and not impact the stability as is the case with mixed-linker MOF-808. However, the synthesis or purchasing of functionalised BTC linkers is costly.

Although this work did not successfully induce defects into MOF-808 through a mixed-linker approach, further work could focus on inducing defects through the addition of modulators and reaction conditions.[10] The introduction of defects in a systematic way has yet to be fully investigated for MOF-808. However, the MOF-808 SBU already has a relatively low connectivity of 6-linkers, therefore missing linker defects may not impact the catalytic activity.

7.3 MOF-composites

In Chapter 6 four materials were successfully used to prepare MOF-808 composite materials using three separate synthesis methods. The fabrics, PET, cotton, silk, and nylon, were chosen due to literature precedent, with each comprising of different functional groups on the surface. The three synthesis methods implemented were room-temperature hydrothermal, sonication, and post-synthetic silane coupling.

The materials synthesised using the room-temperature hydrothermal method all contained MOF-808 as determined by q-NMR spectroscopy. The highest loading was calculated at 29.4% for PET, and the lowest at 4.1% for cotton. This wide range of loadings between the materials indicates that the functional groups within the fabrics impact MOF-808 formation and adhesion to the fabric.

The sono-chemical synthesis method resulted in a very high loading of 72.4% MOF-808 for PET. However, the cotton, silk and nylon fabric recorded a relatively low loading of between 3.5% - 0.8%. This method was therefore not as successful as the room-temperature synthesis, however, this synthesis method requires short reaction times and allows reusability of the reaction solution.

For the silane-coupled synthesis method, relatively low loadings were calculated for all materials, with the highest loading observed for the PET material at 10.6%. Both cotton and nylon had negligible MOF-808 loadings of 0.9% and 1.8% respectively. This was the least successful synthesis method of the three. However, this work did show that silane-coupling is another technique to consider for MOF-composite materials.

All composite samples were tested as catalysts for the hydrolysis of DMNP. Each catalytic test was carried out using 100 mg of sample as MOF-808 loading values may not be accurate. All samples showed catalytic activity and outperformed the blank sample, with the exception of the nylon MOF-808 sample synthesised through silane coupling. No composite material outperformed MOF-808, which was to be expected.

The highest rates were observed for the room-temperature synthesised materials, with the PET material displaying the highest rate overall. This result is in line

with previous literature reports of composite materials using PET.[11] However, the synthesis method reported in this thesis is preferable as it does not use TFA or DMF so is more environmentally friendly and easier to scale.

The samples prepared through sono-chemical synthesis all show catalytic activity despite relatively low loadings. This is a promising initial result as further investigations into this synthesis method may allow higher loadings on the materials in short reaction times, leading to higher catalytic rates. The silane-coupled synthesis also gave promising initial results as the PET, cotton and silk samples were catalytically active. As very little work on this composite material synthesis has been reported to-date, this is an interesting avenue to explore further with respect to MOF materials.

The work carried out in this Thesis on MOF-808 composite materials gives a large scope for further work. The immediate focus should be on achieving accurate loading measurements. The techniques used to determine loading, such as digestion NMR spectroscopy, gave adequate loading values, however, as TGA measurements were unable to support these values, another method should be carried out. Inductively Coupled Plasma Optical Emission Spectroscopy (ICP-OES) analysis would be able to determine the percentage of Zr within each material. This would allow a comparison to the MOF-loadings calculated with q-NMR spectroscopy, and allow accurate calculation of catalysis loading within each experiment.

Porosity measurements should also be carried out on these materials to ensure the porosity of the MOFs have been somewhat retained when combined with a material. Some loss of porosity would be expected due to the material blocking the MOF channels, however, with this knowledge it would allow greater understanding of the catalytic activity.

Alongside further characterisation, work to increase the loadings of MOF-808 onto these fabrics, and to ensure negligible MOF-leaching from the materials should be carried out. Many studies have introduced layers above and below the composite materials to allow the catalytic species within the MOF, but to stop leaching.[12] Additionally these layers may also act as buffers for the catalysis, allowing the reaction to take place at neutral pH, without a buffer in solution.[13]

Finally, the incorporation of mixed-metal and mixed-linker MOF-808 from Chapter 4 and Chapter 5 into composite materials should be carried out. The catalytic testing of these would allow further insights into the performance of each material, and the suitability of these MOFs for real-world applications.

7.4 Catalysis

All catalytic testing in this Thesis has been carried out in the solution state, using a NEM-buffered solution at pH 10. Instead of a nerve agent, the simulant DMNP has been used throughout as it is the closest mimic to sarin, without the safety implications.

In order to advance this work, efforts must be taken to test these materials at a lower, or neutral pH. Work in this area has shown that at a lower pH the catalytic rates of MOFs may change, therefore success at pH 10 does not guarantee successful catalysis at pH 8.[14] Other work has also shown that each MOF has an optimum pH for this catalysis, therefore the mixed-metal MOFs in Chapter 4 should be tested as it was found that the SBU is the determining factor of optimum pH.[15]

Successful reactions in the solid-droplet interface, in the absence of solvent, are also required for these catalysts to be implemented in filters and protective suits. These reactions would require a base to either be present in the composite material, or coordinated into the MOF. As MOF-808 has open metal sites, it may be possible to introduce polymeric bases into the material as previous literature has shown; these bases must be nonvolatile and stable to the by-products produced in the reaction so as not to poison the catalyst.[16]

The final aim would be to test the prepared MOFs and composite materials with live nerve agents, such as sarin, instead of the simulant DMNP. This work would have to be carried out in specialist labs, such as at DSTL, with government collaborators.

7.5 References

[1] J. E. Mondloch, W. Bury, D. Fairen-Jimenez, S. Kwon, E. J. Demarco, M. H. Weston, A. A. Sarjeant, S. T. Nguyen, P. C. Stair, R. Q. Snurr, O. K. Farha and J. T. Hupp, *J. Am. Chem. Soc.*, 2013, **135**, 10294–10297.

[2] K. A. S. Usman, J. W. Maina, S. Seyedin, M. T. Conato, L. M. Payawan, L. F. Dumée and J. M. Razal, *NPG Asia Mater.*, 2020, **12**, 58.

[3] Z. Fang, B. Bueken, D. E. DeVos and R. A. Fischer, *Angew. Chemie., Int. Ed.*, 2015, **54**, 7234–7254.

[4] G. P. M. Bignami, Z. H. Davis, D. M. Dawson, S. A. Morris, S. E. Russell, D. McKay, R. E. Parke, D. Iuga, R. E. Morris and S. E. Ashbrook, *Chem. Sci.*, 2018, **9**, 850–859.

[5] K. A. Lomachenko, J. Jacobsen, A. L. Bugaev, C. Atzori, F. Bonino, S. Bordiga, N. Stock and C. Lamberti, *J. Am. Chem. Soc.*, 2018, **140**, 17379–17383.

[6] S. Yuan, J.-S. Qin, H.-Q. Xu, J. Su, D. Rossi, Y. Chen, L. Zhang, C. Lollar, Q. Wang, H.-L. Jiang, D. H. Son, H. Xu, Z. Huang, X. Zou and H.-C. Zhou, *ACS Cent. Sci.*, 2018, **4**, 105–111.

[7] E. Geravand, F. Farzaneh, R. Gil-San-Millan, F. J. Carmona and J. A. R. Navarro, *Inorg. Chem.*, 2020, **59**, 16160–16167.

[8] T. Islamoglu, M. A. Ortuño, E. Proussaloglou, A. J. Howarth, N. A. Vermeulen, A. Atilgan, A. M. Asiri, C. J. Cramer and O. K. Farha, *Angew. Chemie., Int. Ed.*, 2018, **57**, 1949–1953.

[9] K. Y. Cho, J. Y. Seo, H.-J. Kim, S. J. Pai, X. H. Do, H. G. Yoon, S. S. Hwang, S. S. Han and K.-Y. Baek, *Appl. Catal. B.*, 2019, **245**, 635–647.

[10] G. W. Peterson, M. R. Destefano, S. J. Garibay, A. Ploskonka, M. McEntee, M. Hall, C. J. Karwacki, J. T. Hupp and O. K. Farha, *Chem. Eur. J.*, 2017, **23**, 15913–15916.

[11] K. Ma, T. Islamoglu, Z. Chen, P. Li, M. C. Wasson, Y. Chen, Y. Wang, G. W. Peterson, J. H. Xin and O. K. Farha, *J. Am. Chem. Soc.*, 2019, **141**, 15626–15633.

[12] J. Liu, H. Li, B. Yan, C. Zhong, Y. Zhao, X. Guo and J. Zhong, *ACS Appl. Mater. Interfaces*, 2022, **14**, 53421–53432.

[13] J. Y. Seo, J.-H. Lee, K. Y. Cho, K. Jeong and K.-Y. Baek, *Chem. Mater.*, 2023, **35**, 1624–1632.

[14] J. M. Palomba, C. V. Credille, M. Kalaj, J. B. DeCoste, G. W. Peterson, T. M. Tovar and S. M. Cohen, *Chem. Commun.*, 2018, **54**, 5768–5771.

[15] A. M. Ploskonka and J. B. DeCoste, *J. Hazard. Mater.*, 2019, **375**, 191–197.

[16] T. Islamoglu, S. Goswami, Z. Li, A. J. Howarth, O. K. Farha and J. T. Hupp, *Acc. Chem. Res.*, 2017, **50**, 805–813.